warwick.ac.uk/lib-publications

Effect of internal oxidation in bendability of UHSS

By

Yuyi Zhu

A thesis submitted in partial fulfilment of the requirements for the degree of

Doctor of Philosophy in Engineering

University of Warwick,

Warwick Manufacturing Group, January 2019

Declaration

This thesis is presented in accordance with the regulations for the degree of Doctorate of Philosophy. It has been written and compiled by myself and has not been submitted anywhere else. The work in this thesis has been undertaken by me except where otherwise stated.

Signed: Date:

Abstract

Ductile Ultra High Strength Steels (UHSS), the so-called third generation of Advanced High Strength Steels (AHSS), are increasingly used for automotive applications. The strengthening alloying additions in the dual phase UHSS, such as Mn and Si show significant impact on the oxidation behaviours. The changes in surface and subsurface morphologies due to external and internal oxidation during the steel processing have consequences for the quality and performance of the final product.

The internal oxidation zone (IOZ) initially forms during cooling of the hot rolled product will lead to surface defects of the galvanised steel sheet. This phenomenon is known to affect the formability of the steel sheet. The development of the multi-layered external oxides during hot rolling largely influence the internal oxidation.

This PhD project focuses on three critical studies upon UHSS:

- Characterisation of scale and sub-scale development during steel processing.

- The influence of internal oxidation on the bendability.

- The influence of coiling environment on the internal oxidation.

In-depth analyse have been conducted on the external (scale) and internal (subscale) oxidation layer. A mixed surface characterization methods is designed, therefore, Wustite, magnetite, hematite and fayalite can be identified and localised within the coil-cooled scale structure. The subscale structures are characterised by (Secondary electron microscope) SEM and (Transmission electron microscope) TEM, the nature of the manganese and silicon-enriched precipitates are then understood. The oxide development are monitored on the coil cooled, cold rolled, annealed and galvanised steel sheets, the relationship between the steel processing conditions and surface/subsurface morphologies is determined. The effect of coil cooling temperature, coil geometries as well as the atmospheres within the tightly warped steel sheets can lead to variation in oxides development throughout the coil. A deep internal oxidation layer formed at earlier stages will lead to cracking of the oxidised grain boundaries during cold rolling. Therefore, the follow on gravanising and forming process become invalid.

Deformation experienced during the steel sheet forming processing are simulated by the in-situ bending stage and analysed by the digital image correlation (DIC) technique, based on lab-scale samples. The microscopic strain distribution and failure mechanisms established a link between the near-surface conditions and the forming limit of the final product. The oxidised grain boundaries are

proved to promote crack initiation, whereas the banding structure within the dual phase steel matrix promotes crack propagation.

Industrial heat treatments are replicated in specially designed furnaces with gas analyse technique. The evolution of oxides at elevated temperature and varies coil cooing conditions are studied to elucidate the link between scale decomposition, decarburisation and internal oxidation. Micro-pores are found to form within the fayalite-wustite mixed layer, which is a sign of wustite reduction. The reduction of these wustites is assisted by the steel decarburisation as concentrated CO and CO_2 signals are detected. Meanwhile, the magnetite layer thickness is reduced and oxygen is detected. The reduction of the external oxides is a continuous process, which promotes the internal oxidation consistently during the coil cooling. The shrinkage of the overall scale thickness has no direct influence on the subscale development.

list of abbreviations

AHSS	Advanced high strength steels
BIW	Body in white
BSE	Backscattered electron
CP	Complex phase
CT	Coiling temperatures
DIC	Digital image correlation
DP	Dual phase
EBSD	Electron backscatter diffraction
EDS	Energy Dispersive X-Ray Spectroscopy
FB	Ferritic bainitic
FIB	Focus ion beam
GA	Galvannealed
GHG	Greenhouse gas
GI	Galvanized
HCL	Hydrochloric acid
HF	Hot formed
HPW	High-pressure water
HSS	High strength steel
IOZ	Internal oxidation zone
IR	Infrared
LHT	Laying head temperature
MP	Multiple phases
MS	Martensitic
MZ	Magizinc
OM	Optical microscopy
RDT	Roughing delivery temperature
ROI	Region of interest
RT	Room temperature
RTF	Radiant tube furnace
SE	Secondary electron
SEM	Secondary electron microscope
STEM	Scanning transmission electron microscope
TEM	Transmission electron microscope
TGA	Thermal gravimetry analyses
TRIP	Transformation-induced plasticity
TWIP	Twinning-induced plasticity
UHSS	Ultra high strength steels
XRD	X-ray diffraction
YS	Yield strength

Contents

4

Chapter 1: Introduction

1.1. Background

The reduction of greenhouse gases and CO_2 emissions have become a vital objective to all manufacturing industries due to environmental concerns. European Standards [1, 2] have introduced regulations for the automotive industry to produce new vehicles with reduced fuel consumption and lower CO_2 emissions. Increasingly stringent standards of automobile collision safety regulations [3, 4] require the development of vehicles with high crashworthiness in addition to lower weight. The use of thinner, hence lighter, UHSS sheets with improved (or equivalent) functional properties have shown significant advantages in meeting environmental and safety regulations.

Steels with a tensile strength above 780MPa combined with relatively good ductility (around 20% elongation, but not clearly defined) are defined as UHSS [5, 6]. Cold stamping and roll forming are advanced processes to shape thin sheets, generally 0.5 - 2cm thick depending on the specific alloy, at room temperature [7]. Automobile reinforcement parts, such as bumper beams and pillars are normally shaped from UHSS steel sheets (e.g. dual phase (DP) grades such as DP1000 & complex phase (CP) such as CP1000). The roll forming process shows significant advantages in energy saving and production efficiency when compared to conventional methods, such as hot stamping. Roll forming could also improve the formability of UHSS sheet by deforming material through incremental, localised bending [8].

The surface conditions of the steel play a significant role during the forming process. Apart from the microstructural heterogeneities and decarburisation effects, oxidation is a key factor controlling the surface morphology. An internal study reported that the external and internal oxidation occurs due to the exposure of the material to high temperatures and oxidising atmospheres. Oxides have a higher preference to form at grain boundaries due to the lower nucleation energy being required. The external oxide layer (scale) can be removed by water jet descaling during processing or by acid pickling; however, internal oxides (inclusions) cannot be removed without damaging the steel surface. If the sub-surface grain boundaries of the galvanized steel product are highly decorated with internal oxides, the bending behaviour may be affected.

The thickness of the subscale (equivalent to the internal oxidation zone) in the hot rolled sheet is

determined by the amount of oxygen available as well as the steel compositions and the kinetics (time and temperature exposed) [9].

1.2. Project objectives and challenges

Specific formability is required for the UHSS in automotive markets. The required bending angles vary depending on the strength, microstructure and structure compositions (e.g. dual phase, complex phase, etc.). The commercial products do not always fulfil the bendability angle requested [10]. Although it is known that the main factors influencing bendability are surface conditions and the proportions of steel phases present (bainite, martensite, ferrite), little is known about the mechanisms behind these two factors and their potential interactions on the bending behaviour. With respect to the influence of the surface and near-surface, there are two known sources of surface weakening, which are the internal oxidation during the coil cooling after hot rolling, and the other is the internal oxidation during annealing before galvanising. After coil cooling, the steel sheet is further processed by pickling and cold rolling, which raises the possibility of surface cracking and grain boundary weakening. Therefore, the internal oxidation during coil cooling might be more detrimental to bendability. These coils then undergo annealing prior to galvanizing, potentially introducing further defects. The internal oxidation is not always detectable from the industrialised coils because sampling is normally performed at the coil head/tail. In reality, internal oxidation is more apparent at distances greater than 100m into the hot rolled product, and approximately 200m from the head or tail of the galvanised product (data from internal documents). In this case, modelling internal oxidation kinetics will assist greatly in understanding the relationship of coil position on the sampling and ultimately in controlling product yield.

While the bending tests are focussed on annealed and galvanised steel sheets, as bendability is most important in the final steel product, the internal oxides form initially at the coil cooling stage after hot rolling. After descaling and hot rolling, the steel sheet is coiled and passively cooled. The cooling rate varies within the coil due to its massive size and complex geometry. This makes the development of internal oxides at specific coil positions unpredictable.

Also, when multiple alloying elements are present in the steel, the kinetics and thermodynamics of oxide formation changes with their interactions and possible formation of compound oxides. Generally,

external and internal oxidation occurs simultaneously, which further increases the complexity of modelling efforts to predict the growth of the IOZ.

In this work, the formation and growth of internal oxides are monitored throughout the steel processing stages. Coil cooling, pickling and cold rolling are simulated under lab conditions to understand the development of the surface and subsurface morphology.

The formability of a metal sheet corresponds to the maximum strain or stress it can bear before cracking during the forming process, the bending angle at this strain/stress determines the bendability [2]. Many factors may influence the bendability of a material, such as its mechanical properties, microstructure and the tooling specifications. Higher tensile strength will undoubtedly decrease the bendability, but it is not clear about the influence of various microstructure features on the damage mechanisms during bending. The steel phase proportions and surface conditions are two main factors that influence the bendability. The boundaries of two dissimilar phases, for instance, martensite and ferrite, may act as sources for void and crack initiation. The surface conditions are influenced largely by the presence of oxides [11, 12].

The internal oxidation both after coil cooling and after annealing is potentially a major factor affecting the mechanical properties [13], but no publications are available studying this relation. The extent of oxidation varies within the annealed and galvanised steel coil. The relationship between the internal oxidation depth and the bendability is also unknown. In this study, systematic bending tests are applied to inspect the uniformity of bending behaviour across the width of the galvanised coil. The influence of surface defects on bendability and the failure mechanisms during bending are characterised. By simulating the sheet steel processes, the influence of intermediate processing steps, such as pickling and cold rolling is determined. Full-field deformations are analysed at the microscopic point of view when surface defect and microstructural imperfection exist at the same time.

The oxidation kinetics in coil cooling conditions is studied to understand the formation mechanisms of multi-layer external oxides and its influence on the internal oxidation. The coiling environments are reproduced in lab conditions to understand the phase changes of oxides during the cooling period. The relationship between the scale development and the subsurface oxide growth is characterised.

2.1. Advanced & Ultra High Strength Steels in the automotive industry

Both Advanced High Strength Steels (AHSS) and Ultra High Strength Steels (UHSS) are being used to develop environment-friendly and safe vehicles. They are crucial in the body-in-white (BIW) of vehicles as the structural and safety parts. Fig. 1 shows that by comparing to conventional steels, the AHSS contained car body can achieve 25% mass reduction of the BIW without compromise in mechanical properties. Approximately 9% (117kg) overall weight reduction can be reached for a standard 5-door family car. This weight reduction will lead to 2.2 tonnes of CO_2 saving during the vehicle's lifetime, which is larger than the total amount of CO_2 emission during vehicle production. In addition, every 10% reduction in weight will lead to 5.1% better fuel economy on average and 5.7% (roughly 8kg) less of GHG emission over its full life cycle. All savings are based on negligible cost change in BIW manufacturing [14].
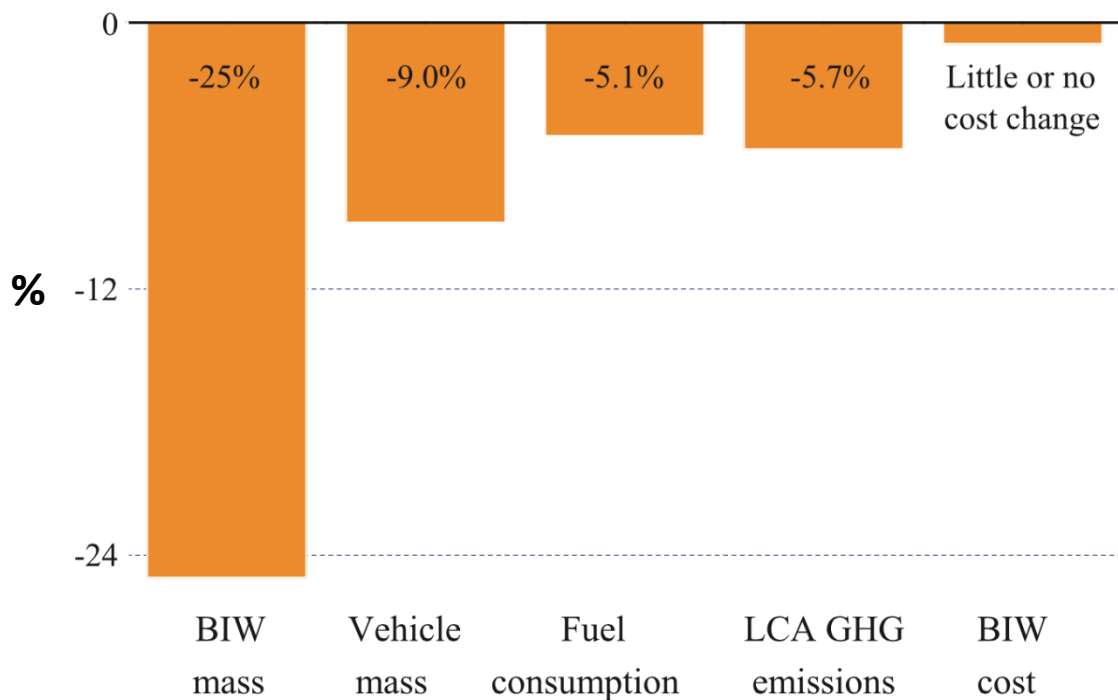
Fig. 1. Mass, fuel, emission and cost-saving by using AHSS as body structure in contrast with conventional steels [14].

UHSS have been developed from AHSS. First and second generation AHSS have various categories, which include dual phase (DP), complex phase (CP), hot formed (HF), ferritic bainitic (FB), martensitic (MS), transformation-induced plasticity (TRIP), and twinning-induced plasticity (TWIP). They are made for specific functional requirements, such as DP and TRIP steels, which show superior behaviour when used in the crash zones of the vehicle, and benefit from their high energy absorption coefficient [5]. Recently, the development of the third generation of AHSS gained significant interest in both commercial and scientific communities. In contrast to the conventional low carbon low alloyed grades, it has improved strength combined with ductility due to its unique composition and microstructure [15]. The properties of different steel families are shown in the global formability diagram (Fig. 2) [5].
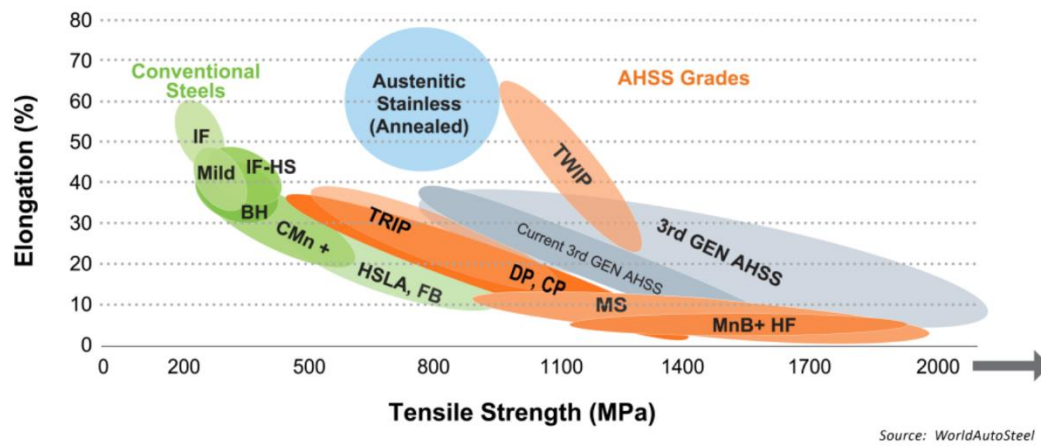
Fig. 2. Fracture elongation and tensile strength for main steel product families [5].

The conventional high strength steel (HSS) has a yield strength from 210 to 550 MPa and tensile strengths from 270 to 700 MPa, whereas AHSS have yield and tensile strengths greater than 550 and 700 MPa respectively [16]. When the tensile strength rises above 780 MPa, but below 1400 MPa, the steel is normally defined as UHSS [5, 6]. Fig. 2 indicated that austenitic stainless steel has a good combination of strength and ductility. Therefore, austenitic stainless steel can satisfy the requirement of many different components that require relatively high strength. However, the price becomes a problem due to the high concentration of alloying elements it contained. Some other steels like hot formable steels can reach more than 1200 MPa tensile strength, but new manufacturing set up is required with high tooling cost. The UHSS is thus designed to achieve high strength and high ductility without compromising the cost [5].

2.2. Categories of UHSS

Reche [2] mentioned that the three leading families of UHSS are DP, CP (MP) and TRIP steels. DP steels contain martensite or martensite/ bainite islands as hard phases dispersed evenly in the softer ferrite matrix. The resulting steels are not only strong and ductile but also have excellent fatigue resistance due to their high strain hardening capacity. DP steels are suitable for automobile structural and reinforcement parts (e.g. longitudinal beams).

CP steels are composed of a much finer microstructure, which can be a mixture of ferrite and bainite or martensite and bainite. Precipitation hardened structures in single bainite microstructure are also possible. The resulting products combine high yield strength (YS) with relatively good formability and resistance spot weldability. CP steels are usually applied to automotive safety parts that require excellent impact resistance (e.g. bumper beams, door reinforcements).

TRIP steels consist of evenly distributed hard bainite and austenite islands within a ductile ferrite matrix. This steel undergoes a transformation-hardening effect, where retained austenite is transformed into martensite under load at high strain rate to inhibit any initiated crack. This crack bunting results from the volume expansion effect during phase transformation. As a result, TRIP steels can delay the onset of necking with improved ductility [17].

2.3. Processing of UHSS

2.3.1. Steel sheet making

To achieve higher strength-ductility balance, the core technology is to control the processing conditions and microstructure to, for example, develop desired phase transformation products and reinforcing phases, like martensite, bainite and retained austenite. Also, weldability and surface qualities need to be optimised to satisfy post-processing requirements, such as galvanising and painting.

It is essential to understand the critical steps in AHSS production. Fig. 3 [2] is an illustration of the TRIP steel production line. After the steelmaking and continuous casting processes, the slab undergoes four main processes: ① hot rolling, ② coiling, ③ cold rolling and ④ annealing. Hot rolling mainly

reduces the slab thickness and controls the thickness uniformity. The temperature during hot rolling is above the recrystallisation temperature of the specific steel (usually above 927°C) to maintain an equiaxed microstructure and prevent the work hardening effect [18]. The steel sheet is descaled before the last train of finishing rolling, then it is coiled for storage and transportation. Details of the coil cooling process will be explained in a later sector (p. 56). Cold rolling is then performed on a sheet that had the oxide scale removed by acid pickling. During cold rolling, it is deformed below the recrystallisation temperature to reach the desired thickness and shape, and the strength increases significantly by strain hardening [19]. The subsequent annealing cycle is aimed to recrystallise the grains, modify the phase proportions and promote the bainitic/martensitic transformation (for complex phase steels) to meet the product specification. The detailed heat treatment process is illustrated in Fig. 4 [2], where Ac_1 and Ac_3 are the temperatures at which austenite begins to form and ferrite completely transforms into austenite, respectively [20].
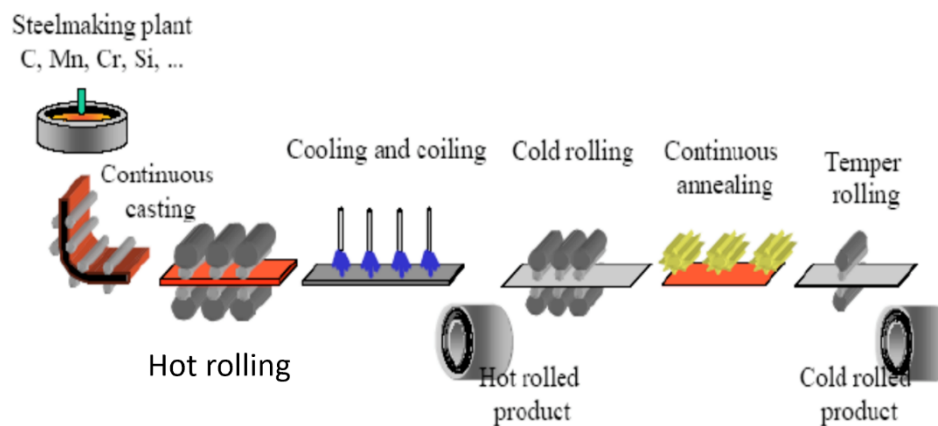
Fig. 3. The processing line of TRIP steels [2].
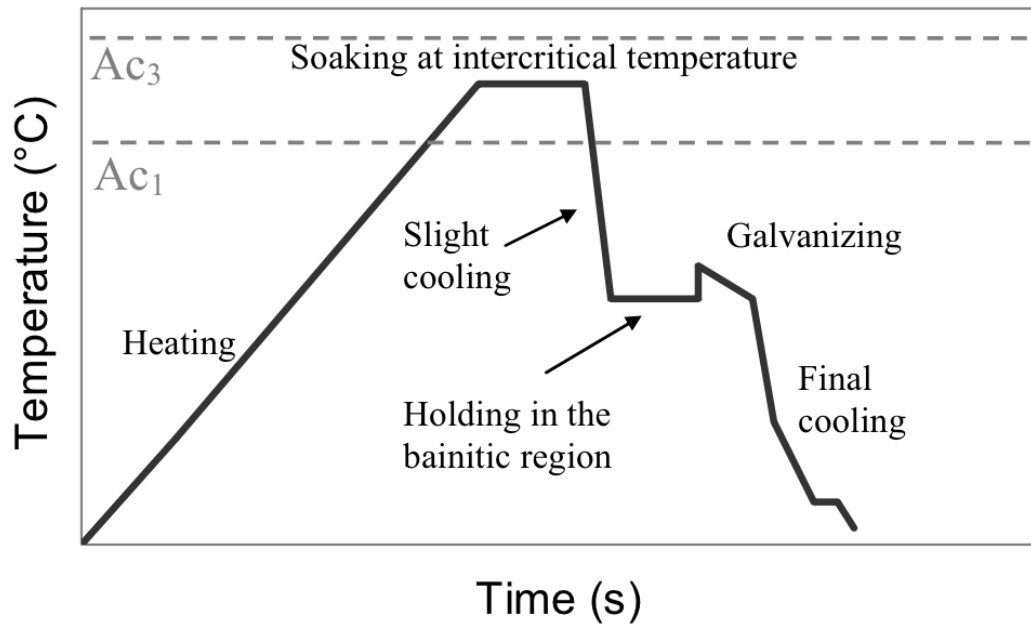
Fig. 4. Annealing cycle for TRIP steels [2]. Ac1 and Ac3 stand for onset and finish temperature of austenitic transformation, respectively.

2.3.2. Galvanising

In the automotive industry, the introduction of a zinc-based coating on the steel surface has given cars significantly increased corrosion performance. The galvanising process not only provides the steel sheet with a physical barrier but also acts as a sacrificial cathodic layer to prevent corrosion of the steel under it [21]. The coating is normally applied by dipping the annealed steel sheet through a molten zinc-based solution bath, an example of the hot-dip galvanising line is given in Fig. 5 [22]. After exiting the zinc pot/bath, the air knife pressure can be adjusted to control the coating thickness and hence the weight. The strip is now a galvanized (GI) steel. After the zinc pot, there is the option of applying a very short annealing process which allows for the formation of galvannealed (GA) coating. Other bath compositions such as magizinc (MZ, a trademark of Tata Steel) or AlSi can also be used.
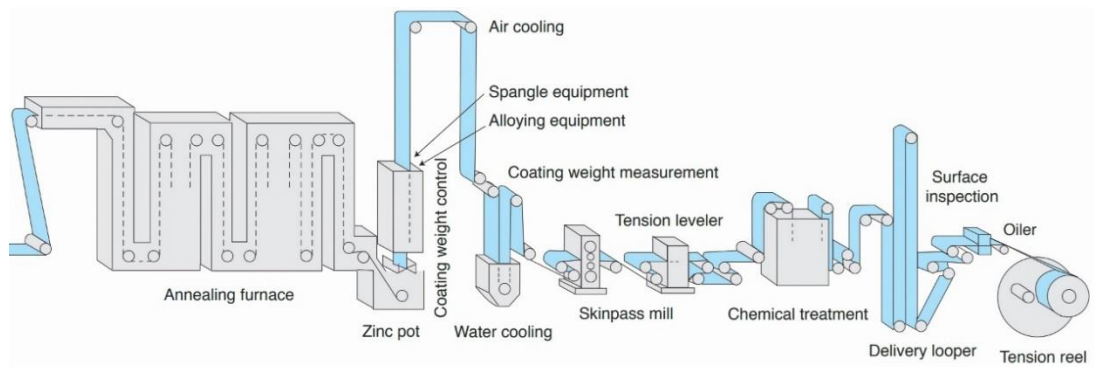
Fig. 5. Hot-dip galvanising line (adapted from [22]).

However, the development of AHSS brings a challenge to the galvanising process. The high content of alloying elements (e.g. Mn and Si) in the steel matrix will oxidise during annealing prior to hot-dip galvanising. The selective oxidation on the steel surface and subsurface have negative influence on the zinc wettability, with defects like bare spots or total delamination occurring [21]. Full oxide formation mechanisms will be explained later (p. 28 & p. 47). A few methods are suggested to improve the zinc adhesion. Bleck [23] mentioned that by increasing the dew point within the annealing atmosphere, external oxidation could be inhibited to maintain a good steel surface finishing for galvanising. However, excessive internal oxidation of selective elements occurs at high dew point, changing the surface as well as near surface properties. Alternatively, pre-oxidation is a well-known method, which improves the surface quality of metallic coated AHSS. Peroxidation consists of controlling the annealing atmosphere, to allow a controlled thickness of iron oxide to grow on the steel sheet surface. When a thin and continuous layer is formed, it can be reduced back to iron and leaves a pure iron top layer ready for galvanising. In this case, the surface quality could be improved significantly and the selective internal oxidation is minimised [24].

2.3.3. Stamping

After the steel processing described above, the coiled steel sheet is sent to automotive industries for product manufacturing. Stamping is a process to shape the thin-walled metal components using punches and dies [7]. Stamping is generally applied on sheet metals with thickness between 0.5 and 3mm, the exact thickness value depends on the steel formability. The formability is the ability of a material to be bent, stretched and drawn. The formability of a material is directly related to its ductility.

15

Stamping conditions, such as the die design, press speed, and lubrication, will also influence the formability [25]. Traditionally, cold stamping is applied in automotive industries. Mori *et al.* [26] mentioned that most of the present steels used in passenger vehicles have tensile strengths less than 600 MPa. However, UHSS have higher tensile strengths and generally lower formability. Failure may occur if the forming conditions are not considered carefully, an example is shown in Fig. 6 [2]. The spring-back effect after stamping of UHSS must also be considered to prevent deterioration in dimensional accuracy. As a result, hot/ warm stamping has been developed, which allows the possibility of larger, stronger and complex shaped UHSS stamped products. Steps involved in hot stamping are shown in Fig. 7 [27]. During hot stamping, UHSS sheets are heated until they are malleable. Rapid cooling is applied after pressing in specifically designed dies to obtain a hardened product with the required shape complexity. The advantage of hot stamping UHSS is the ability to maintain the performance with a 35% weight reduction of individual components [11].

Fig. 6. A long crack formed on the bumper beam after stamping due to overestimated material's formability [2].
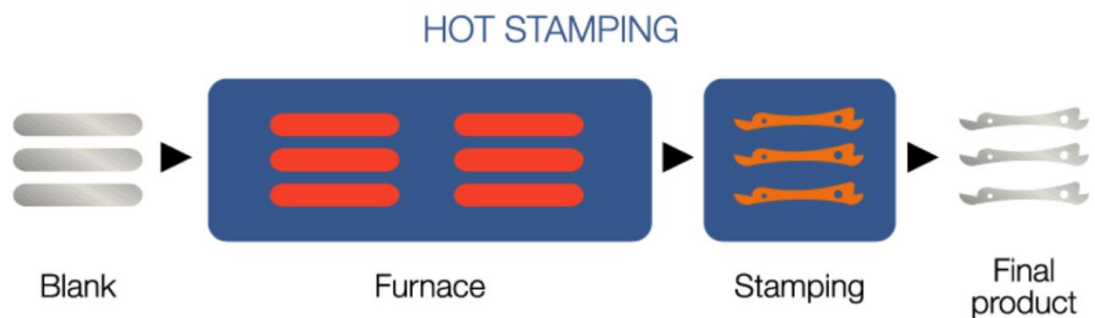
Fig. 7. Illustration of the hot stamping process [27].

Although the steel sheets are heated in a furnace, the temperature will still drop during the transportation to the stamping press. Generally, sheets are heated above the required temperature as compensation. However, as oxidation of steel is much faster at higher temperatures, the subsurface

oxides might also play a role in bendability. Liquid metal embrittlement can occur, and this is one of the challenges of hot stamping GI steels.

Several new stamping methods have been developed to maximise the product size, strength and complexity but minimise the oxidation effects, spring-back and energy cost. For example, Mori *et al.* [26] combined warm and hot stamping with rapid resistance heating; the mechanisms are shown in Fig. 8. In this process, the sheet is held by two electrodes and heated directly inside the die. The time between heating and the forming process is just 0.2 s, which not only prevented temperature drop, but was also insufficient time for oxidation.
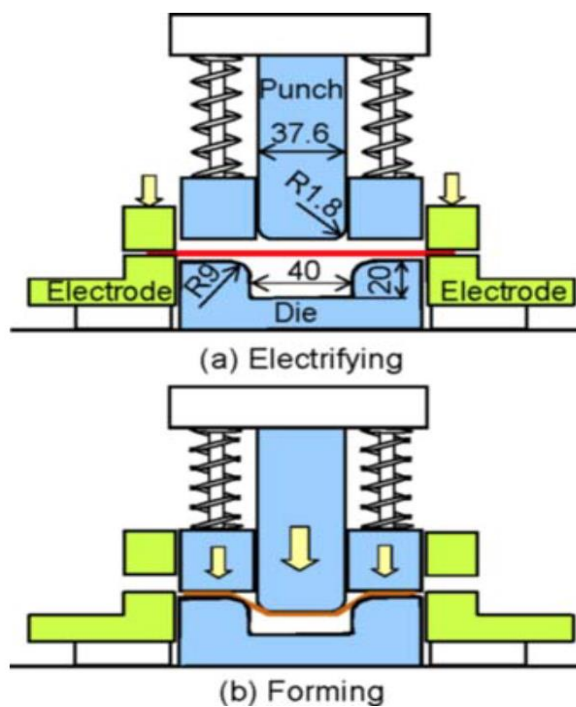
Fig. 8. Hot and warm stamping combined with rapid resistance heating [26].

2.4. Roll forming

Roll forming is a room temperature sheet metal forming process, it shows significant advantages in energy saving and production efficiency compared to conventional methods, such as hot stamping. Roll forming could also improve the formability of UHSS sheet by deforming material through incremental, localised bending. The metal sheet bends as it moves through a series of rollers that are mounted on adjustable stands. The sets of stands could vary from 4 to 25, depending on the

complexity of the final sheet geometry [8]. Han *et al.* [28] described roll forming as a highly non-linear, strongly coupled and multivariable process. Secondary fabrications processes, such as holes, notches, slots and embossments, can be added to the rolling forming production line to reduce the cost and improve the level of integration [29]. Although the steel sheet is bent gradually after passing through each set of rollers, a relatively large spring back effect will still occur, especially for the UHSS. The overbending angles of the last roller and the bend edge radii are two critical parameters to be considered to control the spring back effect [28]. Also, in comparison to the mild steel grades, more rolling steps are required to form UHSS into the desired geometry when spring back is considered [30]. It is important for the roll formable steel sheet to have a good bendability, because otherwise, cracks will initiate before the desired geometry of the final product is achieved. As an example, the author was involved in a parallel roll forming project and observed an industrial trial of the rolling process. Long cracks initiated at the locations where a higher bending angle was required during processing, and the trial sheet failed completely at the exit mills (as shown in Fig. 9). The failure was due to either the wrong estimation of the sheet's bendability, or the wrong set up parameters of the rollers.
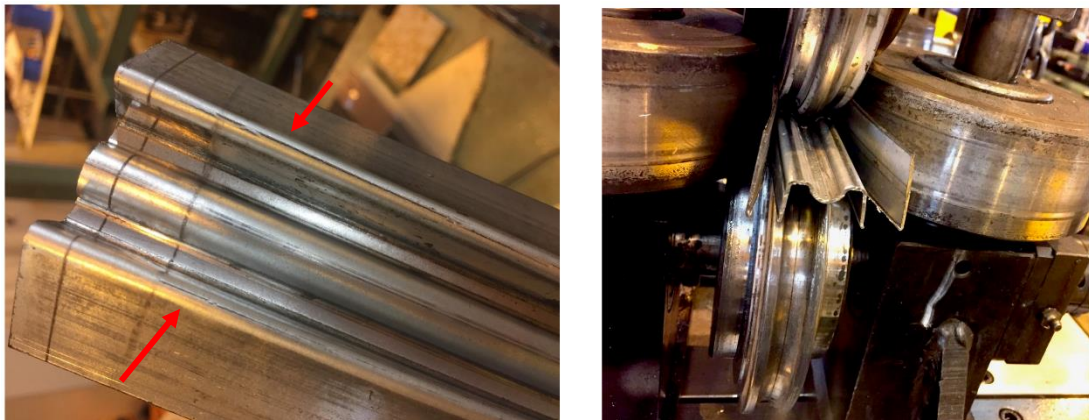
Fig. 9. Roll forming trial sheets failed during the process. The arrows highlight the positions of crack initiation.

2.5. Bending and Bendability

The formability of a metal sheet corresponds to the maximum strain or stress it can reach during the forming process. The formability largely depends on the bending limit, which is the critical strain that leads to crack initiation at the outer surface of the bending zone. The bending limit also refers to the

ratio between the minimum bend radius and the original sheet thickness at which the bending process is accomplished successfully [2, 19]. Bendability of sheet metals can be assessed by applying a series of tests.

There are three categories of bending tests, simple bending is applied without tension, whereas both bending and tension are applied simultaneously during stretch bending and draw bending. The mechanisms are shown in Fig. 10 [31]. However, in reality, 3-point bending undergoes pure bending with a weak tension (negligible), which is induced by the torque on both sides of the sample[2].
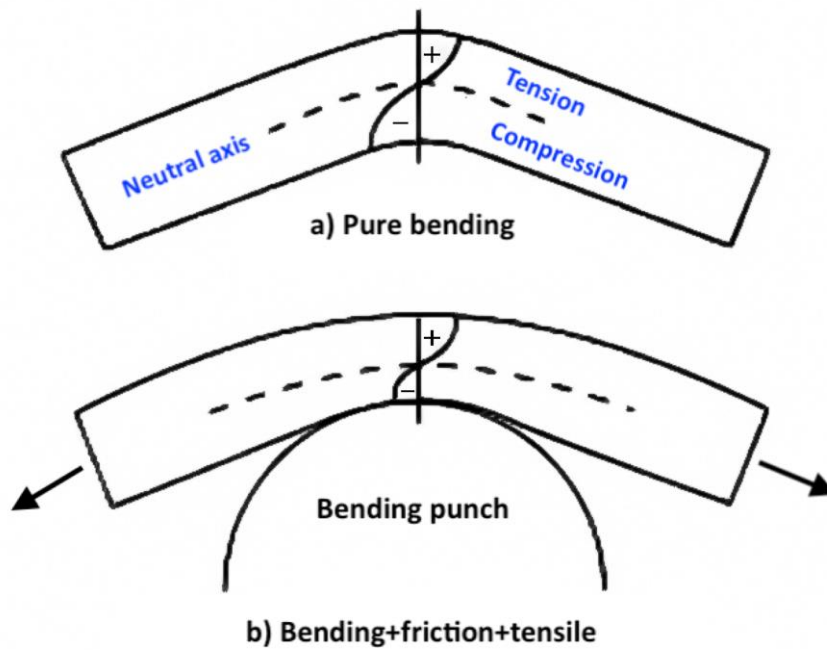
Fig. 10. Illustration of (a), pure bending and (b), bending +friction +tensile with their stress distribution (adapted from [31]).

The deformation in the sample during bending is initially elastic and then transfers to plastic modes until cracks initiate. Kaupper *et al.* [10] mentioned that an inhomogeneous multi-axial state of stress and strain occurs during the bending of sheet metals. Tensile stress presents next to the outside of the bending zone, whereas compression stress exists inside. The boundary between tensile and compression stress zone is called the neutral axis, which is indicated by the dashed line in Fig. 10.

2.5.1. Air bending

The simple set up and high efficiency makes the air bending test the most commonly used method. In this test, the maximum bending angle of a sample sheet for a specified bending radius can be determined. As Fig. 11 shows, an air bending test machine consists of a punch (punch size is adaptable) in the middle and two dies to place the sample. This test can be interrupted as soon as any crack is initiated. The automatic termination of the test is based on any drop of the load-displacement curve, which sketched concurrently during sample bending. A drop in load can directly reflect the presence of microcrack initiation. The test is usually set to stop after 5-10% drop of the load, and the sample is then taken off to check if any crack exists using a magnifying lens.
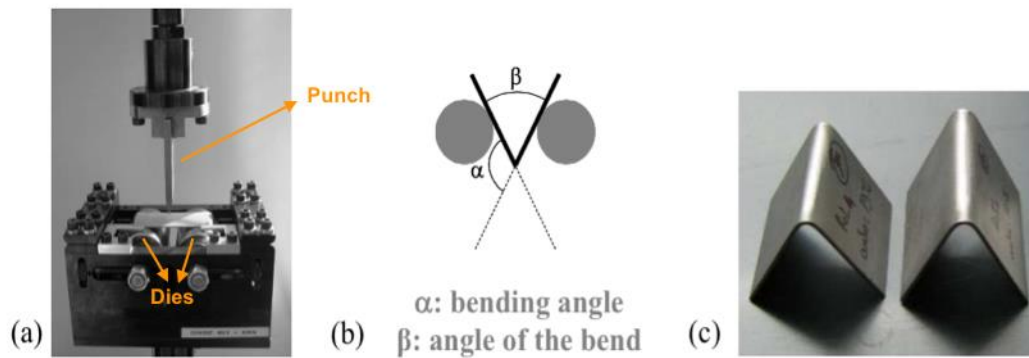
Fig. 11. Illustration of the a) air-bending device, b) bending angle, c) sheet sample after bending test [2].

The air-bending test, however, may not work on samples with high ductility. For example, Reche [2] applied the test on TRIP steel samples with 770 MPa tensile strength and 25% elongation. No cracks initiated until the limit of the device was reached (bending angle >165°). Also, The sheet deformation under the stamping conditions in the automotive industry is more complicated than simple bending. For example, the stretching force induced by the friction between the sheet metal and the mould can not be simulated by the simple bending.

2.5.2. Stretch bending

The stretch bending test provides both tension and bending at the same time because the sample edges are clamped between the die and the blank holder (as shown in Fig. 12). Sheet samples will be more likely to crack under a stretch bending test than air bending because of the extra tensile force applied [2]. In this case, this test is able to determine the bending limit under a varying of punch radii, R. Thus, the R/t ratio (t is the sheet thickness) for each test can be calculated to provide a formability ranking.
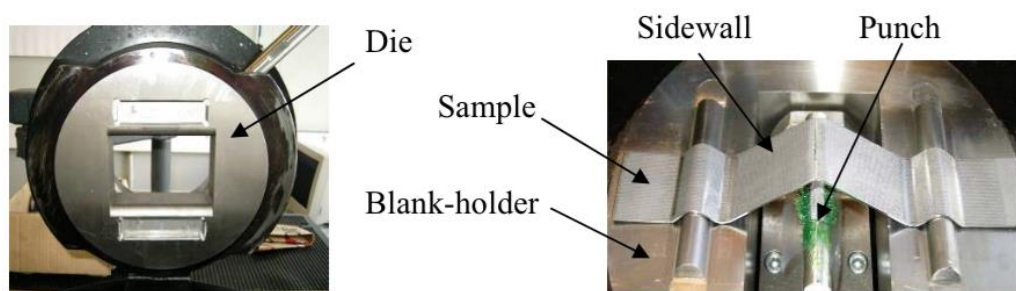
Fig. 12. Illustration of the stretch bending device [2].

However, the sample edges during stretch bending are clamped by a hydraulic press. The test can no longer be interrupted immediately after the first crack initiates as the stored hydraulic energy will push the punch further. The bending angle (α) can only be obtained when the test is finished. α is determined by joining the broken specimens and measuring with a protractor. New devices have been designed to improve the stability, which relies on a very low displacement rate (0.05mm/s) and regular stopping of the test to obtain non-propagating cracks.

Theoretically, the steel sheet thickness during roll forming is not changed. Also, simple bending is involved as the edges are unconstrained. In reality, a slight stretching force is involved due to the contact between the sheet and the rollers, even when well lubricated. The bending profile now involves both bending and stretching. Therefore, a slight amount of thinning effect does occur, and the local strain magnitude is often higher than for simple bending [32].

2.5.3. Bending test improvement

Kaupper *et al.* [10] utilised another bending test in their research, as shown in Fig. 13. In their test, air-bending is applied with the addition of a high resolution (less than 1mm) CCD camera to detect defect size and distribution. In addition, an optical strain measurement system ARAMIS is applied to allow measuring of the deformation and damage distribution at the sample surface (outer fibre). It is suggested to apply two or more bending trials on each set of tests to improve the accuracy and to reflect the real situation in the industrial stamping process.
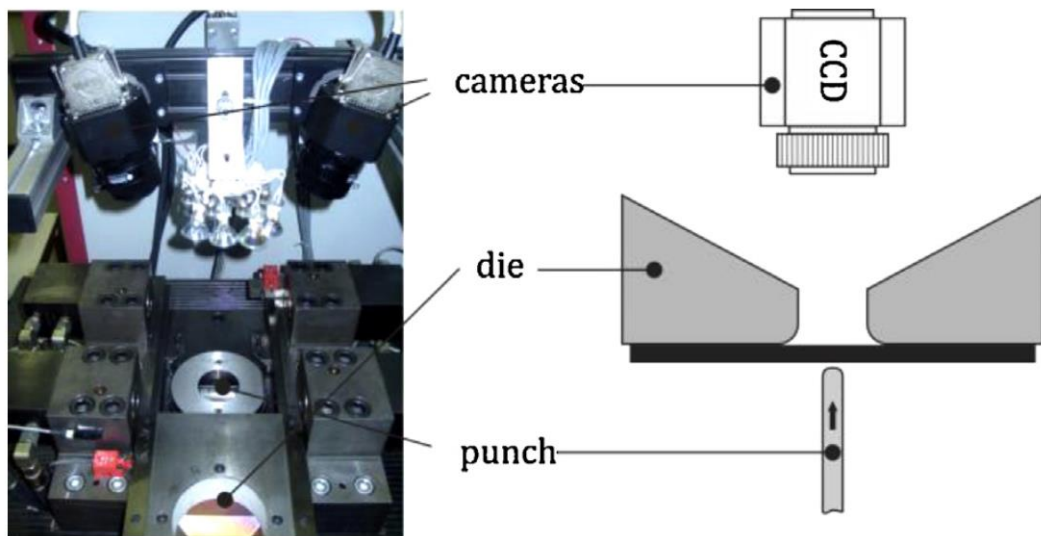
Fig. 13. Illustration of air bending device with an optical strain measurement system [10].

2.6. Failure modes

Many factors may influence the bendability of a material, such as tooling, mechanical properties and microstructure. Higher tensile strength will undoubtedly decrease the bendability, but it is not clear about the influence of various microstructures on the damage mechanisms during bending. Regarding the tooling, Nagataki *et al.* [25] reported that the simple bending test follows shear mode crack initiation, propagation and void nucleation. Steninger *et al.* [33] also clarified that cracks appear at the outer surface of the sample and propagate along shear bands. Also, voids are preferred to expand along the

22

shear direction. In addition, Chien *et al.* [34] found two common failure modes, necking and shear localisation. The necking results from void nucleation, growth and coalescence. Sheet failure depends on the ability to neck of the inner (less strained) fibre. However, the sheet is usually assumed to fail once the outer fibre exceeds its critical limit for safety purposes.

For stretch bending, the failure depends on the R/t value. When the value is under $(R/t)_c$ (c means critical), bending predominates overstretching, whereas failure occurs at the side wall instead of the punch nose when $(R/t)_c$ is reached, as shown in Fig. 14 [2].
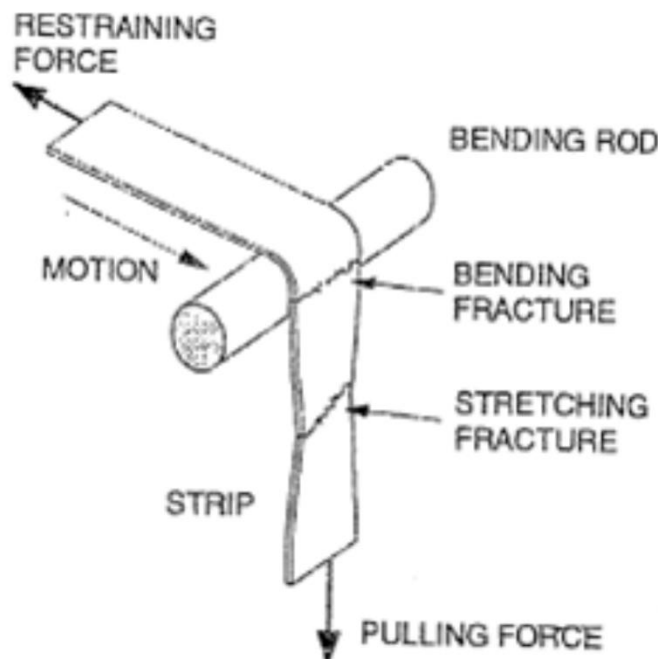
Fig. 14. Failure mechanisms during stretch bending [2].

Internal inhomogeneity is always a factor in damage. Generally, there are two main categories of internal inhomogeneity in steel, inclusions and microstructural heterogeneities (proportion of steel phase present and their distribution). Cracks become more likely to occur during bending if inclusions are present at the surface (or subsurface), hence bendability is lowered [35]. The location, dimensions and orientation of inclusions will be modified after the rolling processes. Inclusions are elongated along the rolling direction and lead to lower bendability in the transverse direction.

On the other hand, in a dual phase (martensite in ferrite matrix) UHSS, Yamazaki *et al.* [11]

demonstrated that the ferrite phase undergoes higher strain than the harder martensite. Also, cracks are more likely to initiate at the boundaries of two phases that exhibit different strain rates during bending. They concluded that although inclusions are preferred to be eliminated in steel, microstructural inhomogeneity has a predominant influence on bendability. However, although the interface between two phases with dissimilar hardness is one of the main sources for void initiation and fracture, the influence of internal oxidation is non-negligible. Internal oxidation occurs during the coil cooling after hot rolling and annealing. Both of the situations might lead to surface weakening [36, 37].

The development of selective phase combinations in steel is essential during steel processing for properties optimisation. Allain [38] applied hole expansion tests on 780 MPa grade steels with different phases combinations. The results are shown in Fig. 15, where elongation decreases and hole expansion ratio (λ, which is a fracture based parameter) increases after transformation of the ferrite matrix into bainite after the controlled annealing process. λ is calculated from:

$$\lambda = \frac{D_h - D_0}{D_0} \times 100 \tag{1}$$

Where Dh and D0 are average hole diameter after rupture and original hole diameter, respectively [29].
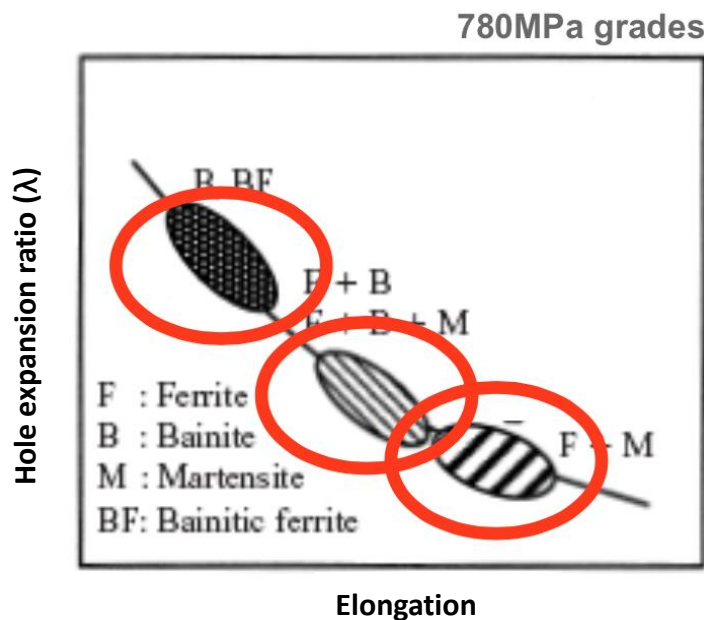
Fig. 15. Hole expansion ratio and elongation profiles of 780 MPa grade steels with ferrite/ martensite, ferrite/bainite and bainite/bainitic ferrite combination of microstructures [38].

The hole expansion test determines the ability of steel edges to resist cracking during stretching. It is

24

important because any excess material after the stamping processes is trimmed off before further operations. The large tensile stresses applied at the edges during trimming may lead to crack initiation. Hence it is clear that bainite and ferrite combination will lead to higher λ than martensite in ferrite matrix although the elongation value decreases. It is always preferred to develop microstructure to increase the hole-expansion ratio without sacrificing the tensile properties [39].

2.6.1. Microsegregation and macrosegregation

During steel processing, banded structures may form during cooling after hot rolling; an image is shown in Fig. 16 [40]. The micro and macrosegregation can explain the banding textures formation. Segregation means heterogeneity of the composition after solidification in the as-cast steel. Microsegregation represents compositional variations at the dendritic scale (between 10 and 100μm), whereas macrosegregation is at product scale (few mm to cm) [2].
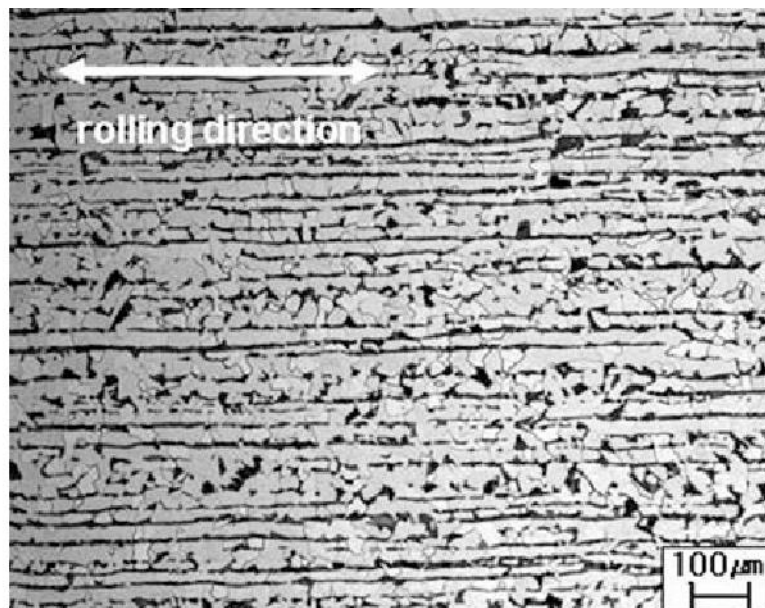
Fig. 16. Banded microstructure in hot-rolled steel [40].

Variations in mechanical properties and microstructure in cast products are caused by segregation and are preferred to be eliminated. Homogenisation heat treatment can reduce the microsegregation

significantly. However, the removal of larger scale macrosegregation is challenging [41].

During the cooling of the continuous casting, columnar grains grow inward from the slab surface with the liquid phase remaining in the centre. The liquid phase is further cooled at a slower rate, which promotes the formation of equiaxed dendrites in the liquid. Dendrites can fracture, and the pieces tend to sink because of their higher density compared to the surrounding liquid. High concentrations of dendrites will suppress further growth of the columnar zone, but the remaining liquid can still flow within the dendrite networks, resulting in a mushy central zone. The macroaggregated zone is formed under bulging and shrinkage of the slab during rolling, as shown in Fig. 17 [2].

Bulging means expansion and compression of the slabs periodically when passing through the rolls. As a result, the interdendritic liquid flow will influence segregation due to the regular deformation of the mushy central zone. Furthermore, shrinkage occurs at the end of solidification, which creates local depressions that suck up segregated liquid into the slab centre. The last remaining liquid phase is enriched with alloying elements, such as Mn and Si, because the solid grains have lower solubility of these elements. Thus, these elements repartition to the liquid during solidification, which leads to axial segregation forming in the centre of the slabs.
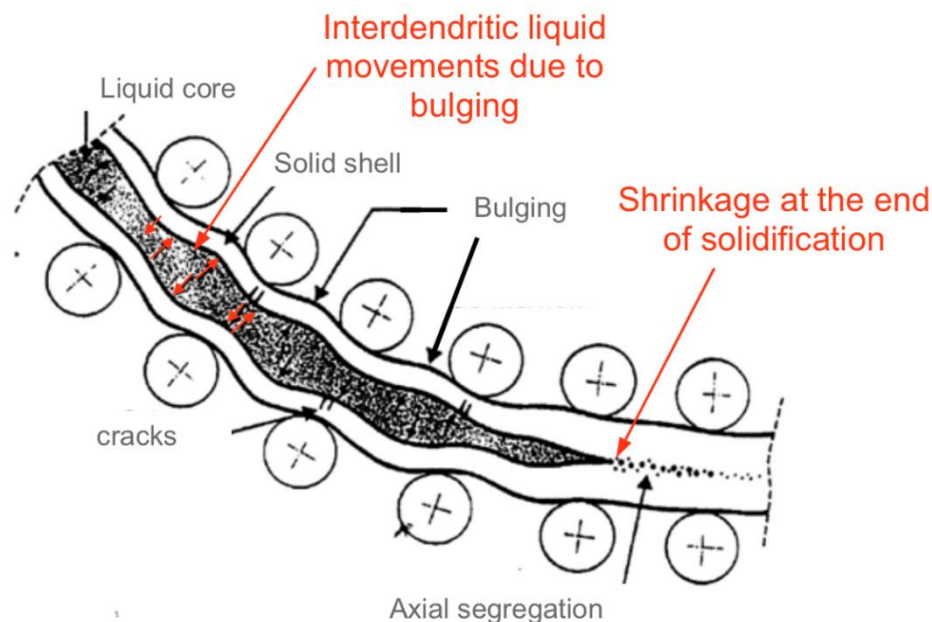
Fig. 17. Bulging and shrinkage of the slab during continuous casting (rolling direction towards the right) before solidification complete [2].

On the other hand, at a smaller length scale, when dendrites are nucleating and growing, solute redistribution occurs and leads to a solute concentration difference between the core and arm of the dendrite. This is described as microsegregation. The dendrite size is larger in the slab centre than edge because of its longer solidification time. In this case, microsegregation is more severe in the centre as compared to the slab surface.

Reche [2] mentioned that the level of microsegregation depends on the diffusion coefficient of the alloying element and the size of dendrites. For example, higher contents of C, Mn and P will promote microsegregation. Refining dendrite size by controlled cooling or superheating treatments will help to lower the level.

In Reche [2] experiments, both air bending and stretch bending were applied on banded samples and the damage modes were recorded via light microscopy. The results show cracks accumulated on the banded structure, as shown in Fig. 18. This is due to the higher local hardness of the bands as compared with the matrix; hence less amount of strain can be sustained before failure. Fig. 18 and Fig. 19 show damage after air-bending and stretch bending tests on TRIP steels, respectively. Thicker bands are determined to be more sensitive to bending than thinner bands. All cracks are propagated in a 45° angle, not only due to the strain fields but also the sensitivity of TRIP-aided steels to strain localisation. In contrast, cracks are more likely to occur at the sample surface/subsurface under air-bending, whereas stretch bending cracks are more likely to take place in the centre. Air-bending is estimated to be more sensitive to banded structures, but central segregation dominates for stretch bending.
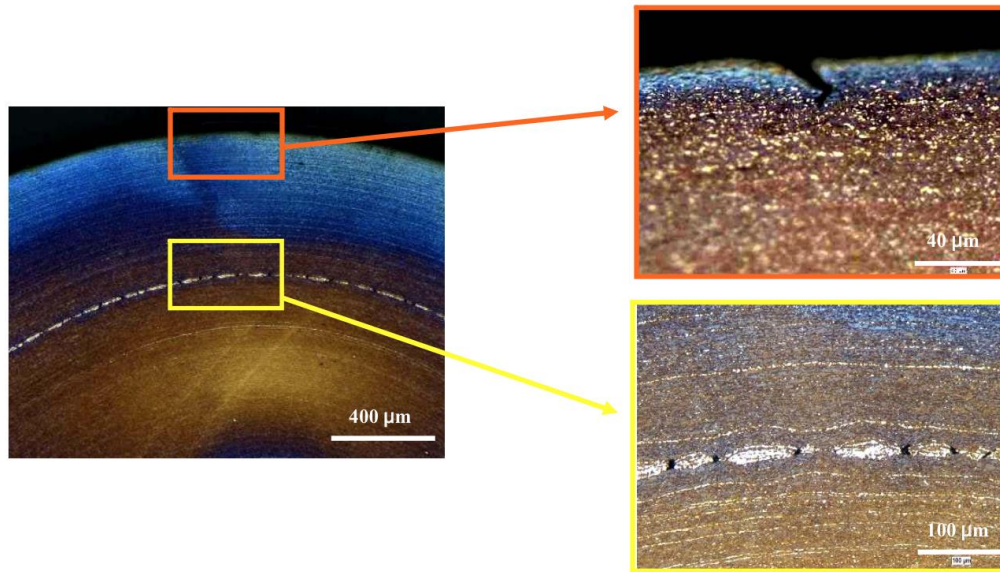
Fig. 18. Cross-section of TRIP-aided steel after air bending test [2]. Example of surface crack and voids formed at the thick macro-segregation bands are highlighted.
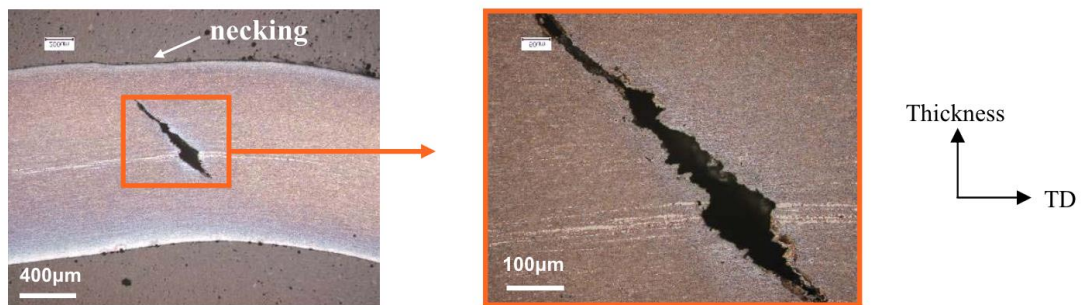
Fig. 19. Cross-section of TRIP-aided steel after interrupted stretch bending test [2].

2.7. Oxidation

2.7.1. Steel oxidation during hot rolling

After casting, hot rolling is performed. The semi-finished steel slabs are reheated to just under their melting point and rolled through successive mills for flat and long products. For flat products, in a conventional hot strip mill, the thickness of slabs can be reduced from around 20 cm to up to 0.16 cm after rolling [42]. The roughing mill is applied to reduce the slab thickness from 20 cm to 3 cm, as shown in Fig. 20 [43]. The roughing delivery temperature (RDT) is between 1000 and 1100°C. Six stands of hot

rolling mills (finishing mills) are then applied to reduce the thickness further (down to 0.16 cm), this will lead to a massive increment in the sheet length as well, a typical hot rolled coil measures 1000 m long. The finishing delivery temperature is between 820 and 920°C. Before the roughing and finishing mills a hydraulic descaling is applied to the surface to eliminate the primary and secondary oxides. Finally, steel sheets are cooled (with cooling rate between 100 and 150°C/s) and then coiled up for storage and transportation [44, 45].
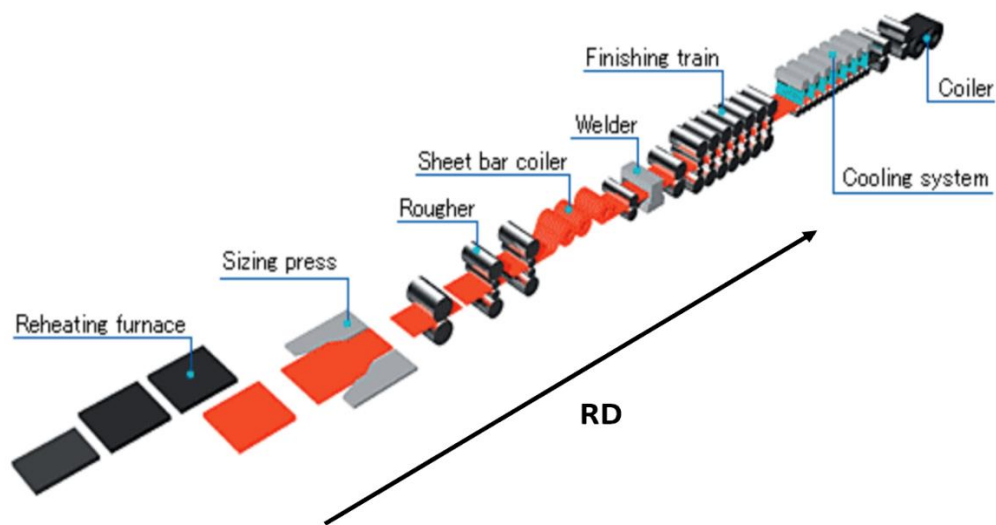
Fig. 20. Steel hot rolling process [43]. The rolling direction is labeled.

Surface oxidation will occur during the hot rolling process due to the high operating temperature and humidity. Surface oxides are mainly iron oxides (called scales) and have a negative influence on steel properties due to the loss of metal and degradation in surface quality. Three layers of oxide are most likely to form on the steel surface under elevated temperature and humid air, which are wustite (FeO), hematite (Fe_2O_3) and magnetite (Fe_3O_4). A typical scale structure is shown in Fig. 21 [46], where the wustite layer is usually thicker and present as an inner layer. Magnetite is thinner than wustite but thicker than hematite and formed as an intermediate layer between the wustite and hematite layer. The hematite, magnetite and wustite layers formed in pure iron under isothermal conditions (in air) has a constant thickness ratio, which is around 1:4:95. This ratio will vary with the composition of the steel. The oxidation rate of steel will be slower than pure iron [45].
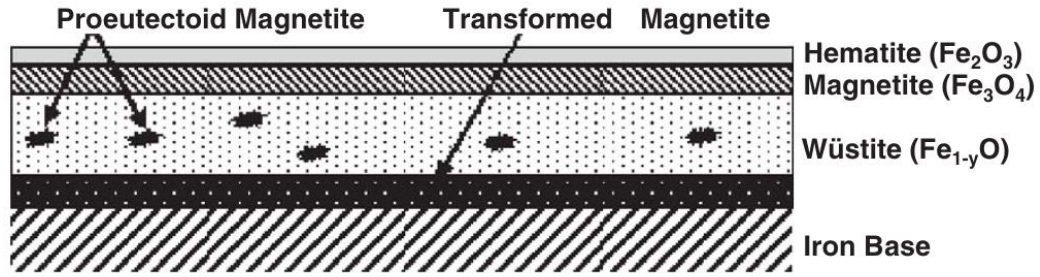
Fig. 21. Sketch of scales formed after hot rolling and cooling process [46].

However, Burke et al. [47] mentioned that it is not reliable to identify the type of scale by their position because the hot working process will always affect the position and thickness of the layers. The microstructure in scales becomes more complicated during the cooling process. Bhattacharya et al. [46] explained that the scale has a majority of wustite with varying proportions of magnetite and small amounts of hematite when the temperature is between 700 and 800°C. However, the magnetite is predominant oxide phase when the temperature is below 600°C, as shown in Fig. 22. Wustite starts to decompose into magnetite below 570°C, the speed depends on the cooling rate. For coiling temperatures (CT) above 600°C and in areas of the coil, where the cooling rate is high (edges and head and tail), retained wustite can be found; while in the rest of the coil, the cooling rate is slow and wustite will decompose into magnetite and ferrite. This microstructure is called decomposed wustite [47].
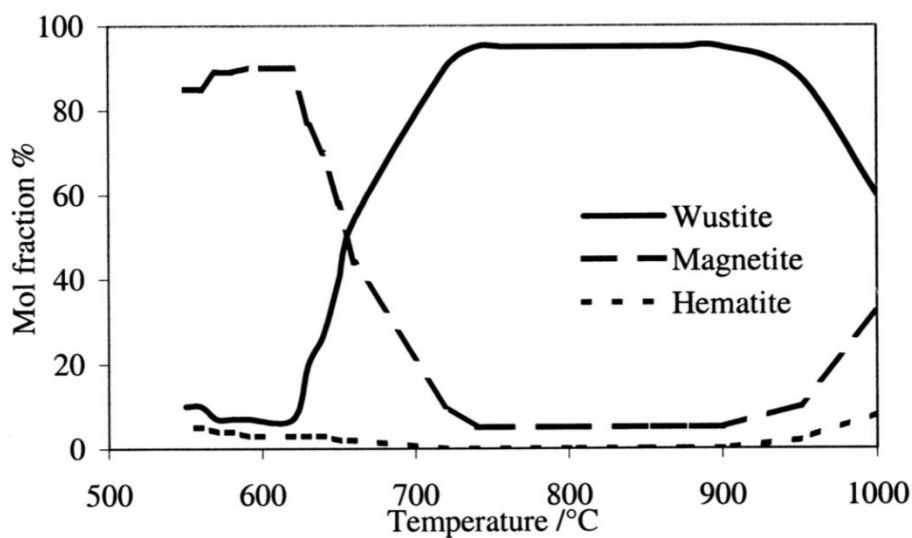
Fig. 22. Variation of iron oxide composition with temperature [47].

2.7.1.1. Iron oxide forming mechanisms

A simple oxidation equation is given to explain the mechanisms of iron/steel oxidation:

$$xM(s) + \frac{y}{2}O_2(g) = M_xO_y(s) \tag{2}$$

where M_xO_y is the solid reaction product, in this case, the iron oxides [48].

If the oxidation reactions take place at the oxygen-metal interface, the MO formed will then separate the two reactants. The reactants will now need to diffuse through the scale to continue the oxidation. This can either be metal ions diffusing outward to the oxide-gas interface or oxygen ions diffuse inward to the metal-oxide interface, or both [48].

These reactions are illustrated in Fig. 23[48].
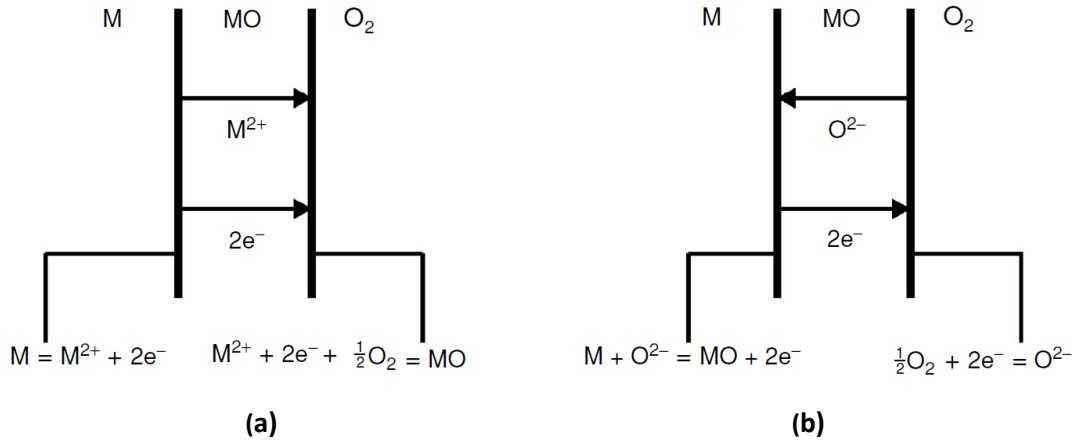
Fig. 23. Diffusion of ions and electrons to form oxides at: a, oxide-gas interface, cation mobile; b, metal-oxide interface, anion mobile [48].

All metal oxides are ionic in nature, and earlier EDS (Energy Dispersive X-Ray Spectroscopy) characterisations [49] shows the iron oxides in the coil cooled samples belong to non-stoichiometric crystals. For example, the wustite (FeO) found is sometimes described as $Fe_{1-y}O$ because of the high concentration of vacancies it contains [50]. Wustite is a p-type metal-deficit semiconductor with a large amount of cation-vacancies present in the crystal. Therefore, the mobility of Fe^{3+}, Fe^{2+} and the electrons are high. The interaction of the Fe lattice with oxygen is as follow: at the beginning, the oxygen ½O is chemisorbed by an electron from the Fe site, so a Fe^{3+} or a hole forms. The chemisorbed oxygen is then ionised fully, which requires another electron, and forms another Fe^{3+}/hole. A Fe^{2+} ion diffuses to the surface to compensate the O^{2-}, which forms a FeO at the oxide-gas interface and leaves

a vacancy in the cation sub-lattice. The whole process can be represented as:

$$\frac{1}{2}O_2 = O_O + 2h^{\cdot} + V''_{Fe}$$ (3)

In the Fe-FeO-Gas system, the rate of oxidation largely depends on the diffusion coefficient of Fe ions through the scale.

The rate of oxidation can be modelled according to Wagner's theory [51]. In reality, many factors will lead to inaccuracy of modelling. For example, the external oxide layer is not perfectly adhered to the entire steel surface, cracks and porosities might be present locally and also introduced during the multiple compression passes of the rolling process. Also, the scale consists of multi-layers of oxides, and as mentioned earlier, the uniformity of each layer is not constant. These factors mean that the diffusivity of ions is highly unpredictable. Lastly, the wustite undergoes phase transformation at 570°C during the coil cooling process, as shown in Fig. 24.
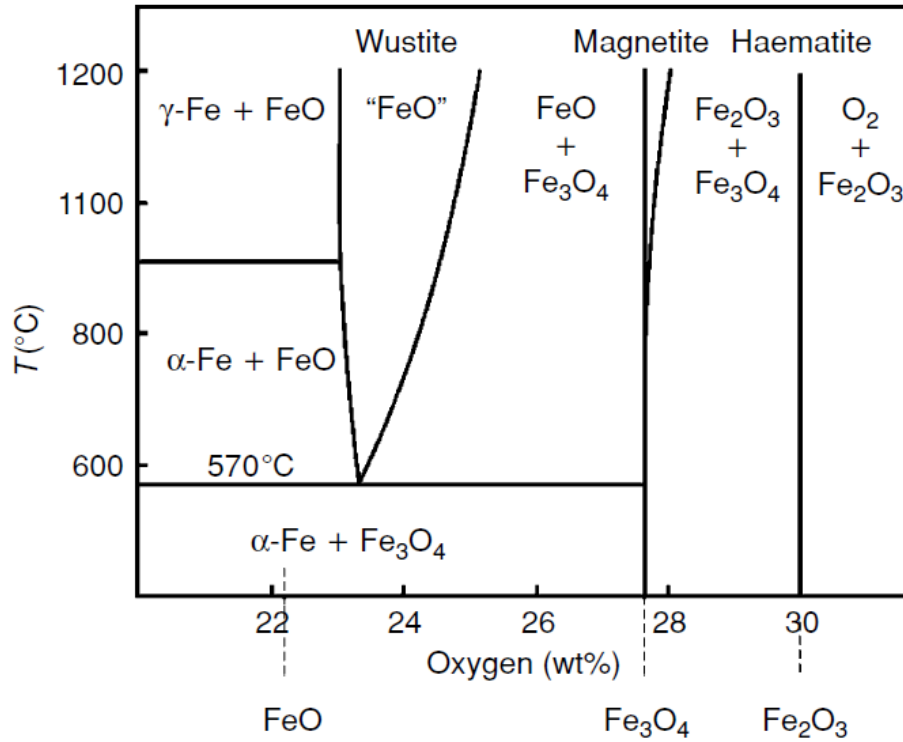
Fig. 24. The iron-oxygen phase diagram [52].

The magnetite has an inverse spinel crystal structure, where Fe^{2+} ions occupy the octahedral sites and the tetrahedral sites are occupied by half of the Fe^{3+} ions. Defects may form on both the octahedral and tetrahedral sites, which allows the diffusion of both divalent and trivalent ions. Below 570°C, the

wustite becomes unstable, where the FeO-Fe$_3$O$_4$ eutectic transformation occurs.

At above 400°C, the hematite α-Fe$_2$O$_3$ is formed due to the oxidation of magnetite. The α-Fe$_2$O$_3$ has a rhombohedral crystal structure, where Fe ions occupying the interstices within the close-packed hexagonal oxygen arrangement. Schwenk [53] suggests that both O and Fe ions should be able to diffuse through the defects, which are O^{2-} vacancies and Fe^{3+} holes. In this case, it is hard to clarify whether new oxides are forming at the interface of magnetite-hematite, or gas-hematite. Using the ion and electron diffusion within a classic three layer iron oxides as summarised by Birks et al. [52] in Fig. 25, the growth of oxides can then be understood.
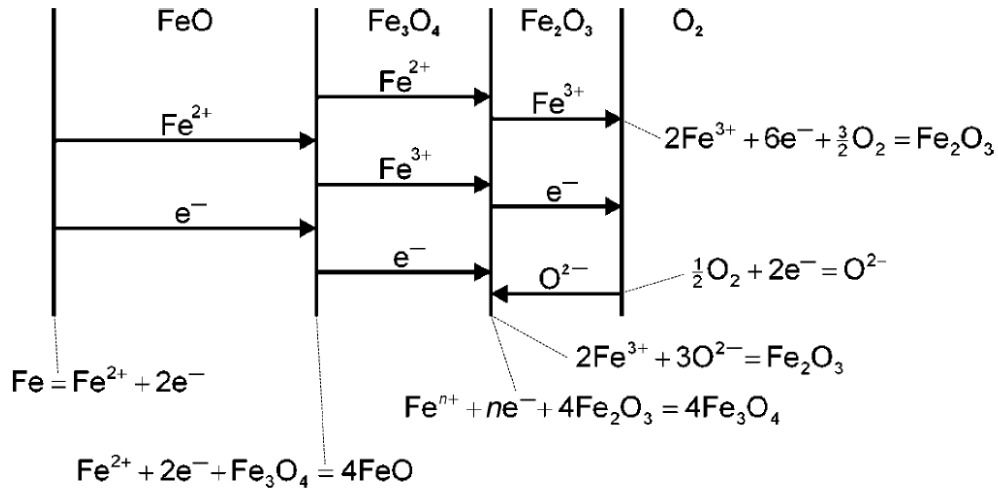
Fig. 25. The oxidations of pure iron, ion and electron diffusion within the Fe, FeO, Fe$_3$O$_4$ and Fe$_2$O$_3$ [52].

In summary, the iron at the matrix ionised and the Fe2+ and electrons diffuse through the wustite layer via vacancies and electron holes. Subsequently, the magnetite at the wustite-magnetite interface is reduced to form wustite:

$$Fe^{2+} + 2e^- + Fe_3O_4 = 4FeO \tag{4}$$

The mobility of Fe^{2+} ions and electrons in the wustite is high and diffusion continues through the magnetite layer via the vacancies on octahedral, tetrahedral sites and the electron holes. At the magnetite-hematite interface, the hematite is consumed, together with the Fe3+, Fe2+ and electrons, to form magnetite:

$$Fe^{n+} + ne^- + 4Fe_2O_3 = 3Fe_3O_4 \tag{5}$$

Assuming both Fe^{3+} and O^{2-} can diffuse through the hematite layer, there will be new hematite forming

at both the gas-hematite and hematite-magnetite interfaces, represented by formulae (6) and (7), respectively:

$$2Fe^{3+} + 6e^- + \frac{3}{2}O_2 = Fe_2O_3 \hspace{4cm} (6)$$

$$2Fe^{3+} + 3O^{2-} = Fe_2O_3 \hspace{4cm} (7)$$

Bertrand [54] found that the oxidation and reduction occur at the same time within the hematite layer. The hematite is reducing to magnetite at the Fe_2O_3-Fe_3O_4 interface while at the same time, Fe^{3+} cations diffuse outward to form new hematite at the scale surface. The overall oxidation rate of the scale highly depends on the cationic diffusion within the magnetite layer because of its greater thickness and larger grain size. Bertrand [54] mentioned that oxygen is able to diffuse to the metal-scale interface through short-circuit paths, such as the grain boundaries. Therefore, the thick magnetite layer also controls the inward diffusion of oxygen and hence the growth kinetics of the internal oxidation layer. This is only valid at above 570°C, the wustite-magnetite transition temperature.

2.7.1.2. Primary, secondary and tertiary scale

Three common types of scales are likely to form during hot rolling, defined as primary, secondary and tertiary scale. Primary scale forms during the reheating process, which takes the longest time to reach the required temperature. Massive oxides (≤2wt% of the steel) can form during this period. The primary scale is removed completely (or almost) by a descaler before the strip enters the first rough roller. The secondary and tertiary scales are more affected by processing because they are formed and deformed during roughing and finishing milling, respectively, as shown in Fig. 26 [42]. During deformation, the oxide deforms plastically together with the steel. However, the plasticity of the oxides depends on both temperature and oxide thickness [55] and therefore, for certain combinations of oxides and temperature, the secondary and tertiary scales might crack with fragments being pressed into the steel matrix. In this case, the oxide will be rolled into the softer steel and form defects on the surface.
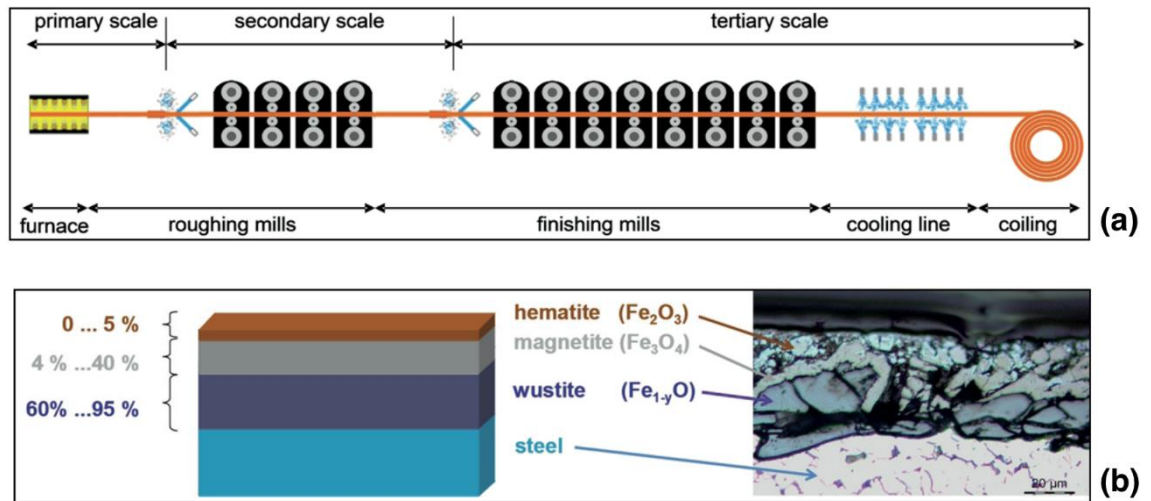
Fig. 26. (a), Primary, secondary and tertiary scale formed during the hot rolling process. (b), the volume fraction of oxide layers in steel [42].

2.7.1.3. Oxidation of alloying elements in steel

Silicon

Oxidation in steel and the resulting scale structure can be significantly influenced by alloying elements. For instance, amorphous SiO_2 appears in silicon enriched steel because Si is less noble than Fe and forms the oxide, as shown in Fig. 27 [56]. However, continuous SiO_2 will only form when the silicon concentration is above 2wt%. At concentration below 2wt%, silicon prefers to precipitate out from the steel matrix and react with the wustite to form the spinel fayalite (Fe_2SiO_4) at the steel/scale interface [57]. Surface defects like rolled-in scale appear in hot-rolled, silicon-containing steels. The fayalite phase has relatively high strength, which acts as a binder between the inner layer of scale and the metal surface [45]. It remains on the steel surface after descaling, and remaining FeO within the eutectic compound oxidise further into red Fe_2O_3 during the subsequent cooling process [58].

Fayalite forms as a liquid phase at above 1170°C. The molten fayalite will penetrate the grain boundaries and form eutectic (FeO/ Fe_2SiO_4) entangled with the steel matrix. An example of the entangled structure in a steel with 0.05 wt% of C and 1.1 wt% of Si is shown in Fig. 28 [59]. The eutectic

fayalite-wustite mixture was formed after 6 hours of heat treatment at 1210°C. Invasion of the fayalite into the grain boundaries of wustite will reduce the descalability significantly and the rolled-in scale phenomena will be enhanced. Chattopadhyay [60] reported that the formation of fayalite dominates and influences the pickling efficiency when the concentration of Si is excess of 0.35wt%.
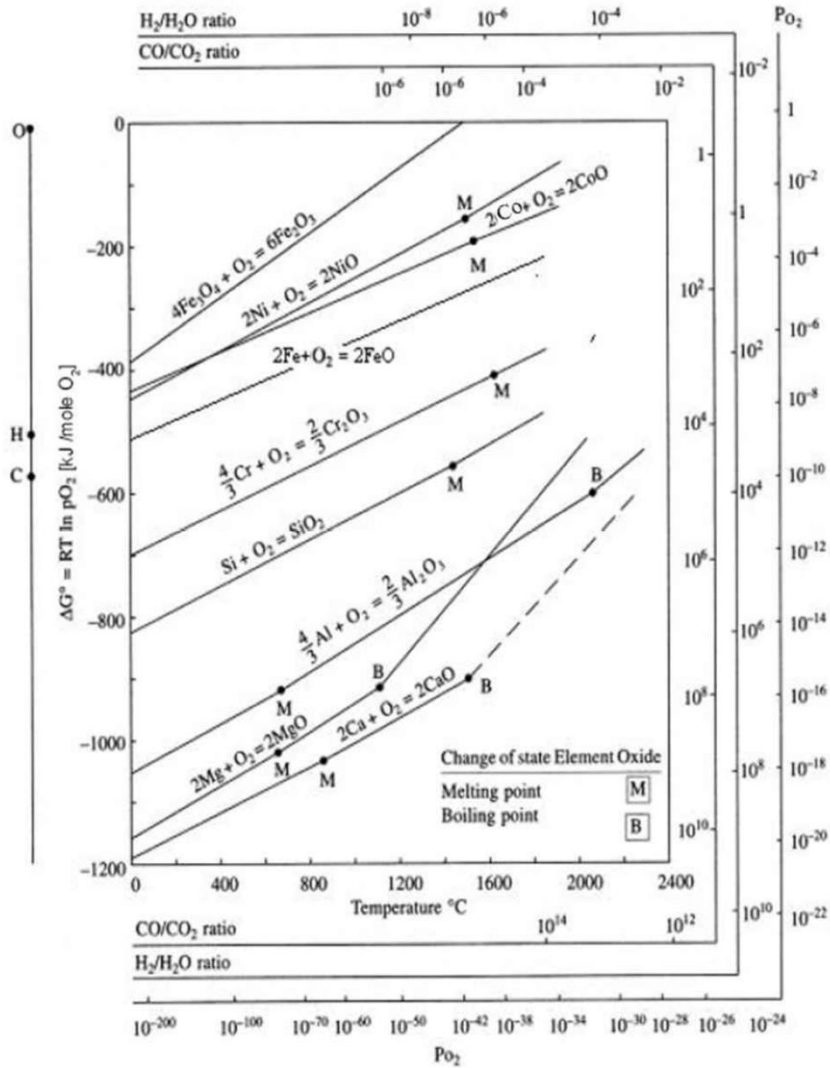
Fig. 27. Ellingham Diagram [56].
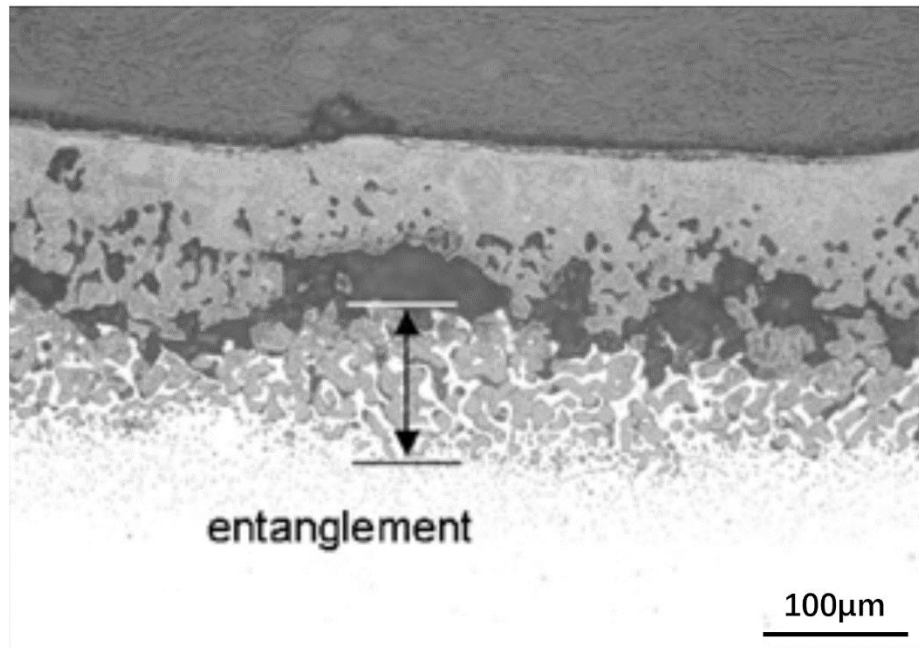
Fig. 28. Micrograph of melted fayalite that has penetrated the steel grain boundaries and formed entangled microstructure. The steel sample contains 0.05 wt% C, 1.1 wt% Si and has been exposed at 1210° C for 6 hours [59].

The solid-state and liquefied fayalite have opposite effects on the steel oxidation behavior. The solid-state Fe_2SiO_4 layer formed below the melting temperature acts as an ion diffusion barrier and prevents further formation of the iron oxides above it. At higher Si concentration, more fayalite will form, so the inhibition effect is enhanced. In this case, the overall scale thickness reduces. However, liquefied fayalite provides fast diffusion paths for the ions at above 1170°C. In this case, higher Si concentrations will now increase in the overall scale thickness [61].

Nickel

Although nickel is relatively noble and less likely to form oxide in steel, a small amount of Ni is always present in wustite. When steel oxidises, Ni will accumulate at the interface of steel and scale. Nickel has a low diffusion coefficient in iron; hence the accumulated Ni is difficult to diffuse to either the bulk steel or the scale. It leads to a much higher Ni concentration at the scale-steel interface than in the bulk [56]. Also, nickel will promote fibrous scale formation and lead to entanglement between different compounds within the scale. During oxidation, Ni is progressively surrounded by wustite, and the

resulting scale has different structures through the thickness. The entire scale can then be differentiated into two layers, called the inner layer and the external layer. The external layer belongs to standard wustite whereas the wustite at inner scale is entangled with the steel matrix. The accumulated Ni metallic particles will act as obstructs and lead to irregular oxidation. The entangled structure will make most of the mechanical descaling methods invalid [59].

If Si and Ni are both contained in steel, more complex scales will form. Melfo [59] mentioned that significantly more scale remains after descaling if 0.05-0.1 wt% Ni was alloyed into 0.02 wt% Si-steel.

As a summary, Fig. 29 compares different scale structures in steels with Si, pure Ni and Si+Ni additions, respectively. The structures developed below or above 1177°C are also compared. The entanglements formed in pure Si-containing steel are due to the melting of fayalite that penetrates the grain boundaries of wustite. The amount of entanglements largely depend on the Si composition.

The entanglements in pure Ni-contained steel are formed by irregular oxidation. The oxidation front is influenced by accumulated Ni particles at the scale/steel interface.

Highly entangled structure with oxidic pegs formed in Si/Ni-containing steel. It is because of the synergetic effect of Ni accumulation and the liquid oxides. The pegs formed by liquid fayalite penetration will further increase the diffusion of silicon and iron, and the oxidation is now accelerated. At elevated temperature, the newly formed wustite/fayalite compound tends to melt continuously and penetrates not only along the grain boundaries but also the irregular oxidic pegs. As a result, Si and Ni-containing in steel will lead to much thicker oxidation layers.
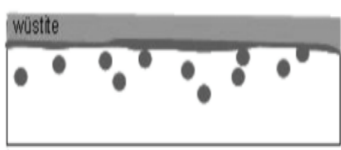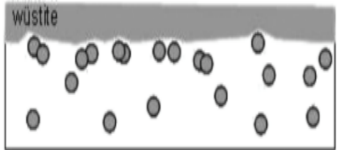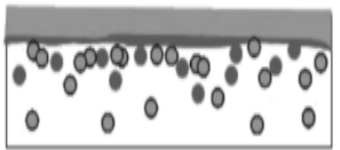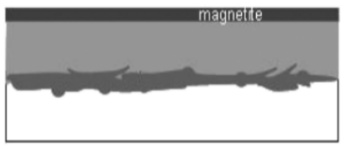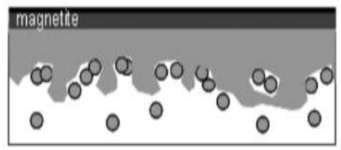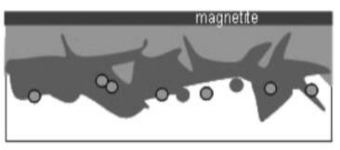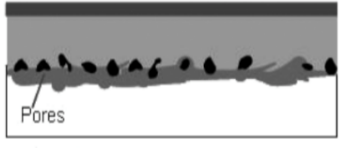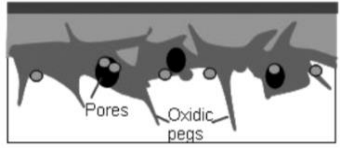
With only Si	With only Ni	With Ni and Si
Oxidation at <1177°C		
FeO/Fe$_2$SiO$_4$ nuclei form internally and externally.	Nickel sits in metallic form. Ni enrichment pushed forward by moving oxidation front.	Combined effects from the Si and Ni only samples.
Oxidation at >1177°C		
FeO/ Fe$_2$SiO$_4$ is in liquid phase: -Forms islands on the interface with wustite. -Can penetrate the grain boundaries of the wustite and the steel forming oxidic pegs. -Accelerates Fe diffusion thus the entire oxide layer is thicker than at lower T. -The entanglement extent depends on the Si content.	Oxidation is irregular due to obstruction by Ni-rich particles. Ni particles engulfed by the solid oxide front. Ni retards Fe diffusion, thinner oxides will form.	Combined effects from the Si and Ni only samples. Thicker entanglement formed.
Cooling down to room temperature		
FeO/ Fe$_2$SiO$_4$ solidifies and shrinks, forming pores.	An entangled layer of wustite and steel is formed. Ni sits in the wustite pores.	Combined effects from the Si and Ni only samples. Thicker entanglement formed with long oxidic pegs.

Fig. 29. Mechanisms of entanglement structure formation in pure Ni, pure Si and Ni/Si mixture under different oxidation temperature (adapted from [56]).

Aluminium

Aluminium and silicon have similar effects on steel. An Al-enriched layer will form at the scale/steel interface. The oxidation rate of the steel is then reduced due to the accumulation of Al-rich oxide compounds that tend to inhibit Fe atom diffusion. The compound formed at the interface is temperature dependent. For instance, when the oxidation atmosphere remains constant at 1atm O_2, Al_2O_3 will form between 500 and 700°C, whereas $FeAl_2O_3$ will form between 700 and 900°C [56]. The melting point of a compound formed by fayalite containing Al is even lower than the fayalite itself, and therefore enhances the liquid phase formation and its consequences.

Manganese

Mn forms more stable oxides than Fe, and it is the most common alloying element in AHSS. Mn atoms substitute for iron atoms during external oxide formation, this oxidation behaviour starts from 500°C. When 2wt% Mn is contained in the steel. Complex Mn oxides could form if Si, Cr or Al are also present in the steel. During the annealing process, both internal and external Mn-containing oxides can form. 100nm MnO precipitates have been reported to form across the steel surface during annealing. However, the precipitates size is very time-dependent as they tend to grow and coalesce to around 1µm in size if the annealing time increases from 60 to 600 seconds (data from internal document).

2.8. Descaling process

Steel oxidation and scale formation are unavoidable at the high temperatures in the atmospheres present during hot rolling, annealing or welding. Scales are a potential source of surface defects, which may cause rejection of the final product or earlier failure of the component during service. For example, if the scales are not removed prior to the wire drawing process, oxides fragments will be pressed into the steel wire and lead to surface quality degradation [62].

As a result, understanding the nature of scale formation and its development becomes critical to the steel manufacturers in order to improve the surface finishing of their products. Generally, scale

formation is undesirable and unavoidable in some processing procedures, and descaling processes are developed to restore the best surface conditions of steels before further processes [9, 63].

2.8.1. Descaling methods

Wide ranges of mechanical descaling methods have been developed to remove primary and secondary scale. In most of the cases, mechanical descaling is based on high-pressure water (HPW) impaction. Bendig et al. [64] mentioned that the descaling effect is achieved by mechanical impaction of the water droplets from the high-pressure nozzle. More importantly, intensive cooling will lead to high-temperature gradients after water spaying. Mechanical and thermodynamic measurements to reveal the force and heat transfer coefficient changes resulting from high-pressure water show sharp peaks that represent thermal shock and impact, as shown in Fig. 30, (a). Thermal shock will force the scales to break up because of the different thermal expansion rates of the scale and the steel matrix. Bendig et al. [64] determined that the effect of shear stress (caused by thermal shock) covers a wider area of the strip surface and with 500 times greater magnitude than the mechanical impact stress. The heat transfer coefficient depends on the water flow rate and the strip transfer speed, as shown in Fig. 30, (b).

Both the porous primary scale (formed in the furnace with oil and gas atmosphere) and the secondary scale (formed during hot rolling) can be descaled by the HPW impaction with high efficiency. The secondary scale in Bendig's experiment was 60-100μm thick, which is much thinner than the primary scale (1-5mm). However, 5 to 10 μm secondary scale will always remain after descaling with high-pressure nozzles because it is more compact and adhesive (described on p. 34) than the primary scale.
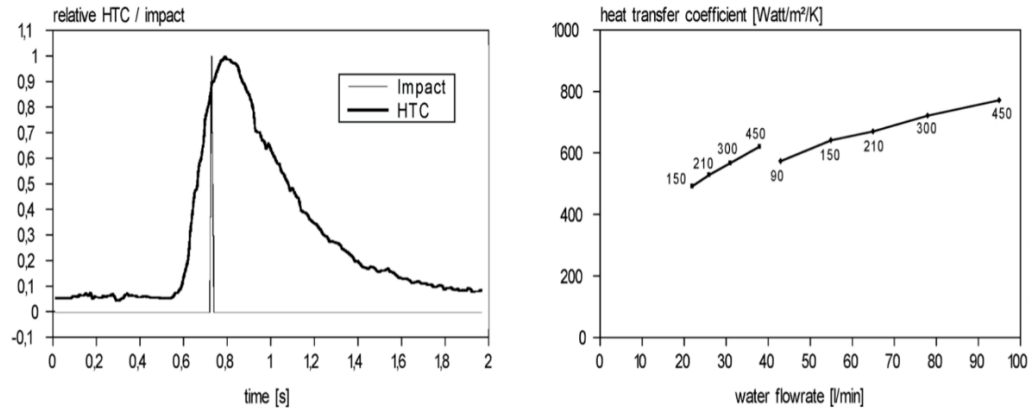
(a)   (b)

Fig. 30. (a), The impact magnitude and heat transfer coefficient change on the strip surface when contact with the water spay. (b), Influence of water flow rate and nozzle size on the heat transfer coefficient [64].

In conclusion, better descaling effects and higher descalability could be achieved by: firstly, develop and optimise the descaler set-up, which relies on both static and dynamic descaler investigation; secondly, understand the steel oxidation behaviours and the properties of the specific scales to assess the response of different scales to descaling; finally, understanding of the last two points provides a strong background for detailed modelling and characterisation of the process.

After removal of the scale in the initial stages of processing by mechanical methods the hot rolled steel is coiled and cooled then, prior to cold rolling, further surface treatment is undertaken. Pickling is a conventional widely used descaling process, where hydrochloric acid (HCl) is applied to corrode away the surface oxides. However, HCl is discouraged nowadays because it has a high tendency to vaporise and lead to severe air pollution. There are three types of wastes produced during pickling, which are used acid, rinsing water and filter press sludge. In addition, undesired under-pickling and over-pickling will occur if the scales are uneven or have different structure/compositions across the surface [62, 63, 65]. As it can be seen, descaling prior to cold rolling poses significant challenges.

2.9. Controlled scale formation

In addition to developing better descaling processes, descalability can also be improved by scale structure modification. As the author mentioned in p. 28, a wustite inner layer, hematite outer layer and magnetite intermediate layer will form under high-temperature exposure during hot rolling. However, magnetite and hematite will also form at the interface of scale and steel if longer oxidation at high temperature is performed. Chattopadhyay *et al.* [63] mentioned that hematite and magnetite are adhesive to the substrate, but wustite is non-adhesive. Laying head temperature (LHT) and cooling rate of the strip on the conveyor will influence the final proportion of different scales significantly. After mechanical descaling, the surface and the descaled powder of a high carbon steel (0.81wt% C) sample were analysed by Raman spectroscopy. The results are shown in Fig. 31. The scale remaining on the sample surface was determined to be hematite. Wustite and magnetite were found in the descaled powder. It proved that hematite has higher adherence to steel and it is harder to be removed by both chemical and mechanical descaling. During cooling after hot rolling, hematite is decomposed from wustite and magnetite. A higher cooling rate will lead to less hematite formation because less time remains for decomposition to take place. Also, appropriate LHT should be maintained before cooling. For example, LHT is desired to remain at 880°C for high carbon steel (0.81C wt%) to slow down hematite growth before the coil cooling process.
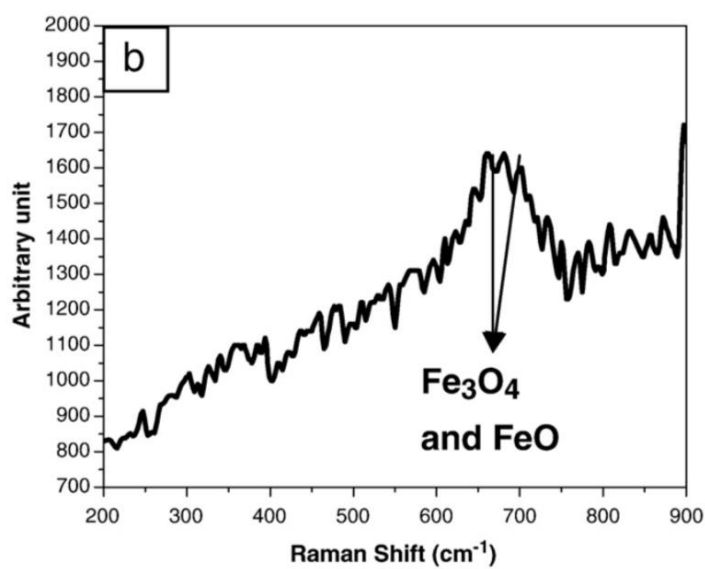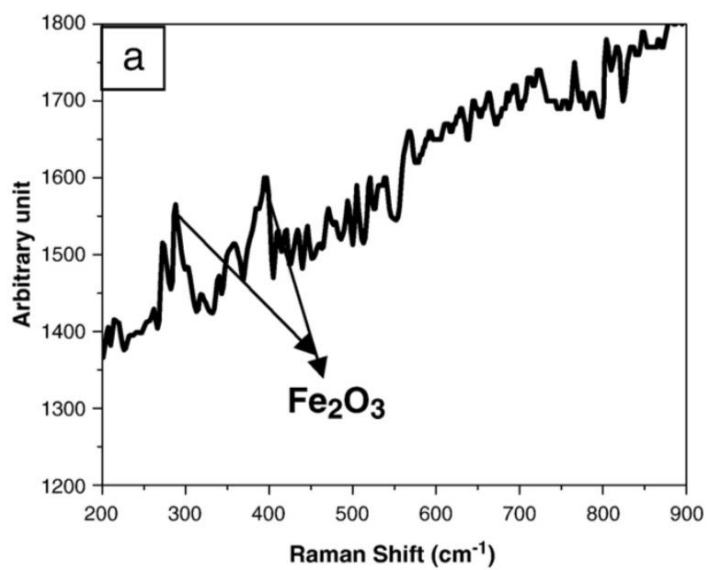
Fig. 31. Raman spectroscopy of (a), sample surface, where hematite appears; (b), descaled powder, where wustite and magnetite are observed [63]. The oxidised 0.81wt% C steel sample was mechanically descaled prior to the test.

Oxidation also depends on the atmospheres. For example, Shi *et al.* [65] mentioned that carbon monoxide, a readily available gas in the steel industry has outstanding scale reduction ability. The reduction process is:

$$CO + FeO = Fe + CO_2 \tag{8}$$

Temperature is the most important parameter in this descaling process. Firstly, the reduction process must take place when the temperature is above 700°C. Otherwise, carbon monoxide has a strong tendency to decompose into carbon and carbon dioxide. The scale reduction rate is also temperature and time-dependent. Fig. 32 shows that the reaction is nearly four times faster when the temperature is 750°C in contrast with 710°C. However, the reaction rate starts to drop above 750°C. Similar tendencies are found when replacing the x-axis from temperature to time, where the peak scale's growth rate is at 180 s. Shi [65] explained that a certain time is required for CO to react with the scale. After 180 seconds, all oxides are removed, CO continues to react with the steel surface as decarburisation. Subsequently, when high density of carbides are formed at near-surface, the amount of mass lost is reduced.
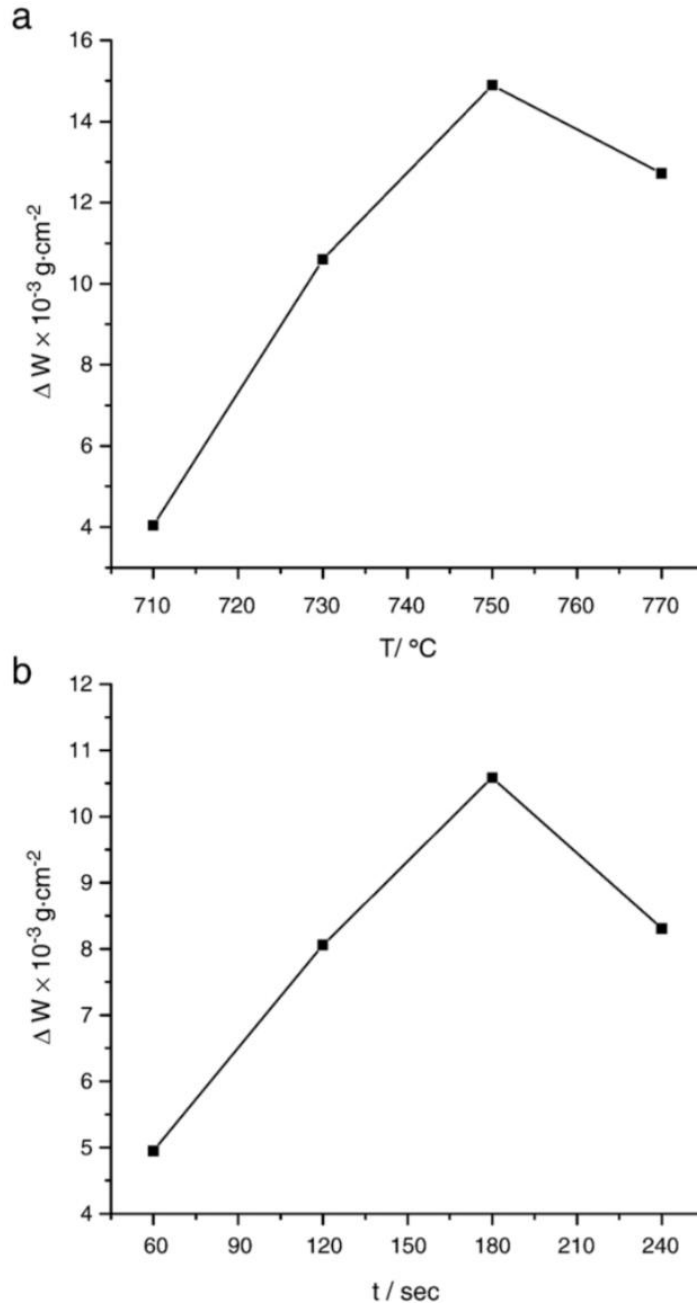
Fig. 32. Mass lost of the steel sample as a function of：(a), temperature; (b), time. The CO flow rate is 3L/min [65].

The formation of oxides is unavoidable from the economical and industrial point of view, as discussed in the previous sections on oxide scales formed during hot rolling. However, external oxides are not always unfavourable during steel processing, particularly during annealing. Lashgari [37] mentioned that during the annealing process, the atmosphere in the radiant tube furnace is oxidising for the alloying elements but reducing for iron oxide. By increasing the dew point and hence raising the

oxidising power over the equilibrium oxygen partial pressure for FeO formation in the direct fire furnace (DFF), wustite scale will form. This surface wustite layer is then reduced to a pure iron layer in the radiant tube furnace (RTF). In this case, delamination and bare spots can be avoided during galvanising through this controlled oxidation.

2.10. Internal oxidation

Vlack [9] reported that oxygen could penetrate through the scale and further into the steel matrix under certain conditions. If the alloying elements (e.g. Si) are more reactive than the Fe, a fine dispersion of oxide inclusions will form close to the sample surface. This oxide inclusion is defined as internal oxidation, and the oxide enriched region is determined to be subscale or internal oxidation zone (IOZ). Normally, scale and subscale form concurrently during steel oxidation. However, external oxidation may occur without any internal oxide formation. Similarly, internal oxidation can also form with the absence of external oxides.

Internal oxides have a higher preference to form at grain boundaries due to the lower nucleation energy required. The grain boundaries also act as fast diffusion pathways for oxygen to penetrate inward. The grain boundary diffusion of oxygen can be up to 60 times faster than bulk diffusion [66]. The IOZ depth shows the region, where oxygen is present in the steel substrate. The IOZ depth depends on the steel compositions and the kinetics (time and temperature exposed) [9].

The scale and subscale formation depends mainly on the reaction between inward diffusion of oxygen and outward diffusion of alloying elements. Fig. 33 shows the oxygen and element concentration across the thinness of a steel sheet [9]. In this diagram, the alloying element is Mn and the steel has an austenitic microstructure. The decrease in Mn concentration towards the surface is due to the formation of MnO. Also, the oxygen concentration keeps decreasing within the subscale and finally turning to zero.
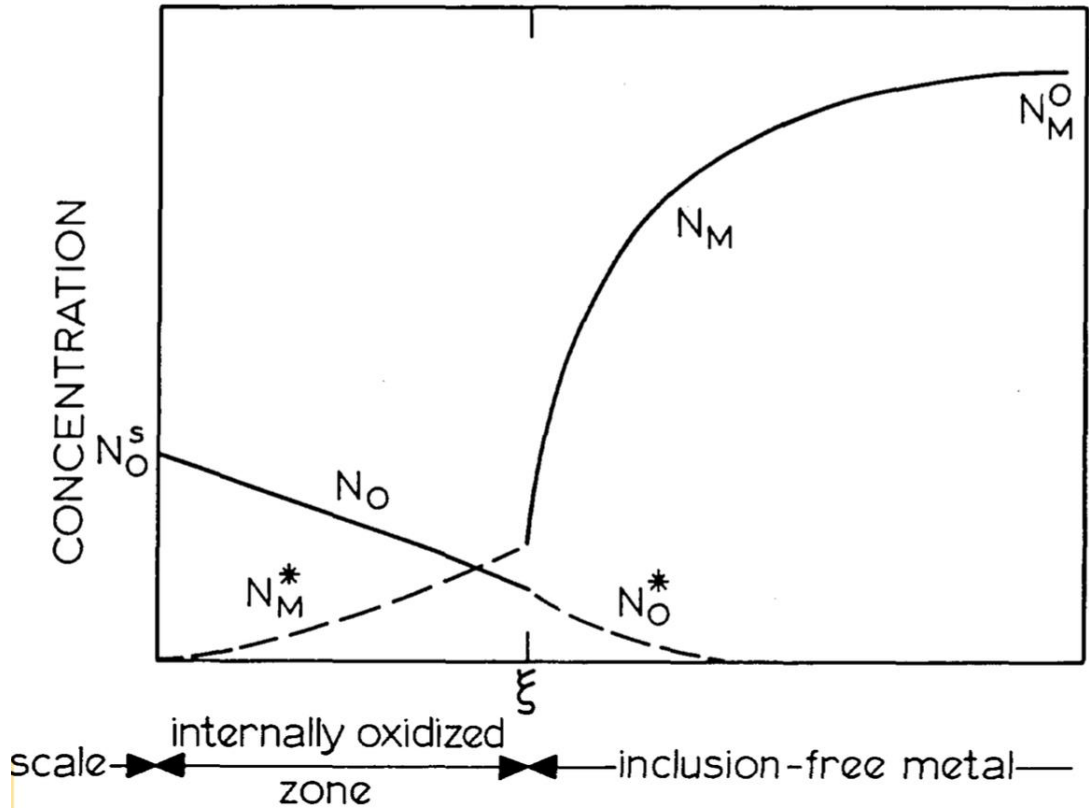
Fig. 33 Concentration depth profile of N_M and oxygen across the thickness of the steel sample. The internally oxidised zone (IOZ) is labelled [9].

In a steady-state condition, for example, when Mn is enriched in the steel matrix, the internal oxidation reaction Mn+O=(MnO)$_s$ will occur within ξ (thickness value) toward the surface. At ξ, the oxygen and Mn atoms have the same flux intensity but opposite direction. Wagner [67] concluded that:

$$\xi^2 = \left(\frac{2N_O^S D_O}{V N_M^O}\right) t \tag{9}$$

where the thickness of the internally oxidised zone is a function of $\sqrt{t}$. N_O^S is the oxygen concentration at scale/steel interface, D_O is the diffusion coefficient, V is the ratio between O and Mn atom within the oxide compound MnO, N_M^O is the Mn concentration in the steel matrix.

Swisher [68] described that the D_O in fcc structure is higher with increasing temperature:

$$logD_O = -\frac{8820}{T} + 0.76 \tag{10}$$

Also, $J = \frac{dm}{dt} = D_O \frac{N_O^{(S)}}{XV_m}$ $(mol\ cm^{-2}s^{-1})$ [52] $\tag{11}$

where $N_O^{(S)}$ is the oxygen solubility in the metal matrix and V_m is the molar volume of the solvent alloy.

48

When J_O is less than -J_m (J means flux and - means opposite direction) at x=0, no internal oxidation will occur, where x is the depth into steel surface. J_O and J_m can be expressed as $D_O(\partial N_O/\partial x)$ and $D_M(\partial N_M/\partial x)$, respectively. In this case, internal oxidation is more likely to form in steels with lower alloying elements contents. However, no oxide will form if the alloying element has negligible concentration within the steel. As a result, ξ is largely depends on the steel composition [9].

Most of the internal oxidation research was performed on steels without scales to simplify the mathematical approach. For example, Wagner's equation shown above is based on samples without any scale formation.

The oxygen activity of surrounding gas has a positive influence on the internal oxidation rate of scale-free steel. However, an inverse relationship was found when scale exists. Rapp [69] mentioned that the growth of IOZ in scaled steel is independent of the oxidation time. The scale formation is an oxygen-consuming process, which acts as a barrier of inward oxygen diffusion. Lashgari [37] mentioned that the partial pressure of oxygen at the steel surface is equal to the ambient if the scale is absent. However, when scale present, the oxygen partial pressure depends on the local equilibrium between the alloy and the scale.

On the other hand, Vlack [9] found that the composition is non-identical across the IOZ. As an example, a Fe-1.0Mn steel sample oxidised at 1350℃, $P_{H_2O}/P_{H_2} = 0.2$ was used to calculate the MnO to FeO ratio via thermodynamic data. The result showed the MnO to FeO ratio at the subscale front is equal to 97:3 but decreased continuously until 77:23 was reached at the surface. In this experiment, no scale covered at the surface.

Vlack [9] mentioned an electron microprobe analysis on Fe-1.55Mn steel. The sample was heat treated at 1260℃. Almost pure wustite was formed at the scale-steel interface, but the MnO/FeO ratio increased to 100:0 at the end of IOZ, as shown in Fig. 34.
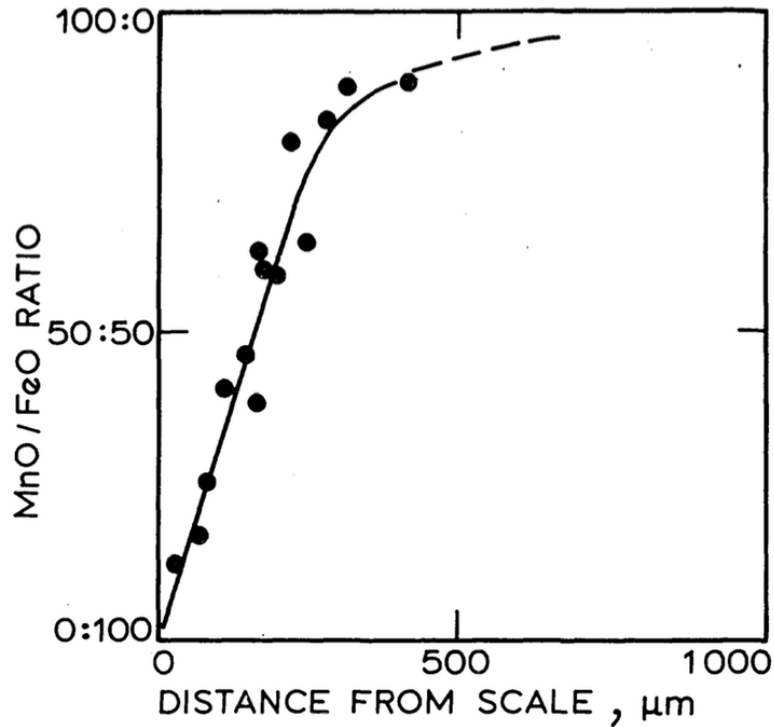
Fig. 34. MnO/FeO ratio from scale surface to subscale front in Fe-1.55Mn steel. The sample was heat treated at 1260°C for 4 hours [9].

If the same characterisation method is applied, the difference in results between scaled and non-scaled samples is mainly due to their distinct oxygen concentration in IOZ. When external and internal oxidation occurs concurrently, the scale grows into the steel and raises the oxygen concentration at any specific point within the IOZ. Also, any oxidised cracks will act as an oxygen source for internal oxidation to occur in surrounding areas [9].

The composition variation is more complex when multiple elements are alloyed into the steel. Generally, the position of a specific type of inclusion largely depends on its deoxidising preference. For example, transparent SiO_2-rich inclusions are formed at the subscale front, whereas MnO/FeO rich inclusions are more likely to form at the middle position of IOZ. This confirmed that Si is a better deoxidiser than Mn (cited report from [9]).

During steel processing, internal oxidation formed during coil cooling after hot rolling and during annealing are two known sources of surface weakening [36, 37]. The internal oxides will lead to working (rolling and forging) defects and alloy element losses. In addition, the IOZ will influence the fatigue life

50

and the effectiveness of heat treatment. Arkhipov et al. [70] found the fatigue behavior is improved if IOZ is removed manually before the test. Also, the formation of oxide inclusions will lead to depletion of the local alloying elements. However, the dispersed inclusions in the IOZ can lead to precipitate strengthening. Creep resistance can often be improved if internal oxidation occurs. For example, in Cu-Al and Fe-Al alloys the formation of inclusions can prevent grain boundary slip effectively.

Lashgari [37] oxidised three samples at 950℃ within N_2 +5 vol% H_2 atmosphere, with the dew point set to 10℃. The samples contained 1.7, 3.5 and 7.0 wt% of Mn, respectively. The results are shown in Fig. 35, where the higher alloying content will lead to greater coarsening effects after 20 hours. Coarsening means an increase in the size of precipitates and with an increase in their spacing as the volume fraction must remain constant at equilibrium. This was confirmed in Fig. 36, which is the BSE image of the same samples. It is obvious that higher content of the alloying element and longer oxidation time will lead to larger inclusions (dark spots) and larger interparticle spacing.
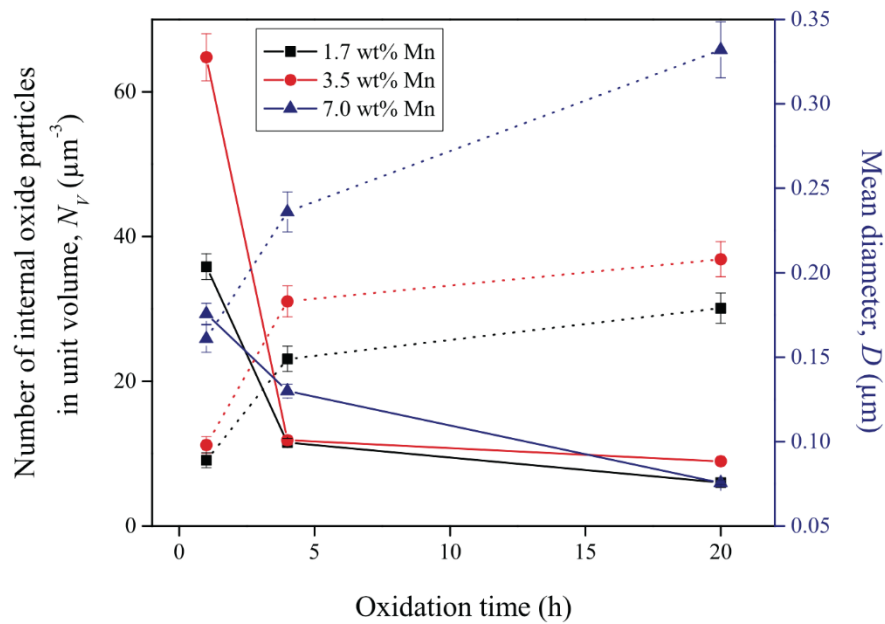
Fig. 35 Number of internal oxide particles in unit volume (solid line) and mean precipitate size (dotted line) versus oxidation time [37].
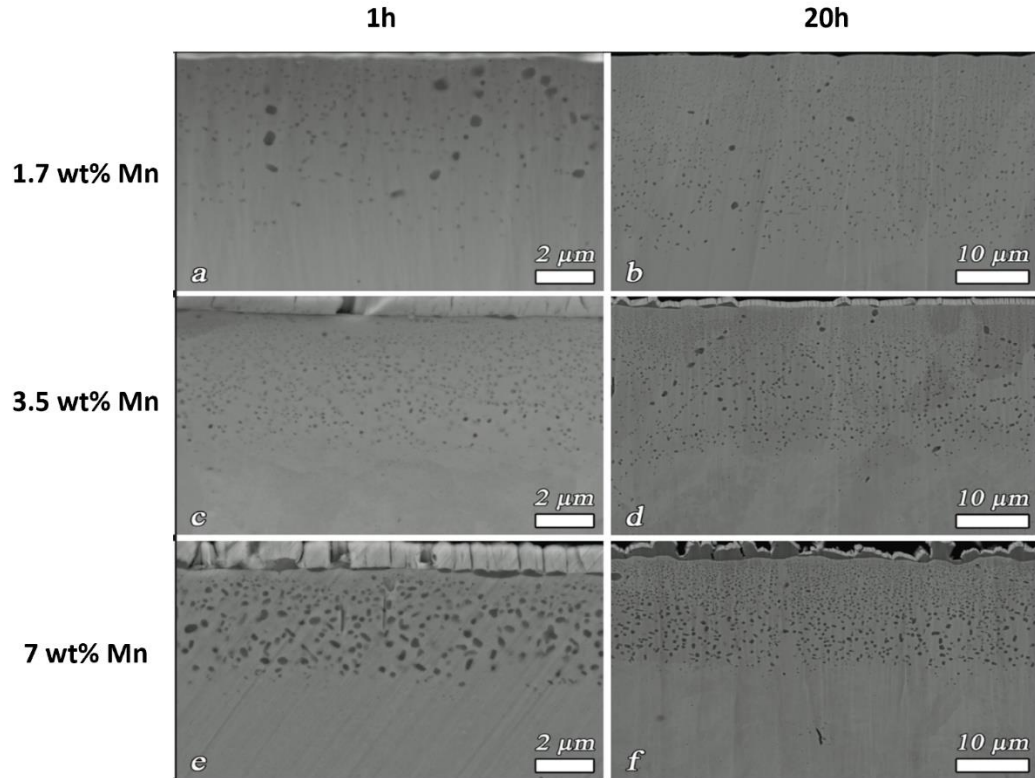
Fig. 36. BSE image of steel sample with 1.7, 3.5 and 7.0 wt% of Mn addition. Each sample is oxidised at 950℃ and in N_2 atmosphere with 5 vol% H_2. The dew point is controlled to be 10℃ [37].

2.10.1. Internal vs external oxidation

Lashgari [37] described a single-phase steel sample as a binary alloy A-B, where A is the matrix and B is the alloying element. A is assumed to be nobler than B. If the oxygen has reasonable solubility in A, then B oxide may form within the metal, which described as internal oxidation. If B is able to diffuse to the steel surface through A, B oxide will form at the surface, which described as external oxidation. Schematic illustrations of internal and external oxidation in A-B alloy are shown in Fig. 37.
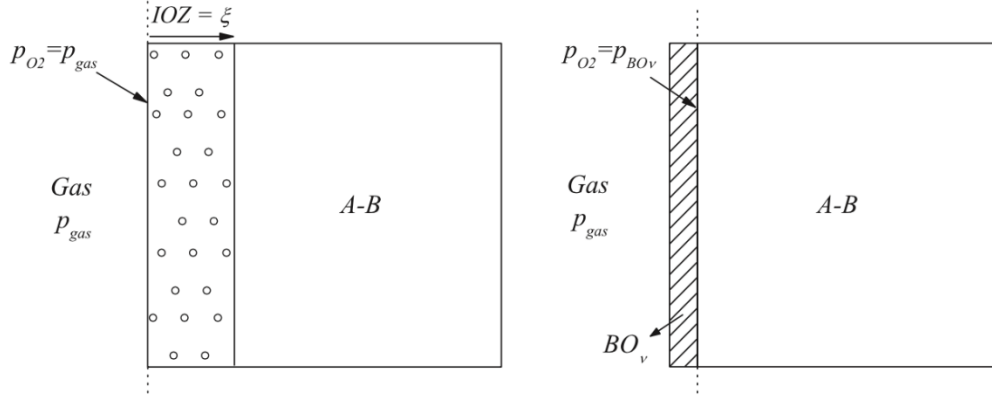
Fig. 37 Internal oxidation (left) and external oxidation (right) in the binary A-B alloy [37].

Meijering [71] mentioned that there are two requirements that must be met for internal oxidation to occur. Firstly, $\Delta G^0_{BO_{vB}} < \Delta G^0_{AO_{vA}}$, where $\Delta G^0_{MO_{vM}}$ represent the standard Gibbs free energy for MO oxide to form in 1 mole of oxygen. V_M is the stoichiometry of the relating oxide. In this case, oxygen has higher affinity for the alloying element, rather than for the matrix. Secondly, $D_O > D_B$, which means the diffusivity of oxygen in the matrix is higher than the diffusivity of the element B in the matrix. Otherwise, external oxidation will occur if $\Delta G^0_{BO_{vB}} > \Delta G^0_{AO_{vA}}$ and $D_O < D_B$. Lashgari [37] mentioned that the oxygen permeability is the critical factor that controls the oxidation mode. Permeability can be described as element concentration times its diffusion coefficient. In this case when $N^{(s)}_O D_O \gg N^{(0)}_B D_B$, internal oxidation occurs.

Internal oxidation can happen individually or simultaneously with external oxidation in steel. If other parameters remain constant, the concentration of a specific alloying element is required to be higher than a critical value to sustain scale growth and without subscale formation. Therefore, the minimum concentration of element B required to form scale only and subscale-free steel can be expressed as [37]:

$$N^{(0)}_{B\ min} = \frac{V^{A-B}_m}{V^{BO_v}_m} \left[\frac{\pi K_p}{2\widetilde{D}_{AB}}\right]^{\frac{1}{2}} \tag{12}$$

where K_p is the parabolic B scale growth rate constant, $\widetilde{D}_{AB}$ is independent of the concentration and represents the interdiffusion coefficient in A-B alloy.

$$k_p = \frac{X^2}{2t} \tag{13}$$

where X is the scale thickness and t is the oxidation time.

The diffusion rate is enhanced when the volume fraction of internal oxides increase within the IOZ.

This is due to faster oxygen diffusion speed along the oxide-matrix interface as compared to the lattice diffusion [37]. Rapp [72] also mentioned that oxygen prefers to diffuse through the interfaces. However, the enhancement effect no longer exists when a critical volume fraction of oxide precipitates is reached. Excess accumulation of precipitates acts as oxygen diffusion barriers and tends to inhibit any further internal oxidation behaviour. Subsequently, oxygen is unable to diffuse inwardly, but alloying elements are able to diffuse outwardly. The internal oxidation is then transfers to external oxidation.

2.10.2. Solubility product of precipitates

Lashgari [37] mentioned that the solubility product of internal oxide precipitates has a significant influence on the distribution of inclusions formed. Fig. 38 shows that in low solubility product oxides, the internal oxides present evenly across the IOZ and the oxygen concentration becomes zero at the oxidation front. Also, the concentration of the solute element becomes zero near the surface. In contrast, Fig. 39 explains that when the solubility product of oxides is high, alloying elements oxidase continuously during the IOZ formation. In this case, the solute concentration is not 0 in the IOZ and oxygen concentration does not decrease to 0 at the oxidation front. Also, the amount of precipitates varies across the IOZ (refer to Fig. 40 [37]).

The volume fraction of precipitates across the IOZ can be determined, an example can be given with the Mn alloyed samples, which has been described in section 2.10. Firstly, the higher content of Mn will certainly lead to a higher volume fraction of precipitates. Secondly, the volume fraction of oxide remains constant from the sample surface to the bulk until a certain depth is reached. Then, the volume fraction drops at a relatively fast rate towards the oxidation front (zero). Therefore, MnO is determined to have a relatively low solubility product, but not extremely low.

Moreover, Lashgari [37] clarified that the oxidation mode (either external or internal) could be predicted if the dew point and the initial element concentration are known.
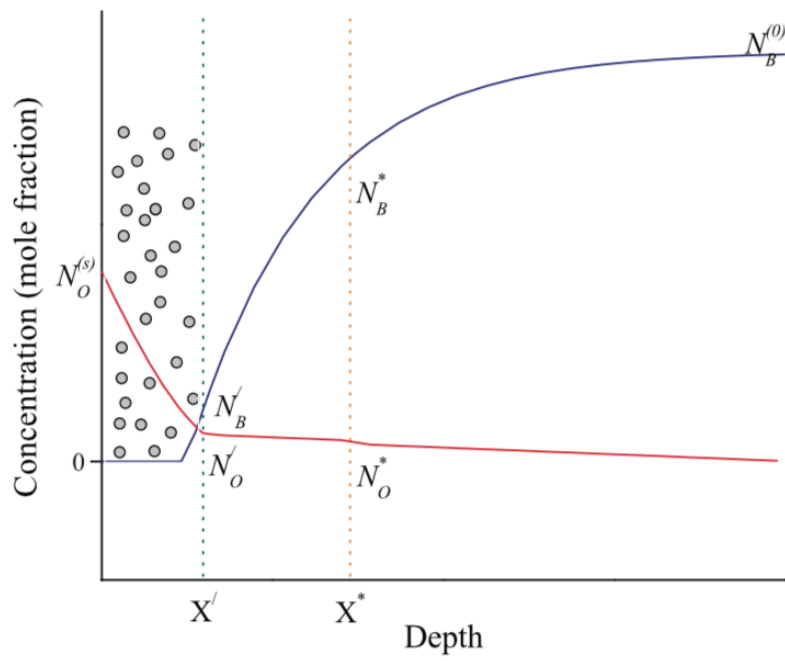
Fig. 38. Concentration variation of oxygen, alloying element and low solubility product oxide across the steel thickness [37].
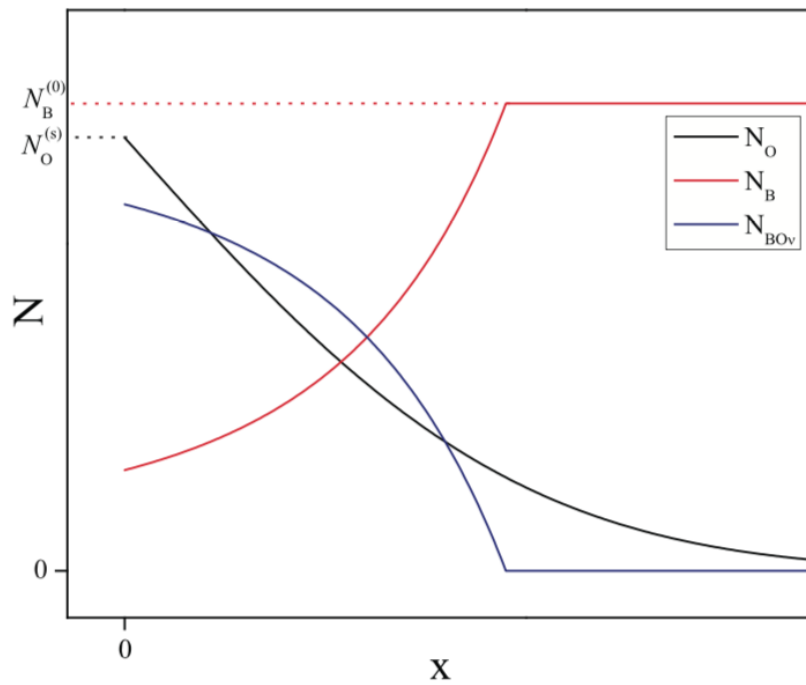
Fig. 39. Concentration variation of oxygen, alloying element and high solubility product oxide across the steel thickness [37].
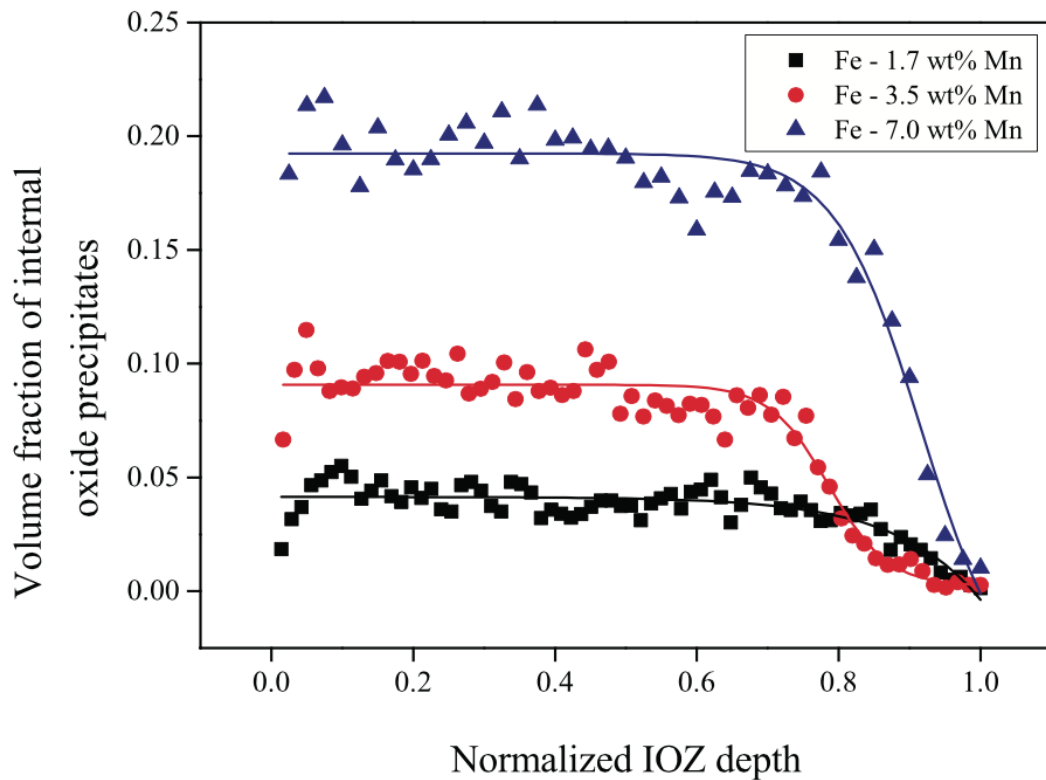
Fig. 40. The volume fraction of precipitates versus normalised IOZ depth of Mn alloyed steel samples that contain 1.7, 3.5 and 7.9wt% of Mn. Samples are oxidised at 950°C for 20 hours. N_2 atmosphere with 5 vol% H_2 and 10°C of dew point is pervaded [37].

2.11. Coil cooling

At the finishing mill of the hot rolling line, the strip temperature is between 820 and 910°C (full hot rolling processing details could be reviewed in section 2.3.1). Typical steel oxide structures could form within this temperature range, with a thin hematite layer present at the surface, thick wustite layer at the scale-steel interface and at the magnetite layer in between. The strip is then cooled rapidly by water spray and coiled up at 500-720°C [73]. The cooling water spray at this stage also acts as a mechanical descaling tool to remove some of the tertiary scales before the strip is coiled. However, complete removal of all the scales is impossible (refer to p40). If oxygen is available, the three-layered scale structure will always form at above 570°C. When the temperature drops below 570°C, wustite becomes unstable and starts to decompose into magnetite.

2.11.1. External oxides developed during coil cooling

A typical steel coil is shown in Fig. 41, where 1km in length can be reached when fully extended [74]. During the cooling process, the outer wraps and the edges of the coil will undergo faster cooling than the inner wraps. Also, the cooling rate depends on the coil size and ambient temperature. Various cooling rates inside the coil will lead to significant differences in scale development. This makes the following descaling process (pickling before cold rolling) become more complicated. For example, magnetite layer formation at the interface of the wustite and steel matrix will slow down the pickling speed by delaying the electrochemical process. Chen [73] mentioned that it is essential to understand the mechanism of scale formation and to identify the conditions under which they form. However, the relationship between the coil scale and cooling conditions is still not clear, particularly from a quantitative aspect.

Chashchin [75] monitored the temperature changes within a coil by placing thermocouples at turns 3, 36 and 51 (54 turns in total). The coil had 21.4 t mass, 1500 mm in width and 5.5mm strip thickness. The coiling process started at 761°C, and the temperature changes are illustrated in

Fig. 42 and Fig. 43.

Fig. 41. A Tata steel structural steel coil [74].
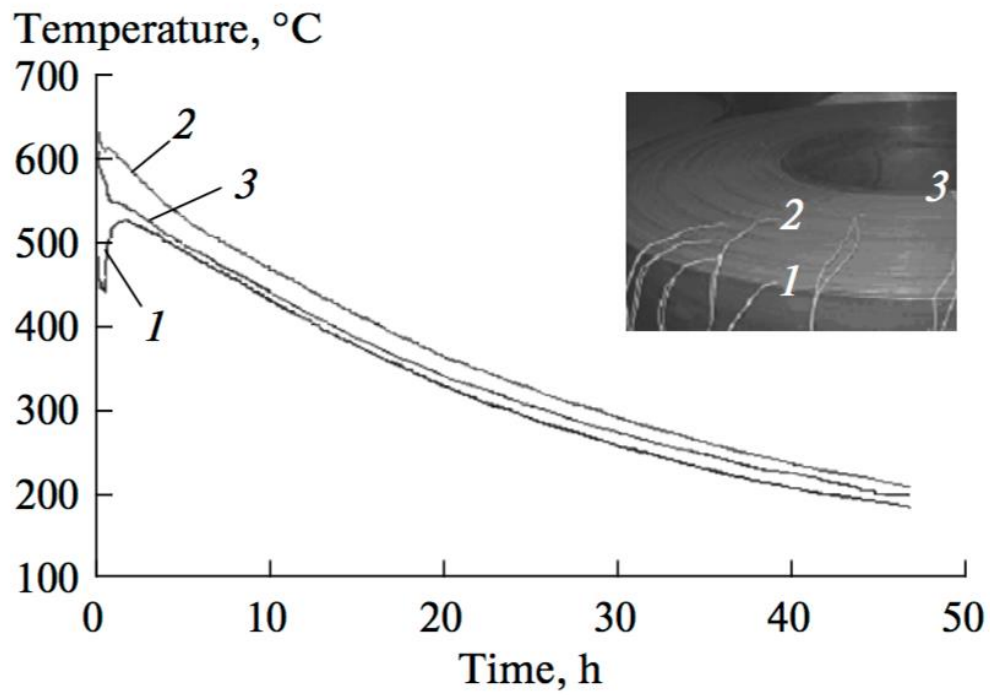
Fig. 42. The coil cooling temperature versus time curves, where the thermocouples are placed at 1: turn 3; 2: turn 36; 3: turn 51 [75].
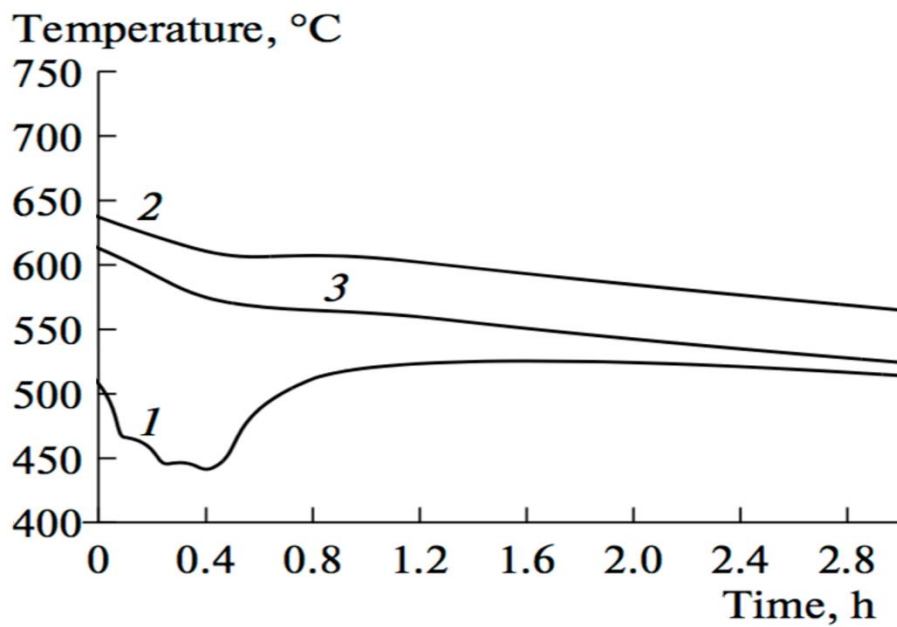
Fig. 43. The coil cooling temperature versus time curves at the initial stage (0-3h), where the thermocouples are placed at 1: turn 3; 2: turn 36; 3: turn 51 [75].

The middle of the coil (where thermocouple 2 is) has the slowest cooling rate. In the beginning, a relatively large temperature drop occurred at the outer coil, where the influence of the ambient temperature is greater. The coil was transported to the thermostat base and the cooling conditions were establishing during this period. Chashchin [75] mentioned that after around 24 hours, the middle coils (hottest areas) were cooled below 300°C. Any further monitoring is unnecessary because the scale development is stopped at these temperatures.

The internal turns of coils are wrapped tightly with each other, which means only the parts exposed to the air (outermost, innermost and the edge) will gain sufficient interaction with the free-flowing oxygen. In this case, Chen [73] designed his experiment to simulate both of these situations. Samples were pre-oxidised in air at 880°C for few seconds to simulate the conditions at the finishing mills of the hot rolling line. Coiling simulation started at temperatures between 300 and 730°C and the cooling rate was varied from 1 to 60°C/min. Majority of the experiments were performed in 99.99% N_2 atmosphere, which aims to simulate the low oxygen environment inside the coil. The remaining experiments were performed in ambient air to simulate the oxygen abundant environment at the surfaces and edges of the coil. The steel samples involved in their experiments were cold rolled, mild steel alloyed with 0.06wt% C and 0.25wt%Mn and a thickness of 0.8 mm.

As a result, oxidation at 880°C developed the classic three-layered scale (as described in section 3.1). The thickness of magnetite and hematite is depended on the cooling rate and oxygen content. Similarly, during the coiling simulation, wustite remained if the cooling rate was sufficiently high, although some magnetite precipitates were always found within the wustite layer. This scale structure is defined as Type I, as shown in Fig. 44 [73]. The study went on to classify the types of scale structure as described in the following paragraphs.
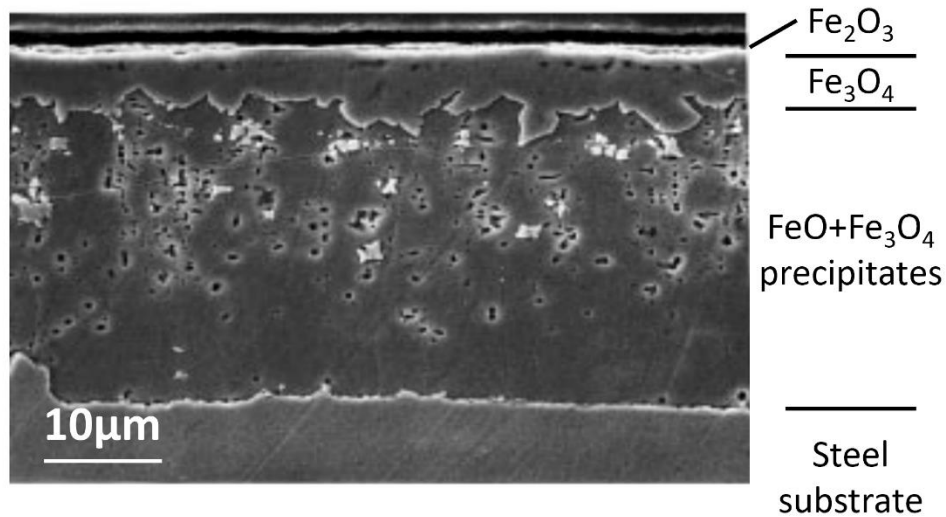
Fig. 44. BSE image of Type I scale, oxidised from 650°C with cooling rate of 15°C/min. [adapted from [73]].

Type II scale is formed when higher CT or slower cooling speed is applied. A continuous magnetite layer will appear between the wustite and steel substrate. Also, the amount of magnetite precipitates within the wustite is more than in type I scale, as shown in Fig. 45.

Type III scale is likely to form when even higher CT or lower cooling rate is performed. In this case, almost the entire wustite layer is decomposed into a mixture of magnetite-iron eutectoid (the majority) and precipitated magnetite (the minority). The type III scale formed is shown in Fig. 46 [73].
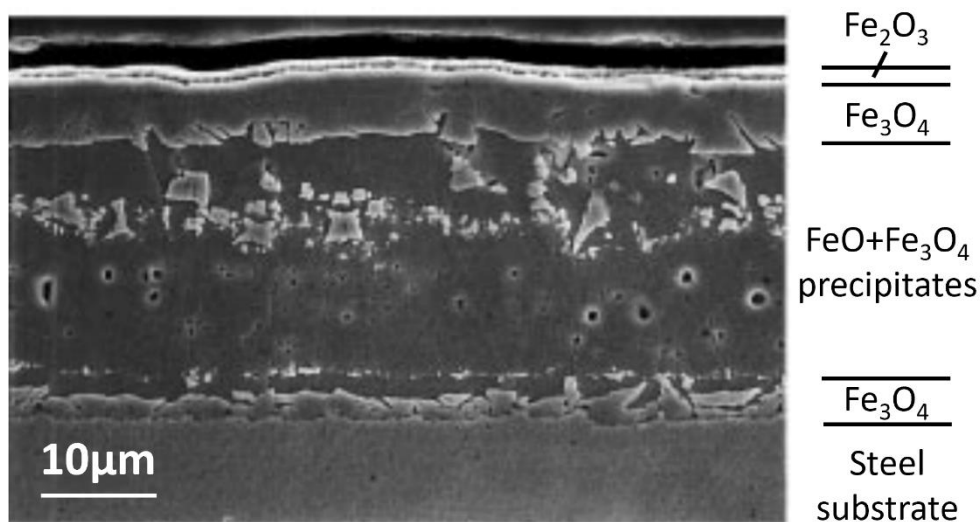
Fig. 45. BSE image of Type II scale, oxidised from 650°C with cooling rate of 5°C/min. [adapted from [73]].
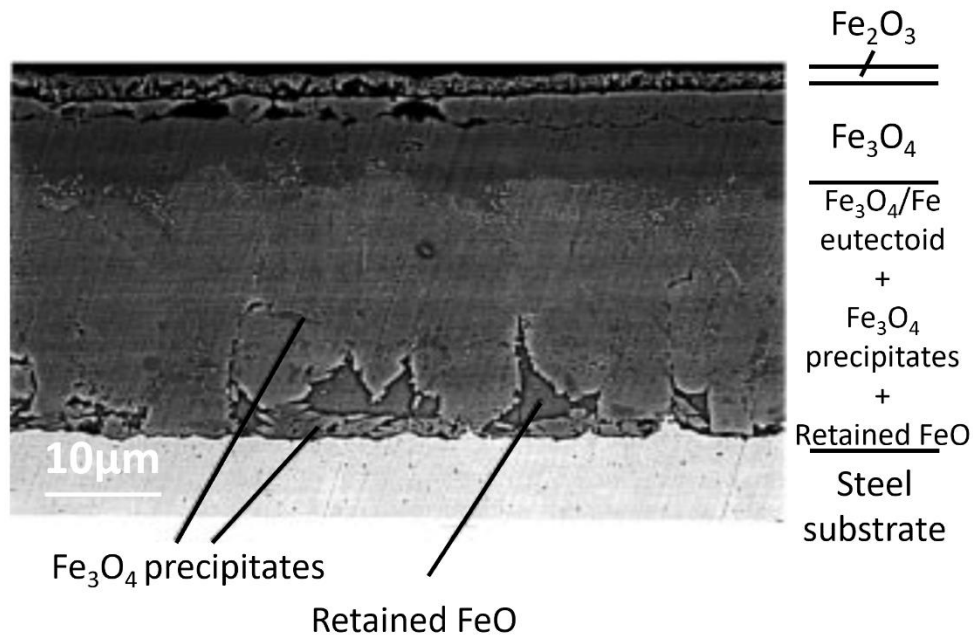
Fig. 46. BSE image of Type III scale, oxidised from 650°C with the cooling rate of 1°C/min. [adapted from [73]].

The formation of any specific scale type is determined by the combination of coiling temperature and cooling rate, as summarised in Fig. 47. For example, at 550°C, 30°C/min cooling rate needs to be reached to form Type I scale. However, 2°C/min is enough to form the same scale if the CT is 300°C. Similarly, 5°C/min cooling rate combined with 450-700°C CT will lead to the formation of Type II scale. However, if the cooling rate is lower to 2°C/min, Type III scale is more likely to form.

The decomposition from wustite to magnetite is believed to be iron deposition, followed by direct magnetite formation [73]. At temperatures below 570°C, the wustite closest to the steel substrate first becomes supersaturated with iron and oxygen. The supersaturated iron prefers to deposit onto the steel substrate directly and leave the wustite with a more abundant oxygen content. The steel substrate is acting as a heterogeneous nucleation centre for iron to deposit, which requires relatively lower energy. The remained oxygen-supersaturated wustite has a greater driving force to transform into magnetite nuclei and has higher tendency to form at the steel-scale interface as well. If the cooling rate is low enough, the magnetite nuclei will have enough time to grow and finally become a continuous layer (also called a magnetite seam) [76].

On the other hand, only a relatively thin hematite layer could be found when experiments were performed in nitrogen. Tanei et al. [77] mentioned that the hematite layer at the surface changes into

magnetite by holding at 550°C in a nitrogen atmosphere. It is probably because of the hematite in this term is decomposed and acting as an additional oxygen-rich source for other oxides to grow.

Birosca [76] mentioned that when the temperature remains high for longer, thicker scales will form due to faster diffusion of iron and oxygen ions. The diffusion rate also depends on other factors, such as the amount of porosity in the scale and the surface conditions. Cracks and defects at surface/subsurface will raise the oxygen diffusion rate locally.
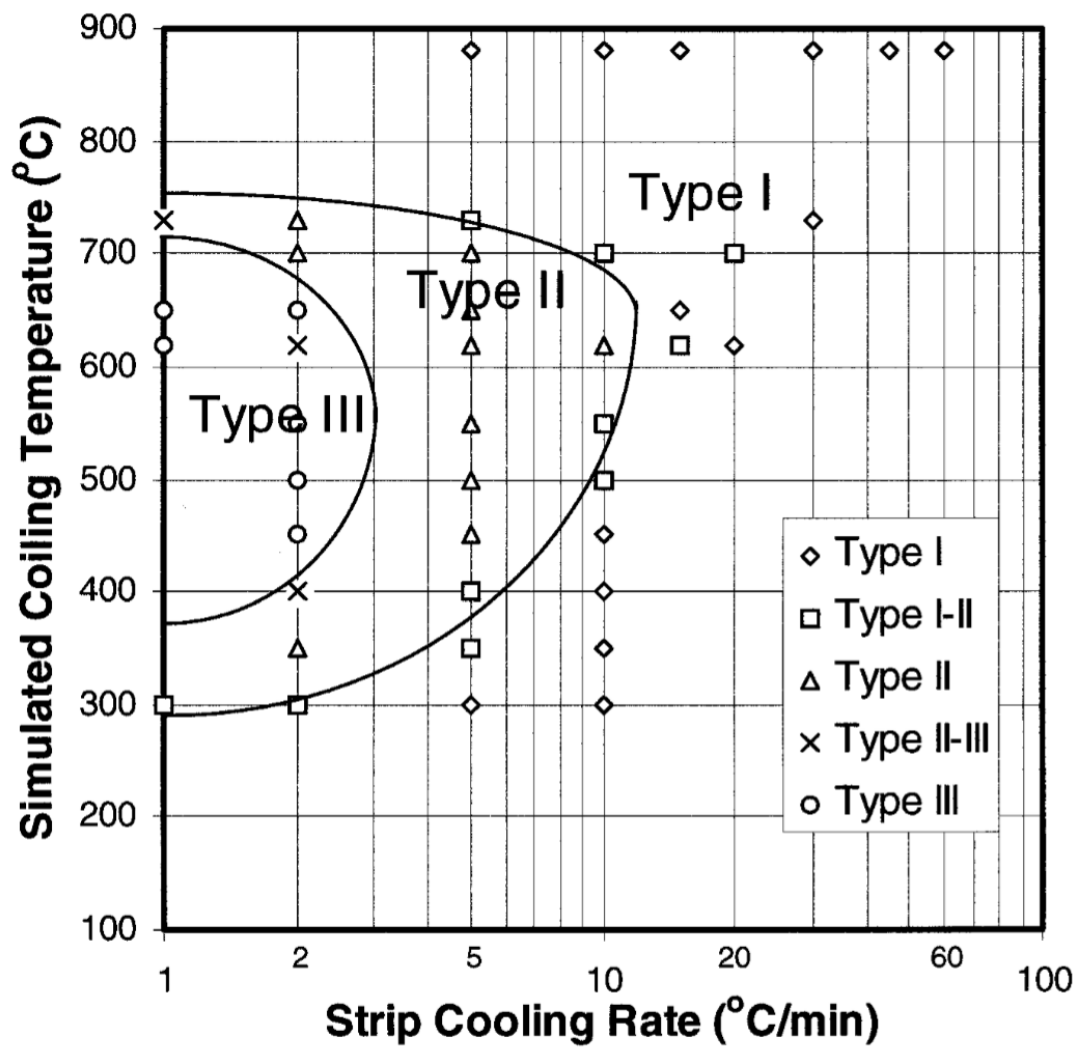
Fig. 47. An indication of the type of scale formed as a function of strip cooling rate and simulated coiling temperature [73].

2.11.2. Internal oxide developed during coil cooling

The cooling rate varies within the steel coil during the cooling stage, owing to its complex geometry. Deeper IOZ is found at inner parts of coils as the local cooling rate is lower, whereas negligible IOZ appears at the head, tail and edge of the coil [49]. Internal reports show that under the industrial coil cooling conditions, the subscale stopped growing at temperature below 550 °C .

At the hottest areas of a coil, selective internal oxides will form along the grain boundaries and grow further into the steel matrix. Cracks become more likely to initiate and open through these grain boundaries after pickling or cold rolling. In this case, bendability is significantly influenced by internal oxidation, a full study will be reported later (p. 118). The depth of internal oxide zone is strongly related to the time spent at high temperature during coil cooling. The oxide formed internally is also largely depends on the presence of scales when the steel sheet is tightly wrapped, so the access of oxygen from ambient air is limited [66]. Fig. 48 is an example of a cross-section of an internally oxidised steel subsurface. An approximately 25µm thick IOZ was found that penetrated into the steel surface through the grain boundaries. The coil cooling was simulated at 700 °C, and the sample contained 1 wt% Mn and 0.4wt% Si. EDS maps confirmed that the grain boundaries contain by Mn-Si enriched oxides.
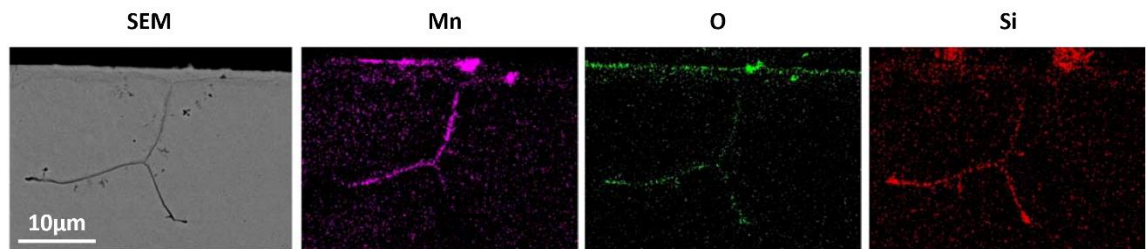
Fig. 48. SEM cross-section images, EDS manganese, oxygen and silicon maps of internally oxidized steel subsurface. The sample contains 1wt% Mn and 0.4wt% Si, oxidized at 700°C. [adapted from [66]]. All micrographs share the same scale bar.

Internal documents also show that the internal oxidation becomes apparent beyond 2% of the total coil length from the head and 1% away from the tail of the coil. The depth raises and reaches a constant magnitude at approximately 20% of the coil length form the head and tail. Similarly, the depth increases and reaches a constant value after around 1/3 from the edge. It has also been shown that

the temperature remains high for longer at the regions described above. When other conditions remain constant, a 700°C CT will double the IOZ thickness compared to coiling at 620°C. Chashchin [75] mentioned that when the temperature is below 300°C, the scale development is stopped. The internal oxidation depth is also significantly influenced by the alloying element. It has been mentioned (p. 47) that when multiple elements are alloyed into the steel, the formation and position of a specific oxide inclusions are largely dependent on its deoxidising preference. For example, Mn requires higher partial oxygen pressure to form internal oxide in steel than Si and Al (Al<Si<Mn). Under same coiling conditions, 1.8-2.2%Mn and 0.5%Cr alloyed steel will show a thinner IOZ than the same steels that contain an additional 0.25%Si or 0.7%Al.

2.11.3. Steel microstructure developed during coil cooling

Regarding the microstructure, Lee [78] reported the influence of CT and finishing mill thickness reduction ratio (during hot rolling) on the microstructure of low carbon, Mn and Si-containing steel samples. The results are shown in Fig. 49, where higher CT (a) will lead to larger grains, hence coarser microstructures than lower CT (b, c, d). When the other factors remain constant, the steel with larger grains has lower strength and toughness, but higher elongation. In the meantime, a higher reduction ratio will lead to finer microstructure (e, f). The combination of high reduction ratio during hot rolling and low CT during coiling will certainly make the grain size even smaller (g). Lee concluded that the effectiveness of toughness enhancement could be ranked as: Low CT>thickness reduction ration at finishing mill>low rolling temperature. However, ductility will be sacrificed if CT gets low.
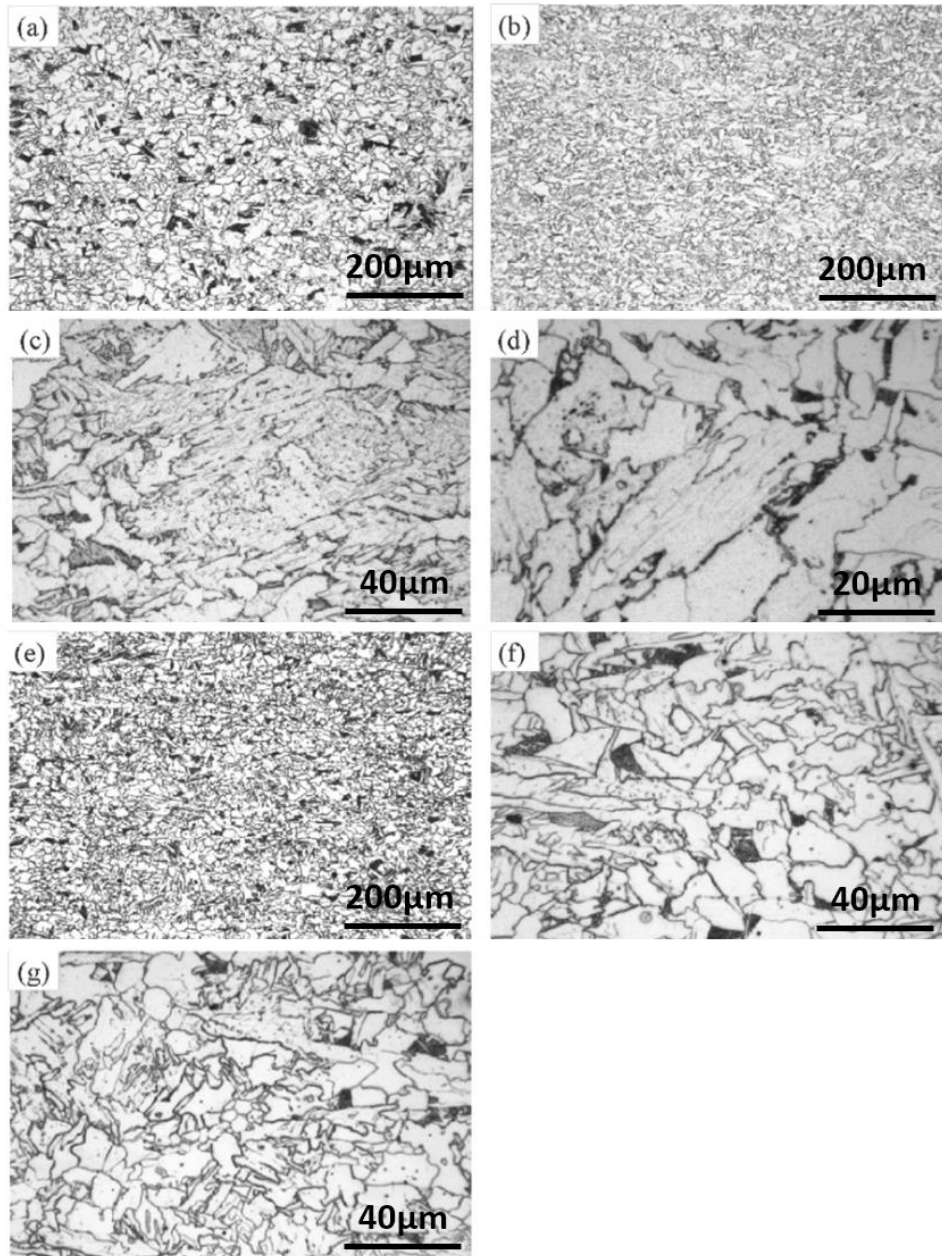
Fig. 49. The microstructure of low carbon steel samples (1.7wt%Mn, 0.6wt% Si) after hot rolling and coil cooling. (a) Coarser grains due to higher CT, (b, c, d) Finer grains under lower CT. (e, f) finer grains due to higher thickness reduction ratio. (g) Finest microstructure when high thickness reduction ratio and low CT were applied simultaneously [78].

2.12. Oxidation in coil cooling conditions.

The oxygen activity of the surrounding gas has a significant influence on the internal oxidation rate of scale-free steel. However, an inverse relationship was found when scale exists. Rapp [69] mentioned

that the growth of the internally oxidised zone in scale-contained steel is independent of the oxidation time. The scale formation is an oxygen-consuming process, and acts as a barrier of inward oxygen diffusion. Lashgari [37] mentioned that the partial pressure of oxygen at the steel surface is equal to the ambient if the scale is absent. However, the oxygen partial pressure depends on the local equilibrium between the alloy and the scale if external oxidation is present.

In this study, the relationship between external and internal oxidation is critical because both of these reactions consume oxygen, which is limited in the tightly wrapped coil. It is assumed that the external oxides are formed before the sheet has been coiled completely. The fast-moving sheet transferring speed and the moisture created by the descaling water jet should provide sufficient oxygen for external oxidation to form within a few seconds (from internal discussions).

It is also possible that some of the oxygen required for internal oxidation in the hot rolled coil might coming from the external oxides formed prior to coiling. These iron oxides might start to decompose during the coil cooling, providing an oxygen in the tightly wrapped coils. The internal oxidation is driven by the relative oxidation of the elements present at temperature and the oxygen from the decomposition becomes more significant than the outward diffusion of Si/Mn to form internal oxides. The decomposition reactions of iron oxides can be described by [79]:

$$\frac{2}{y} Fe_x O_y = \frac{2x}{y} Fe + O_2 \tag{14}$$

This reaction occurs spontaneously when the Gibbs free energy difference (ΔG) between the reaction products and the reactant is negative:

$$\Delta G_1^0 = \frac{2x}{y} G^0(Fe) + G^0(O_2) - \frac{2}{y} G^0\left(Fe_x O_y\right) \tag{15}$$

$$\Delta G^0 = -RT \ln K \tag{16}$$

where R (gas constant) is 8.314Jmol^{-1}K^{-1}, T is the temperature and K is the equilibrium constant, which determines the reaction direction and can be calculated by:

$$K = \frac{a^{\frac{2x}{y}}(Fe) \cdot a(O_2)}{a^{\frac{y}{z}}(Fe_x O_y)} \tag{17}$$

K=p(O$_2$), when assuming O$_2$ is an ideal gas. In this case (16) is now re-writing as:

$$P(O_2) = \exp\left(-\frac{\Delta G_1^0}{RT}\right) \tag{18}$$

Hryha [80] calculated and plotted a diagram of temperature dependency of the oxygen partial pressure for several oxides, as shown in Fig. 50. For each oxide, the conditions below the line mean reduction

is favourable and the dissociated state is more stable.
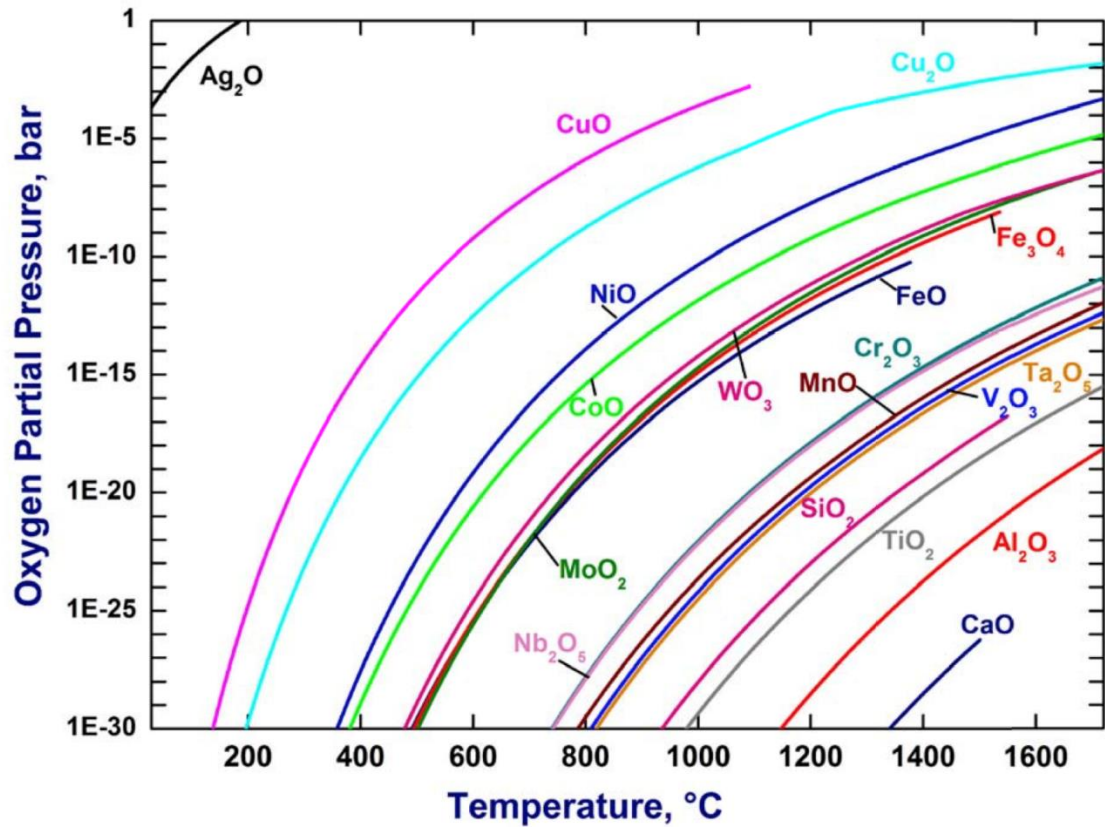
Fig. 50. Equilibrium conditions of oxides under factors of the oxygen partial pressure and temperature [80].

The results show that although the iron oxides can be reduced to provide oxygen for the internal oxidation theoretically, the actual oxygen partial pressure is not enough for any of the reduction reactions to happen under 650°C. In this case, Hryha et al. [80] proposes that the local partial oxygen pressure under coil cooling condition is neither low enough for the external iron oxides to reduce nor high enough to diffuse through the steel matrix to form internal oxides.

However, Brocking et al. [81] did researches on the coil cooled steel sheet, which has similar compositions and heat-treatment histories to the samples studied in this project. The results (as shown in Fig. 51) shows iron nodules are present at the scale surface, which is trusted to be formed due to the surface iron oxide reduction.

Element	Wt%	At%
O K	32.15	57.41
Si K	15.6	15.87
Fe K	52.25	26.73
Total	100.00	100.00
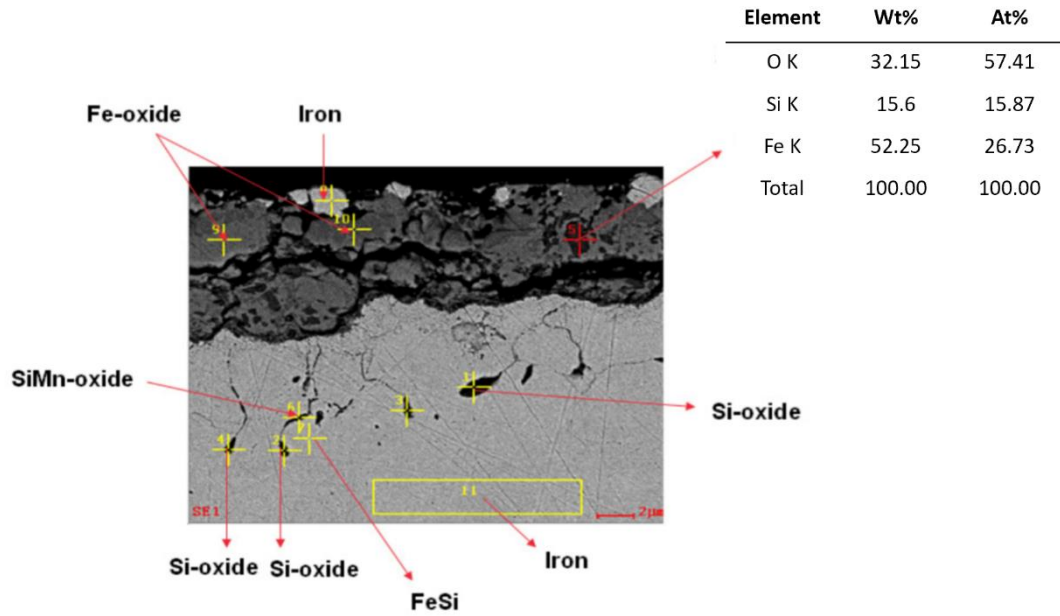
Fig. 51. A typical scale area analysed by EDS. The microstructure and phases presented are similar to the steel A studied in this project[81].

2.12.1. The influence of decarburisation on oxide development.

A new assumption was made by the author in this project that the decarburisation effect promotes the reduction of the external iron oxides during the coil cooling process. Schatt [82] mentioned that reducing agents, such as H_2 or CO are introduced to help with the reduction process in many industrial applications. As mentioned previously (p43), Shi *et al.* [65] also state that carbon monoxide is a readily available gas in the steel industry and has outstanding scale reduction ability. None of these reducing agents is introduced into the coiling environment artificially. However, decarburisation happens simultaneously at elevated temperature. The outward diffusion of carbon from steel to oxides within a relatively enclosed environment (tightly wrapped coil) could promote the reduction of iron oxides. In general, the carbothermal reaction could be [79]:

$$\frac{2}{y} Fe_x O_y + 2C = \frac{2x}{y} Fe + 2CO \tag{19}$$

As an example, the outward diffusion of carbon starts to react with the wustite at the scale-steel interface [52]:

$$FeO + C = Fe + CO \quad \Delta G = 147763 - 150.07 \cdot T \, J \tag{20}$$

The resulting carbon monoxide can further be involved in the indirect carbothermal reduction [79]:

$$\frac{2}{y} Fe_x O_y + 2CO = \frac{2x}{y} Fe + 2CO_2 \tag{21}$$

Evidence was given by Holm [83], as steel samples with known carbon content (0.039%) were oxidised in air at 400°C and then reduced in vacuum at 800°C for 15-20 minutes. The oxidation and reduction heat treatments are repeated on the same sample for a number of cycles. The result shows that, at the first few heating cycles, the oxidised sample surface are completely transformed back to iron after the reduction process. The carbon content drops gradually after each reduction process. The brightening effect (due to oxides reduced back to iron) gradually decreases after a few cycles and was no longer present at the sixth cycle. The carbon content drops to 0.04% after the fifth reduction. It was concluded that the high-purity iron (≤0.001% of C) could not be brightened under vacuum at up to 1250°C.

From the backscattered images (Fig. 51), the iron nodules are mainly formed at the surface of the external oxide layer, which is a sign of hematite reduction. However, hematite to iron reduction does not occur in one step; three reactions are normally involved [84]:

$$Fe_2O_3 + \frac{1}{3}CO = \frac{2}{3}Fe_3O_4 + \frac{1}{3}CO_2 \tag{22}$$

where ΔH_{973K} =-11.73KJ/mol, $\Delta G_{973K} = -31.8 KJ/mol$

$$Fe_3O_4 + CO = 3FeO + CO_2 \tag{23}$$

where $\Delta H_{973K} = 10.3$KJ/mol, $\Delta G_{973K} = -2.74 KJ/mol$

$$FeO + CO = Fe + CO_2 \tag{24}$$

where $\Delta H_{973K} = -18.43$KJ/mol, $\Delta G_{973K} = 2.94 KJ/mol$

The negative Gibbs free energy value means the hematite can easily reduce to magnetite. Reduction from magnetite to wustite and iron is also possible at 973K (701 ° C), depending on the CO concentration. Yi [85] mentioned that hematite starts to dissociate step by step at temperatures above 571°C. The current study will explore whether the carbon in a high alloyed steel plays an important role in the scale and subscale development and provide further insight into the interaction between iron oxide reduction and internal oxidation in low oxygen environment, such as that experienced in a

tightly wrapped coil after hot rolling.

Chen [84] also plotted the thermodynamic equilibrium diagram of iron oxides as a function of temperature and CO concentration, as shown in Fig. 52. The boundary reaction of CO and CO_2 ($C + CO_2(g) \Leftrightarrow 2CO(g)$) is represented as line 5.

In this case, the hematite can reduce to magnetite without problem. Reduction from magnetite to wustite and iron is also possible at 701°C, depending on the CO concentration. The only difficulty is to explain how the surface hematite is reduced during the coil cooling, but the magnetite and wustite remain unchanged (will be discussed in Chapter 6).

Yi [85] applies a Fe_2O_3, Fe and Al_2O_3 powder mixture (1:1:1) onto steel pieces that without any surface oxide. The samples are sealed tightly in steel capsules during the heat treatments to isolate air. In Yi's research, Fe_2O_3 is selected as the 'oxygen source' for internal oxidation, but the reason of using hematite instead of magnetite and wustite is not explained. It is likely that hematite contains the highest amount of oxygen than the other two common iron oxides. Yi further explains that hematite starts to dissociate step by step at temperature above 571°C.

The internal oxidation follows a parabolic rate law:

$$x^2 = K_p \cdot t \tag{25}$$

where x is the internal oxidation depth, t is the oxidation time and K_p is a constant rate of internal oxidation. The K_p value increases at higher oxidation temperature and lower concentration of alloying elements. It is also influenced by the surface scale and subsurface grain size.

$$K_p = K_p^* \exp\left(-\frac{Q_k}{RT}\right) \tag{26}$$

where K_p^* is a constant for each steel and Q_k is the internal oxidation activation energy.
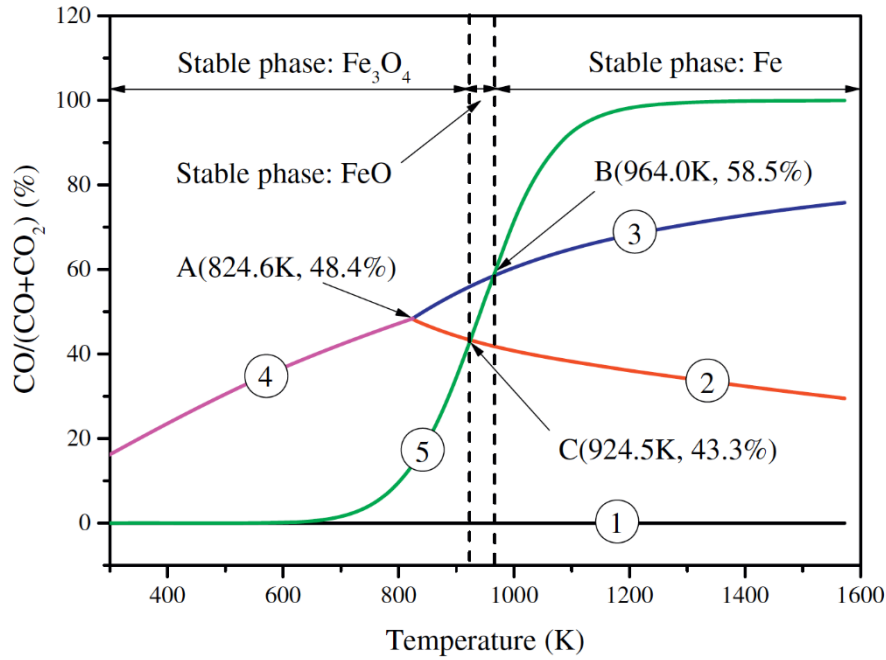
Fig. 52. Thermodynamic equilibrium of iron oxides reduction and CO-CO2 boundary reaction. 1, $Fe_2O_3 \rightarrow Fe_3O_4$; 2, $Fe_3O_4 \rightarrow FeO$; 3, $FeO \rightarrow Fe$; 4, $Fe_3O_4 \rightarrow Fe$; 5, $CO \Leftrightarrow CO_2$ [84].

Bertrand [54] found that the oxidation kinetics are reduced by water vapour. By comparing to oxidation tests in dry air, the thickness of hematite layer increased while magnetite became thinner. Thermal gravimetry analyses (TGA) showed that 2vol% H_2O in air decreased the mass gain of steel at 400°C and the magnitude is not affected by the gas flow rate. The presence of water vapour tends to separate the scale from the bulk steel, which inhibits the ion diffusion for oxidation. The presence of H_2O at the steel surface promoted the nucleation rate of the surface oxide. The higher nucleation rate will lead to smaller grain size of the oxides.

Regarding the scale surface developed in air+ 2vol% H_2O and at elevated temperature, Bertrand [54] found α-Fe_2O_3 in whiskers or platelets shape. In contrast, small rounded crystallites with open porosities are found in the samples oxidised in dry air.

2.13. Summary

In summary, the nature of the oxidation of steel samples has been reported to be influenced by a variety of factors – composition, temperature, atmosphere being the most widely investigated and

reported in the literature. Other factors, such as differences in surface roughness can also alter the behavior for a given steel exposed under the same conditions. From the final product perspective, the characteristics of the surface and near surface will have significant effects on mechanical behavior, such as bendability. A major challenge is relating to the condition experienced in a steel mill to the final products and to simulate appropriate conditions in a laboratory environment. It is the aim of the present study to investigate the role of coil cooling conditions on oxidation and to determine the effect of surface and near surface microstructure on the bending behavior of the steel strip.

Chapter 3: Properties of the received samples and the selection of characterisation techniques.

The work present in this chapter aims to understand the basic properties of the steel sheet samples received from the industry partner and analysed and discussed in the following chapters. Surface and subsurface features of the as-received coil cooled samples are inspected. The relationship between the local scale colours and the external/internal oxide structures around the areas is understood. The extent of decarburisation is studied on both of the hot rolled and galvanised coil samples. A new scale and subscale inspection method is established for more effective measurements.

3.1. Introduction

Hot rolled and coil cooled samples were received from Tata steel, Ijmuiden plant based in the Netherlands. Sample A is a dual phase steel in the development phase, which tend to have deep internal oxidation zone (~14microns when coiled at 650°C). It has relatively higher Mn and moderate Si content, whereas the concentration of other elements (e.g. Cr and Al) are significantly lower compared to current dual phase steels. The trace element additions have no significant impact on the development of oxides and are not studied in this project. The samples are taken from the hot rolled and coil cooled stage, the thickness and composition are shown in Table 1. The compositions are constant in all of the hot rolled and annealed dual phase samples mentioned in this project. All of the hot rolled, coil cooled, galvanized and annealed DP1000 samples mentioned in this study belong to trial material, none of them has been produced commercially.

Table 1. Thickness and compositions of steel A.

		wt%							
	Thickness	**C**	**Mn**	**Si**	**Cr**	**Al**	**P**	**S**	**Cu**
Steel A	**3mm**	**0.2**	**2.1**	**1**	**0.06**	**0.03**	**＜0.013**	**＜0.003**	**0.04**

A typical steel coil is shown in Fig. 53, the name of coil positions are labelled on the coil and the sketch

of a fully extended sheet sketch. During the cooling process, the outer and inner hot rolled coils as well as the edges will undergo faster cooling than the mid-coil material. A comparison of cooling rates between the edge and mid-width position at constant coil length is given in Fig. 54. The cooling rate also depends on the coil size and ambient temperature. In addition, the oxygen level will also vary with distance from the coil edges and head. The position-dependence of the cooling rate and oxygen availability inside the coil leads to significant differences in the development of external and internal oxides.
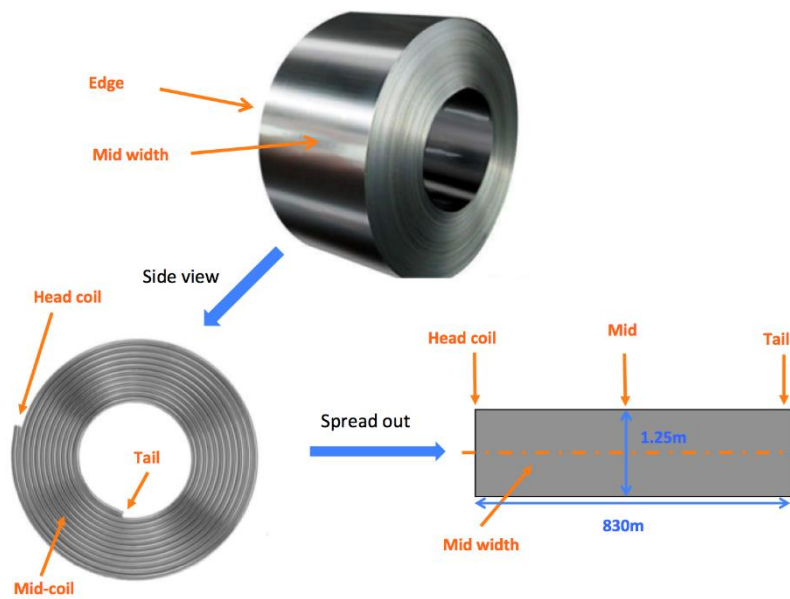
Fig. 53. Hot rolled coil with the side view, coil positions are also labelled on fully extended sheet sketch.
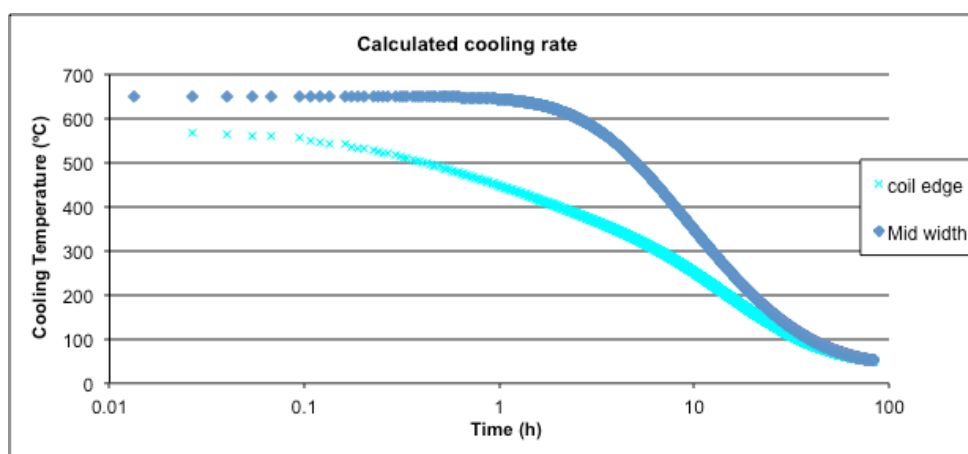
Fig. 54. The calculated (by industrial partner) cooling rate of a typical hot-rolled coil at the edge and mid-width positions of mid-coil.

For a clearer illustration, the reference locations of all the DP1000 samples studied in this and the following chapters are summarised in Table 2.

Table 2. Summary of the reference locations of DP1000 coil samples studied in this project.

DP1000 (Steel A)		Hot rolled + coil cooled		Annealed	
		Scale remained	Scale removed	Galvanised	IOZ removed
Head coil	Edge	1	5	9	13
	Mid-width	2	6	10	14
Mid coil	Edge	3	7	11	15
	Mid-width	4	8	12	16

Macroscopic observations revealed three different colours (grey scale) found at the mid-length and mid-width of the hot rolled sheet surface (location 4, refer to Table 2). The as called dark scale, grey scale and clean grey surface and are illustrated in Fig. 55, all the scales elongate along the rolling direction (as labelled). In contrast, the typical surface features at the coil head (location 1 and 2, refer to Table 2) are shown in

Fig. 56. The surface appears "cleaner" than at the mid-coil, and negligible dark scales are found.
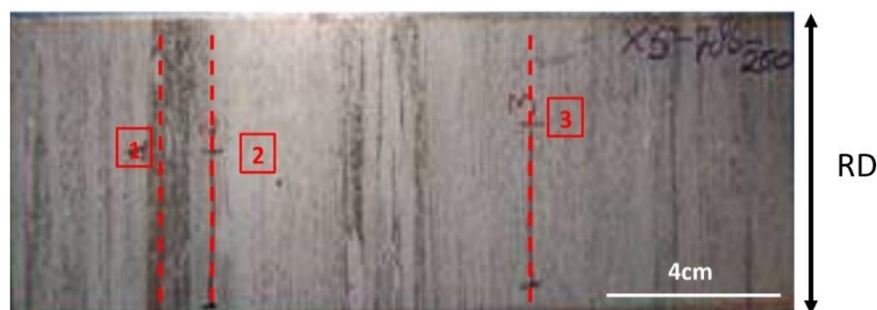
Fig. 55. Steel A surface texture, photo taken from the mid-length and mid-width of the hot rolled coil. Line 1, 2, 3 identify areas of dark scale, grey scale and clean grey surface respectively. The sheet rolling direction is labelled.
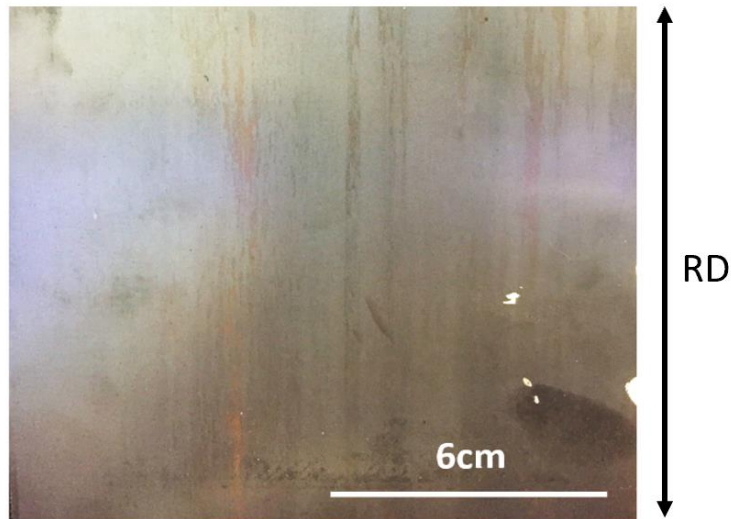
Fig. 56. Steel A surface texture, taken from the head-coil. The sheet rolling direction is labelled.

3.2. Experimental

The as-received steel sheets from the mid coil length and mid width (location 4, refer to Table 2) were cut into 40x40mm pieces by a guillotine; the cutting plan is illustrated in Fig. 57. The pieces are cut further to 20*10mm using a high concentration diamond saw with slow speed (2-3mm/min) to minimise damage to the brittle scales. The edges of the 40*40mm squares were cut away to remove the region with high residual stress caused by the guillotine blade. Samples were oriented to view the cross-section and were conductively mounted and polished using a sequence of 400, 9, 3 and 0.05μm grinding/polishing pads. The grinding pad is made of SiC. Some samples had thicker oxide layers, which may make them more susceptible to delamination at scale-steel interface. Cold mounting in a conducting epoxy resin was applied alternatively to prevent damage caused from the high pressure and temperature of the hot conductive mounting. Ni powder can be added to the epoxy resin with the ratio of 1:1 (by weight) to make the cold mount conductive.
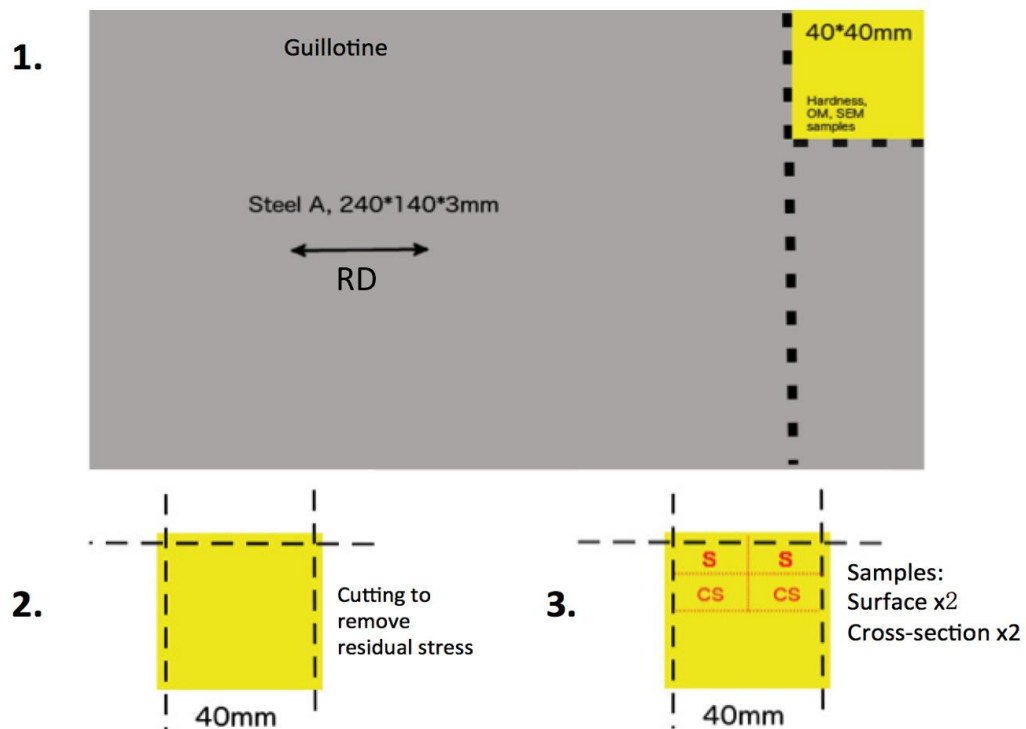
Fig. 57. Cutting plan for sample sheets. Two identical samples are cut within the same sheet location (as shown in 3.) to test both of the hot and cold conductive mounting methods. The sheet rolling direction is labelled.

Optical microscopy (OM) was used to examine the cross-sections. The OM samples were immersed in 2% nitric acid solution for 10 to 20 seconds for etching to form contrast between different phases (e.g. martensite and ferrite).

Due to the fine grain size and thin scale/subscale thickness, higher magnification images are taken using a secondary electron microscope (SEM). To obtain these images, a 4-5 kV beam voltage, 4mm working distance, 60mm aperture were used for imaging with both the in-lens and secondary electron detectors. Backscattered images were taken using an accelerating voltage of 10kV with a 120mm aperture.

Vickers hardness tests are performed under 500g-1kg indents load. Ten measurements were made on each sample at interested locations. Each indentation was performed 2.5 times the indent diagonal apart from the others.

3.3. Results and discussion

3.3.1. OM observations

Fig. 58 presents a typical image obtained using the optical microscope from the cross-section of the hot-rolled steel A (dual phase steel). The majority of grains are elongated along the rolling direction, and deformation bands are observed. In this case, the recrystallisation process is uncompleted. Akpan [86] found similar features on the hot rolled steel sheets. He mentioned that the elongated microstructure is due to high thickness reduction ratio (thickness at the exit is only 3mm, about 0.14 reduction ratio) during hot rolling along with insufficient temperature and time to eliminate all the deformation bands. However, Fig. 59 fine grains characteristic of recrystallisation, most of them near surface regions. The equiaxed grains at the surface could also be a sign of decarburisation and loss of the alloying element within the grains [87].

Numerous bright layers mixed with a few darker bands are found within the bulk. The brighter bands are formed of deformed ferrite grains, while the darker bands should belong to pearlite (a lamellar mixture of cementite and ferrite). Widmanstätten ferrite [88] also appears in the microstructure, as shown in Fig. 60. This is unavoidable if large deformation and recrystallization occurred. Martensite can not be easily identified in the OM images, and it may not exist in the microstructure at the hot-rolling stage. The martensite and ferrite mixture structure of DP steel product is mainly formed during the annealing process.

Fig. 58. OM cross-section image of dual phase steel A. The sheet rolling direction is labelled.

Fig. 59. OM cross-section image of dual phase steel A. The boundary between the brighter and darker scale layers is highlighted by the dashed line.
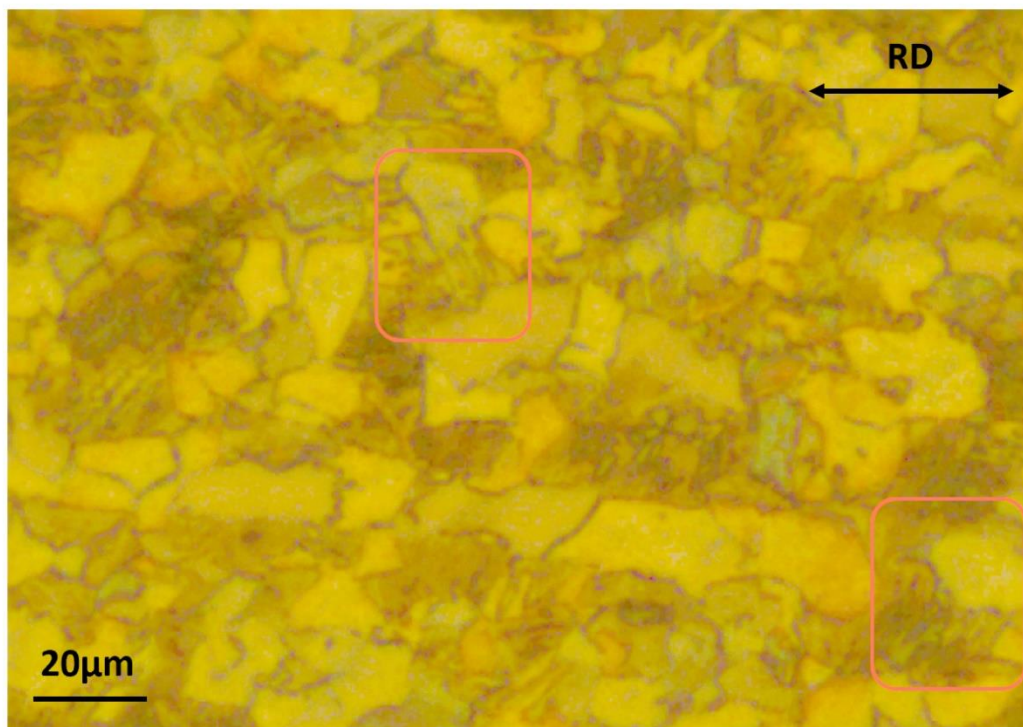
Fig. 60. OM cross-section image of dual phase steel A. Examples of widmanstätten ferrite are circled.

Regarding the oxidation behaviour, Fig. 59 is an OM image taken from the near-surface area. An approximately 5µm thick layer formed evenly at steel surface, as shown in Fig. 59. The scale consists of 2 parts, a brighter layer formed at the surface and a darker layer at the scale-steel interface. The difference in colour is a potential sign of compositional difference, but the nital etchant is not typically

used for oxide characterisation. Also, the external oxide layer of steel A is relatively thin ($\leqslant 20\mu m$) and the optical microscope has limited resolution to observe more detailed features.

3.3.2. SEM observations

Microstructures of nital etched steel A were taken by both in-lens, secondary electron (SE) and backscattered electron (BSE) detectors, where representative images will be presented in the following sections. All images were taken from the cross-sections of the hot rolled steel sheets at the head-coil (between location 1 and 2, refer to Table 2). Fig. 61 shows the microstructure of steel A at near surface, where the grains stay undeformed. The scale thickness is confirmed to be less than $5\mu m$. In addition, a high density of porosity is found at the scale-steel interface. One possible explanation is the iron diffused outward to form the scale faster than bulk diffusion in the steel, leaving behind vacancies that coalesced to form pores. Another explanation could be precipitates or inclusions inherent in the steel or formed during processing were pulled out during sample preparation (grinding and polishing), leaving holes. Also, this could be a specific phenomenon during the batch production as no porosity exist in the samples from the other coils received. Examining Fig. 61 and Fig. 62, which were taking from the subsurface and mid- thickness of the sheet, respectively, confirms that the grains near the surface were fully recrystallised. Only grains at particular areas, especially at mid-thickness are elongated and the deformation bands were not fully eliminated.
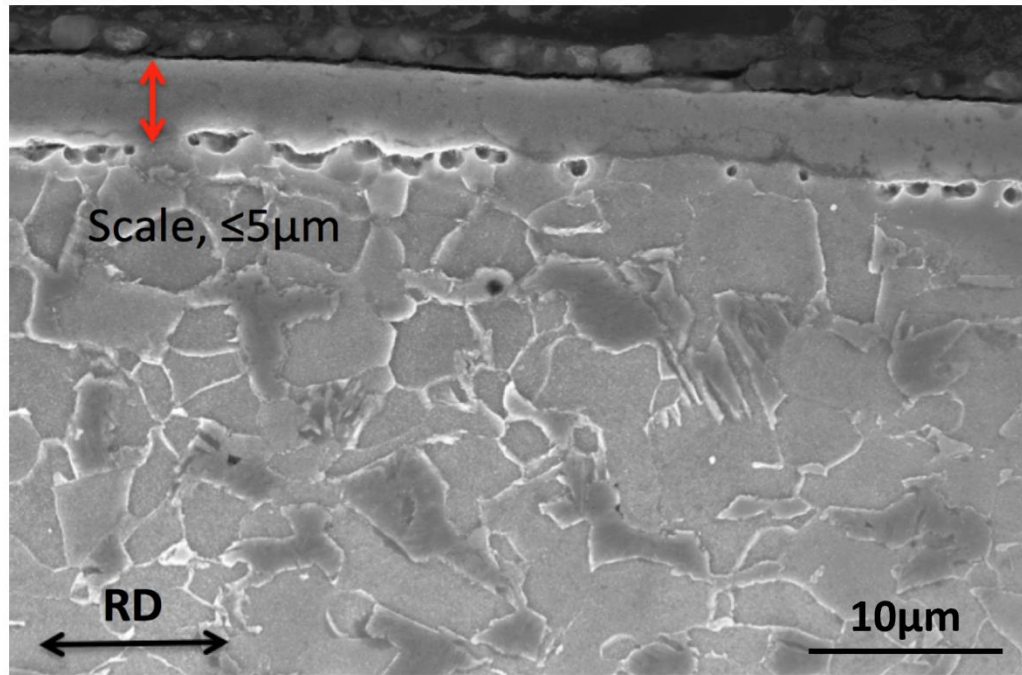
Fig. 61. SEM inlens image of dual phase steel A. The scale is located at the top of the image.
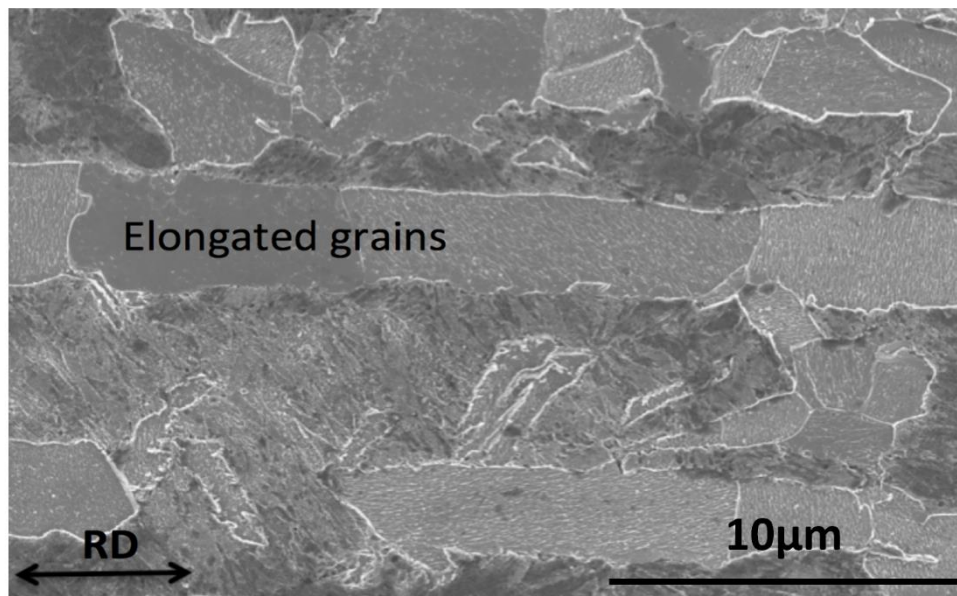
Fig. 62. SEM in-lens image of dual phase steel A. Elongated grains along the rolling direction are labelled.

The external oxide layer was imaged with higher magnification. Fig. 63 was taken using the in-lens detector, the structure illustrated is very similar to those SE and BSE images. The scale is generally well bonded to the steel substrate, except those positions with pores. The SEM image confirms the observation from OM images that the scale consists two distinctive layers (separated by the dashed line). The top layer (around 3-4 µm thick, above the dashed line) is relatively homogeneous in the grey scale and with few pores contained. The bottom layer (1-2µm thick, below the dashed line) forms at the scale-steel interface. This layer appears like a mixture of irregular darker grey areas in the lighter grey matrix. The variation in element concentration across the scale will be presented and discussed in the next chapter to identify the oxides that comprising the scale.
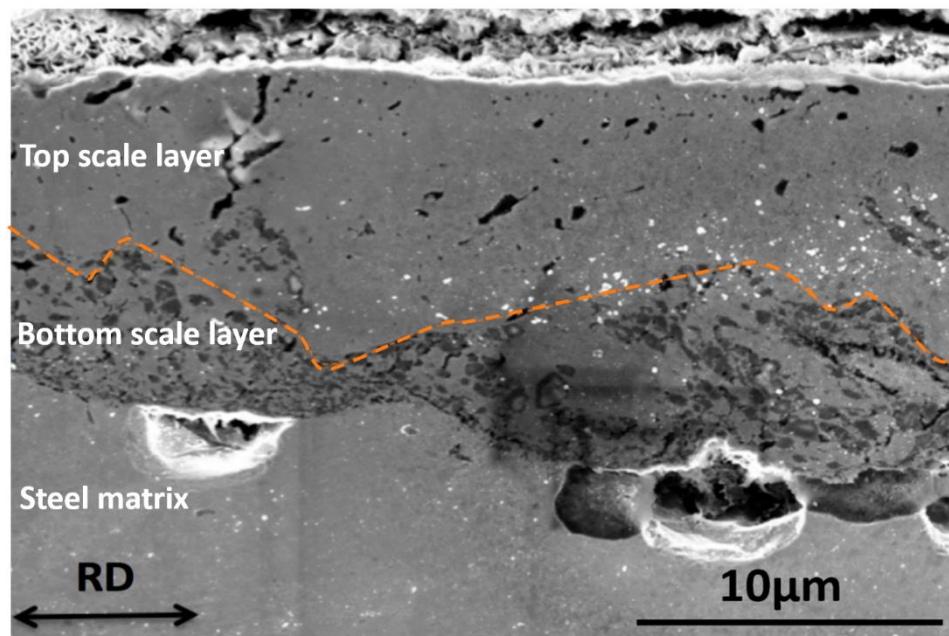
Fig. 63. SEM in-lens image of the scale area of the dual phase steel A at the head-coil. Two distinctive scale layers are separated by the dashed line.

The images mentioned above were all taken from the head-coil directly after coil cooling (between location 1 and 2, refer to Table 2). No internal oxidation was found mainly due to the high cooling rate. Mounted samples that were taken from the mid-coil and mid-width (location 4, refer to Table 2) were sent from the industry, the "very dark", "grey" and "clean grey" scales (refer to Fig. 55) were imaged via the BSE detector.

Fig. 64 and Fig. 65 are BSE images that taken from mid-length and mid-width of the coil at a very dark scale position (position 1). By comparing to the scale at the head-coil (as shown in Fig. 63), an extra

layer of around 8-10µm appears at the top (highlighted). This layer appears to be a loose compaction of oxide particles.
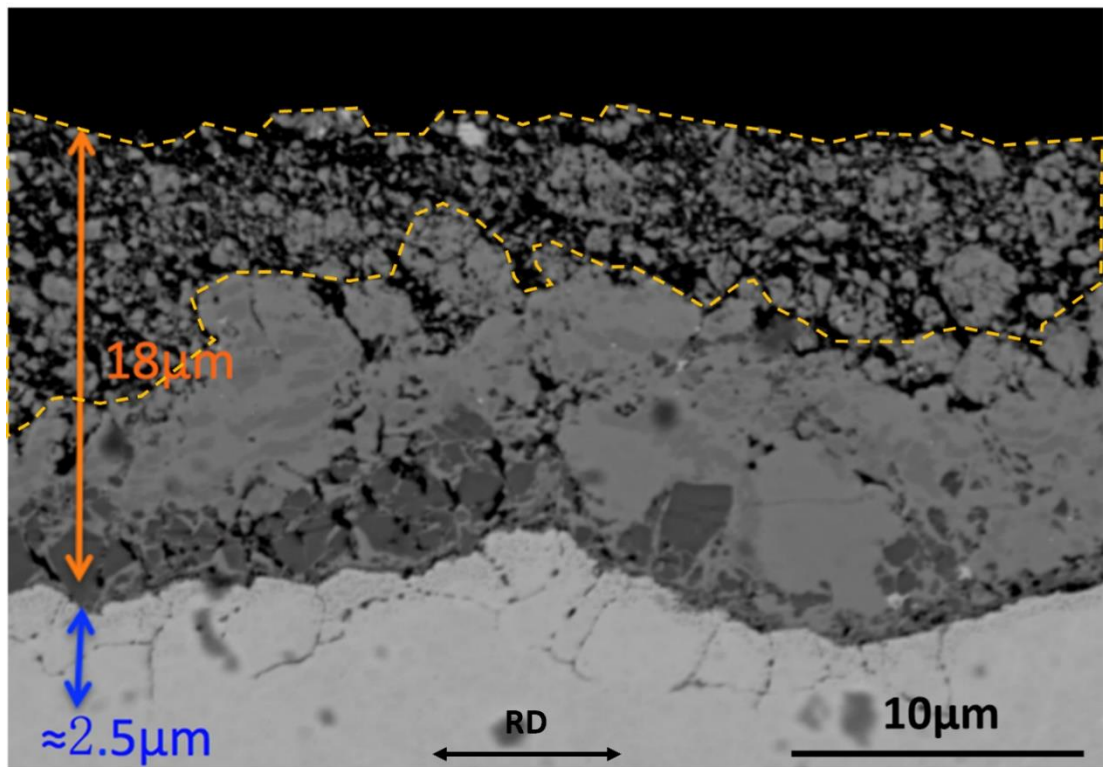
Fig. 64. BSE image of dual phase steel A, at the near-surface region. The sample was taken from the mid-length, mid-width of the coil and at the 'very dark scale position'. The extra scale layer (compared with Fig. 63) formed at the top surface is highlighted.

An internal oxidation layer could be found in the steel substrate and penetrated through grain boundaries to around 2.5µm in depth. Fine precipitates are also found within 1µm from the steel surface (dashed area in Fig. 65). However, the composition of these precipitates will be hard to verify due to their size.
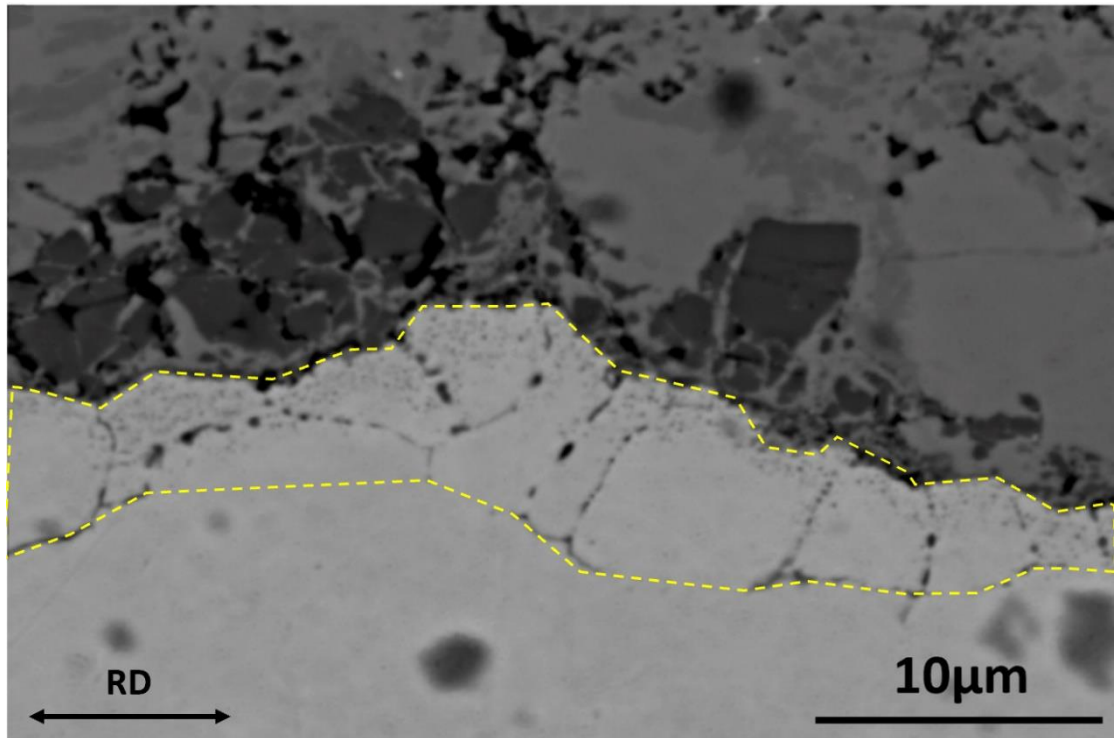
Fig. 65. BSE image of dual phase steel A, at the near-surface region. The sample was taken from the mid-length and mid-width of the coil and at the 'very dark scale' position.

Regarding the grey scale region (position 2), the scale and subscale thickness is measured to be 10 and <3µm, respectively. Fig. 66 illustrated that the scale structure is similar to the head-coil sample (refer to Fig. 63), but with higher thickness. No loose layer is found at the scale surface. The depth of internal oxidation looks slightly less than in the very dark scale position possibly because more grain boundaries are oriented in horizontal direction when compared to Fig. 64.
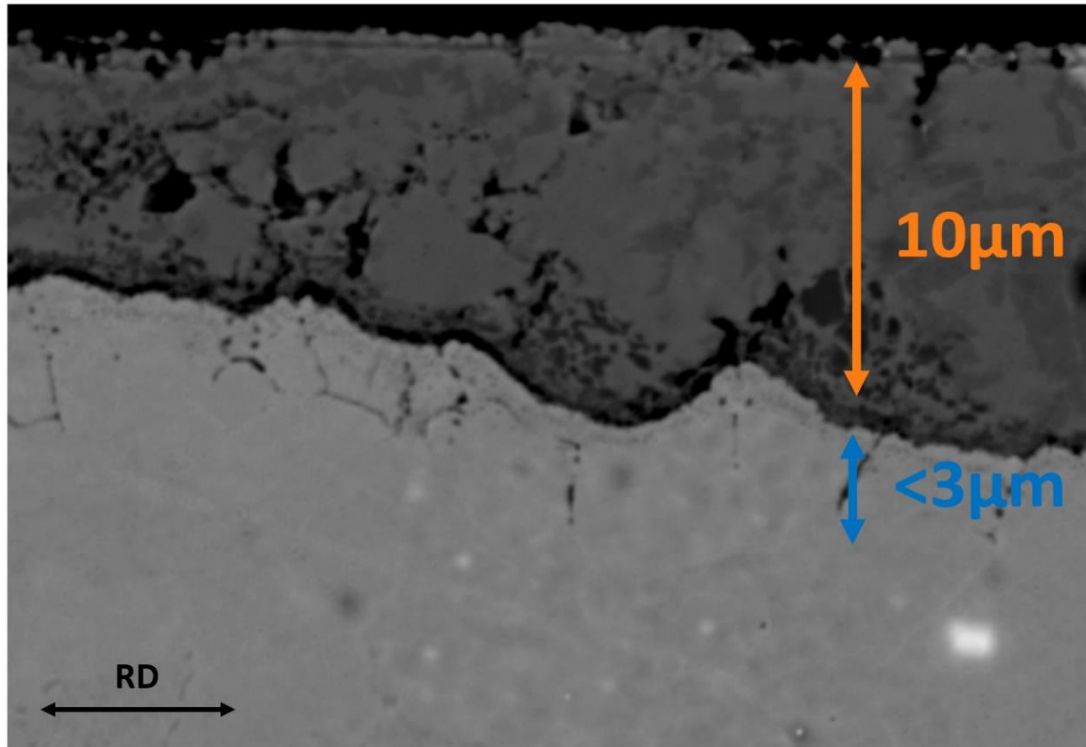
Fig. 66. BSE image of dual phase steel A, at the near-surface region. The sample was taken from the mid-length and mid-width of the coil and at the 'grey scale' position.

Fig. 67 and Fig. 68 are BSE image of scale and subscale at a 'clean grey scale' position (position 3). The 8μm scale is the thinnest of all three positions, but the 8μm internal oxidation depth is thicker than the other two. The scale/subscale structure is in general agreement with the features reported by Brocking et al. [81], who did research on the same steel and same position. The results (refer to Fig. 51) shows scale contains iron (mainly at the surface) and iron oxides, with the black patterns being either cracks (darker in color) or small fayalite particles. The scale-steel interface consists of iron oxides intermixed with fayalite. The oxides at grain boundaries were reported to be rich in Si and Mn. The only different feature is the high Si containing nuclei found at the tip of the grain boundaries, which is not found in the current research, as detailed later.

By comparing Fig. 64, Fig. 66 and Fig. 67, the internal oxidation depth appears to be inversely related to the scale thickness. The scales formed at these three positions should consist of different compositions, and is reported later in this thesis (Chapter 4). The presence of external oxides may act as a potential source of oxygen. If these oxides begin to decompose, the oxygen diffusion coefficient through oxides may vary [81]. Also, cracks are more likely to initiate within the thicker scale and lead

to poor bonding with the steel substrate. Therefore, less oxygen diffusion paths between the scale and steel are available for subscale development.

It is difficult to explain the formation of bright iron nodules at the surface of the clean grey scale, although similar features were found previously (refer to Fig. 51). More analysis and discussions will be given in the following chapter (p. 106).
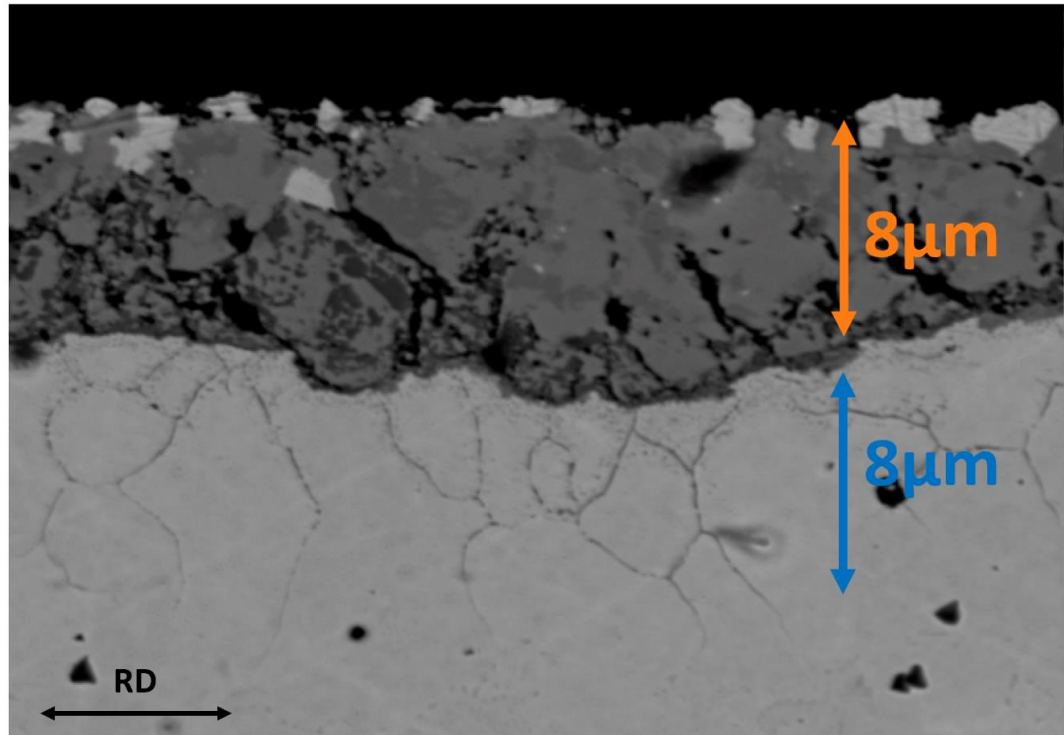
Fig. 67. BSE image of dual phase steel A, at the near-surface region. The sample was taken from the mid-length and mid-width of the coil and at the 'clean grey' scale position.
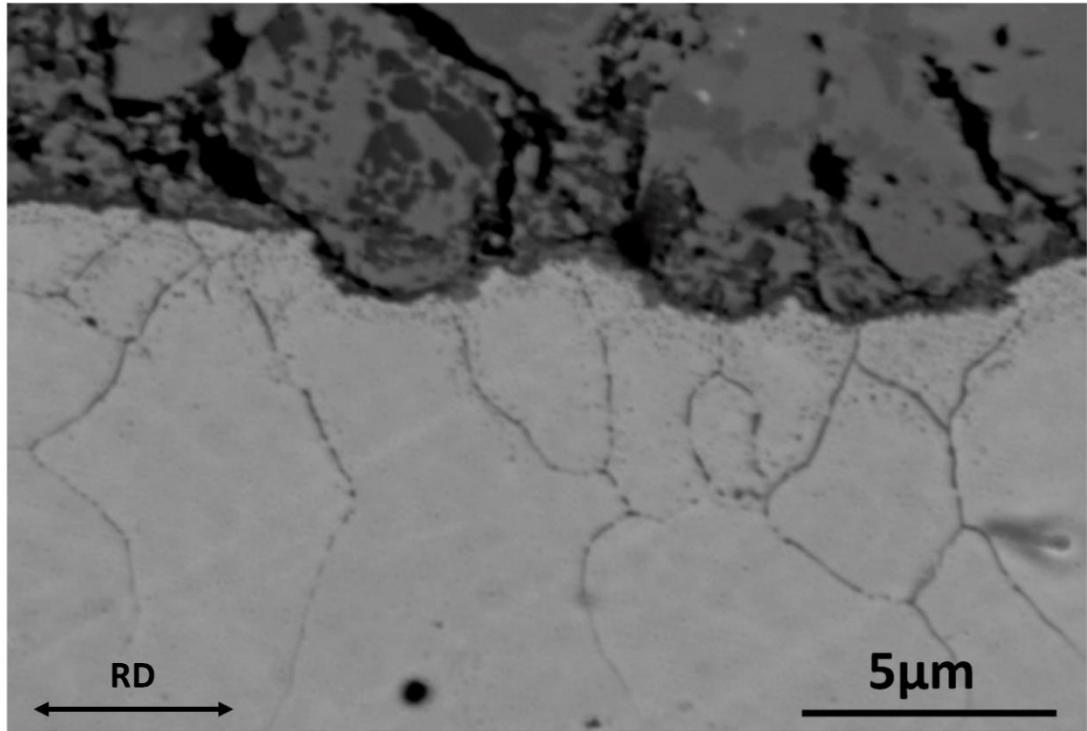
Fig. 68. BSE image of dual phase steel A, at the near-surface region. The sample was taken from mid-coil, mid-width and at the 'clean grey' scale position.

3.3.3. The relationship between surface features and internal oxidation depth

When measuring the internal oxidation depth of as-received samples, it was found that the value varies across the surface. It was confirmed that the surface features like external scale structure affect the growth of oxides internally. The bonding between scale and substrate also influences the internal oxidation significantly. These uncertainties make the depth of the internal oxidation measurements more challenging.

The previous measurement was mainly done on selected areas by using SEM images. It was assumed that the higher resolution and magnification under SEM provides more precise readings. However, the problems become more apparent as the number of samples analysed increase, especially when determining the average IOZ depth of a large sample. As an example, two as received batches of samples are measured, they are taking from the same coil at the same position (between location 3 and 4, refer to Table 2). For each sample, five random positions were chosen by SEM and five measurements were applied at each position. This means the average IOZ depth of each sample at a

coil location is calculated from 25 SEM measurements. In principle, the resulting IOZ depth should be identical or very close; however, the actual values measured are not comparable between the two sets of samples, as shown in Fig. 69.
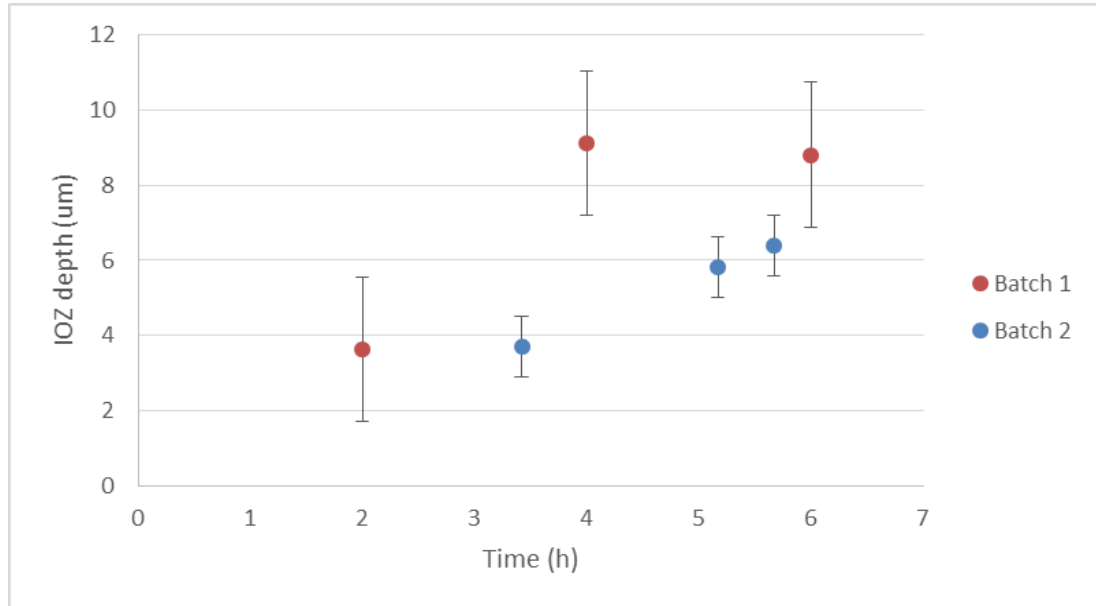
Fig. 69. IOZ depth measurement of two batches of as-received samples. All samples were originally taken from the sample coil and position.

As the results, a new standard of IOZ depth measurement must be made to minimise the uncertainties caused by random surface features.

3.3.3.1. IOZ depth measurement standard

An illustration of the new methodology (has not been used previously) is shown in Fig. 70. The optical microscope is chosen for "macro" view of the steel surface regions. Two samples (cross-sections view) of a given coil location (between location 3 and 4, refer to Table 2) and surface appearance are mounted face-to-face (the red dashed line highlights the interface) to save preparation time and aid in preserving the oxide from delamination. When the dark-field function is activated on the OM, the oxides and steel matrix turn black, whereas defects (pores, gaps and opened grain boundaries) turn to white/gold. The OM dark field effectively identifies the surface and target locations for measurement (a). When targeting is completed, the microscope is switched back to the bright-field mode with high brightness (b). The aim is to illuminate the scale structures and check the bonding between scale and

steel. Subsequently, the brightness is lowered down for IOZ depth measurement (c). Similar to the previous method, five positions are chosen (not randomly this time) on each sample and followed by five measurements at each position (d).
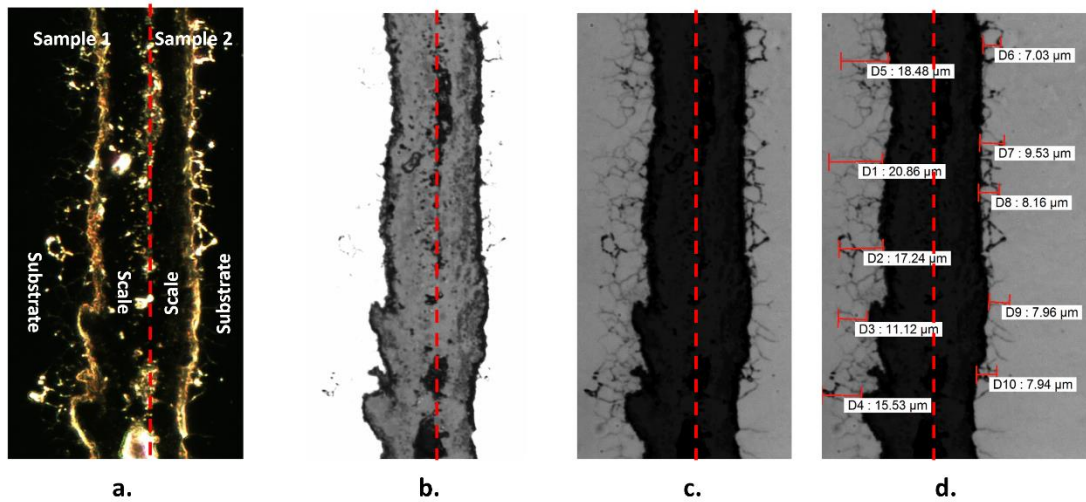
Fig. 70. IOZ depth measurement standard. (a), targeting; (b), scale inspection; (c), subscale inspection; (d), measuring.

By comparing samples 1 and 2 shown in Fig. 70, thinner IOZ is found when more dark clusters (potentially fayalite phase) are present at the scale-steel interface (sample 2, refer to image d). It is believed that oxygen becomes more laborious to penetrate the steel if a continuous layer with the dark clusters exists locally.

However, this relationship gets inverted at some other positions within the same coil, and an example is shown in Fig. 71. A depth of 8.2μm IOZ is found under a thick layer (sample 4), whereas 5.6μm IOZ presents when the layer is discontinuous (sample 3). While checking the bonding between the scale and steel substrate, a noticeable horizontal crack is found at the interface of sample 3; bonding remains good on sample 4. By comparing sample 1 to 4, it is clear that although the local IOZ depth is influenced by both of the scale adhesion and the scale structure, the contact between scale and steel matrix appears to have a greater influence.
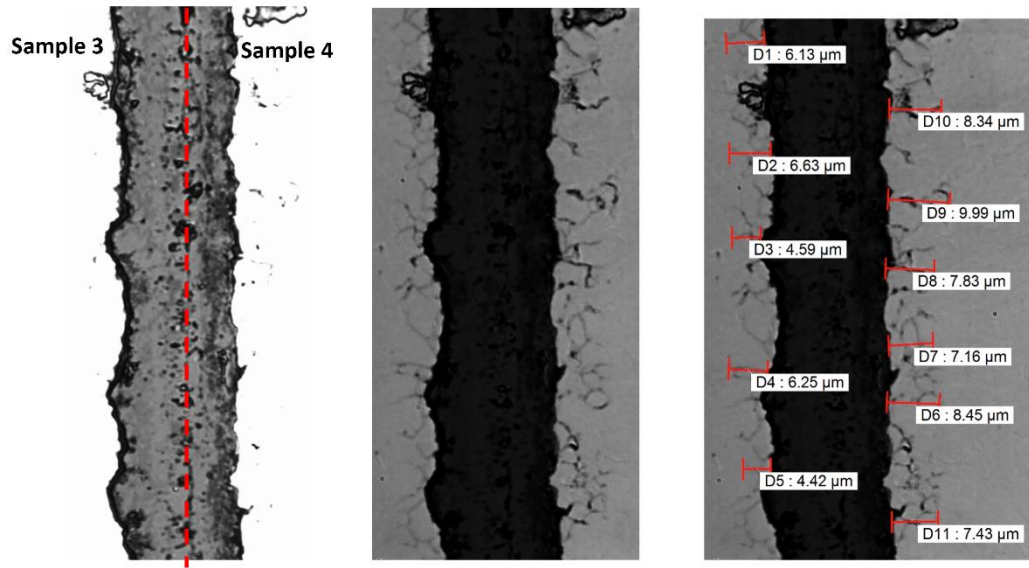
Fig. 71. OM bright-field images of sample 3 and 4, where sample 3 has a discontinuous fayalite layer and poor scale adhesion, sample 4 has a continuous fayalite layer and good scale adhesion.

Another example is shown in Fig. 72, where good and poor scale adhesion appear in the same frame (separated by the red dash line). In sample 5, an IOZ depth of 9.9 µm is found when the scale is in firm contact with the steel substrate, whereas the value reduces to 6.6 µm when the contact is lost. The scale structure is constant throughout the frame.

For the hot rolled and coil cooled DP1000 samples studied in this project, the scale normally bonded firmly to the steel matrix from a macroscopical point of view. Also, vast majority of the scale contains a continuous 'darker' interfacial layer. Therefore, the average IOZ depth value of the follow on samples should be measured on more common positions (with good scale-steel bonding and continuous 'darker' interfacial layer) in the in order to minimise uncertainties.
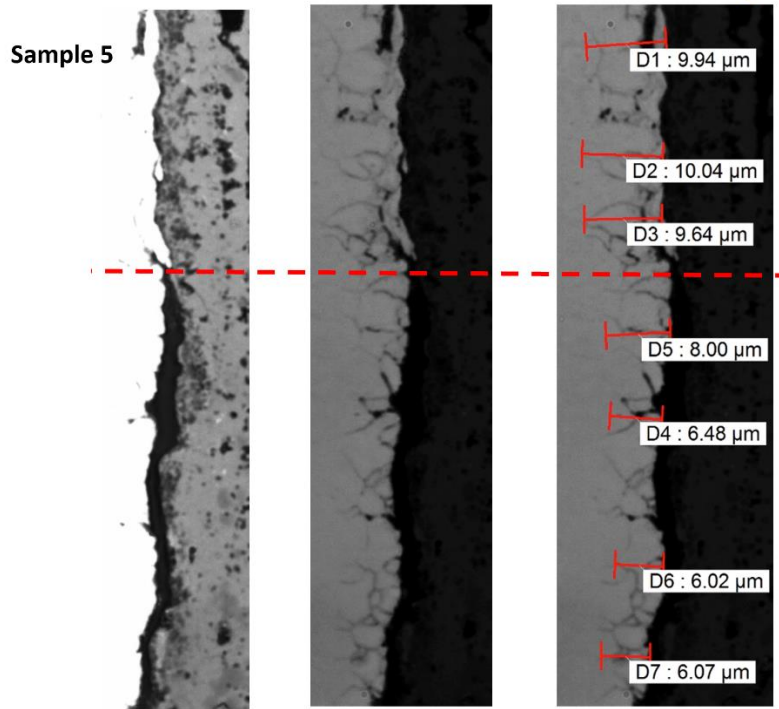
Fig. 72. OM bright-field images of sample 5, where good and poor scale-steel adhesion appears in the same frame.

3.3.4. Decarburisation of the hot rolled and annealed coil samples

The extent of decarburisation in the hot rolled and in the annealed coils was measured on mounted cross-sections using the optical microscope and the method described in the previous section. Four samples are taken from the hot rolled and cooled coil at constant length (approximately 700m away from the tail). The features found at this coil length should represent the general situation within the coil, apart from the head and tail (from private industrial communication). An illustration of the sampling positions is shown in Fig. 73. Sample A and B are taken from the edge and near edge (between location 1 and 3, refer to Table 2), respectively. Sample C and D are both from the near mid-width positions (between location 2 and 4, refer to Table 2). OM images show that a pearlite deficient layer at the near surface region of sample B, C and D, whereas the near surface microstructure in sample A is identical to the bulk. The decarburisation depth was measured by the thickness of the pearlite deficient layer (pearlite has higher carbon content than ferrite). Therefore, no decarburisation occurs at the coil edge due to the relatively faster cooling rate from the coiling starting temperature

(approximately 650°C). For the other cases, a 5μm decarburisation layer was present at B and this value increases to around 25μm at the mid-width (C and D).
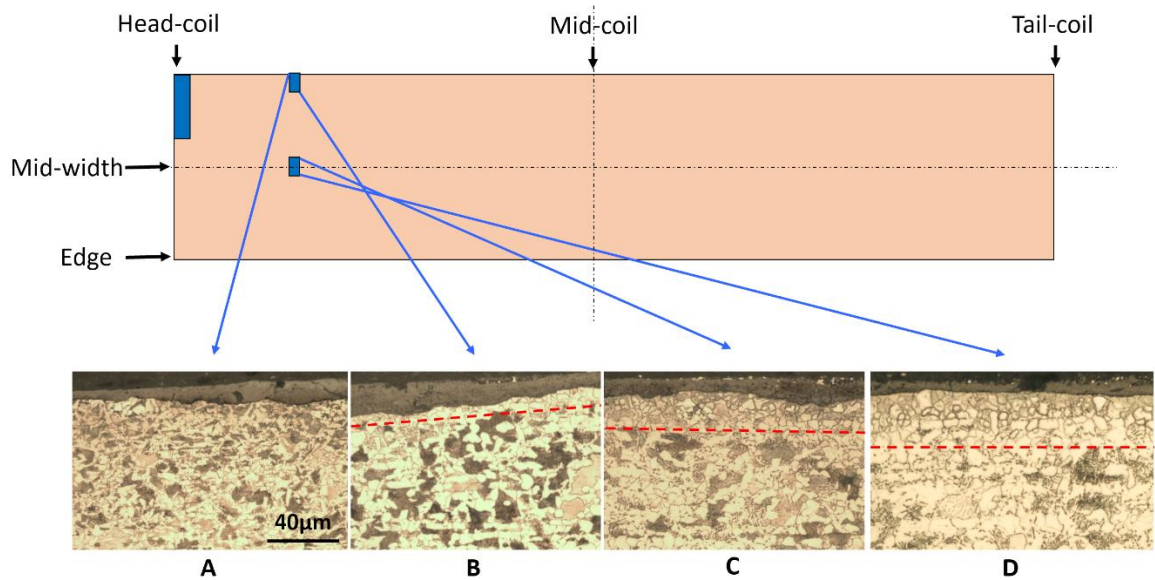
Fig. 73. Decarburisation depth measurement on the hot rolled and coil cooled samples at different width positions. All four samples are taken from constant coil length (approximately 700m away from the tail). A, B, C and D are all cross-section image and with horizontal rolling direction.

The decarburisation depth within the annealed coil is significantly greater. The samples are taken from the mid annealed coil (between location 11 and 12, refer to Table 2). After etching in the nitric acid solution, a brighter layer appears at the near surface region of the annealed samples, an example is shown in Fig. 74. The bright layer is approximately 65μm thick, and this roughly represents the decarburisation depth. Hardness indentations were taken on both of the bright layer region and the steel bulk. The results found that the bulk is 20HV harder than the bright layer (20 indents taken from each layer). It proves that the layer appears brighter due to the deficiency of harder phase (martensite) resulting from decarburization and is not an edge effect artefact from the sample polishing.
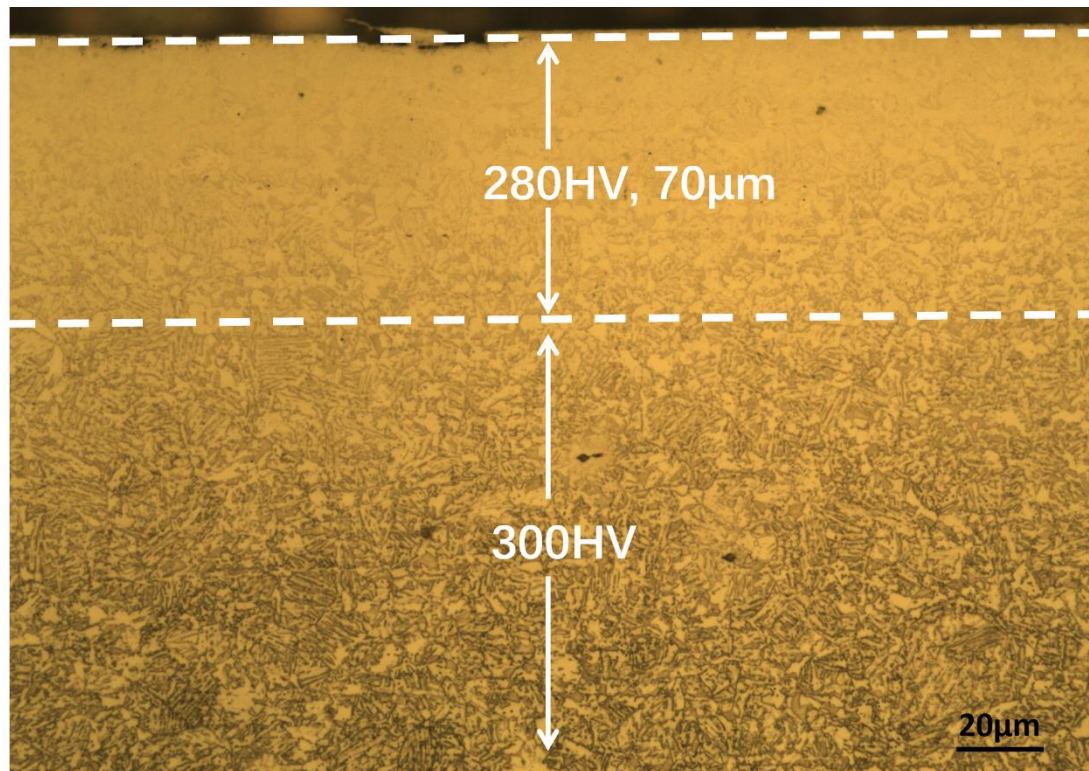
Fig. 74. Decarburisation depth measurement on the annealed coil samples, combined with hardness measurements.

3.4. Summary

Surface and subsurface features of the as-received coil cooled samples are inspected. In general, the steel grains toward the sheet surfaces tend to recrystallise more than the matrix due to surface decarburisation and loss of the alloying elements within those grains. The extent of decarburisation is studied on both of the hot rolled and galvanised coil samples. Thicker decarburisation layer is found at the inner (both in length and width) coil locations, and the local hardness value drop due to the loss of alloying elements.

The relationship between the local scale colours and the external/internal oxide structures around the areas is understood. Under the optical microscope, the scale consists of 2 parts, a brighter layer formed at the surface and a darker layer at the scale-steel interface. SEM further shows the bottom darker layer appears like a mixture of irregular darker grey particles in the lighter grey matrix.

No internal oxidation was found at the coil head and edge (location 1, 2 and 3, refer to Table 2), mainly due to the higher coil cooling rate. At the inner coil (between location 2 & 4 as well as 3 & 4, refer to

Table 2), three typical scale structure were found via the BSE detector and can be differentiated by their grey-scale when looking at the sheet surface. Moreover, deeper IOZ can be found at the inner coil, the depth depends largely on the external oxide structure. The extent of internal oxidation appears to be inversely related to the scale thickness.

A new scale and subscale inspection method rely on the OM bright and dark field complementary imaging is established for more accurate IOZ depth measurements. This method is proved to be more effective and will be utilized for all the IOZ depth measurements in the following chapters.

Chapter 4: Characterisation of scale and sub-scale development in ultra high strength steels during processing

The work presented here focuses on the simulation of surface and subsurface reactions that lead to the formation of the internal oxides. Further, it aims to establish a link between the near-surface conditions and the formability of the final product. The internal oxidation depth largely depends on the temperature, atmosphere, top surface composition and alloying additions. The hot rolled, coil cooled, pickled, cold rolled and annealed sample surfaces are characterized to create a better understanding of how internal oxides are developed during the whole strip steel production process. The surface and subsurface morphologies at varies coil (hot rolled and annealed) positions are studied. Microstructural characterisation, including OM, SEM EDS, EBSD, XRD and STEM, were used to determine the nature of the external and internal oxides that formed throughout the steel processing.

4.1. Experimental

Hot rolled and galvanised sheet samples were provided by Tata Steel with 0.2wt% C, 2.1wt% Mn and 1wt% Si additions (from the same steel A coil studied in the Chapter 3). The hot rolled samples are 3mm thick and the galvanised samples are 1.5mm thick.

Samples were taken from the head, mid, tail as well as edge and mid-width of the coil. The cross-sections of sheet samples were carefully cut and polished for SEM imaging. Vibrational polishing was applied to further improve the indexing rate of EBSD patterns.

Images of surface and subsurface features were obtained by the Zeiss Sigma FEG-SEM with in-lens, secondary electron (SE) and backscattered electron (BSE) detectors. The settings are identical to the previous studies (p76). Elemental information at selective areas/points can be identified via the energy dispersive spectroscopy (EDS) detector. Fe, Si, Mn and O are selected for the EDS analyses. 20kV beam voltage, 8.5mm working distance and 240mm aperture were used. The EDS mapping aims to find out the concentration variation of the selected elements within an area, for example, the scale and subscale regions. The EDS point analysis quantifies the compositions within the oxides by showing the

weight/atomic percentage at the selected point. It helps to identify different phases within the external oxide layer.

Electron backscatter diffraction (EBSD) was applied to determine the grain orientation and phase distribution. The ideal working distance is 18.5mm, 120 hough resolution and 4*4 binning help the identification of oxides, such as wustite and magnetite. The sample stage was tilted to 70° for EBSD analysis. Also, the largest aperture size and approximately 85 nA probe current were chosen for effective EBSD data collection.

Ion miller will be used if the index rate of EBSD results is low (due to inappropriate polishing), especially at the scales. 8, 3 and 0.5keV are applied for 1 hour each and with 5, 4 and 3 degrees of beam angle, respectively.

TEM characterisation was used to investigate surface oxides and internal inclusions, which are generally less than 200nm in size. TEM samples were produced by FIB (focus ion beam) lift-out, and the final sample thickness is less than 200nm. Elemental information of the nano-inclusions were carried out by the build-in EDS detector.

Cold rolling was simulated in a pilot mill using manual lubrication. A thickness reduction of 50% was achieved by passing the sample sheets through the well-lubricated rolls several times while gradually reducing the gap between the rollers. The mill settings are recorded in Table 3. Samples were taken after each rolling stage to track the raise in hardness value as well as the surface deformation. Rolling was applied on hot rolled sheets with and without external oxides (close to location 4 and 8, respectively, refer to Table 2). Three micrometer measurements were taken on the sheet after each rolling step. The influence of scale and surface roughness on subsurface deformation will then be understood. The scale was removed by using 10% HCl at 80°C for approximately 30 seconds. A corrosion inhibitor was added to prevent acid corrosion of the bulk steel, which would preferentially occur at the grain boundaries near the surface.

Table 3. Mills setting and the actual sheet thickness reduction during cold rolling simulation.

Gap between mills (mm)	3	2.5	2	1.66	1.2	0.9	0.67	0.38	0.09
Sheet thickness (mm)	3	2.94	2.85	2.71	2.49	2.18	1.9	1.74	1.5

4.2. Results and Discussion

4.2.1. Hot rolling and coil cooling

Fig. 75. (a) is an EBSD band contrast map of the hot rolled and cooled coil (cross-section view). The sample was taken from the steel A, location 4 (refer to Table 2). A layered texture appears throughout the thickness. Layers of larger equiaxed grains alternate with layers of aggregated small grains. The average size within the larger grain size layers is 5µm and ≤1µm for the grains within the small grain layers. The combination of EBSD phase identification and hardness test results established the nature of the larger grains as ferrite and small grains as a mixture of pearlite and ferrite. The micro-segregation effect is suggested to be the cause of layered structure formation. The higher Mn content (also depend on the Mn-C ratio [89]) in UHSS promotes micro-segregation during continuous casting and this texture remained after hot rolling [3]. The grain orientations in the normal direction are illustrated by the inverse pole figure colours (Fig. 75. (b)). The grain boundaries are defined by >10° misorientation. The pole figures prove that the grains are randomly orientated after the hot rolling and coil cooling process.
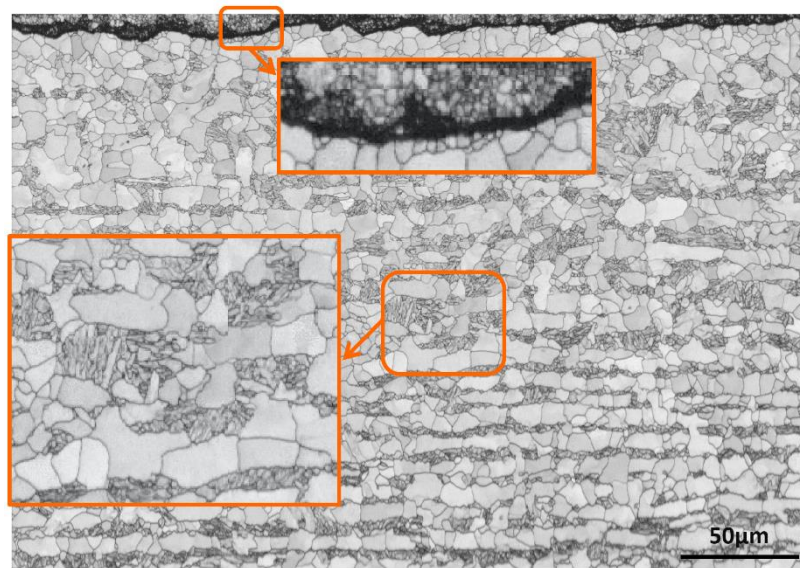
(a)
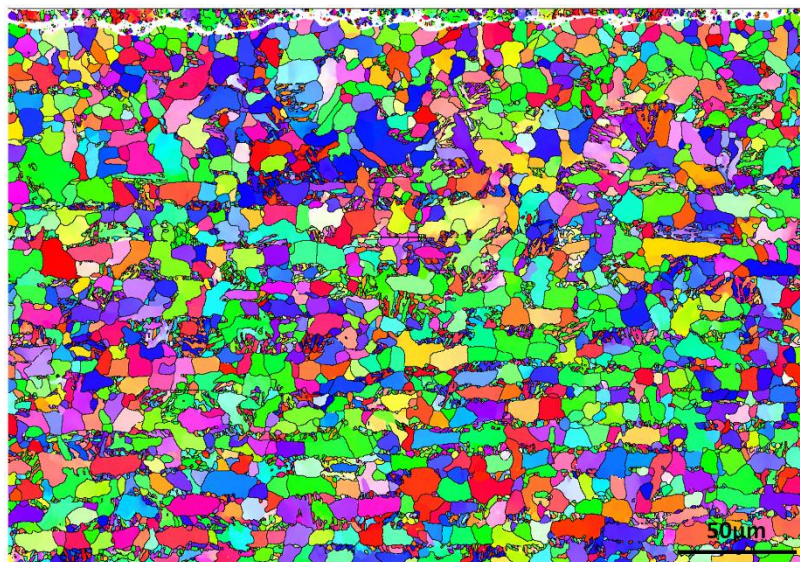
(b)
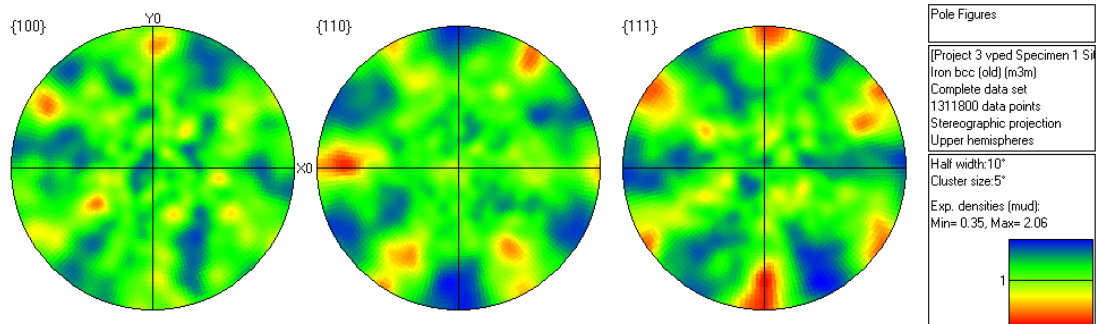
(c)

Fig. 75. EBSD results of the hot-rolled and coil cooled steel sheet. The cross-section was taken parallel to the rolling direction, and the surface is towards the top. (a). Band contrast map with pearlite and scale areas magnified; (b). Inverse pole figure coloring (z-direction); (c). pole figures.

For about 20μm from the edge into the material, ferrite dominates the subsurface region. The lack of pearlite within this region may be caused by decarburisation. Involvement of the other alloying elements (Si and Mn) in the scale formation will also cause a subtle change to the chemical composition of this region and hence result in a different microstructure.

In addition, the band contrast map shows that the external oxides have much smaller grain size. More detailed studies on the scale area will be carried out in the next section (p99).

4.2.1.1. Head-coil

After coil cooling, the scale formed at the head-coil surface (location 2, refer to Table 2) is less than 5μm thick, this value increases to 16μm at the mid-coil (location 4, refer to Table 2). The following images (Fig. 76 and Fig. 77) show the representative structure of the external oxide layer.

The scale is composed of at least four different types of oxides. The difference in morphology can be seen in the EBSD band contrast image (Fig. 76). The scale surface is occupied by a thin layer of fine oxide with the maximum size of 1μm. This layer is not continuous and the thickness is approximately 12% of the whole scale. EBSD identified this layer to be hematite (Fe_2O_3). A thicker layer formed underneath, consisting of larger grains (1-6μm). A brighter texture can be seen within these grains under the back-scattered mode, an example is shown in Fig. 77. During heating/cooling, wustite decomposed into magnetite-ferrite eutectoid at 570°C. Fig. 77 shows the Fe_3O_4 grains identified by EBSD consist Fe_3O_4/Fe eutectoid texture, where the large grains are magnetite (Fe_3O_4) and the bright eutectoid structures are iron precipitated during the transformation[73].
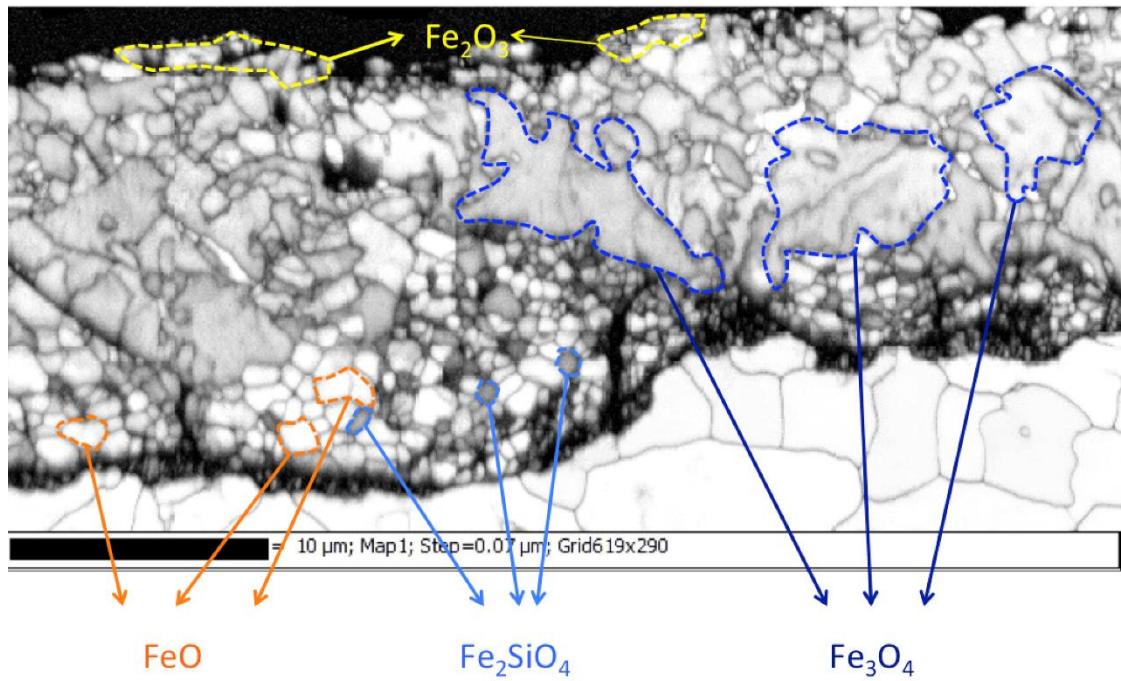
Fig. 76. EBSD band contrast image of the external oxide, sample taken from the hot rolled coil cooled steel sheet (location 2, refer to Table 2). Positions of typical oxides (Fe_2O_3, FeO, Fe_2SiO_4, Fe_3O_4) within the scale are labelled.
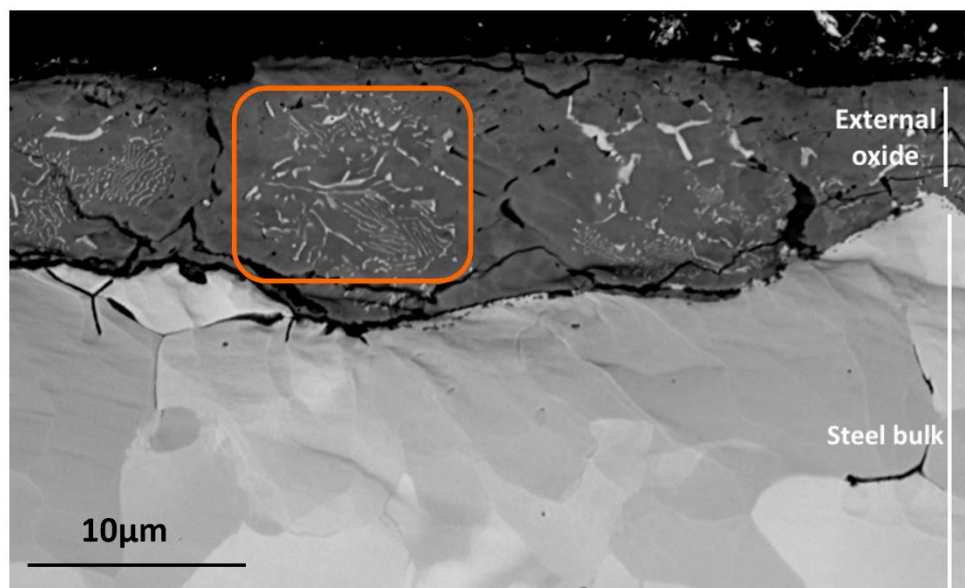
Fig. 77. Backscattered image illustrating the detail of the magnetite grains identified in Fig. 76 (circled), showing the Fe_3O_4/Fe eutectoid. The surface is towards the top.

An uneven interfacial layer was found between the Fe_3O_4/Fe eutectoid layer and the steel matrix, indicated by the dotted line in Fig. 78. The thickness of this layer varies from 1 to 6µm. The EBSD scan

in Fig. 76 shows that this interfacial layer is formed of two types of grains, which can be differentiated by the band contrast grey level. The brighter grains are 0.5-2μm in size and the darker grains appear smaller. Fig. 78 is the secondary electron (SE) image taken from the same position (the in-lens and BSE detector will also work). Dense sub-micron inclusions could be seen under SEM by using the in-lens detector. The positions of these inclusions match with the darker grains in Fig. 76 (identical to the interfacial layer mention in Fig. 63). EDS results are shown in Fig. 79, where the scale-steel interface is decorated by silicon and manganese enriched oxides, consistent with the EBSD results.
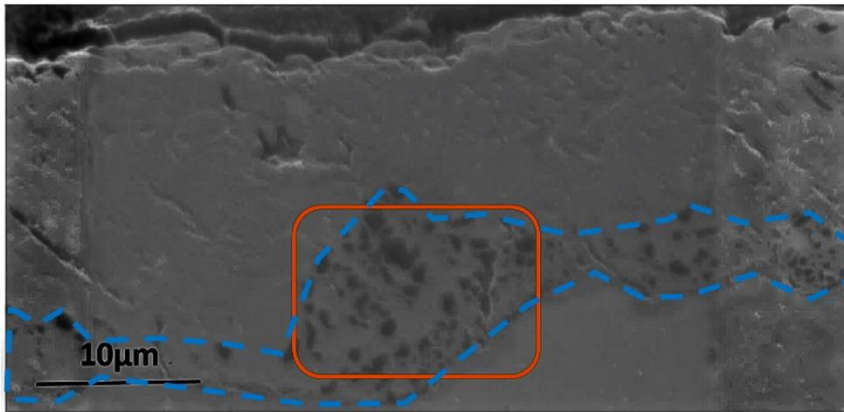
Fig. 78. Secondary electron image of the external oxide of hot rolled and coil cooled steel. Example of dark fayalite inclusions are circled at the scale-steel interface layer (highlighted with the blue dot line). Sample was taken from the head of coil. The surface is towards the top.
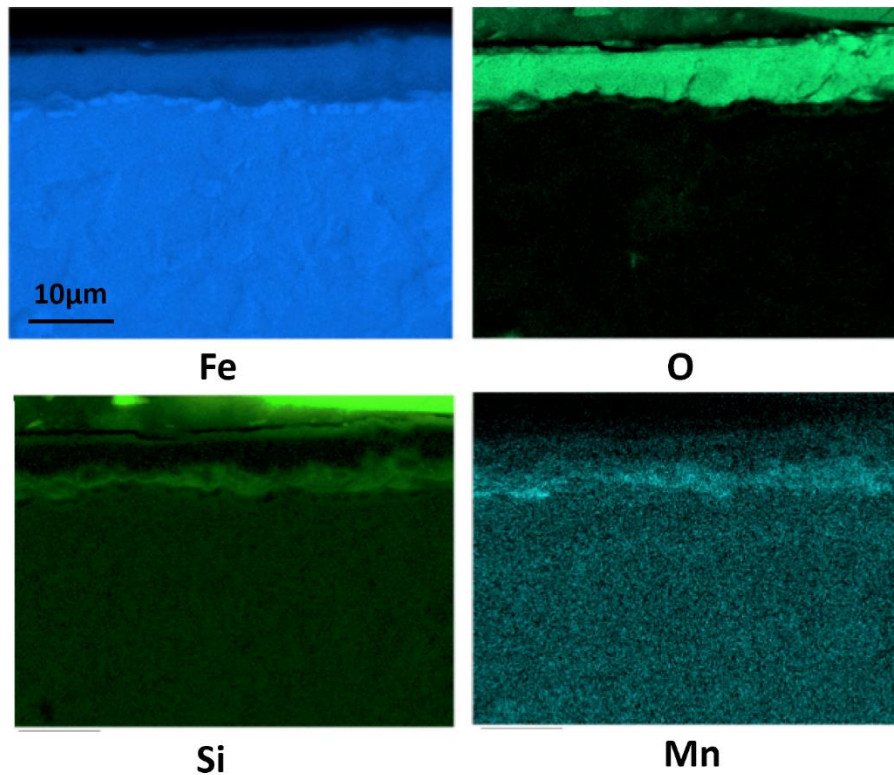
Fig. 79. EDS mapping results of the surface region of hot rolled and coil cooled steel on the head. O, Fe, Si and Mn are present within the scale. Sample was taken from the head of hot-rolled coil. All maps have the same scale bar.

It has been suggested that the silicon-enriched phase is actually fayalite (Fe_2SiO_4) [56, 57, 60]. Fayalite forms as a liquid phase when the temperature exceeds 1170°C during hot rolling. Liquid fayalite then acts as a binder between the inner layer of scale and the metal surface. More importantly, Song [57] explained that the fayalite/wustite eutectic phase could also form in the solid solution below the melting point of fayalite. The resulting structure has FeO/Fe_2SiO_4 ratio of 46:54, which is lower than the compound formed above the melting point (23:77) [57]. The EDS mapping result shows no Si signal at the magnetite grain boundaries, which means fayalite did not melt and penetrate into the adjacent phases. Hence the fayalite/wustite interfacial layer was formed below the melting point during hot rolling and coil cooling.

Regarding Mn at the interfacial layer, manganese oxide is thermodynamically more stable than iron oxide, and it can form at lower oxygen potentials. Both manganese and iron have bcc crystal structures with similar atomic radii; therefore, Mn atoms are able to substitute iron atoms during wustite formation, thus MnO can be found within the FeO structure.

XRD was performed on both pickled and non-pickled sheet surface, the results are shown in Fig. 80. It has been proved that pickling removed most of the external oxides. The results confirmed that after pickling, the entire scale has been removed. The peaks on the red curve are contributed to pure iron remained. In contrast, iron, Wustite and Magnetite were found with cubic structure before pickling. Fe_2O_3 (rhombohedral), iron silicon ($Fe_{0.75}Si_{0.25}$) and Mn_3O_4 are also found. By combining SEM images with XRD, EDS and EBSD results, the composition and position of a specific oxide within the scale are assured.

The sample used for XRD analysis contains both external and internal oxides. XRD results proved that the scale is formed by varies types of oxides. However, the x-ray diffraction technique is not sensitive enough in determining inclusions and grain boundary precipitates. Also, many compounds, such as iron silicon phases form similar peaks within the XRD database. Although $Fe_{0.75}Si_{0.25}$ and Mn_3O_4 are likely to be the interfacial compound between the iron oxides and steel matrix, evidence from XRD results alone is still insufficient. The previous study mentioned that the silicon-enriched phase is actually fayalite (Fe_2SiO_4) [56]. Fayalite will be in the liquid phase at above 1170°C during hot rolling. Liquid fayalite will act as a binder between the inner layer of scale and the metal surface. Also, liquid fayalite will penetrate into the grain boundaries and form the eutectic compound (FeO/ Fe_2SiO_4). In this case, the iron-silicon peaks may belong to fayalite.

Manganese is more active to form oxide than Fe and the Mn atoms are able to take place the iron atoms during wustite formation, thus MnO or Mn_3O_4 could form during steel oxidation. This oxidation behaviour starts from 500°C when 2%Mn is contained in the steel (data from an internal document). This explains why Mn signal and Mn_3O_4 peaks could always be found in the scale by EDS and XRD analysis.
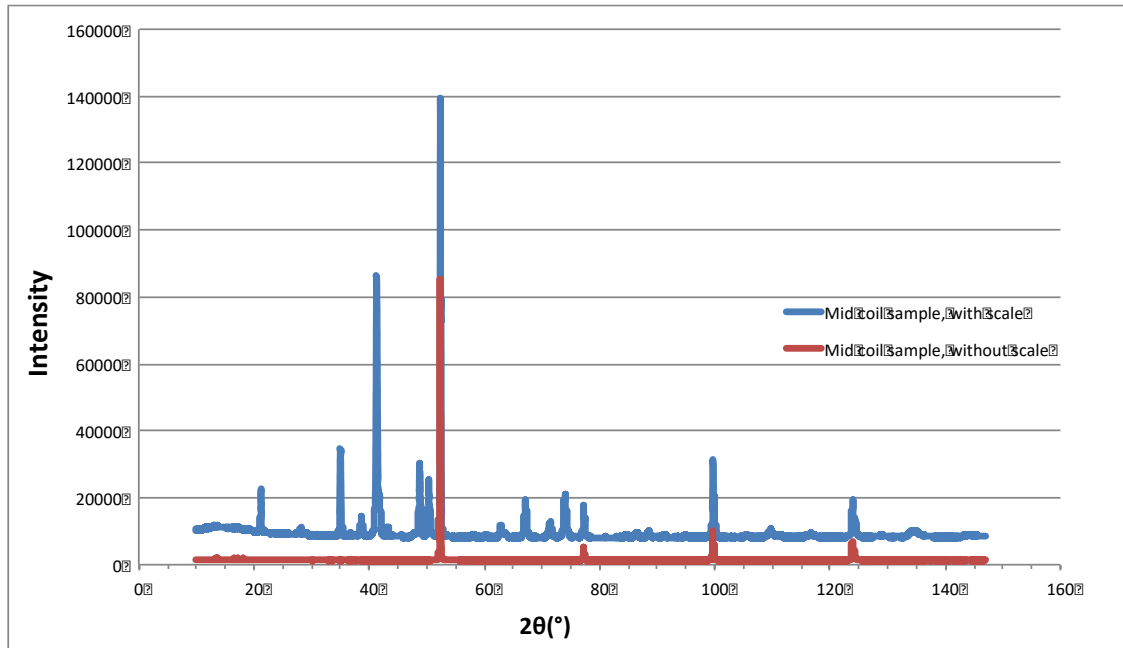
Fig. 80. XRD spectra of hot-rolled + coil-cooled steel with and without pickled surface (location 2, refer to Table 2).

Fig. 76 illustrated that the interfacial oxide layer is formed by a mixture of submicron dark grains and slightly bigger, brighter gains. The earlier results have suggested the darker phases to be fayalite or silicon-iron phases; the brighter grains are iron oxide, but the compositions are still not clear. EBSD is applied on the scale again to confirm the locations of hematite, magnetite and more importantly, wustite. Wustite and magnetite are in cubic and inverse spinel crystal structure, respectively. However, on the EBSD database, Fe_3O_4 and FeO are both assumed to be in the cubic structure, which means the system can hardly differentiate these two oxides. After refining the settings, including the binning and hough resolution values, the difference between Kikuchi patterns of these two oxides become noticeable. The EBSD results on iron oxides localization as well as the Kikuchi patterns of wustite and magnetite are shown in Fig. 81.
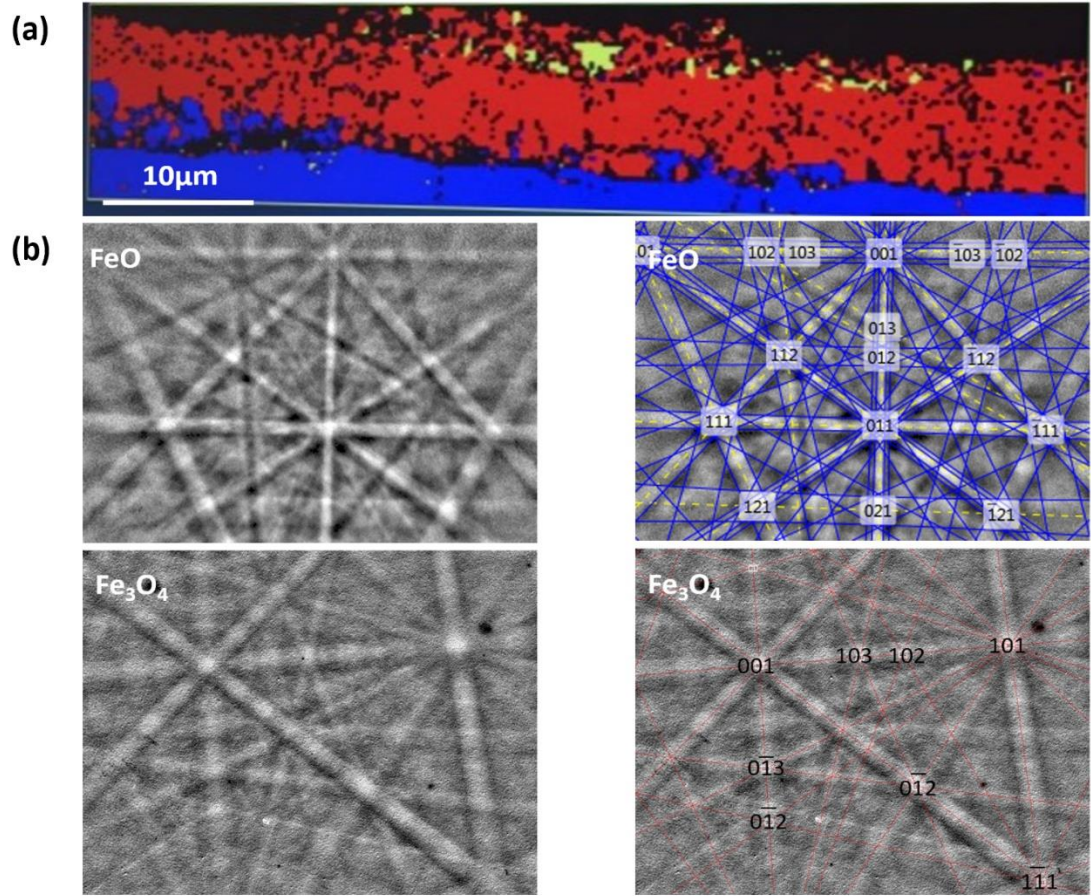
Fig. 81. (a). EBSD phase identification results on the scale region, where yellow, red and blue means the positions of hematite, magnetite and wustite/iron respectively. (b). Kikuchi pattern of wustite and magnetite are shown.

By overlapping the EBSD phase identification results with the band contrast map (Fig. 76), its clear that the brighter grains formed next to the fayalite grains belongs to wustite. The coloured map also verified the presence of hematite and magnetite, although the pure iron within the iron/magnetite eutectoid is not detectable due to its size.

An additional STEM cross-section view is shown in Fig. 82, where the shape and size of all the oxide phases match with the SEM-EBSD band contrast map (refer to Fig. 76). Therefore, the method mentioned above is proved to be an effective and efficient way for thin scale characterisation, even when the grains at the scale-steel interface are in sub-micron size. On the other hand, the smaller grain size found at the interface matches Bertrand [54] viewpoint, where the presence of H_2O at the steel surface (in this case, from the descaling water before coiling up) promotes the nucleation rate of the surface oxide. The higher nucleation rate will lead to smaller grain size of the oxides.
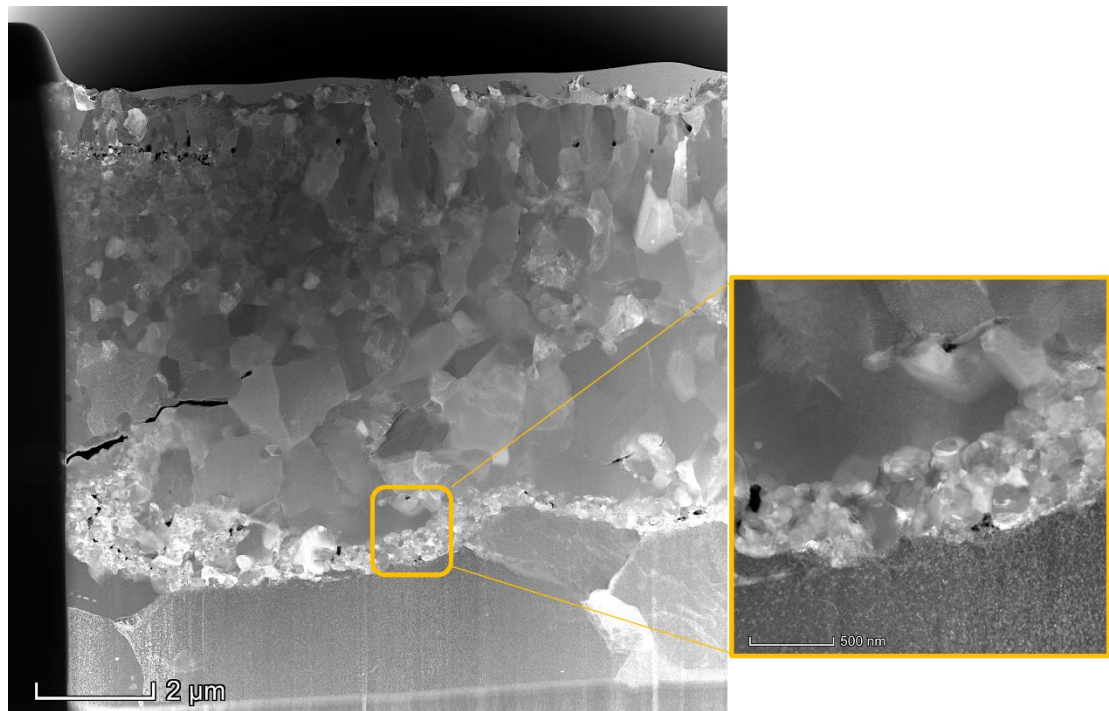
Fig. 82. STEM cross-section view of the scale area. The fayalite region is shown in higher magnification. Sample taken from the hot rolled coil cooled steel sheet.

4.2.1.2. Mid-coil

During the coil cooling, the head-coils cool faster compared to the mid-coil regions, hence no significant internal oxidation was found at the head (and tail). In contrast, observations from the mid-section of the coil revealed differences from the head-coil oxide morphology, representative micrographs from the mid-length of the coil are shown in Fig. 83 (sample taken from location 3 and 4, refer to Table 2).

(a)   **(b)**
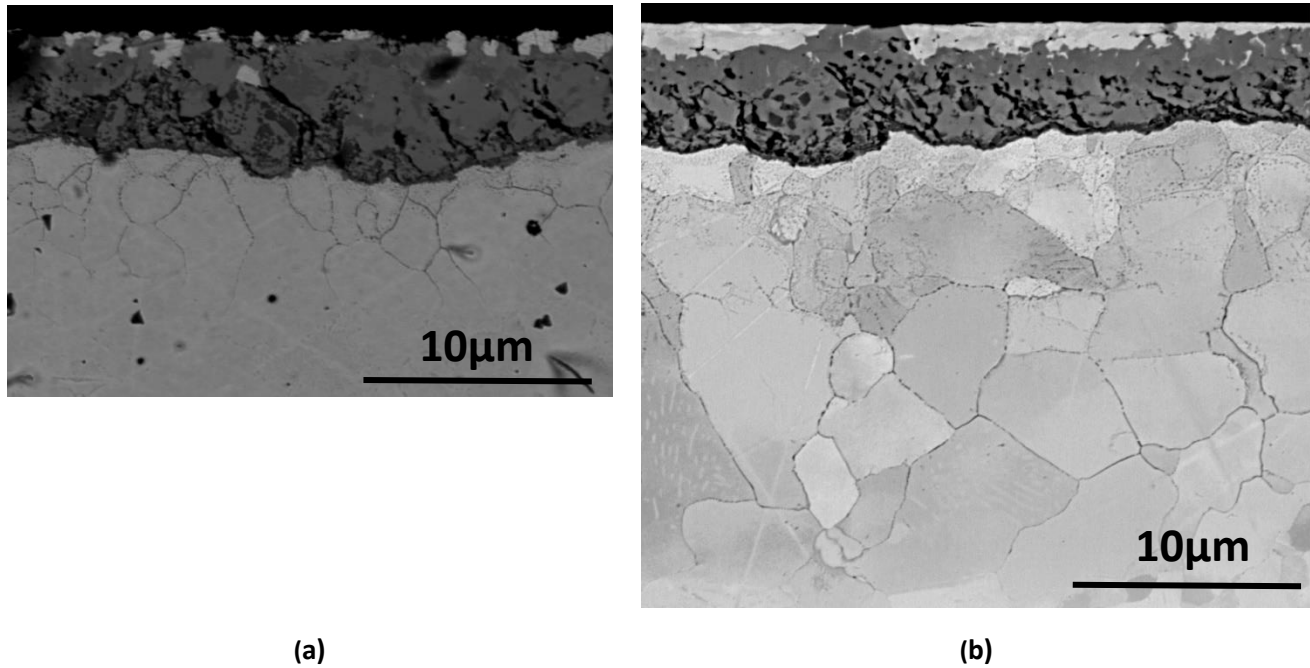
Fig. 83. Backscattered cross-section image of the scale and subscale regions at (a). edge (location 3, refer to Table 2); (b). mid-width (location 4, refer to Table 2) of the hot-rolled coil. Both samples are taken from the mid-length of the coil. The surface is towards the top and the rolling direction is horizontal.

As mentioned earlier (p. 80), iron nodules are found at the scale surface. By comparing samples cut from the mid-length (location 3 and 4, refer to Table 2), larger amounts of iron nodules are present at the mid-width (Fig. 83. (b).) than the edge (Fig. 83. (a).). At typical locations, an almost continuous pure iron layer (formed by connecting individual nodules) is found at the mid-width. It was suggested that, during coil cooling, the inner coils are tightly wrapped together, limiting the access to oxygen. However, the internal oxidation layer found at the mid-coil means the local partial oxygen pressure must be sufficiently high to make oxygen diffusivity higher than alloying element diffusivity. It is proposed that the iron nodules form when the tertiary scale (especially the oxygen-enriched hematite) is reduced by the less noble alloying elements and then act as the source of oxygen for internal oxidation [90]. The cooing rate at mid-width (location 4, refer to Table 2) is lower than the head (location 1 and 2) and edge (location 3), thus more surface oxides are reduced back to iron.

However, the scale surface mainly consists of hematite (refer to Fig. 76), the reduction from hematite to iron cannot be achieved in one step (refer to equation 21-23, p. 69). It will be difficult for the surface hematite to reduce back to iron, but the other oxides (magnetite, wustite and silicon oxide) not.

SEM images are taken from the top surface view, as shown in Fig. 84. It seems the iron nodules does not belong to the scale as they are slightly bulging from the surface. Another assumption is made, where the iron nodules come from somewhere during the steel processing (possibly from the descaling water) and then been flattened during the coiling. However, by comparing the top scale views (Fig. 84, (a) and (b)), the density of iron nodules is 19.4% higher at the mid-width (location 4, refer to Table 2) than the edge (location 3). The reason based on this assumption is still unknown.

(a)   (b)
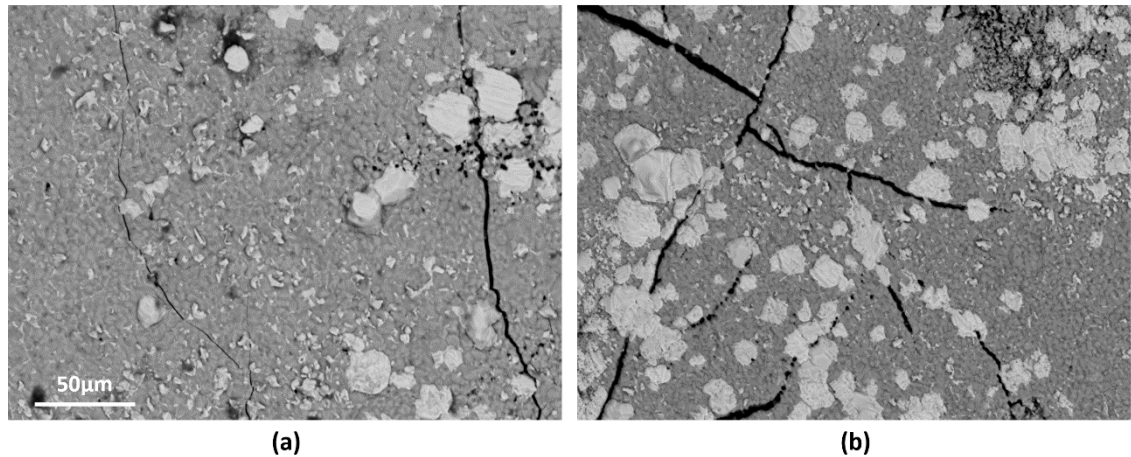
Fig. 84. Backscattered top-view image of the scale at (a). edge; (b). mid-width of the hot-rolled coil. Both samples are taken from the mid-length of the coil. Both images are taken under the same magnification.

Apart from the iron nodule layer, the magnetite and wustite/fayalite layer within the scale remains at their original position as in the head-coil external oxide (location 1 and 2, refer to Table 2).

4.2.1.2.1. Internal oxides

The major difference in oxide morphology between the head (location 1 and 2, refer to Table 2) and mid-coil sheet (location 3 and 4) is the internal oxides. In the mid-coil, the internal oxidation affected zone has a maximum depth of 18µm, whereas no significant internal oxidation was found at the head-coil. Two forms of internal oxidation are found in samples from the mid-coil region (refer to Fig. 83). One is intergranular while the other is transgranular. Intergranular oxides formed and accumulated at subsurface grain boundaries, whereas transgranular oxides formed as precipitates within the steel grains. Higher densities of transgranular precipitates are formed towards the surface. However, at

deeper regions (depth depending on the total IOZ depth), the density decreased significantly, and the precipitates tended to form close to the grain boundaries. Internal oxidation follows several elementary processes. Oxygen goes into the steel via either direct volume diffusion from the surface to the bulk or via grain boundary diffusion. When heating temperature and time remain constant, oxygen penetrates deeper via the grain boundaries than by surface diffusion. When grain boundaries are fully occupied by oxygen or oxide, partial leakage of oxygen occurs from boundaries into the grains, resulting in both intergranular and transgranular subsurface oxides in addition to the external scale [91, 92].

The variation of IOZ depth from the mid-coil edge (location 3, refer to Table 2) to the mid-width (location 4) is plotted in Fig. 85, focusing on the first 20% of the width and the inner 40-60%. It seems that the growth of the IOZ decelerates towards the mid-width. The maximum IOZ depth in mid-coil at the mid-width is approximately 18µm. The IOZ depth measured within 40% and 60% of the total width almost doubled the values reported previously (internal report). It has been shown that when heat treatment conditions and the Mn content are constant, the IOZ depth is much less in Si-free sheets. More severe grain boundary oxidation was found in a Fe-x%Mn-y%Si iron-based model alloy compared to binary Fe-x%Mn or Fe-y%Si alloys [66].
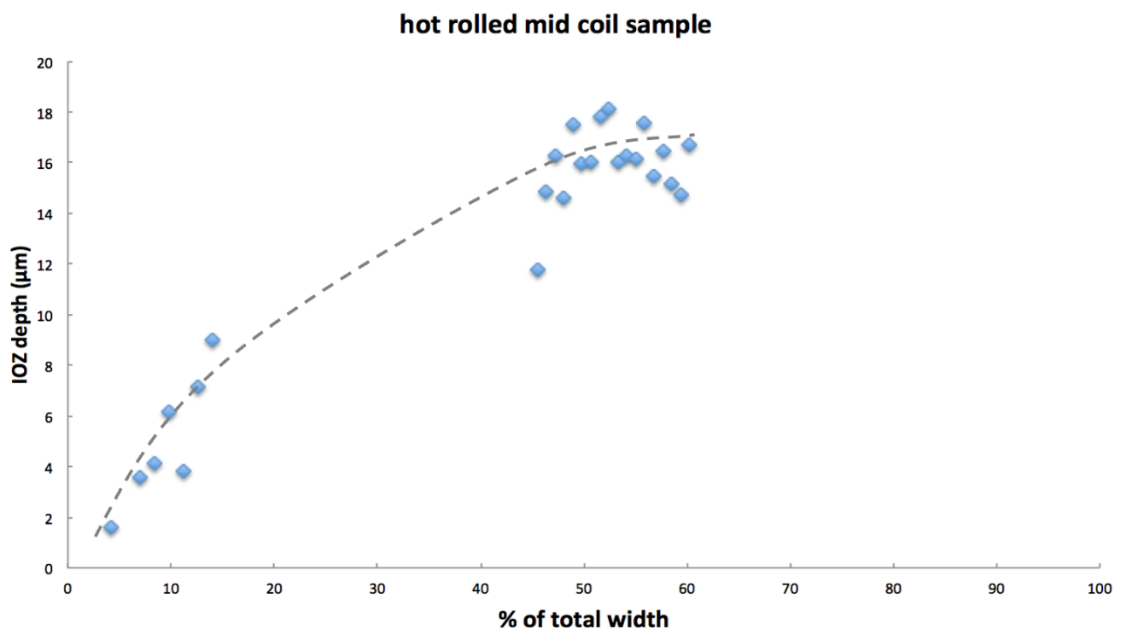
Fig. 85. Internal oxidation depth along the edge of hot-rolled mid-coil sample with a trend line added.

Previous reports have employed EDS mapping to characterise internal oxidation at mid-coil positions [57, 66]. Mn, O and Si were found at grain boundaries. However, the geometry and compositions of internal oxides have not been fully clarified. Here, TEM characterisation was applied at IOZ regions to study the nature of the nano-sized oxides, as shown in Fig. 86. High densities of rhombic precipitates, with sizes of ≤10 to 50 nm, were found near grain boundaries. The density and size decreased towards the centre of the grains. This is consistent with Mao et al.'s [93] model of oxygen diffusion in the subsurface region. Oxides found at the grain boundaries displayed different geometries. They are larger in size and the density is high enough to fill the grain boundaries. By comparing The SEM and TEM images, the dark dots and subsurface grain boundaries in Fig. 83 are refuted to be pores or gaps.

a.   500nm   b.   70nm
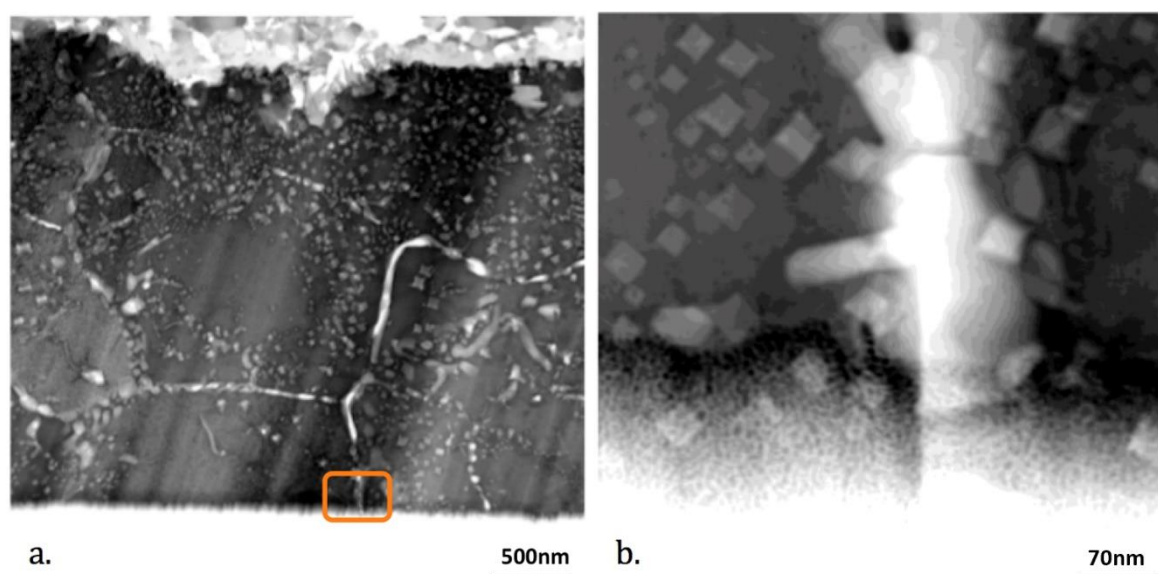
Fig. 86. (a). TEM image of internal oxidation zone, starting from the scale/steel interface (at the top) to 6µm in depth. The sample was taken from the hot rolled mid-coil at the mid-width (location 4, refer to Table 2). (b). Higher magnification image at the circled area.

The elemental analyse results are carried out by the STEM-EDS, as shown in Fig. 87. The iron signal is weak in all oxygen-enriched regions. Moreover, Si, O and Mn signals appear at the same locations (at nm scale). Semi-quantitative results revealed extremely high oxygen concentration (up to 79 at%) at the grain boundaries with moderate Si content (15.5 at%). Fe and Mn were at lower levels, 8.8 wt% and 7.7 wt% respectively. From the data collected, it is still difficult to tell if the internal oxides belong to SiO_2, Fe_2SiO_4 or the other phases, because the error in oxygen measuring is too high (up to 140%).

More details about the compositions of these inclusions are given in appendix 1 (p. 187).

The results suggest that the precipitates and grain boundary inclusions are composed of Si enriched oxides. This suggests that during coil cooling, the hematite reduced into pure iron and oxygen ions. The oxygen ions have sufficient partial oxygen pressure to diffuse inward to the steel matrix and react with the Si to form oxide. The oxide appears non-stoichiometric containing small amounts of Mn. Previous studies [44, 45] reported that the Si at grain boundaries may also come from the Fe_2SiO_4 or SiO_2 phases at the scale-steel interface.

On the other hand, Vlack [9] found that the compositions of oxides are non-identical across the IOZ. When Fe-1.0Mn steel is oxidised at 1350°C and $P_{H_2O}/P_{H_2} = 0.2$ was used to calculate the MnO to FeO ratio via thermodynamic data. MnO to FeO ratio at the subscale front is approximately 97:3 but decreases continuously until 77:23 was reached at the surface. The composition variation is more complex when multiple elements are alloyed into the steel. Generally, the position of a specific type of oxide largely depends on its de-oxidizing preference. For example, Vlack [9] mentioned that transparent SiO_2-rich oxides are formed at the subscale front, whereas MnO/FeO rich inclusions are more likely to form in the middle positions of IOZ. This confirmed that Si is a reducing agent compared to Mn. The variation of oxides ratio across the IOZ as well as its relationship with the partial oxygen pressure (pO2) will be understood by further on studies in this thesis.
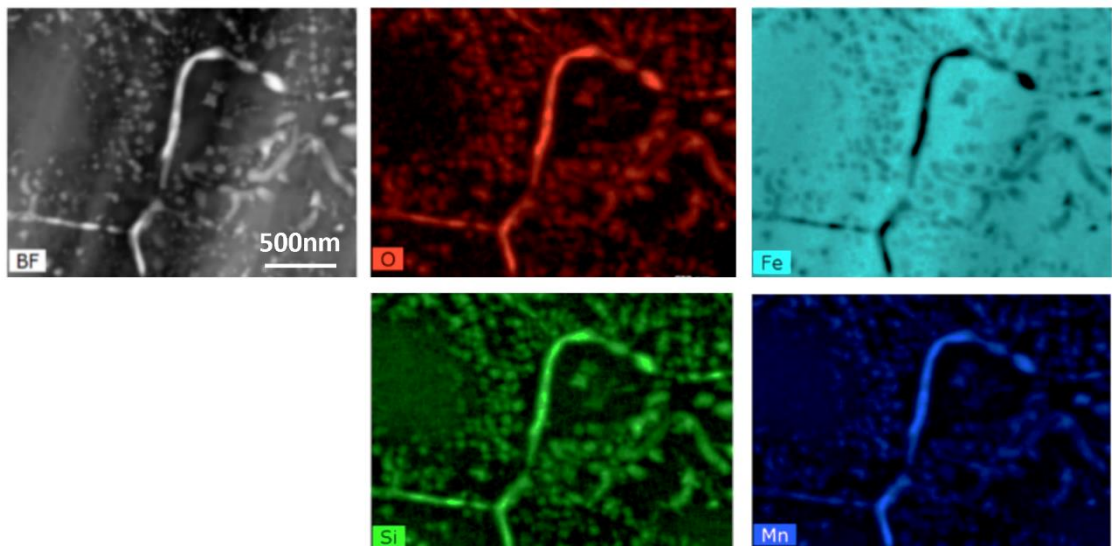
Fig. 87. STEM-EDS mapping of internal oxides. The sample was taken from the hot-rolled mid-coil at the mid-width.

4.2.2. Simulation of cold rolling conditions

Cold rolling was simulated under lab conditions in order to study the deformation mechanisms of oxide-enriched regions (refer to p. 95). The deformation of the near surface region due to cold rolling is shown in Fig. 88. Up to 52% thickness reduction and 25% hardness increase were achieved due to rolling. The steel surface remains flat and grains are elongated parallel to the rolling direction. Cold rolling compressed the IOZ depth from 13.4 μm to 7 μm. This value varies depending on the sampling position and the original depth of the IOZ. Cracks were found at subsurface region after 40% thickness reduction, but may have initiated at the earlier stage (between 17% and 40%). Cracks were only present within the IOZ and not in the steel after cold rolling. Subsurface cracks appear to initiate from the grain boundaries, which are decorated by oxides. Cracks propagated along these oxidised grain boundaries, which slightly opened up during further cold rolling.
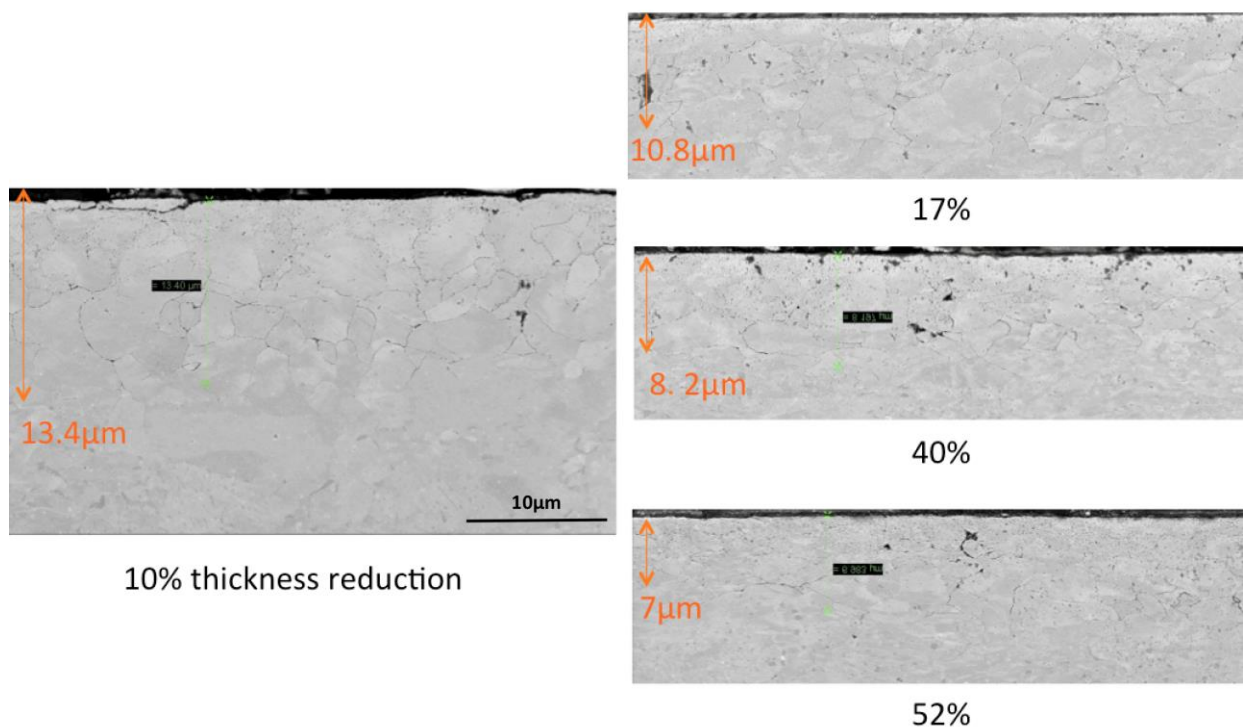
Fig. 88. Deformation of the IOZ during cold rolling simulation. The sample is coil-cooled DP1000 steel A taken from the mid-coil and mid-width with surface pickled (loaction 8, refer to Table 2).

Further, the shape of oxidised grain boundaries has changed after cold rolling. Before cold rolling the ferrite grains within the IOZ are equiaxed. It means that all grain boundaries are non-directional. In

principle, the total length of vertical grain boundaries is equal to the horizontal within a squared area.

However, when the grains are deformed after cold rolling, both grains and boundaries are elongated along the rolling direction. In this case, longer horizontal grain boundaries can be found within a square. This feature plays an important role in the subscale morphology development during annealing.

In contrast, the transformation of the subsurface morphology of an un-pickled sheet is shown in Fig. 89. The external scale layer broke up during the rolling process due to its brittle nature. Harder oxide fragments were pressed into the softer ferrite and the surface roughness increased. However, no cracks were found within the IOZ. It is assumed that when scale is absent, rolling forces are directly applied directly onto the smooth ferrite surface. Due to the circular geometry of the rolls, the actual area in contact between rolls and the sheet is relatively small. The resulting pressures are sufficient to separate two adjacent grains if oxides are present at their shared boundary. However, when an external scale is present, the force is applied to its fragments. The irregular shape of the oxide fragments distributes the force to different directions and reduces the local pressure experienced at the grain boundaries, which drops below the needed level to break them apart.

Further, the shape of oxidised grain boundaries has changed after cold rolling. Before cold rolling the ferrite grains within the IOZ are equiaxed. It means that all grain boundaries are non-directional. In principle, the total length of vertical grain boundaries is equal to the horizontal within a squared area. However, when the grains are deformed after cold rolling, both grains and boundaries are elongated along the rolling direction. In this case, longer horizontal grain boundaries can be found within a square. This feature plays an important role in the subscale morphology development during annealing.
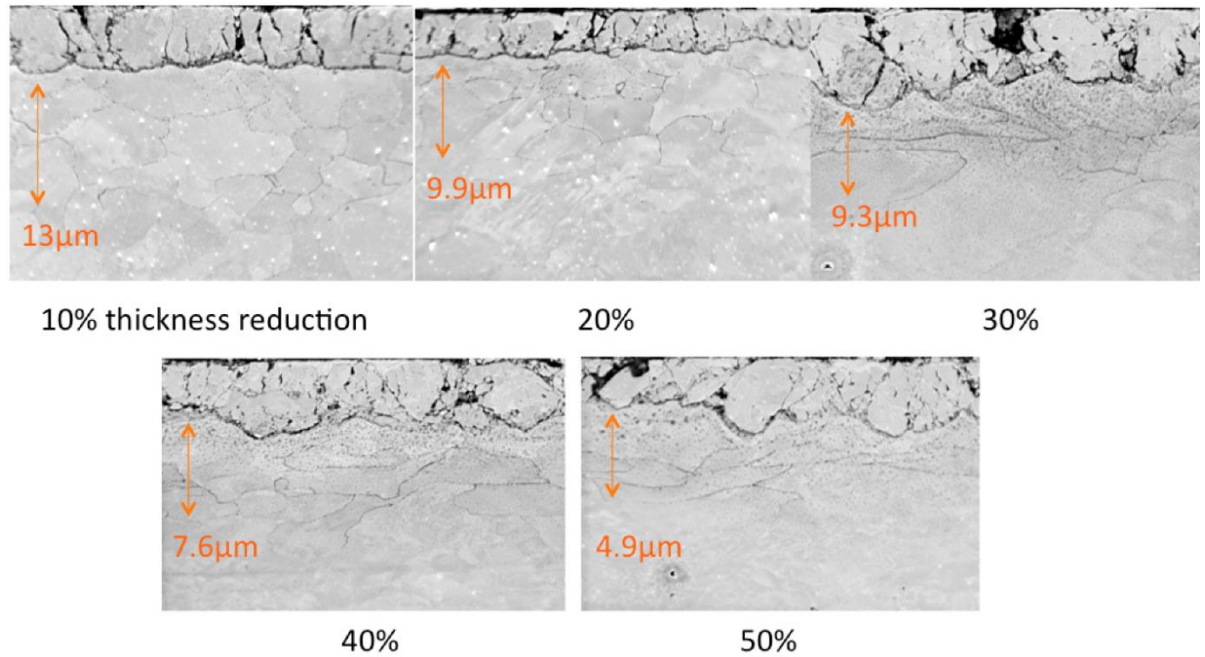
Fig. 89. Deforming of the near-surface region during cold rolling simulation. The sample is coil-cooled DP1000 steel A taken from the mid-coil and mid-width with scale remained (loaction 4, refer to Table 2).

4.2.3. Annealing

The annealed samples were also industrially processed and were analysed using similar methods as hot rolled samples. The comparison between tail (identical to the head) and mid-coil sample at variable coil widths is shown in Fig. 90. At the coil edge (location 9 and 11, refer to Table 2), around 1-2µm of internal oxide is formed in both tail and mid-coil. At the tail-coil, a maximum IOZ depth of 4.25µm was measured starting at 30% of the total width (location between 9 and 10, refer to Table 2). In contrast, at a mid-coil section (location between 11 and 12), the IOZ depth increased rapidly along the width. The gradient starts to drop from 22% of the total width and the maximum IOZ depth throughout the width was 8.75µm (at 28% of total width).
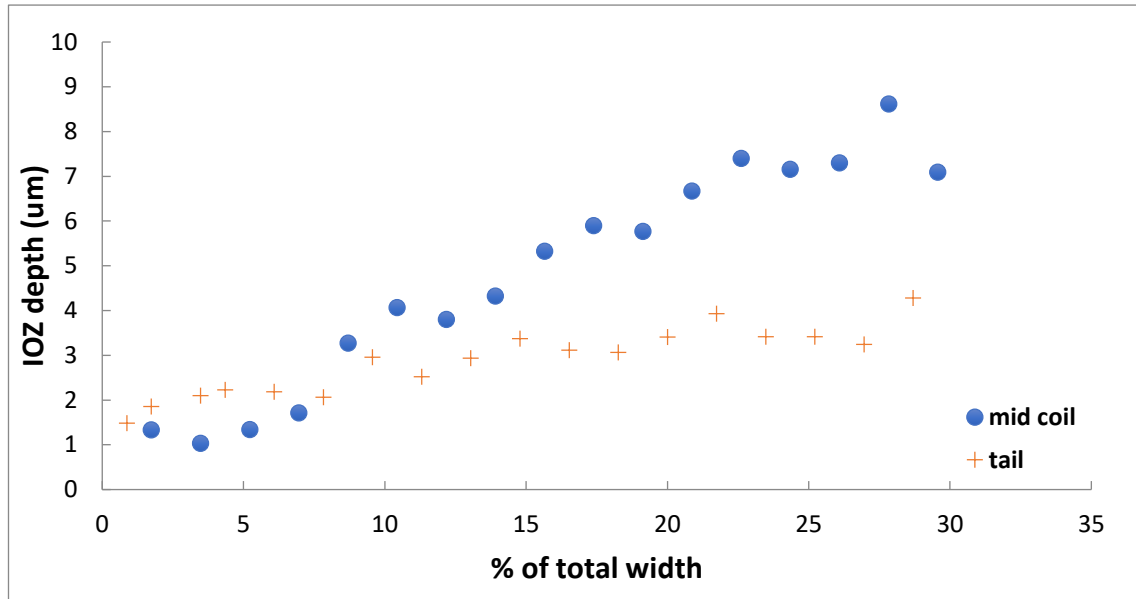
Fig. 90. Internal oxidation depth at different positions of the annealed coil.

The surface morphologies of galvanised mid-coil sheet are shown in Fig. 91. Instead of external oxides, a zinc layer covers the steel surface. After the annealing process, EBSD results confirmed that the original ferrite grains (at the hot rolling stage) are transformed into a dual-phase microstructure, consisting mostly of ferrite and martensite. However, the subsurface region still consists of pure ferrite due to the decarburization effect. A pure ferrite subscale was found at the hot rolling stage, as mentioned earlier. After the annealing process, at the coil edge (location 11, refer to Table 2), few precipitates were found at grain boundaries and the steel surface remained smooth. By comparing with the hot rolled and coil cooled microstructure (refer to Fig. 83 (a)), where oxides decorated most of the grain boundaries at the edge (location 3, refer to Table 2), fewer were found after annealing (as shown in Fig. 91 (a)). It is suggested that ferrite grains were recrystallized during annealing and the newly formed ferrite grain boundaries have not been influenced by internal oxidation. Due to the controlled atmosphere and more importantly, the lack of an external oxide layer, the formation of internal oxidation is less likely during annealing.

At locations away from the edge, more complex surface features are formed, as shown in Fig. 91 (b). and (c). High density of severe cracking was found within the IOZ, which lead to opened surface cracks. Some of the cracks are cross-linked, and ferrite clusters appeared to spall off from the surface. Abundant zinc was found in the large cracks (Fig. 92), suggesting that molten zinc penetrated into the

115

opened surface during galvanisation.

After cold rolling, the oxidised grain boundaries tend to deform and lay parallel to the rolling direction (as shown in Fig. 89). Cracks were also found after cold rolling, as shown in Fig. 88. In contrast, more cracks were found at the oxidised grain boundaries after annealing. Apart from the larger cracks that lead to surface opening, there are still a certain amount of micro-cracks that formed underneath the surface. EDS showed that no molten zinc was penetrated into these micro-cracks if they did not connect to the steel surface directly (as shown in Fig. 92, Zn map). However, a high density in cracks can destabilise the subsurface layer. Earlier internal studies have found steel fragments on the spelt zinc layer after severe bending of the galvanised sheets. This means although the bonding between zinc coating and steel substrate is strong, a loose subscale decorated with cracks and oxides is highly sensitive to mechanical forces.
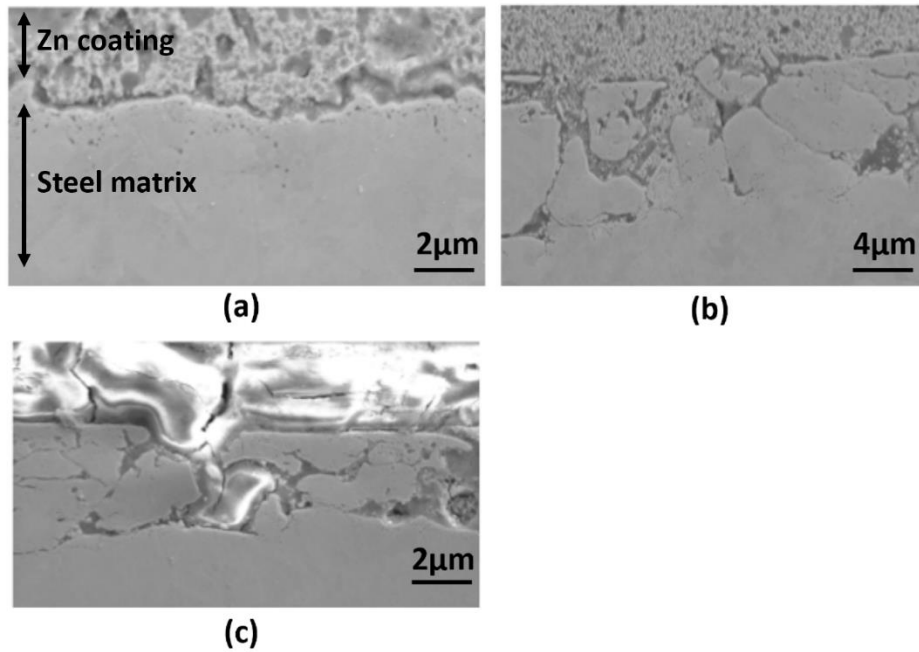
Fig. 91. Secondary electron image of annealed and galvanised steel surface at mid-coil, 5% (a), 22% (b) and 38% (c) of the total width. (a) is close to location 11 (refer to Table 2) while (b) and (c) are toward to location 12.
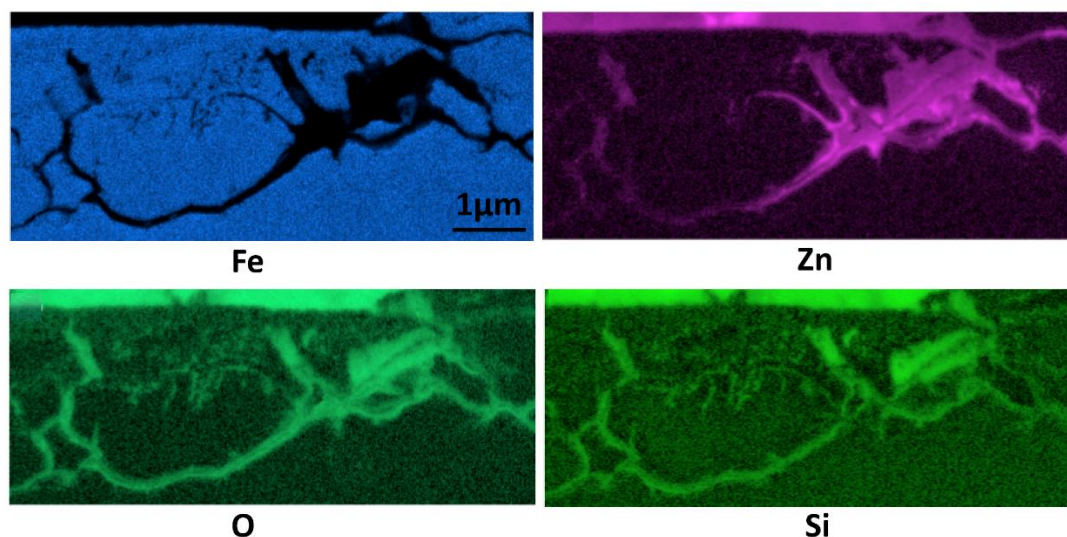
Fig. 92. EDS maps of galvanised steel surfaces. The sample was taken close to location 12 (refer to Table 2) and the surface is towards the top.

4.3. Summary

In-depth analysis, utilising SEM imaging, EDS, EBSD and XRD, found relative locations of wustite, magnetite, hematite, fayalite and manganese oxides within the external oxide layer of hot-rolled industrial product. STEM and EDS were employed to characterise the Si-enriched internal oxides (< 200nm). The iron nodules found at the scale surface could either came from hematite decomposition or as contaminates during the steel processing.

The scale and subscale morphologies changed during steel processing. In the dual phase steels studied, which contains Mn and Si, multi-layered external oxides are formed during hot rolling, which provide sufficient oxygen partial pressure for internal oxidation to happen in the tightly wrapped coil on the areas of the coil that undergo lower cooling rates during coil cooling. The deepest IOZ could be found at the mid-coil and mid-width position, whereas the subsurface is only slightly influenced at the head and edge of the coil. Cracks occur at the oxidised grain boundaries after the cold rolling simulation. The IOZ is squeezed and the internal oxides are elongated parallel to the cold rolling direction. During annealing, molten zinc penetrates into the opened surface cracks, and the bendability of the sheet is potentially reduced. Cross-linked horizontal cracks weaken the bonding between the subsurface and the steel matrix, which leads to coating failure during bending/forming.

Chapter 5. Influence of internal Oxidation on the bendability of Ultra High Strength Steels

The work presented here focuses on simulation of the surface and subsurface deformation during the steel sheet forming process by using an *in-situ* 3-point bending stage and digital image correlation (DIC). Two different bending grip geometries were applied to obtain the full details of the deformation. The microscopic strain distribution and failure mechanism are analysed to establish a link between the near-surface conditions and the formability of the final product. As discussed in the previous chapter, the internal oxidation depth varies within the steel coil, owing to the different cooling rates and atmospheric conditions depending on the position in the coil. Samples with different internal oxidation depths are tested to find out the critical conditions that lead to failure during the forming process.

5.1. Introduction

The development of subscale morphology during steel processing has been described in earlier chapters and is reported in the literature [49]. Two forms of internal oxides are found in the as received DP1000 ultra high strength steel sheet samples, which are oxide aggregates at grain boundaries and precipitates within the grains. Cracks were observed to initiate at the oxidised grain boundaries during cold rolling simulation. The cold rolling was also found to compress the IOZ and elongate the oxidised grain boundaries along the rolling direction. After annealing, molten zinc was observed to have penetrated the opened surface cracks during the galvanising process [49]. The typical subsurface features of coil cooled and annealed sheet were illustrated in early chapters (refer to Fig. 83 and Fig. 91, respectively). The defects found in surface and subsurface regions are expected to influence the bendability of the final product.

Bending tests help to assess bendability of sheet metals. Many factors may influence the bendability of a material, such as its mechanical properties, microstructure, and the tooling specifications. Higher tensile strengths will undoubtedly decrease the bendability, but the influence of the various microstructure features on the damage mechanisms during bending are not well characterized, particularly with respect to the surface and subsurface.

During steel sheet bending tests, both inclusions and microstructural heterogeneities (such as

proportions and distributions of phases) can be classified as internal inhomogeneities, which have a negative influence on the bendability. Cracks become more likely to occur during bending if inclusions are present at the surface and subsurface regions, hence bendability is lowered. The location, dimensions and orientation of inclusions can alter during the rolling processes. Inclusions are elongated along the rolling direction and lead to lower bendability in the transverse direction.

In this study, systematic bending tests are applied to inspect the uniformity of bending behaviour across the galvanised UHSS coil. The influence of surface defects on bendability and the failure mechanisms during bending are characterised from a microscopic point of view. This is achieved using an *in-situ* bending stage, which can be inserted into the SEM chamber to track the real-time micro-crack development during bending tests. The combination of the bending tests and strain measurements derived from DIC results (post-process of the SEM images) allows investigation of full-field deformation from a microscopic point of view.

5.2. Experimental

5.2.1. Sample preparation

The bending samples are taken from three DP1000 Steel A, galvanised coils (trials) provided by Tata Steel with identical compositions (0.2wt% C, 2.1wt% Mn and 1wt% Si). The samples are taken mainly from the mid-length of two coils in this study. The as called coil 1 and 2 have identical composition and both of them are internally oxidised. The variation of IOZ depth across the coils were characterised in the earlier study [49] and chapter (refer to p. 114).

The bending samples have constant dimensions of 50 x 4.5 x 1.5mm, and are cut from the sheets using an abrasive blade at with a speed of 4000 rpm and a 10 mm/min feed rate. Samples were taken from the mid-length of the coil and from the edge to the centre (from location 11 to 12, refer to Table 2). The longest side (50mm) of the sample is parallel to the coil rolling direction, making the bend axis is perpendicular to the rolling direction during bending tests. One of the sample edges (facing the electron beam) was polished to optimize the quality of the SEM images taken during bending. To

reduce variation in the test data, it is important that the sample width and thickness was identical for each test. The sample thickness is continuously 1.5 mm throughout the coil, and the width needs to be controlled precisely during cutting. To further minimise scatter in introduced by variations in sample geometry, each set of samples was clamped and polished together; an example is shown in Fig. 94. The clamped samples were ground and polished by hand on using 320, 9, 3, and 0.0 5µm polishing pads sequentially at 150 rpm, and appropriate diamond suspensions were added to assist polishing. Samples were then cleaned individually with isopropanol in an ultrasonic bath. The external and internal oxidation layers remain unaffected after the preparation. The top zinc layer is also retained.

To produce baseline test data, samples without an IOZ (sampling from location between 15 and 16, refer to Table 2) were prepared by polishing the sample surface down to 3 µm roughness average, which successfully removed the surface/subsurface defects and the top zinc layer before bending. The aim is to compare the behaviour of surface deformation between the samples with and without an internal oxidation layer.
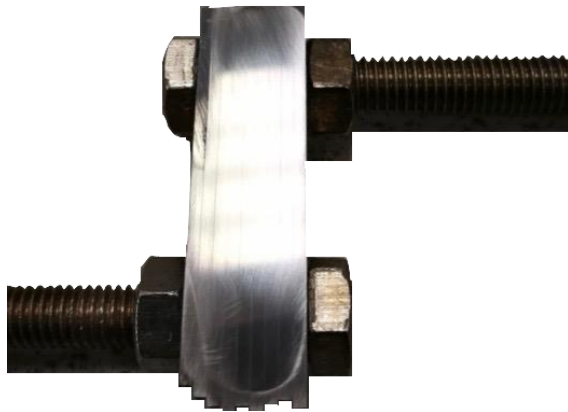
Fig. 93. Clamped of 9 sample pieces to achieve constant width value after grinding and polishing.

5.2.2. Bending tests

As mentioned earlier, the bendability can be carried out using an *in-situ* tensile and bending stage with 5 kN load cell (DEBEN W/C). The sample is clamped onto the grips with a 10 N holding force and then

the entire bending stage is placed into the SEM chamber. The polished side is placed towards the electron beam source for imaging. Conditions of 10 kV beam voltage, 120 mm aperture size, backscattered detector and 12 mm working distance are selected for optimum image quality. The bending tests were performed under 1 mm/min punch displacement speed.

The load P and extension δ (punch displacement) data are recorded every 500ms. The bending stress σ and strain ε, sometimes also called flexural stress σ_f and flexural strain ε_f can be calculated by the following equations [94]:

$$\sigma_f = \frac{3PL}{2bh^2} \tag{27}$$

and for the sample with rectangular cross-section,

$$\text{and } \varepsilon_f = \frac{6\delta h}{L^2} \tag{28}$$

Where L means support span, b & h are the width and thickness of the specimen, respectively.

The bending test can be interrupted to capture images, and it is essential to maintain constant parameters (position, magnification, brightness and contrast) for each image to enable the DIC strain analyses. Consistent images were processed via DaVis DIC software; 25 x 25 subset size and step size from 1 to 8 were selected for optimal determination of strain distribution and localisation. The subset size influences both spatial resolution and accuracy, the error for 25 x 25 subset size is estimated to be 0.07% [95].

Two sets of bending grips are used in this study. The original grips have 2.5mm punch tip radius and 20mm span between the support tips; the other grips are machined to achieve sharper punch tip and shorter span. The geometries of grips are illustrated in Fig. 94. (a) and (b). The aim of having the modified grips is to allow higher bending angle and smaller bending radii. Samples were showing no sign to crack at the maximum punch displacement for the original grips (4.5mm, approximately equal to 37° bending angle). After several modifications (designed by the author and machined by the workshop), a 0.3mm punch radius, 12mm span between the tips of supporting pins and 9.4mm maximum punch displacement was chosen, which allows much sharper bending and therefore defects, such as voids and surface crack propagation could be observed.

(a)   **(b)**   **(C)**
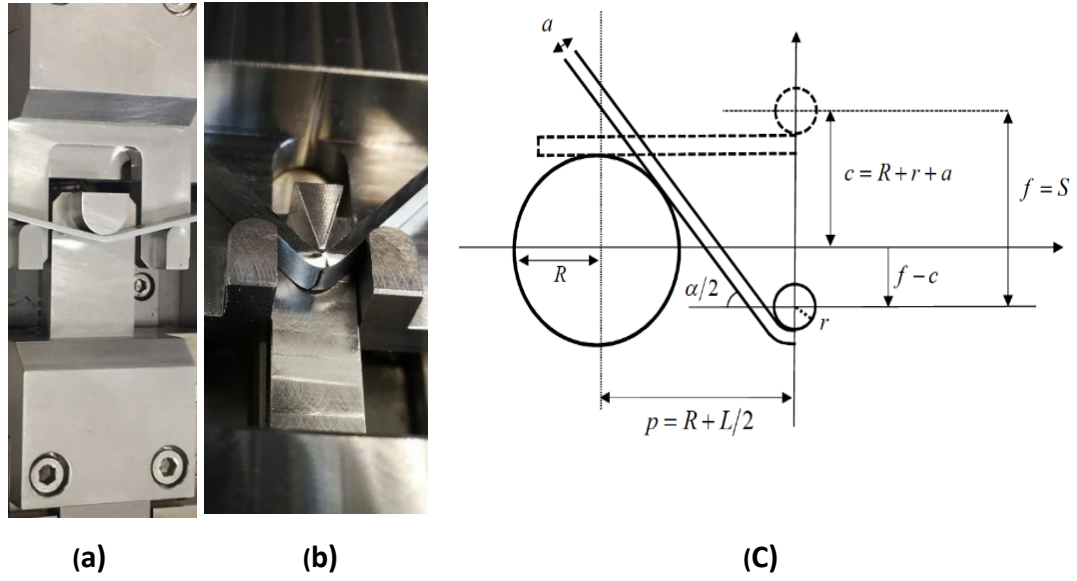
Fig. 94. (a), Original bending grips design with 2.5mm punch radius and 20mm span between supporting pins. (b), Modified bending grips design with 0.3mm punch radius and 12mm span. (C), Parameters for bending angle α calculation according to ISO 7434 [96].

The bending angle α can be determined from the punch stroke f and it is calculated according to the ISO 7438 testing standard [96], as shown in Fig. 94 (a):

$$\sin\frac{\alpha}{2} = \frac{p \times c + W \times (f-c)}{p^2 + (f-c)^2} \tag{29}$$

or $\cos\frac{\alpha}{2} = \frac{W \times p - c \times (f-c)}{p^2 + (f-c)^2}$ (30)

With $W = \sqrt{p^2 + (f-c)^2 - c^2}$ and $c = R + a + r$

R: Supporting pin's radius, r: punch tip radius, *f:* punch stroke, a: sample thickness, p: distance between the vertical plane of the punch and the tips of supporting pins.

5.2.2.1. Zero-deformation experiment

The reliability and stability of the SEM imaging system are checked by the zero-deformation method [97]. Once appropriate magnification and sample position are selected, seven images are taken and numbered in chronological order from 1 to 7. All images are taken before the bending process. The region of interest and calculation step size stays constant to the bending experiments. The first image was set as the reference image for DIC calculation. A region of interest (ROI) with a size of 1450×1095 pixels (equivalent to 142×107 µm^2) was selected from the reference image DIC to measure the relative

displacement fields of the ROI in further seven images. In the DIC correlation process, the calculation step was set as 2 pixels and the size of the subset was selected as 39×39 pixels. The results are shown in Table 4, where the wobbling of the SEM system at the start state is less than 0.0004 and -0.0005 pixels in the horizontal and vertical direction, respectively. The magnitude of error is negligible when comparing to the 16 μm/s bending tip displacement rate and the large sample deformations (details shown in the next chapter). Therefore, the DIC image processing will not be affected.

Table 4. The mean values and standard deviation of measured displacement in horizontal (exx) and vertical (eyy) directions in the zero-deformation experiment.

Image pairs	2 to 1	3 to 1	4 to 1	5 to 1	6 to 1	7 to 1
Mean (exx)	0.0003	0.0003	0.0004	0.0004	0.0003	0.0003
Stdev (exx)	0.004	0.004	0.005	0.004	0.004	0.005
Mean (eyy)	-0.0005	-0.0007	-0.0002	-0.0005	0.0000	0.0003
Stdev (eyy)	0.005	0.004	0.005	0.005	0.005	0.005

5.3. Results and discussion

The typical subsurface features of the annealed DP1000 sheet at the mid-coil was illustrated in Fig. 91 (c) where large amount of defects were illustrated. The damaged subsurface layer is trusted to influence the bendability of the final product.

Regarding the steel matrix, EBSD band contrast maps of the edge and mid-width coil samples are summarised in Fig. 95. A significant amount of martensitic grains appears in the image (a) and (b), owing to the faster local cooling rate at the coil-edge (location 11, refer to Table 2). The near-edge regions (5% at both sides) are normally discarded due to the unsatisfied bending properties, which will be explained later on. By comparing the image (d) and (f), it can be seen that the microstructures are similar in samples at 5% and 30% of the coil width; the average grain size is 3.7 and 3.4 μm at the mid-thickness of each sample, respectively. Band structures are found in both samples, resulting from microsegregation during casting or imperfections developed in the annealing process [98]. By comparing image (c) and (e) with (d) and (f), respectively, the band structure is more apparent at mid-thickness of the sheet than the surface, although a few ferrite bands still appear at the surface (labelled in image (e)). The elongated ferrite grains are believed to alter the mechanical properties of the steel

sheet, especially when these grains form a continuous layer. Decarburisation appears to have occurred in all three samples, as ferrite dominates in the sub-surface regions, this was confirmed by earlier OM and hardness characterisations (p91). The surface depletion of carbon content makes the steel sheet surface softer than the bulk, which theoretically increases the tolerance against bending [99].

(a)

(b)

(c)

(d)

(e)

(f)
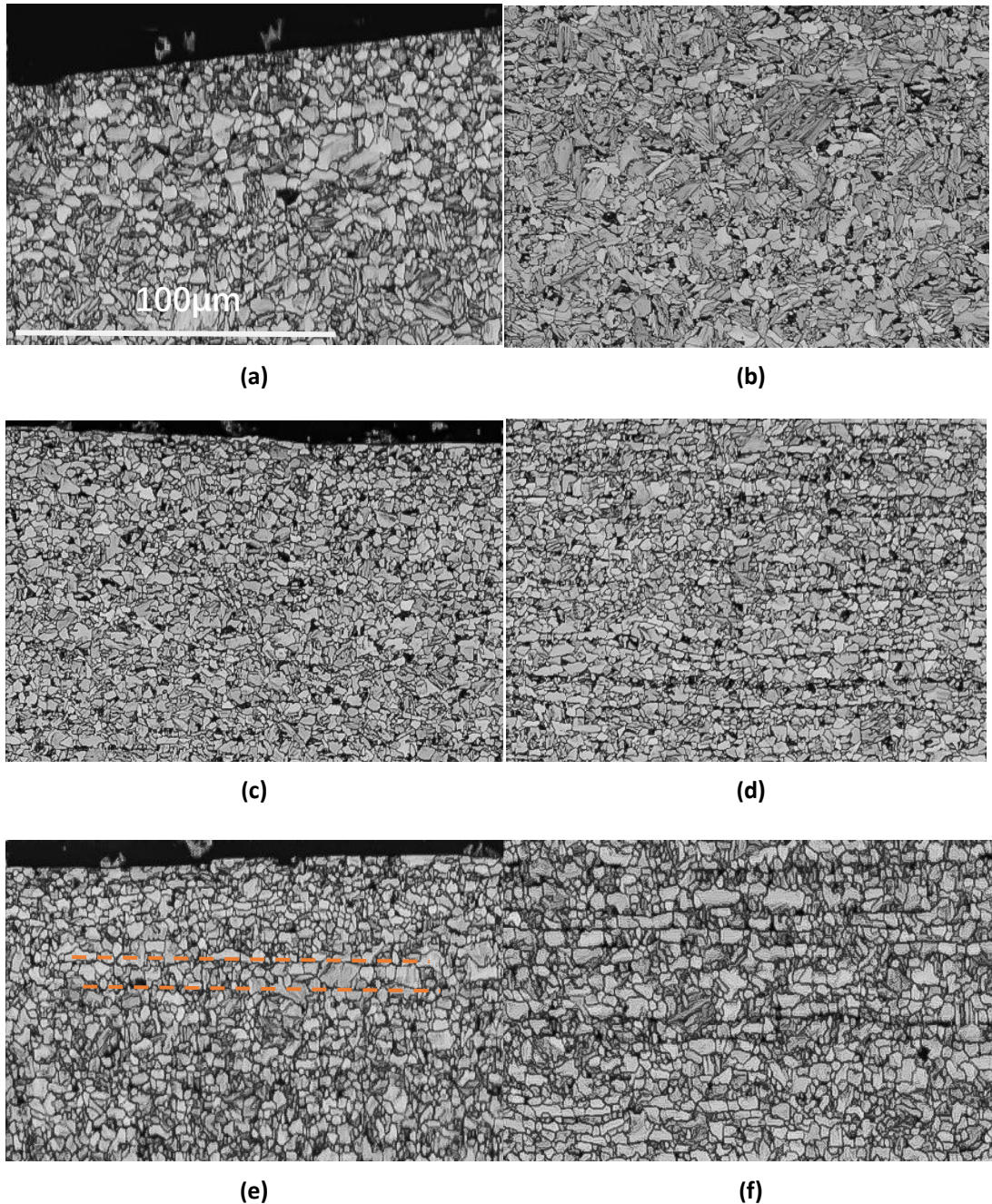
Fig. 95. EBSD band contrast images of samples from the annealed coil at: (a), coil edge and at the surface; (b), coil edge and at mid-thickness; (c), 5% apart from the coil edge and at the surface; (d), 5% apart from the coil edge and at mid-thickness; (e), 30% apart from the coil edge and at the surface; (f), 30% apart from the coil edge and at mid-thickness. All images are taken under the same magnification.

5.3.1. Bending - test series 1 (2.5mm punch radius and 20mm support span).

Bending tests were performed on samples from both the edges (location 11, refer to Table 2) and inner-width (between location 11 and 12) of two DP1000 steel A coils. All samples were taken from the mid-length of the coil; an example is shown in Fig. 96, a 2.5mm radius punch was used. For both coils, samples from the edge show significantly lower strength than those from the inner-width. Under the same conditions, the maximum load achieved by samples from the edge of coil 1 is 17.8% lower than the samples located 18 cm from the edge towards the mid-width (For coil 1, this is 12.17% of the width). Further tests proved that at the mid-length of the coil, a 16% drop in the flexural stress value is found between a coil-edge sample to one taken at 12% of the total width.

The bending angle α is calculated by using equation (29) and it is reflected as the second x-axis shown in the Fig. 96. Micro-cracks should initiate, which can be reflected by load value drop. As a result of these changes, the bending angle at ultimate load is paramount when comparing samples.

Samples from the mid-length of coil 1, taken at points between 10-20% from the edge (close to location 11, refer to Table 2) are compared. Under constant bending rate and grip configurations, the samples can be bent to 46.7 ° without micro-crack forming. A slight difference is found from samples taken from this same distance from the head of the same coil, but at different width positions (for example, at 12.17% and 15.65% of the total width in coil 1) is either caused by localized microstructural heterogeneities or differences in the sample widths.
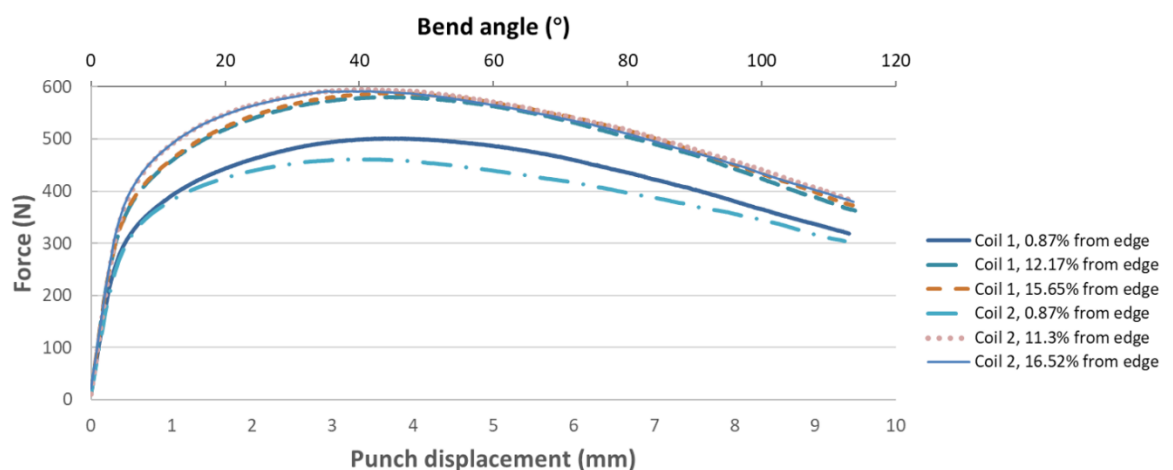
Fig. 96. Bending curves of coil 1 and 2. 2.5mm radius punch was used.

The SEM images recorded as the deformation progress towards failure captured a microscopic point of view, and an example is shown in Fig. 97. The sample is taken from the mid-length of coil 1, and 20% from the edge, where the internal oxidation zone is approximately $10\mu m$ thick (refer to Chapter 4). Chapter 4 and previous report [49] have shown that the grain boundaries within IOZ are decorated with silicon-rich oxides after the coil cooling process. The grains within the IOZ underwent compression and recrystallisation after cold rolling and annealing, respectively. The grain boundary oxidation was assumed to loosen the bonding between grains after cold rolling. The current experiments show that those oxidised grain boundaries opened quickly at the initial stage of the bending tests, as shown in Fig. 97 (a). This image was taken before reaching the yield strain (<0.5% bending strain). Beyond the yield point, slip bands start to appear across the bulk materials. With increasing load/bending, the oxidised grain boundaries start to open continuously. Fig. 97 (b) was taken prior to the ultimate load (<8% bending strain); all the oxidised grain boundaries are opened at this stage. However, there is no sign of crack propagation towards the bulk steel at this strain. It was assumed that the sample starts to fail after the ultimate load [49]. At >8.5% bending strain, voids were observed, and examples are highlighted in Fig. 97 (c). The voids formation explains the reason behind the load drop. By comparing the microstructure at the same position before and after bending, the voids are most likely to form at the boundary between ferrite and martensite grains, especially when the contact length between them is relatively long. The evidence is given in Fig. 98, which was taken before bending. By comparing to the microstructure after bending, the positions of microcracks are highlighted (cracks forming at subsurface due to internal oxidation are excluded). Fig. 97 (d) is taken at maximum punch stroke, and neither surface crack propagation nor voids interconnection is found at the end of the test. The same phenomenon occurs in all samples from the mid-coil.
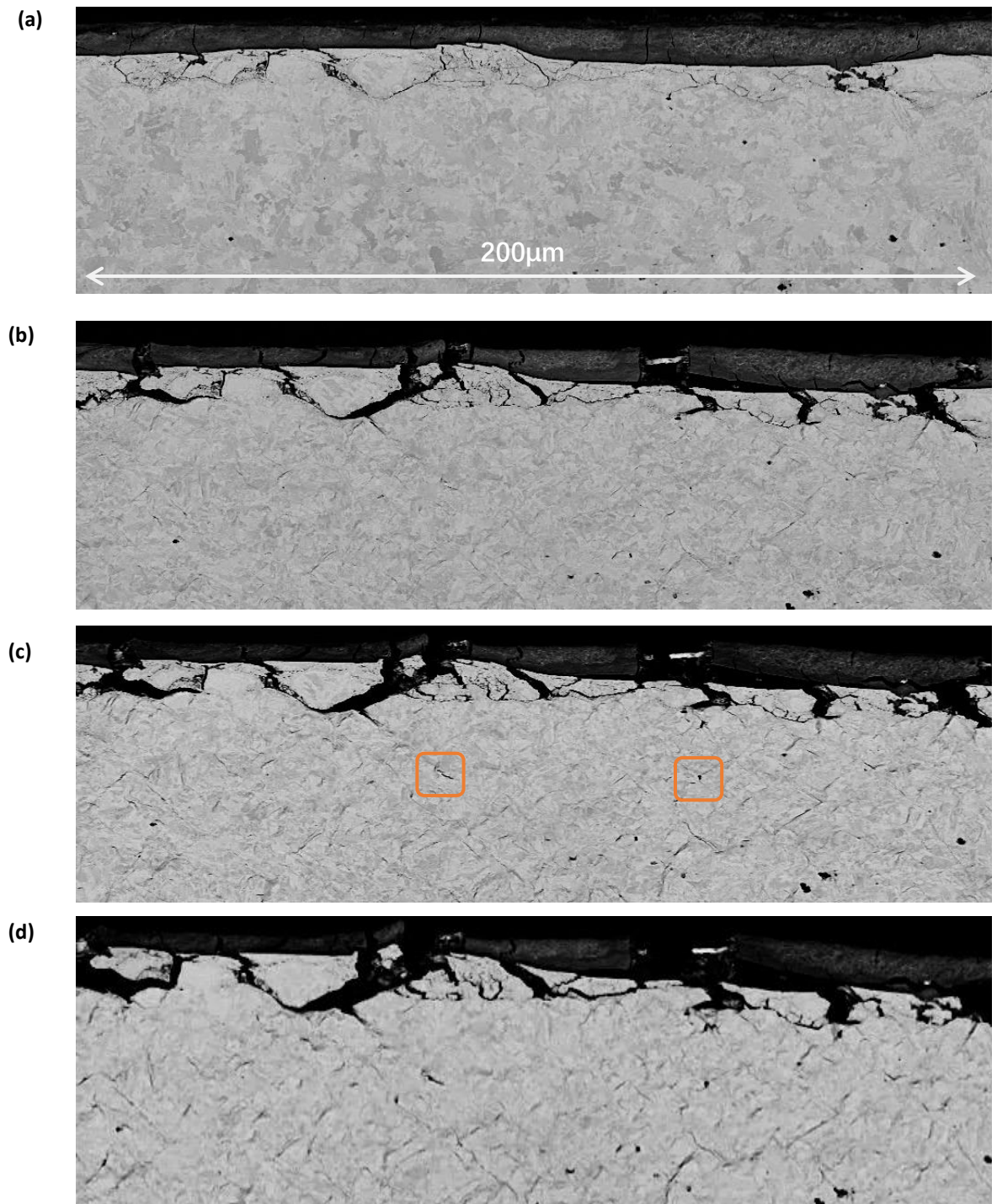
Fig. 97. SEM images taking during in-situ bending test: (a). at the beginning of the test; (b). when load-extension curve approaching the ultimate load; (c). when the load-extension curve passed the ultimate load; (d). at maximum punch stroke. The tension side under bending is towards the top of the images. The grip with 2.5mm punch radius and 20mm support span was used. The boxes in (c) indicate the locations of void initiation.
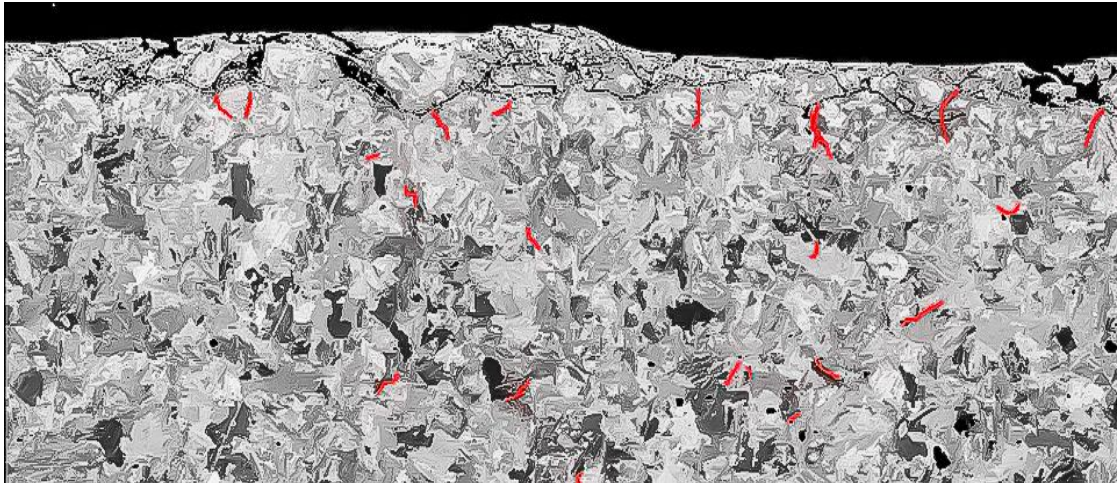
Fig. 98. SEM backscattered image of DP1000 before the bending test. By comparing to the image after bending, the void formation positions are highlighted on the original microstructure.

Surface/subsurface characterisation on annealed coil samples (refer to p. 114) have shown a high density of oxidised grain boundaries present at the subsurface. They are not only cross-linked with each other but also elongated parallel to the cold rolling direction [49]. The assumption was made that a loose subscale decorated with cracks and oxides is highly sensitive to mechanical forces. The bending test has proved that the entire subsurface layer becomes loose as a large number of horizontal cracks tends to cause separation of the layer from the bulk. Coatings applied to the sheet surface will then be lost if the entire subsurface layer has weak bonding with the substrate.

Through post-processing of the SEM images, DIC results visualise the local strain distribution during the bending. In
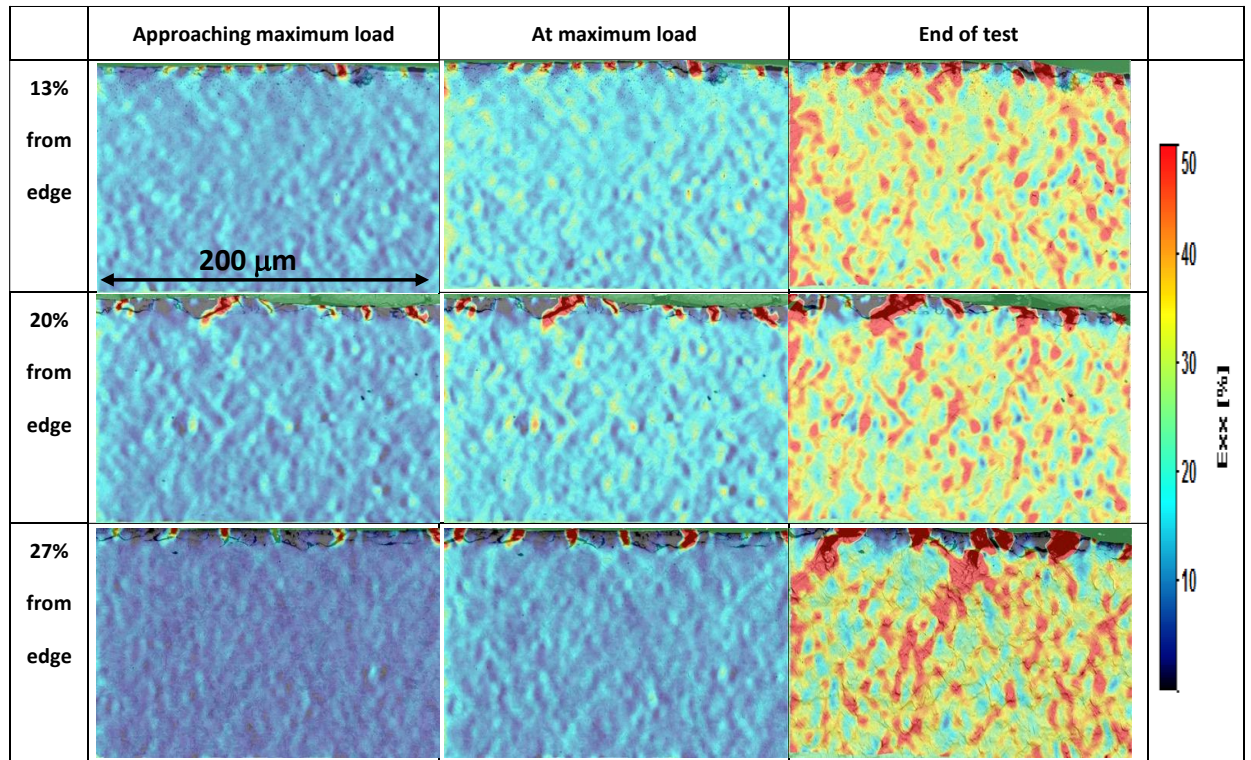
Fig. 99, samples from coil 1 at mid-length and various width positions are compared. DIC maps at three critical stages- prior to the maximum load, at maximum load and the end of punch stroke- of each sample during bending are also illustrated. In

	Approaching maximum load	At maximum load	End of test
13% from edge			
20% from edge			
27% from edge			

200 μm
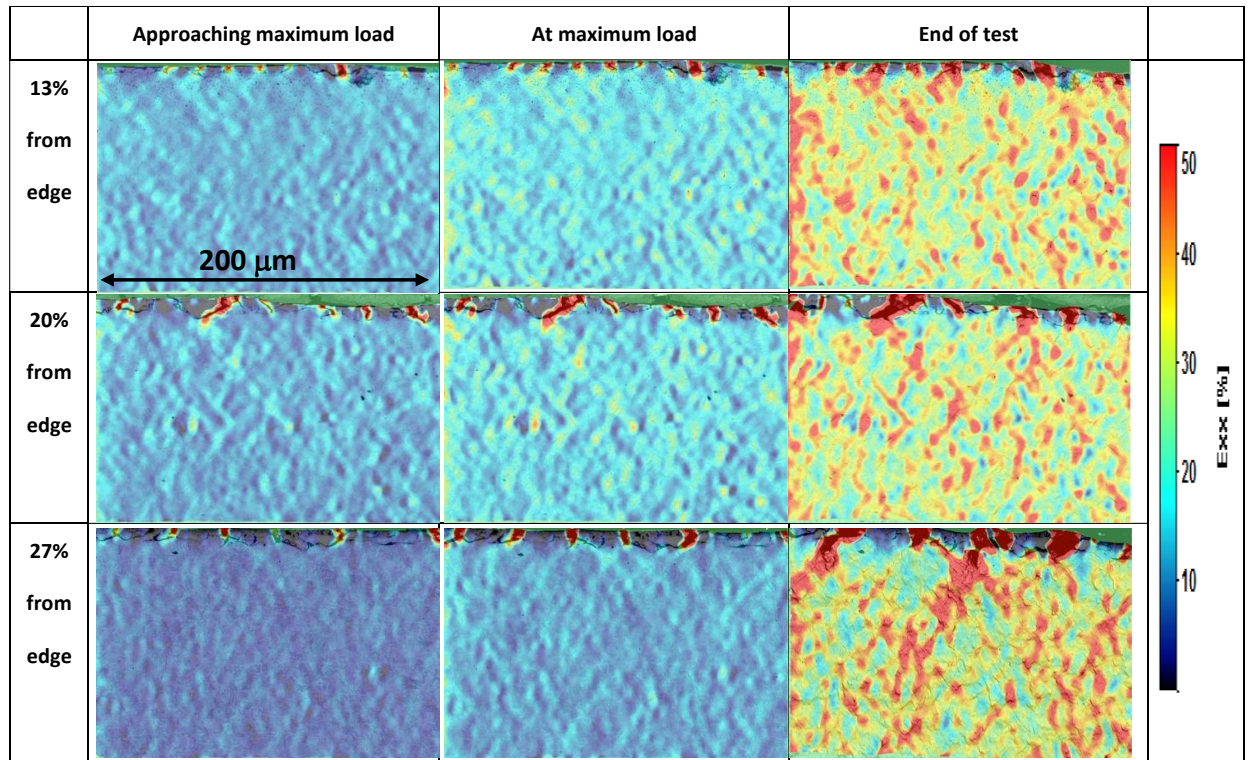
Fig. 99, the scale bar of strain values in the horizontal direction (exx) is set to a constant range (0-0.5).

All DIC maps are processed from the BSE images at the outer bending zone, so the entire frames are

under tension during bending. Each frame in
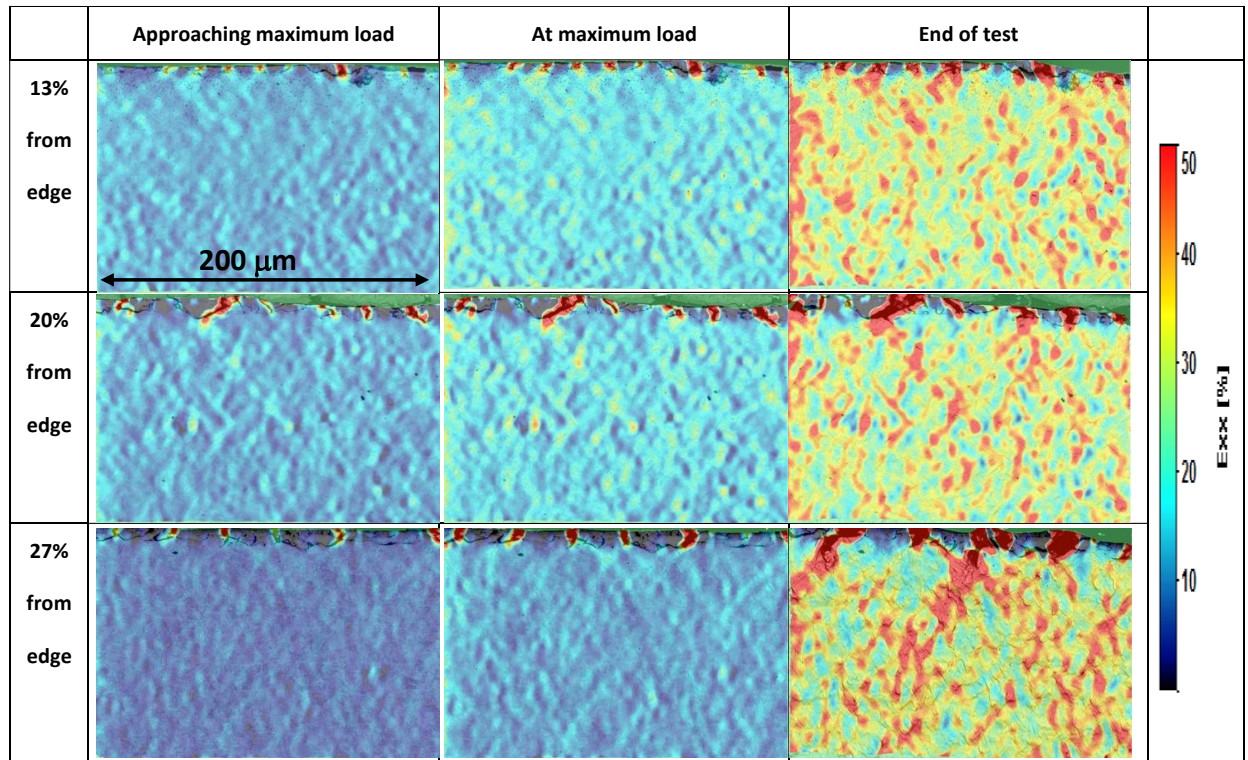
Fig. 99 is approximately 200μm in the horizontal direction and 150 μm deep from the steel surface.

The build-in extensometer shows the total strain in the horizontal direction at maximum punch stroke

is approximately 0.32, and -0.2 in the vertical direction. The negative value proved that the total

thickness decreases during bending.

	Approaching maximum load	At maximum load	End of test	
13% from edge				
20% from edge				
27% from edge				

Fig. 99. DIC results processed from BSE images. Samples are taken from the mid-length of coil 1, at 13%, 20% and 27% of the total width. Grips with 2.5mm punch tip and 20mm supports span have been used. All images were taken under the same magnification.

In

	Approaching maximum load	At maximum load	End of test
13% from edge			
20% from edge			
27% from edge			
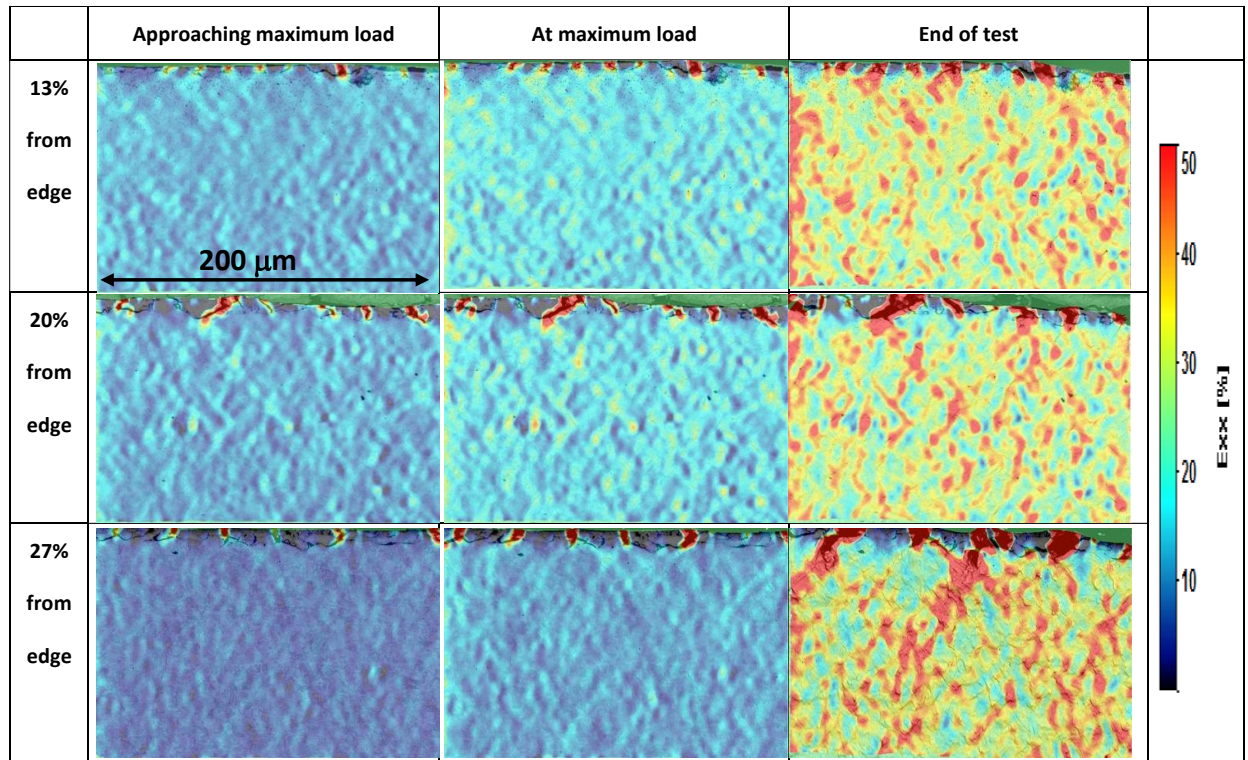
Fig. 99, all three samples went through relatively uniform deformation while approaching the maximum load. Only oxidised grain boundaries at the sheet surface opened at this stage, these positions with higher local strain values are highlighted in orange colour on the DIC images. The corrugated shape colouring matches with the slip bands observed in the corresponding SEM images. At the maximum load, localised strain fields are found on samples 13% and 20% from the edge. The positions matched with the crossover of slip bands, and voids have a higher preference to form at these locations. At the maximum punch stroke, high density of localised strains are found, the magnitude of strains at these positions are much higher than the overall horizontal strain (approx. 0.32) of the frames.

When the bending progressed towards the end, the individual localised strain fields tend to connect with each other, suggesting that voids may begin to interconnect, although this phenomenon has not been found in this test. Microscopically, maximum shear typically occurs at 45° to the loading axis. At 45°, the stress required to slip bcc crystal is at minimum value:

$$\tau = \frac{F}{A} \cos \lambda \cos \emptyset \qquad\qquad\qquad\qquad\qquad\qquad\qquad\qquad (31)$$

Where cosλcosϕ is the Schmid factor, τ is the shear stress, F is the load and A is the area.

Macroscopically, the interconnection of these major parallel strain fields forms shear bands, which are also at 45° (approximately) towards the bending direction. Ghadbeigi [100] and Alharbi [101] have reported bands of local strain orientated at around 45° towards the loading direction on DP1000 steel sheet (based on tensile samples).

The IOZ depth is 4.62, 8.34 and 8.57μm for samples 13%, 20% and 27% from the edge (edge means location 11, refer to Table 2), respectively. It is clear that deeper oxidised grain boundaries locally promote the connection of strain fields, which potentially leads to earlier failure of the material. For this series of bending tests, neither bending curves or SEM images (refer to Fig. 96 and Fig. 97) showed surface crack propagation or voids interconnection at maximum punch stroke. Similar results are found on sample 13% and 20% from the edge. At 27% from the edge, the surface cracks are relatively thicker, and part of the cracks start to propagate into the steel matrix. The magnitude of local strains increases as surface cracks propagate. The localised strains at the surface then tend to connect with the bulk strain fields, which formed due to the crossing of slip bands within the steel.

Samples without IOZ from the mid-length and identical width positions (from location 15 to 16, refer to Table 2) of the coil were tested under the same conditions. The DIC maps are plotted to compare with the samples with an internal oxidation layer. For the results shown in Fig. 100, any horizontal strain greater than 0.75 is left as blank to reduce the dominance of the high strain values in the opened grain boundaries at the surface. Thus, the lower magnitude of strains in the rest of areas are plotted more clearly and with better contrast.

At identical bending angles and sampling areas, the sample with IOZ exhibited seven places where local strains are greater than 0.75. Six are in the subsurface at the tip of oxidised and opened grain boundaries. In contrast, only two positions exceeding this strain are found at the surface of the sample without the IOZ. This is evidence that the presence of IOZ provides more sites for cracks to nucleate and propagate from the surface. Hence the samples with IOZ are more likely to fail from the surface. Comparison of the strain distribution in bulk for samples with and without the IOZ showed no significant difference. These observations indicate that at the maximum punch stroke of the grips used

in this test series, the presence of the IOZ creates more surface defects for cracks to nucleate but has no apparent influence on the local strain magnitude and the development of slip bands in the bulk.
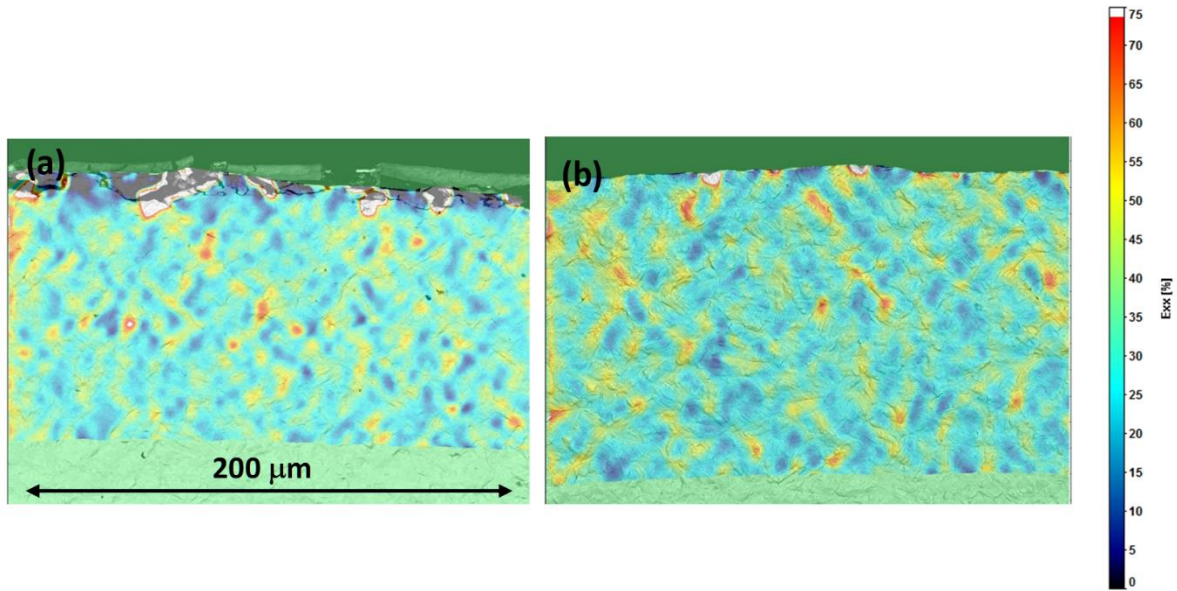
Fig. 100. DIC maps at maximum punch stroke (0.25mm tip, 20mm span). Samples are cut from coil 1 mid-length at 20% from the edge, (a). based on the original surface morphology, (b). based on the polished surface (no internal oxidation remained). Both images were taken under the same magnification.

By comparing the DIC maps plotted throughout the bending process (as shown in Fig. 101), a significant difference in deformation mechanism is found for samples with and without a thicker IOZ. Two samples have been taken from the mid-length and at 28% of the coil width, and the IOZ of one sample is polished away. The original IOZ thickness before polishing is approximately 8.5 μm. The DIC results are summarised in Fig. 101. At lower strain (frame exx 10%), both of the samples exhibit uniform deformation; oxidised grain boundaries opened in the sample with IOZ (12, refer to Table 2). At e_{xx} 20% of the frame, higher strains start to localise at the tips of cracked grain boundaries, and their magnitude is higher than the strains at slip bands within the bulk. In contrast, the surface suffers the same amount of strain to the bulk in the sample without IOZ (16, refer to Table 2). At 30% elongation, higher strains localised at the subsurface, and new cracks formed at the tip of opened and oxidised grain boundaries. The strains at those positions (circled in the frame) raises to above 0.9.

These surface local strains tend to crosslink with the inner slip bands and leads to the formation of concentrated high strains fields, again at 45° to the loading direction. This phenomenon has not been found in the sample that had the IOZ removed, although concentrated strain fields are also found within the bulk. However, the magnitude of major strains at the sheet surface is not any higher than the bulk. No cracks have been found at the surface at the same elongation value. The surface and bulk undergo the same amount of strain during bending. These observations provide evidence that in the absence of internal oxidation, the sample failure may not initiate at the surface.
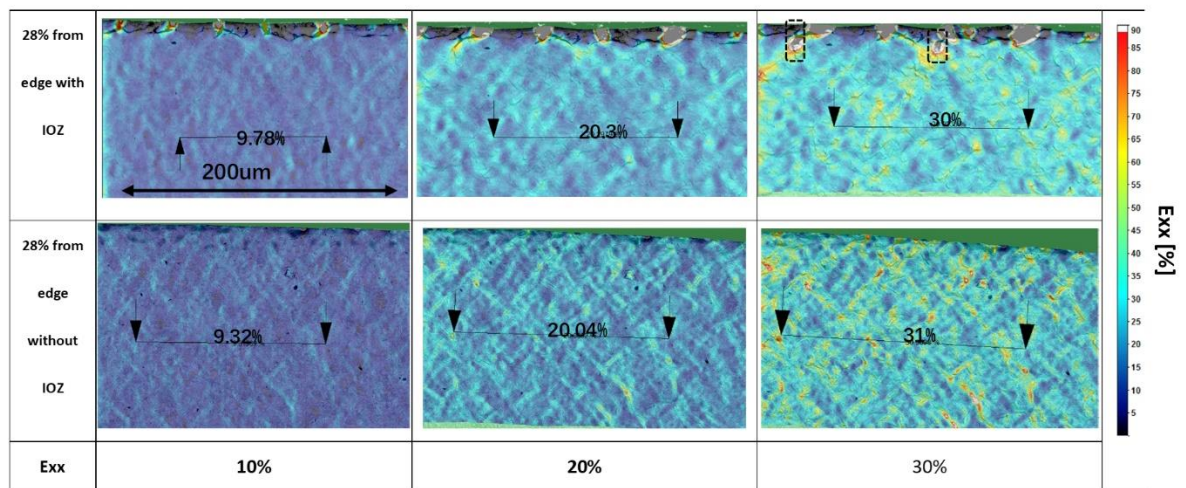
Fig. 101. DIC results processed from BSE images. Samples are taken from the mid-length of coil 1, at 28% of the total width. Grips with 2.5mm punch tip and 20mm supports span were used. The frames are 200x100μm. the Exx value of the sample matrix are measured by the virtual extensometer.

None of the bending samples mentioned above cracked at the maximum punch stroke as the annealed samples show good ductility. In this case, a different, but weaker sample is chosen to give some idea about how failure would occur in sheet metal. The 3mm thick hot rolled and cooled DP1000 Steel A samples are selected. The bending samples are taken from the head-coil (between location 1 and 2, refer to Table 2)with no IOZ formed. These samples failed completely after bending by using the test series 1 grip configurations.

During bending, slip bands formed and eventually resulted in micro-voids nucleation. The structure of micro-voids is shown in Fig. 102 (c), where the more prominent pore in the middle is formed at the intersection of two slip bands. A smaller pore is circled next to it, which is just about to grow. At lower magnification (Fig. 102 (a)), a high density of micro-voids is observed preferentially arranged into lines that are 45° to the loading direction (trend lines are drawn on the image). This matches with the DIC findings on the annealed samples, where higher strains tend to localise in this same direction during bending. At higher bending angle, cracks form due to the connection of micro-voids. In Fig. 102 (b), a crack can be seen propagating along a line of higher local density of micro-voids.

At the head-coil, no surface cracks were observed throughout the bending progress. In Fig. 102 (a). Also, no micro-voids are found at the subsurface ($\leqslant 50\mu m$). In contrast, 11 micro-voids are found within the area 100-150μm apart from the sheet surface. The findings from Fig. 101 and Fig. 102 provide evidence that the failure starts from the inner material when the steel surface is free from damage, whereas cracks initiate and propagate from the surface when IOZ is present.
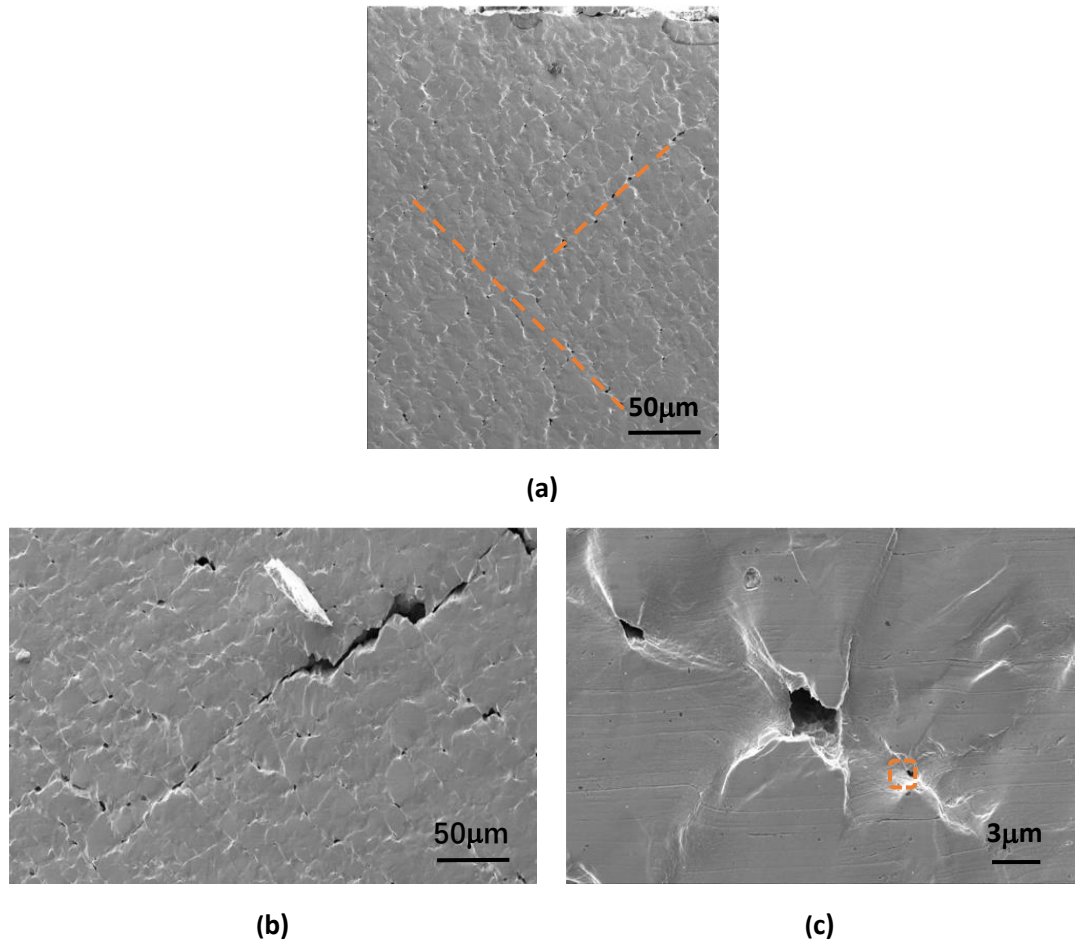
Fig. 102. SE images of hot rolled DP1000 taking during the In-situ bending test. (a), Micro-voids formed and tended to connect with each other, the preferential direction is highlighted. Sheet surface is at the top; (b), Crack formed due to the interconnection of micro-voids; (c), High magnification view of microvoids and the slip bands around them.

5.3.2. Bending - test series 2 (0.3mm punch radius and 12mm support span).

As mentioned in the experimental chapter, the bending grips are modified to allow a higher maximum bending angle and a smaller bending radius. Systematic bending tests and DIC analysis were conducted on galvanised DP1000 samples, using the procedures described for Test series 1. There are several reasons to use the new grip. Their maximum 137.5° bending angle combined with the 0.3 mm punch tip will promote failure of all samples during bending. No cracking was observed for the annealed samples described in the previous section, apart from the oxidised grain boundaries at the surface. As a result, the bendability angle of samples from different coil positions is still not clear using the punch from Series 1. From the bending curves shown in Fig. 96, the load decreases steadily after the

maximum values are reached. It indicates that the formation of voids is faster than the work hardening [102]. However, no sudden drops in load are observed, hence the load-displacement curves recorded show that fracture has not occurred. Collecting this last piece of information will provide additional insight to aid understanding of the influence of internal oxidation depth on maximum bendability. Lastly, void connection and crack development were not observed on annealed samples as it is believed the load was too low. The modified grips have been designed to allow higher loads and larger bending angle to be applied and have also designed with an overall geometry that satisfies the bending test standard [96].

As in Series 1 tests, the bending samples were taken from the mid-length of the coil which has 5% removed from both sides sampling to avoid the regions with significantly different strengths as observed in Series 1 tests (see Figure 98). As a result, in the case of the Series 2 tests, the sample taken closest to the edge (labelled as 0.87%) is about 5.87% from the original edge (location 11, refer to Table 2).

The test data for Series 2 is presented in Fig. 103. By using the 0.3mm tip and 12mm supports span, the samples from 10-20% of the coil edge reached their maximum load value at approximately 40°. As the bending angle increased, samples start to fail and the load value drops rapidly when 0.3mm punch is used, as shown in Fig. 103. The load value decreases smoothly at higher angle when 2.5mm punch is used (refer to Fig. 96). The difference is promoted by the use of the 2.2mm smaller new punch tip. When 12mm supports span is used, the strain requires to achieve 40° bending angle is 0.15, while for the 20 mm support span used in Series 1, the strain at maximum load was around 0.21.
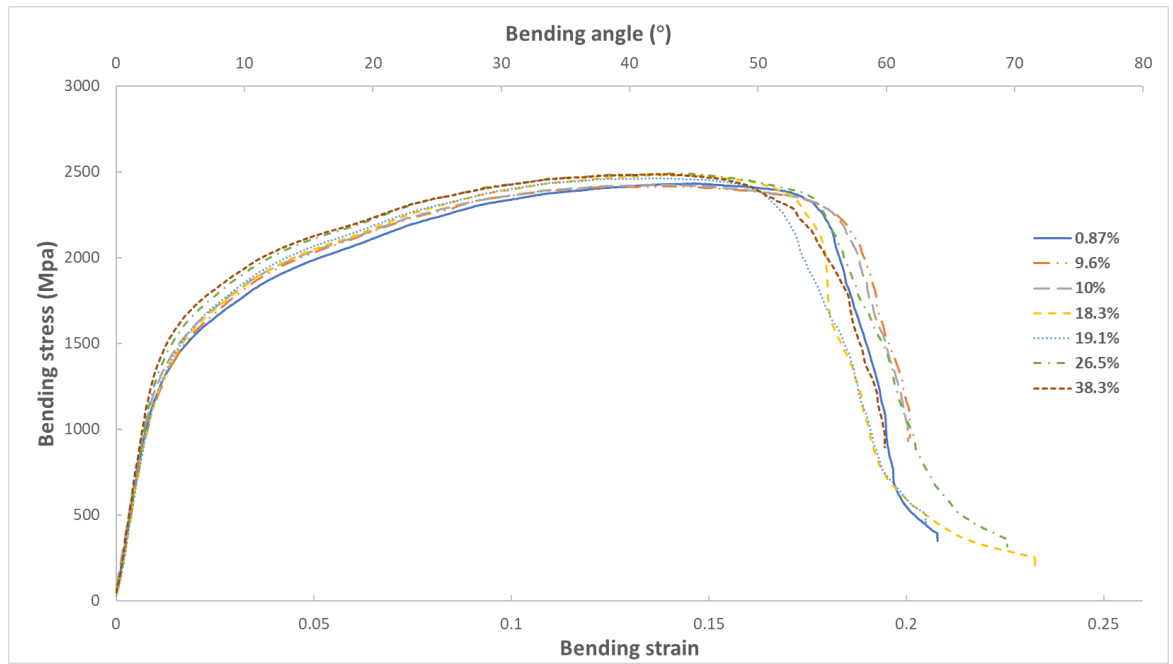
Fig. 103. Bending curves of coil 2 at various edge positions. 0.3mm radius punch was used.

The Young's modulus and work hardening factors of coil 2 samples are summarised in Table 5.

The strain hardening exponent *n* can be calculated by:

$$\sigma^T = K(\varepsilon^T)^n \tag{32}$$

where σ and ε are engineering stress and strain; σ^T and ε^T are true stress and true strain. *K* is the strength coefficient, which is the stress when $\varepsilon^T = 1$

$$\sigma^T = \sigma(1 + \varepsilon) \tag{33}$$

and $\varepsilon^T = \ln(1 + \varepsilon)$ (34)

These two equations are only valid before necking.

Table 5. IOZ depth, Young's modulus and strain hardening exponent n of the coil 2 bending samples.

Coil width position	0.87%	9.6%	10%	18.3%	19.1%	26.5%	38.3%
IOZ depth (μm)	3.9	8.1	7.6	10.1	9.9	11.6	11.1
Young's modulus(10⁻⁹Pa)	134.3	132.7	132.2	137.8	136.5	142.3	152.5
Strain hardening exponent	0.3	0.28	0.28	0.29	0.28	0.27	0.26

Generally, the Young's modulus is higher for inner-width samples by compared the near-edge samples. At the start of bending, the curves should not be affected by the internal oxidation as the cracking of oxidised grain boundaries during elastic deformation is negligible. Thus, the variation in Young's modulus is assumed to relate to variation in microstructural heterogeneity (phase fractions and distributions) from sample-to-sample (refer to Fig. 95). At constant coil length, the current bending results show up to 13.5% variation in Young's modulus between samples from 0.87% and 38.3% of the coil width.

In the plastic deformation region, the oxidised grain boundaries were observed to crack quickly. Although the strain hardening exponent varies between each sample, it is clear that thicker IOZs reduce the extent of work hardening effect. A 15% difference is found by comparing the samples taken from 0.87% and 38.3% of the coil width. There is a roughly three times difference in IOZ depth between these two samples.

The maximum bending angle before failure of each sample is listed in Table 6. It is assumed that the sample starts to fail once the maximum bending stress is reached. The material from near the edge of the coil has 3.87 μm IOZ and it can be bend to 41.6° without cracking. The sample at 38.3% of the total width shows a smaller bending angle, which is 38.5°. The difference in IOZ depth between these two samples is 7.27 μm, which leads to 7.3% difference in the bending angle at fracture. From Table 6, it is clear that the bending angle at fracture drops in the presence of a thick IOZ (≥7.55μm) at the sample surface. However, the precise relationship between the IOZ depth and the critical bending angle is unknown.

Table 6. A summary of in-situ bending tests results of coil cooled samples (coil 2). Sample dimensions and IOZ depth are measured, bending stress, strain and angle at maximum load is recorded.

Bending tests DP1000 samples, 0.3mm punch radius					
% to edge	Sample width (mm)	IOZ depth (μm)	Max bending stress (Mpa)	Max bending strain	Bending angle at max stress (°)
0.87	3.64	3.87	2434	0.146	41.6
9.6	3.63	8.11	2418	0.139	39.3
10	3.63	7.55	2426	0.136	38.3
18.3	3.63	10.11	2483	0.137	38.4
19.1	3.57	9.92	2464	0.135	37.7
26.5	3.65	11.56	2492	0.14	39.3
38.3	3.35	11.14	2488	0.137	38.5

The DIC map is processed from the backscattered images taken during the Series 2 tests. The critical features during the test are summarised in Fig. 104. The data presented are representative and were taken from a sample in the mid-length of coil 2, at 20% of the total width where the IOZ depth is approximately 9 μm.

At the earlier stages of bending, the deformation behaviour is similar to Series 1, tested using the 2.5mm bending tip (refer to Fig. 97). For this sample, images were taken at lower magnification, allowing more macroscopic features to be observed. In Fig. 104, images (a) and (b) show when the surface oxidised grain boundaries open and just about to propagate. Clear signs of strain localisation can be found in the DIC map. The strain bands high-lighted in (b) are emanate from the oxidised surface grain boundary, although the crack has not started to propagate at this stage. Image (c) and (d) are taken from beyond the ultimate load value (>13% bending strain). At this stage, micro-cracks starts to form, two examples are circled in (c). The data collected from previous bending tests (Series 1) ends here as maximum punch stroke is reached. An assumption was made from previous bending tests that the presence of IOZ will promote the connection of local strain fields, which will potentially lead to earlier failure of the material. The more severe bending tests (Series 2) found that cracks initiate from the oxidised sheet surface and tend to propagate along the high strain bands. In image (e) and (f), surface cracks grow into the steel matrix. Trend lines are added to illustrate the direction of two major cracks. The sample failed completely at the end of the bending test, (g) and (h) are the last images

taken within the scanned area. By comparing image (e) and (g), the left crack tends to split into two cracks during propagation (new trend line added in image g), whereas the right crack develops along the original trend line. The difference is caused by the presence of voids. For the left crack, the splitting starts once the main crack touches the void, which is circled in red in image (c). As shown in Fig. 104 (c), the voids are forming at the intersection of two (or even more) slip bands. Assuming a crack is coming from the top, once it reaches the void, it has the possibility to deflect along the direction of both of the slip bands.

Another typical void is circled on image (c) in yellow, it lies at the intersection of two strain bands refer to the DIC map (Fig. 104. (h)). The size of this void grows rapidly during bending by comparison to the others, which do not form at the intersection.

The up-to-date in-situ bending test results suggest that the intersection of slip bands prefer to occur at the grain boundaries. Therefore, the voids formation is highly influenced by the grain size, shape and phase proportion within the microstructure. In contrast, the growth and connection of voids are more dependent on the strain bands localisation and the shearing direction, respectively. The internal oxidation will lead to surface cracking at the early stage of bending. This certainly has an influence on the strain development and therefore promotes the sample failure.

(a)

(b)

(c)

(d)

(e)

(f)

Exx (%)

(g)   **(h)**
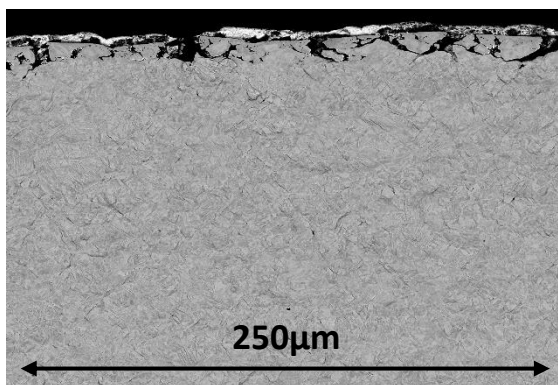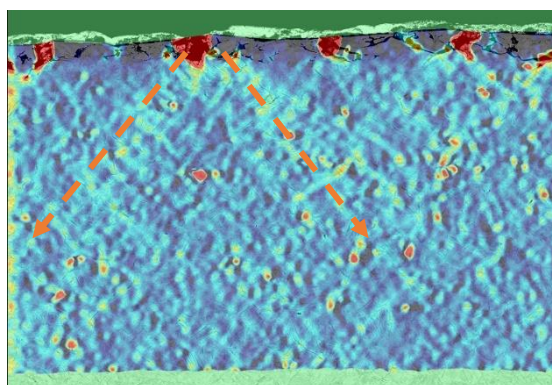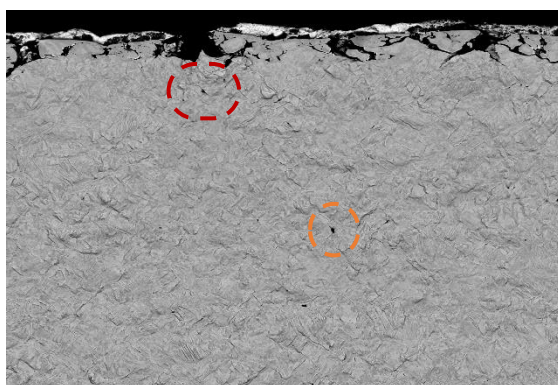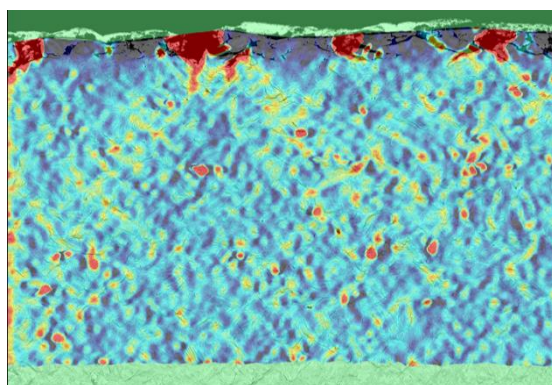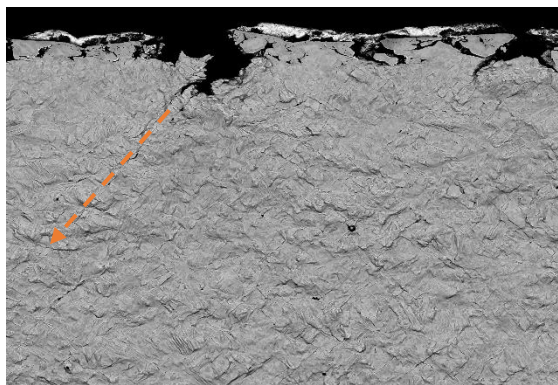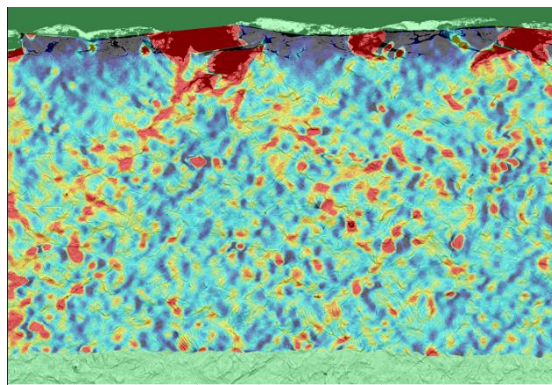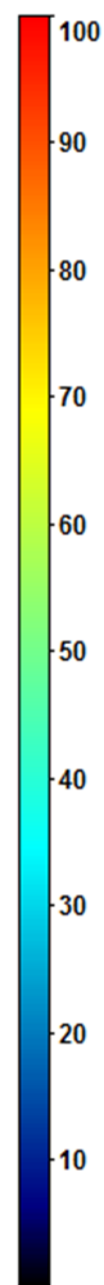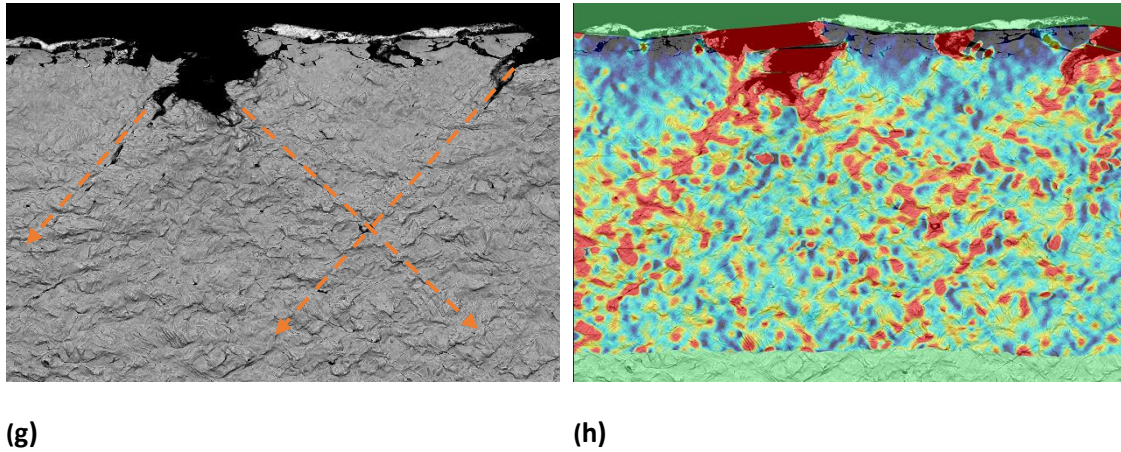
Fig. 104. BSE images and DIC maps at critical stages of the in-situ bending process, where (a) and (b) were taken at the beginning of test. (c) and (d) when voids initiated. (e) and (f) when surface crack grows and touches the void. (g) and (h) when crack passed through the void. 0.3mm bending tip and 12mm supports span used. The sample is taken from coil 2, mid-length and 20% of the width. All images were taken under the same magnification.

5.3.3. Fracture surface analyse results

The sharper bending tip and shorter supports span show several advantages, as mentioned earlier. The bending stage and grips are designed to allow cross-section analysis of the bending samples. However, this design does not allow viewing from the top. From previous bending tests, surface cracks initiation and propagation are found and the samples are failed at the end of tests. However, the cracks captured by SEM are usually not the primary crack, which leads to failure, as shown in Fig. 105 (a). Although the frame was focused at the top surface and vertical to the punch tip, the major crack was present to the left and outside of the frame.

A top view image was taken after the bending (as shown in Fig. 105 (b)), the crack lies on the centre at the mid-width and deflected while approaching the sides. The sample width is a constant value before bending, but curvature was found at both sides after bending, trend lines are added at one side. It proves that the width value is shrinking under tension and expanding under compression.

The grains at the mid-width are tightly surrounded by each other, so the deformation motion of these crystals are constrained. The crystals at mid-width are more likely to fail when comparing to the side due to limited relaxation. In contrast, the crystals at the sample side have at least one face free against each other. The bending leads to tension or compression of the crystal along the x-direction. Therefore

the crystals at sample sides can either shrink or expand in the y-direction to keep the volume constant, which reflects as shrinking or expanding in width macroscopically. The curvature high-lighted (orange) in Fig. 105 (b) is believed to alter the local hardening exponent; this explains the reason for crack deflection while approaching the sides.

(a)

(b)
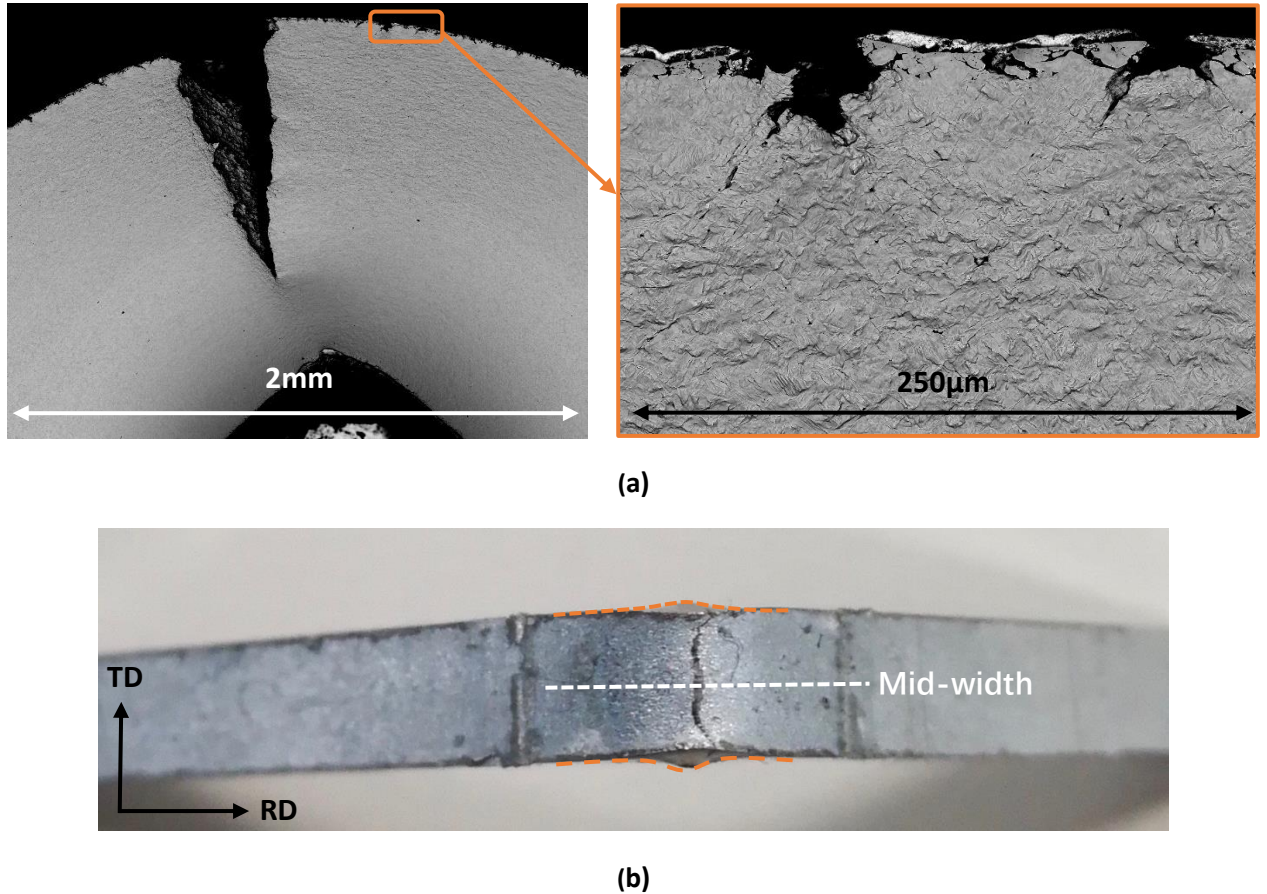
Fig. 105. Macroscopic view of the fractured sample, (a), from the cross-section; (b), from the top.

As a result, the first crack is more likely to initiate at the mid-width and located vertically to the bending tip. The current bending-stage configuration cannot see the first crack initiation. Also, the location of deflected crack at the cross-section is not predictable. The fracture surface is characterised by SEM with the function of extra depth in focus. Two samples are taken from the coil 2, both of them have approximately 10 μm thick internal oxidation layer. One of the samples has surfaces polished before bending to remove the IOZ, the fracture surfaces of these two samples are compared. From the

bending curves illustrated in earlier tests, no sudden drop in load value can be seen from any of the samples. The fracture surfaces illustrated in Fig. 106 and Fig. 107 again proved that the DP1000 samples have outstanding ductility. A high proportion of dimples and voids are found on the fracture surface combined with a minority of cleavage planes. At higher magnification, more intergranular fractures are found at the surface of the unpolished sample, as shown in Fig. 106 (b) and (c). This corresponds to the easy opening of the oxidised grain boundaries within the internal oxidation layer. Dimples dominated the fracture surface beyond the IOZ, the cracking mode is now transforming from intergranular to transgranular. Shear zones are found in this sample and an example is shown in the image (b). Most of the shear zones are found below the IOZ in this sample. Pokluda *et al.* [102] explained that the shear zones are areas, where the crack was initiated by ductile fracture accompanied by long-range shear coalescence of microvoids with the notch root. The notch roots in this sample are the oxidised grain boundary tips. It provides evidence that the steel sheet fails from the surface when IOZ present, this matches with the previous results from the in-situ bending tests and DIC analyses.
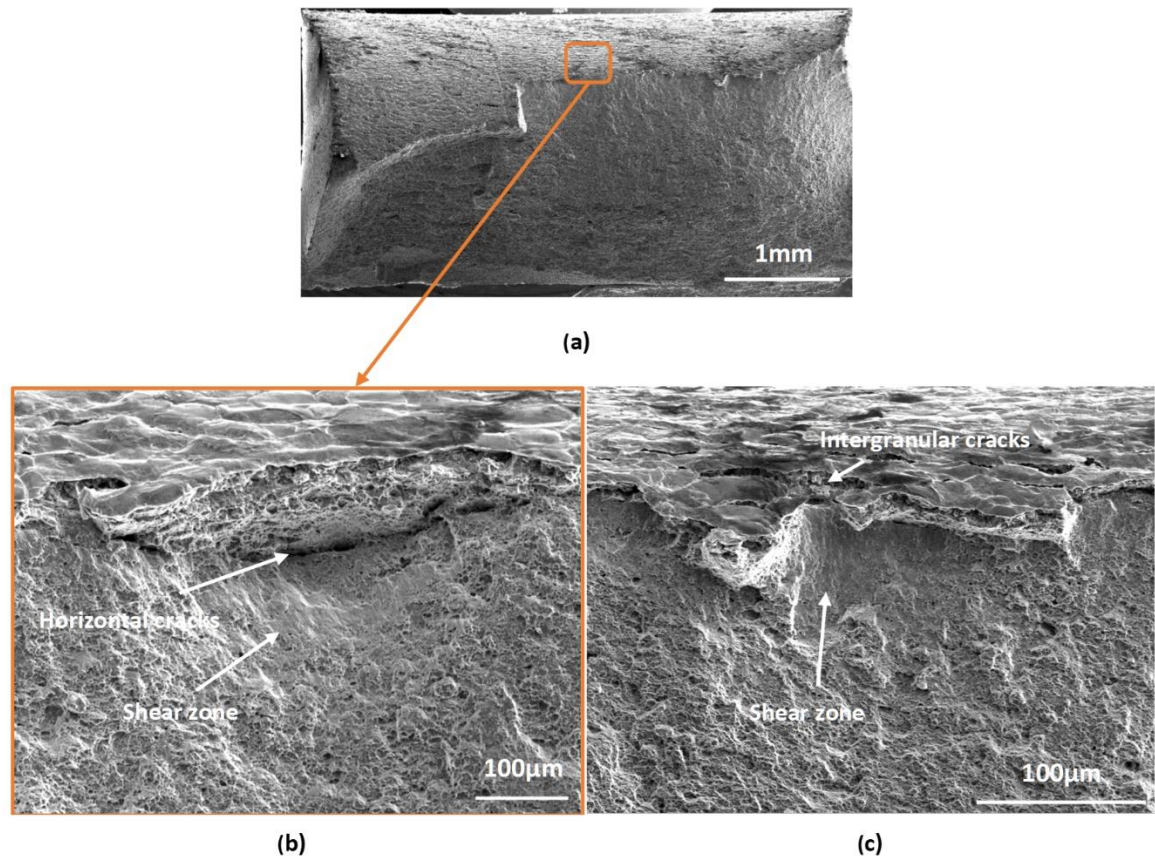
Fig. 106. The fracture surface of the DP1000 sample with 10 µm thick internal oxidation layer. The positions of intergranular cracks, long horizontal cracks and shear zones are labelled. Image (a) is an overview of the fracture surface, (b) and (c) are taken at higher magnification near the sample surface.

Fig. 106 (b) is a higher magnification view of the circled area in image (a). Unlike the other positions, a long horizontal crack is found at approximately 80µm into the surface and followed by a deep shear zone below it. The formation of this crack should not be related to internal oxidation as its location is well below the IOZ. By reviewing the microstructure of the annealed DP1000 samples, the location of this horizontal crack matches with the banded structure, which has been illustrated earlier in Fig. 95. The nature of the banded structure is layers of grains with dissimilar phases, such as a ferrite rich layer with a ferrite + martensite/bainite layer adjust to it. Cracks are easier to initiate at the boundary of two dissimilar grains. This has been proved earlier in Fig. 98. Longer crack could happen if banded structure appears as the dissimilar grains are now becoming dissimilar layers. The banded structure is mainly formed due to microsegregation during casting or imperfect annealing process. As a result, the fracture surface characterisation proved that the bendability of UHSS is not only influenced by internal oxidation, but also the banded microtexture.

148

In contrast, the fracture surface of the sample with polished surfaces are shown in Fig. 107. In this sample, nither intergranular fracture, nor horizontal crack are found. A deeper shear zone is found at the near surface region. It can be seen in Fig. 107. (b) that the shear zones are found throughout the surface to more than 200μm in depth. An extension in the shear zone means the fracture should occur at higher strain, as less micro-defect from at the surface of this sample. Long horizontal cracks are found in this sample, as shown in Fig. 107. (c), it proved again that the steel sheet is weaken when banding structure exist. Unlike the sample with IOZ, no horizontal crack is found near the shear zone. Therefore, the band itself does not initiate crack, but it promotes crack propagation if a crack is approaching.
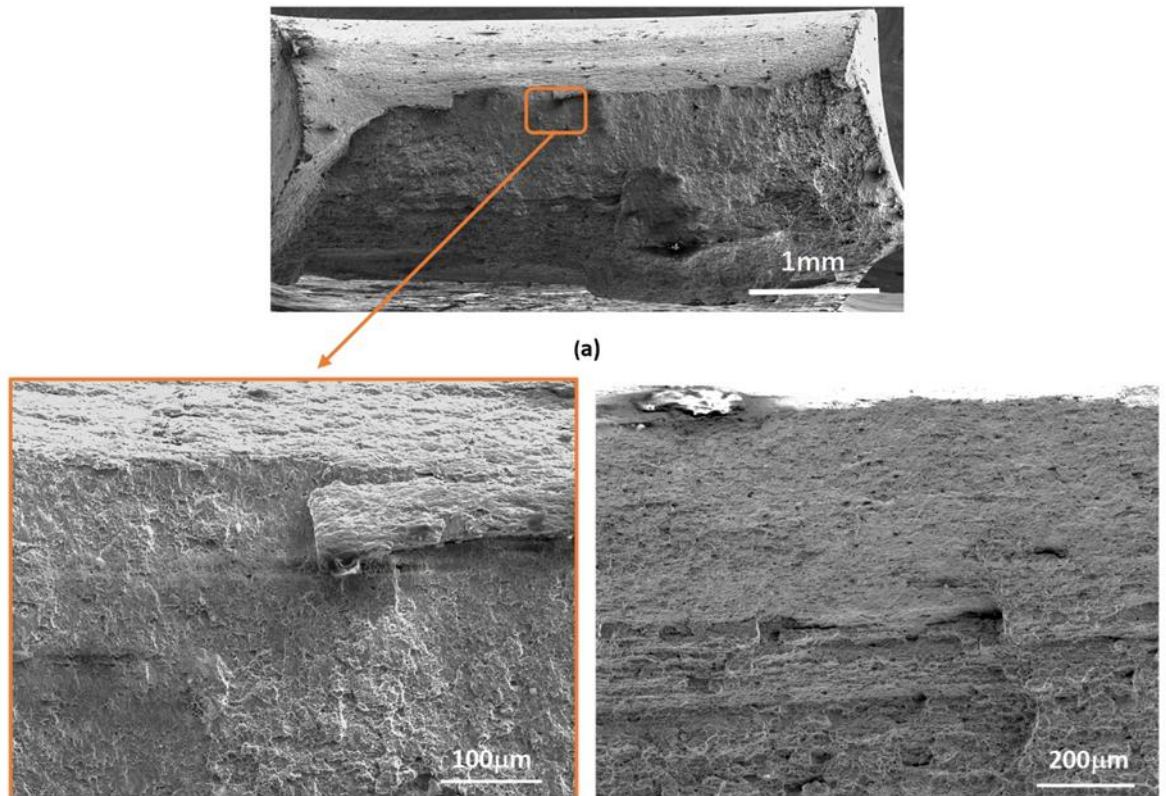
Fig. 107. The fracture surface of the DP1000 sample with internal oxidation layers polished away beforehand. Image (a) is an overview of the fracture surface, (b) and (c) are taken at higher magnification near the sample surface.

5.4. Summary

This work presented here focuses on bending characterisations of DP1000 samples taking from annealed and galvanised coils.

At the mid-coil length, a significant amount of martensite appears at 5% of the width from the coil edge. Banding structures are found in the other areas along the coil-width, the banding is more severe in the sample interior than the surface.

5.4.1. The results from bending tests with grip 1 (2.5mm punch tip and 20mm supports span):

During bending, the entire subsurface layer becomes loose and tends to separate from the bulk. Voids are found at the boundary of ferrite and martensite grains as a sign of load value drop beyond the ultimate point.

By combining the SEM and DIC results, deformation occurs evenly across the bulk materials when approaching the maximum load. Localised strains start to form at the crossover of slip bands at the maximum load, which is a sign of void formation. At the maximum punch stroke, the localised strain fields tend to connect together and form shear bands, it is a sign of void interconnection.

When IOZ is present, higher strains tend to localise at the subsurface, new cracks would form at the tip of the opened and oxidised grain boundaries. When IOZ is absent, the surface and bulk suffer from the same amount of local strains during bending, which shows no sign for the sample to fail from the surface.

5.4.2. The results from bending tests with grip 2 (0.3mm punch tip and 12mm supports span) shows:

The stress-strain curve is more dependent on the microstructure of the bulk material during elastic deformation, whereas the IOZ depth has greater influence during plastic deformation. A thicker IOZ will undoubtedly weaken the work hardening effect. The IOZ becomes thicker when approaching the mid-width of the coil, the samples here show lower bendability than at the outer-width. However, the precise relationship between the IOZ depth and the critical bending angle is unknown because of the microstructure heterogeneity need also to be considered.

By combining the SEM and DIC results, the strain bands are sourced from the oxidised surface grain

boundary although the crack has not started to propagate at this stage. At higher bending angle of all the tested samples, cracks are observed to propagate along the strain bands, starting from the oxidised and opened grain boundaries.

The presence of voids plays an important role, splitting or deflection will occur once a crack propagates towards it. The void size grows rapidly if it is located at the intersection of two concentrated strain field bands. The formation of voids is more dependent on the grain size, shape and phase proportion, whereas the growth and connection of voids are more dependent on the strain field localisation and the shearing direction, respectively.

The fracture surfaces are analysed on samples with and without a 10μm thick IOZ. When the IOZ exist, more intergranular fractures are found at the surface, whereas transgranular fracture dominated the areas beyond the IOZ. Shear zones are found close to the IOZ, which indicates the locations, where the initial cracks start during bending. Horizontal fractures appear during bending, owing to the banding texture. The interface of two adjusting bands near shear zones is more likely to crack when the IOZ is present. By comparison to the sample without an IOZ at the surface, it proved that the banding structure promotes crack propagation if a crack is approaching, although the bands themselves do not initiate a crack.

Chapter 6: Influence of coiling environment on the internal oxidation of UHSS

This chapter reports on studies of the development of scale and subscale structures during steel processing and assesses the relationship between the depth of the IOZ and bendability. To simulate the oxidation and reduction reactions taking place during steel processing, a number of heat treatments were performed on high alloyed steel and pure iron samples in controlled atmospheres. The findings aim to link decarburisation and iron oxide reduction with the development of external and internal oxides.

6.1. Introduction

From the experiments in the other chapters, it is clear that the formation of internal oxides is significantly related to the external oxidation layer. The flat steel sheet is descaled by water jet before passing through the last train of hot rolling mills to remove scales that formed earlier. The steel surface was considered to be ideally free form the primary and secondary scale before coiling, although a layer of tertiary scale will still remain [103]. In addition, when Si concentration is high, a fayalite interfacial layer will form between the iron oxide layer and the steel matrix. The oxides mentioned above have been deformed by the finishing mills. Fractures may occur, but most of the residual oxides are coiled up together with the steel sheets during the coiling process. [49]

Most of the internal oxidation reactions occur during the coil cooling process after hot rolling, and a much shallower layer of internal oxides can occur during the annealing process (refer to p. 114). It is believed that the oxygen required for internal oxidation in the hot rolled coil is provided by the external iron oxides (tertiary scale) as the tightly coiled steel sheet has limited access to oxygen. The pickling process before cold rolling removes the external iron oxide layer. The absence of external oxides reduces the formation of internal oxides significantly during annealing.

Regarding the hot rolled coil at mid-length, earlier chapters reported that the internal oxidation depth is 4 μm at the edge and 18 μm at the mid-width (refer to Fig. 85). However, the total thickness of the external oxide layer remains constant (compositions may vary) throughout the width of the coil [49]. The significant growth in the internal oxidation depth is believed to be related to the scale decomposition.

In this study, the coil cooling conditions are reproduced to understand the external/internal oxidation mechanisms. The relationship between oxide phase transformation and coiling temperature is a key factor in understanding the development of the internal oxidation zone. A route to gain insight into the role of oxidation decomposition is the analysis of residual gases to investigate if other gases (other than oxygen) are involved in the oxidation/reduction reactions and if these gases promote the local oxidation rate.

6.2. Experimental

6.2.1. IR furnace heat treatments

Two alloys were studied. DP1000 Steel A (0.2wt% C, 2wt% Mn and 1wt% Si) from the hot rolled and cooled coil is used again. All of the samples are taken from a constant length and width position of the coil to minimise the influence of microstructural heterogeneities. The high alloyed steel A samples are cut to approximately 15 x 15 mm squares to fit the crucible. One of the surfaces is ground by p400 sandpaper and then polished down to 3 μm roughness. The aim is not only to remove the original scale and subscale layer but also to produce a clean and flat surface finish, so new external and internal oxides can grow from the clean surface during the lateral furnace heat treatment.

Steel sample B is made of pure electrolytic iron with a negligible amount of carbon content (>99.995% Fe purity). The samples are cut and prepared the same way as Steel A. The pure iron samples are acting as reference samples to elucidate the influence of carbon diffusion in oxidation and reduction behaviours.

An infrared (IR) furnace was specially designed and set up for this study. There are several advantages of using the IR furnace, including a fast and controllable heating (up to 100°C/s) and the precise control of chamber atmospheres. The heating and cooling history of the tested samples are summarised in Table 7. The samples are pre-heated to 1000°C in air for around one minute; the aim is to produce an external oxide layer similar to the tertiary scale layer. According to the processing conditions in the industry, the hot rolled steel is exposed to the humid air of the industrial mill environment during the finishing rolling, between temperatures of 1050 and 860ºC, followed by water cooling in the run-out-

table before it is coiled up at 650ºC. In these experiments, the preheating temperature is set to 1000°C to simulate the temperature at the finishing mills. Subsequently, the samples are cooled down from 1000 to 650°C within 2 minutes to simulate the start temperature of coil cooling. At the same time, the furnace chamber is pumped down to around 10^{-6} mbar, followed by back-filling with dry argon gas. The temperature is kept constant at 650°C for different soaking times to allow for the development of internal oxides. Finally, the samples are cooled to room temperature. The cooling rate needs to be fast enough to avoid scale phase transformation during the cooling, but slow enough to protect the scale from spallation due to thermal shock.

Table 7. Heat treatment tests on high alloyed steel (A) and pure iron (B) samples.

		Air	Ar		
No.	Sample	Pre-heating	Coiling T (°C)	Holding time (min)	Cooling to RT (min)
1	A			0	
2	A			60	
3	A	1000°C, 1min	650	180	20
4	B			0	
5	B			60	
6	B			180	

*T: temperature, RT: room temperature.

Further, a second set of heat treatments on the two steels was conducted and in this case, variations of the cooling curve were applied. Oxidation is still done at same conditions, but the samples now undergo smoother cooling from 650°C to the room temperature, following the temperature-time paths as shown in Table 8. The cooling curves are now more closely matching the inputs for industry-modelled results (refer to Fig. 54). These tests aim to reveal any phase changes within the scale during the cooling process and to reproduce the scale/subscale microstructure that was obtained from the original coil cooled sample (refer to Fig. 77 and Fig. 109).

Table 8．Heat treatment tests on the high alloyed steel (A) and pure iron (B) samples. The cooling curve matches the industry modelling results.

		Air	Ar			
No.	Sample	Pre-heating	650-620°C	620-545°C	545-390°C	390-50°C
7	A	1000°C, 1min	60min	120min	240min	20min
8	B					

A gas spectrometer (Hidden Analytical, HPR20) was connected to the IR furnace chamber, which precisely monitors the gas compositions during the heat treatments for simulating the coil cooling. The aim is to detect the products from the oxide reduction reactions. Any variation in Ar, O_2, CO and CO_2 content will be recorded. The gas spectrometer does not have a detector targeted for CO; therefore, both N_2 and CO will be considered as the same gas due to their same atomic weight. However, this should not affect the test results as the N_2 content should be constant throughout the experiments and any variation in N_2/CO signal should arise from change in CO concentration.

6.2.2. Confocal furnace heat treatments

Samples from Steel A were prepared for heat treatment using the High Temperature Confocal Scanning Laser Microscope (HT-CSLM) [104]. The samples are surface polished as previously and cut into 3 x 3mm squares. The heating plans are summarised in Fig. 108. Three samples were heated from 200 to 1000°C with the highest achievable heating rate (approximately 4°C/s). The pre-heating process is carried out in air to simulate the oxidation before coil cooling. Once a thin scale is formed, the samples are cooled to 550, 600 and 650°C, respectively, to simulate various coiling starting temperatures. The atmosphere was switched to moist Ar once 1000°C is reached. The aim is to simulate the environment within the tightly wrapped coils, where free-flowing oxygen is absent, but a certain amount of water is present (from the descaling water jet). This is achieved by flowing the pure Ar gas through room temperature distilled water before entering the furnace chamber. The three samples are then held at 550, 600 and 650°C, respectively, for 30 minutes to allow interactions between the external and internal oxidation products. These experimental simulations of the industrial coil cooling process aim

to determine the influence of coiling starting temperature on the IOZ depth. The confocal microscope also allows the development of oxides at the top surface of the samples to be monitored in real-time.
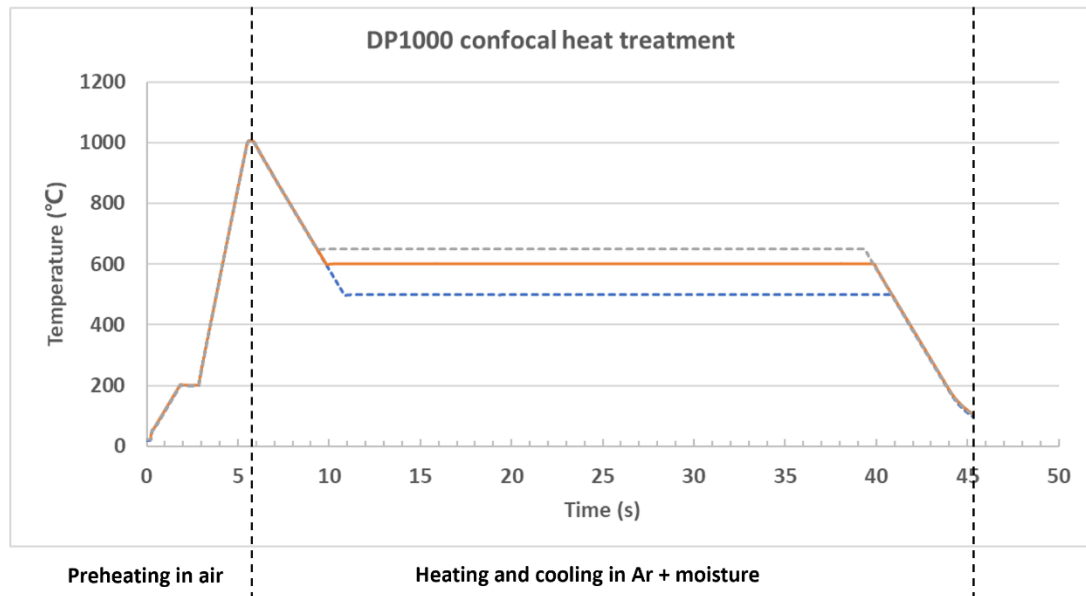
Fig. 108. Sketch of the confocal heat treatment profiles. All three samples were preheated under the same condition, but then held at three different temperatures, which are 550,600 and 650° C.

6.2.3. Microstructure characterisation

The heat-treated samples were then conductively mounted in bakelite and polished from 400 μm down to 0.05 μm for microstructural characterisation. Appropriate silica/alumina suspensions (same to the roughness of the pads) are applied onto the pads to assist polishing. A 0.02 μm non-crystallised colloidal silica suspension is used instead of the conventional 0.05 μm suspension to minimise the corrosion effect, which potentially forms porosity via a chemical attack during the last step polishing. The mounted samples were cleaned in an ultrasonic bath to remove any residual contaminants and hence improve the accuracy of EDS results.

A JEOL 7800F SEM was used in this study. The cross-sectional images were taken by using a backscattered detector, with the smallest available aperture size. A 5keV electron beam voltage was used for imaging, while 20keV was used for EDS and EBSD analyses. The working distance was approximately 10μm for imaging and EDS and 18.5μm for EBSD. The sample stage was tilted to 70° for

EBSD analysis. Also, the largest aperture size and approximately 85 nA probe current were chosen for effective EBSD data collection.

6.3. Results and discussion

A typical scale microstructure of the as-received DP1000 mid-coil sample is shown in Fig. 109. The compositions of these oxides are characterised in the earlier chapter (p. 97) and in [49]. In summary, iron nodules and loose hematite are found at the top surface, whereas a mixture of nano-sized silicon oxide and wustite grains are formed at the scale-steel interface. Large magnetite and magnetite-iron eutectic grains dominate the intermediate layer. Also, the IOZ is formed at the subsurface; the thickness varies from 2 to 18 µm depending on the coil positions.
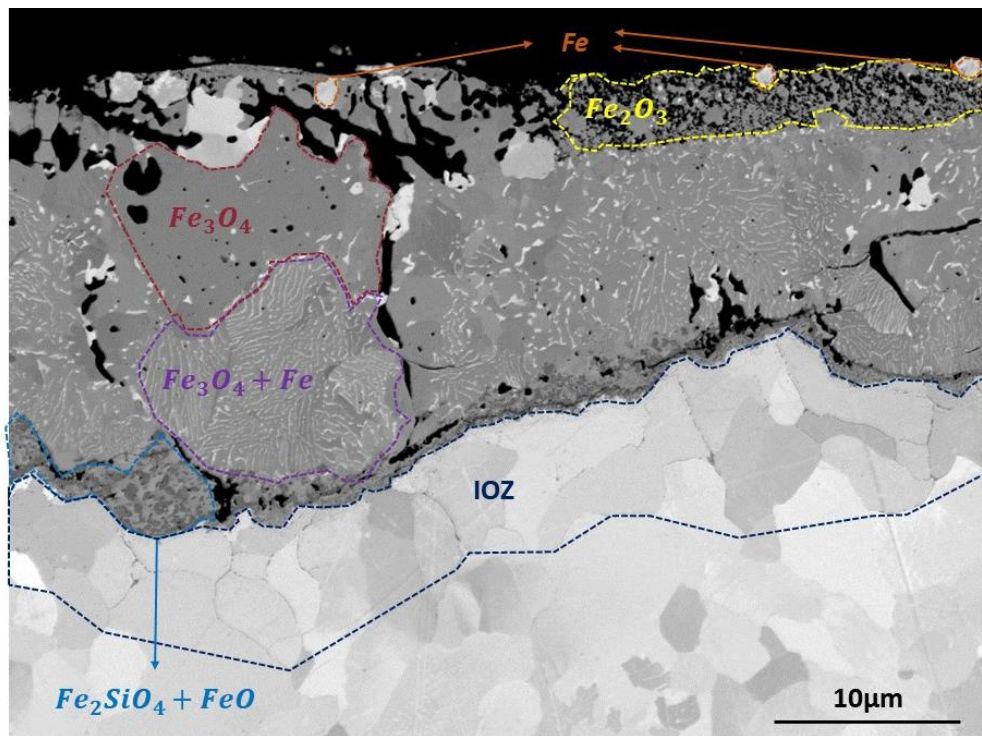
Fig. 109. Backscattered image of the typical scale and subscale microstructure at the coil colled steel sheet surface.

A higher magnification view is given in Fig. 110, where the two forms of magnetite are circled in different colours. The phase diagram (refer to Fig. 24) shows that pro-eutectic transformation should happen during cooling, and evidence of it is given from the presence of two forms of αFe- Fe_3O_4 formed during the cooling process. The pro-eutectic transformation is circled in orange, where iron

precipitates out on the grain boundaries at temperatures above 570°C. The local wustite is now no longer supersaturated in iron; therefore, no extra iron is able to precipitate out during the following Fe_3O_4-FeO transformation. This pro-eutectic magnetite layer is relatively thick because the time taken to cool from the coiling starting temperature to the eutectic temperature is slow at the inner-coils. Subsequently, the rest of magnetite follows the eutectic transformation, this is circled in blue with iron eutectic textures clearly seen within the magnetic grains. These pro-eutectic and eutectic transformation can be reviewed in earlier chapter (p. 32).

Fe_2SiO_4 nano-grains are also found as a mixture with wustite at the interface of steel and eutectic magnetite. The amorphous SiO_2 will form at the surface of Si-enriched steels. In the finishing mill conditions, there is sufficient oxygen to form FeO, and the SiO_2 reacts with the FeO to form Fe_2SiO_4 [52].
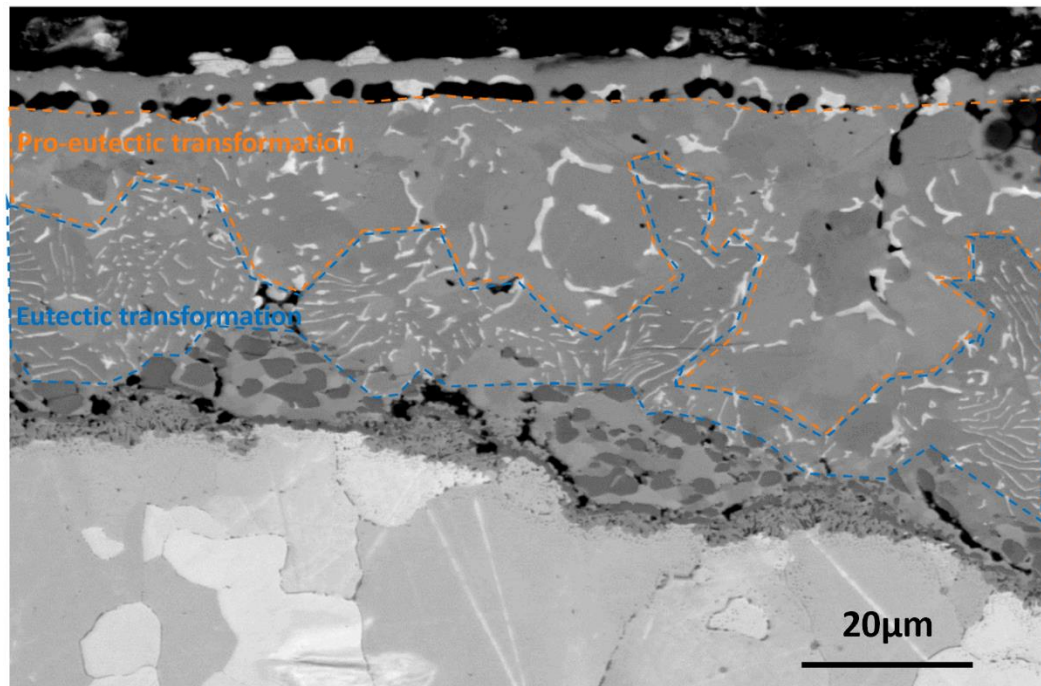
Fig. 110. Backscattered image of the steel oxides, the magnetite layer formed above the eutectic temperature is circled in orange; the magnetite layer formed below the eutectic temperature is circled in blue.

6.3.1. Pure iron reference samples

The heat-treated pure iron samples (steel B) are characterised in the same way. Fig. 111. (a). illustrates the scale structure of pre-heated sample (No. 4). The back-scattered image shows a thick and dense scale (approx. 62 µm thick) formed at the sample surface during the 1-minute pre-heating stage. Two uniform oxide layers are found within the scale as identified by using EBSD, as shown in Fig. 111. (b). A 6 µm magnetite layer forms at the top scale surface, while the thicker (56 µm) wustite layer dominates between the magnetite layer and the iron matrix. The EBSD band contrast map highlights the grain boundaries of the oxides. The magnetite layer consists of relatively equiaxed grains, whereas the wustite grains exhibit a long columnar shape. It is believed that the wustite grains initially form at the iron surface and grow in random directions. Once they reach a size that starts impingement against each other, growth in the horizontal direction is inhibited and vertical growth becomes preferential. The phenomenon of oxide growth in the preferential direction agrees with Juricic *et al*.'s [105] findings. Many reports [45, 46] state that the classic iron scale consists of hematite, magnetite and wustite in a 1:4:95 thickness ratio under isothermal conditions. It roughly matches with the scale composition in the pre-heated iron sample. The 1% of hematite layer was not identified by EBSD, which is either because of the relatively large step size chosen could not discriminate it, or it was lost due to poor edge retention during the sample preparation.
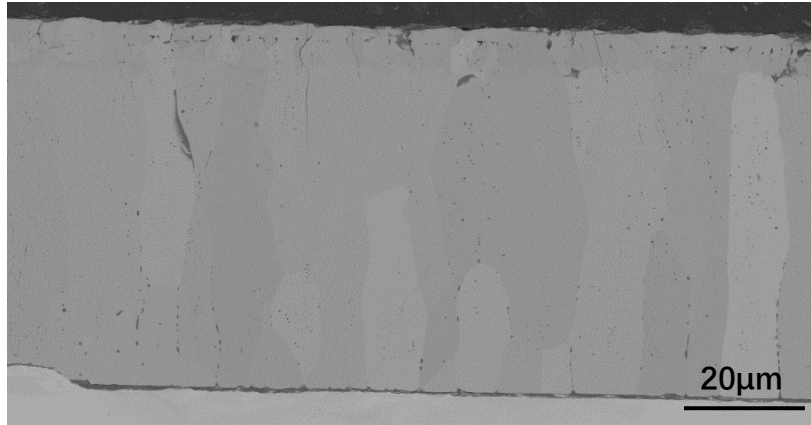
(a)
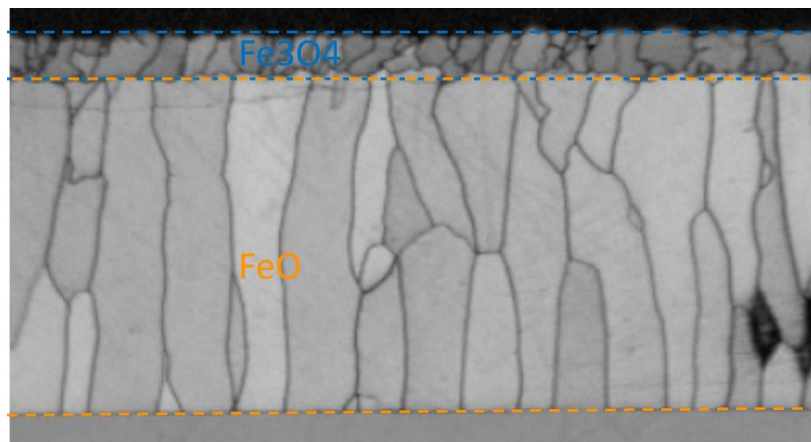
(b)

Fig. 111. The microstructure of preheated Fe sample (No.4). (a), Back-scattered image showing the scale structure; (b), EBSD band contrast image highlights the grain boundaries and localises the wustite and magnetite layers. The BSE and EBSD images are taken from the same sample but from different positions. Both microstructures were taken under the same magnification.

Two samples (No. 5 and 6) were pre-heated and followed by holding at 650°C for 1 and 3 hours, respectively. The scale structures are shown in Fig. 112. Wustite still dominated the scale in both cases. Unlike the pre-heated sample (No.4), the top magnetite layer is now reduced during the holding period, which leaves a loose powder-like layer. Detailed compositional analyses on this layer were difficult because of the powder size and uneven edge finishing. However, EDS point analysis results show that both FeO, Fe_2O_3 and Fe exist within this layer. Therefore, two reactions are assumed to occur during the holding period, which are (1) magnetite to wustite and (2) wustite to iron reduction.

Apart from the top layer, the majority of the scale is still wustite. The vertical length of the columnar grains decreases during the holding period. In the pre-heated sample (No.4), the vertical length of a

single wustite grain is same as the thickness of the wustite layer. In contrast, around 3-4 wustite grains align vertically to form the layer in the sample No.6. This shows that the original wustite grains start to recrystallise at 650°C. The total scale thickness decreases from 62 μm to 46 μm after one hour holding. This value decreases further to 39 μm after 3 hours.

On the other hand, the holding increases the porosity within the wustite layer. The area in percentage of the porosity within the scale of samples No. 4, 5 and 6 were determined to be 0.73%, 1.34% and 2.52%, respectively. Oxygen-rich inclusions are found in some of the pores, but the majority of the pores are empty.

Due to the relatively fast cooling rate (approx. 30°C/min) applied from 650°C to room temperature, the wustite phase does not have time to transform to the more stable magnetite at ≤570°C. This is an advantage of using the infrared furnace, as the real scale microstructures at high temperature can now be captured.

(a)   **(b)**
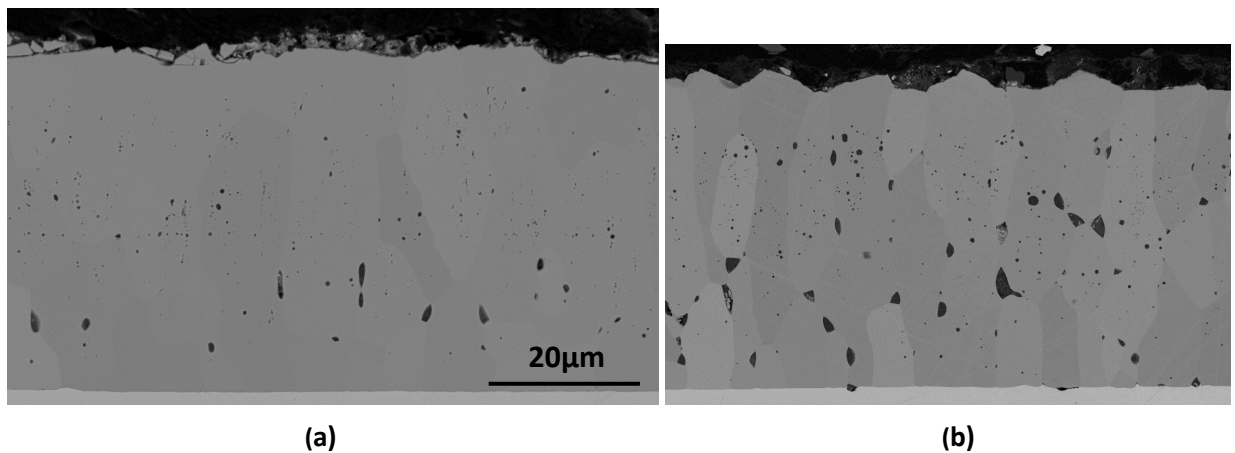
Fig. 112. The microstructure of the Fe sample's scale that was pre-heated and held at 650°C for: (a), 60 minutes (No.5) and (b), 180 minutes (No.6). The backscattered detector was used. Both microstructures were taken under the same magnification.

In contrast, smoother cooling is applied to sample No. 8. The cooling rate is now significantly slower in comparison to the other iron samples (No. 4, 5, 6). Therefore, the eutectic transformation (wustite to ferrite + magnetite) is now obtained, as shown in Fig. 113. The slower cooling leads to a more complex oxide structure, which is similar to the as-received coil cooled DP1000 sample (refer to Fig. 77 and Fig. 109). The backscattered image shows compositional contrast as various grey shades. EDS point analyses were applied in grains with of different grey scale, Fe, FeO, Fe_3O_4, and Fe0- Fe_3O_4 eutectic phase were identified and localised, as labelled in Fig. 113. The EDS point identification results are summarised in

Table 9. Although the Fe- Fe_3O_4 eutectic phase has similar Fe:O ratio to the FeO, the unique morphology of the eutectic phase makes them distinguishable. The Fe_3O_4 phase can also be distinguished from the oxide mixtures by using EDS maps, an example is shown in Fig. 114. The magnetite grains clearly show stronger oxygen signals and weaker Fe signals than the other phases (negligible amount of hematite exists). This method is also applied to other samples for quick identification of magnetite and wustite.
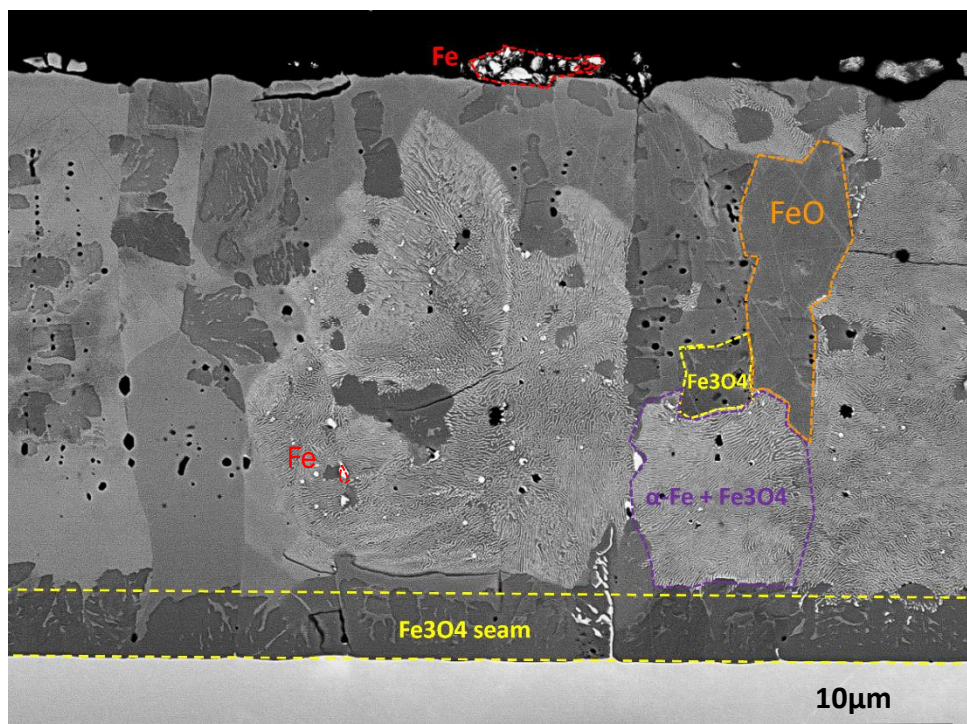
Fig. 113. Microstructure of the Fe sample scale that was pre-heated at 1000°C and coil cooled (lab simulation) from 650°C to room temperature (No.8).

Table 9. EDS point analyses result in highlighted grains in Fig. 113.

Colour highlighted in Fig. 113	Fe (at%)	O (at%)	Likely phase
(red)	90.2	9.8	Fe
(orange)	51.6	48.4	FeO
(yellow)	45.4	54.6	Fe_3O_4
(purple)	51	49	Fe+ Fe_3O_4

Secondary electron image

O
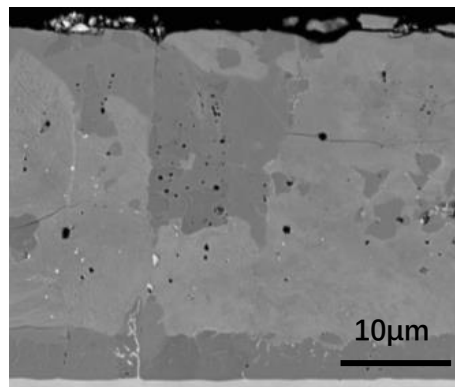
Fe
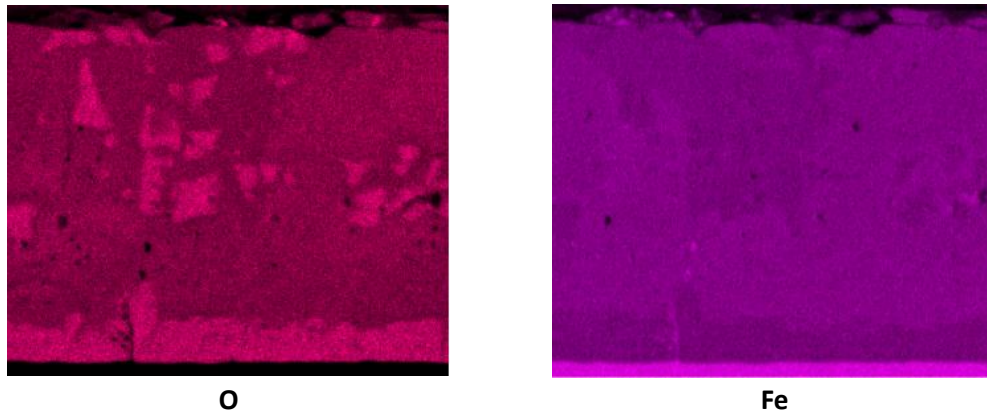
Fig. 114. EDS illustration of the of O and Fe concentrations within the scale of the lab coil cooled sample (No.8). All three micrographs share the same scale bar.

As mentioned in the literature review, neither of the FeO to Fe_3O_4 nor to Fe+Fe_3O_4 phase transformations that happen during the coil cooling simulation will generate oxygen. In addition, iron particles are found within the scale, mainly forming within the eutectic phase. These result from the iron precipitation from the super-saturated wustite during the eutectic transformation. In this case as

well, no oxygen (in) is generated during the iron precipitation.

It is now clear that the complex microstructure formed during the slow coil cooling does not actually generate any oxygen to support internal oxidation. Theoretically, oxygen is generated during the reduction of the surface magnetite layer (formed during pre-heating, refer to Fig. 111). Fig. 111 and Fig. 112 prove that the magnetite layer reduced quickly at the initial stage of coil cooling. The reduction reactions should happen before the thick wustite layer starts to transform. However, it is hard to tell if this surface magnetite layer is the primary oxygen source for internal oxidation. When the steel sheets are coiled up, the ability for oxygen ions to diffuse inward through the thick wustite layer is unknown. Regarding the overall scale thickness and the porosity, the information from all the Fe samples mentioned above is summarised in Table 10. The total scale thickness continues to decrease while exposed at high temperature, regardless of the phase changes within it. By comparing samples No.4, 5 and 6, more pores are formed when holding at high temperature. However, the amount of porosity drops massively after slower cooling (No.8) as a volume change occurs during the wustite to magnetite phase transformation. The crystal volume is 83.45Å^3 for wustite and 590.6 Å^3 for magnetite [106].

Table 10. Summary of the total scale thickness and porosity of the heat-treated pure iron samples (B). The values of porosity were measured by ImageJ.

Fe samples	No.4	No.5	No.6	No.8
Total scale thickness (μm)	62.5	45.6	38.3	31.3
Porosity (%)	0.73	1.34	2.52	0.83

6.3.2. DP1000 lab heat treated samples

The microstructure of lab heat-treated DP1000 samples are also characterised. The pre-heated scale structure (No.1) is illustrated in Fig. 115, where three layers can be seen. Similar to the pre-heated Fe sample (No4.), the top surface is formed by a 5.9 μm thick continuous magnetite layer. The thickest (22.5 μm) layer is also formed by long columnar grains directly below the magnetite layer. Unlike the Fe, a large amount of porosity (15% of the area) is present within this layer, especially at the interface between the columnar layer and the top magnetite layer.

In addition, a 5 μm thick layer forms at the scale steel interface. This layer is formed by two different oxides, which have different grey scales under backscattered imaging. This interfacial layer with this typical microstructure was characterised previously (refer to Chapter 4), and it was found to be a mixture of nano-sized silicon oxide and wustite. An EDS mapping confirmed high Si and O concentrations in this layer. The results are shown in Fig. 116. This fayalite layer was not found in any of the Fe samples as the metal contains negligible Si.

The overall scale thickness of sample No.1 (preheated steel A) is 33.4 μm. It is almost halved in comparison with the pre-heated Fe sample, although the same heat treatments are applied to both of the samples. This is also due to the difference in Si content. The diffusivity of Si in the iron oxides is slow. Therefore Si would prefer to form oxides close the steel surface [61]. The outward diffusion of Fe is inhibited once the Si riched layer is developed and covers the entire steel surface. This also explains the formation of a large amount of porosity within the intermediate layer. No Si is contained in the pure iron sample (No.4), so the diffusion of Fe and O ions are not affected. In sample No.1, the top magnetite is the only layer that remains compact and has a similar thickness to the top layer of sample No.4. This proves that the top magnetite layer is formed earlier than the other two layers, so that the diffusion of ions is not yet been inhibited by the fayalite layer.

Moreover, the EDS map results (as shown in Fig. 116) found that the upper part of the intermediate layer is actually formed by oxide with higher oxygen contents than the lower part. The upper and lower parts are highlighted in white and blue, respectively. EDS point analyses found that the upper oxide is magnetite.
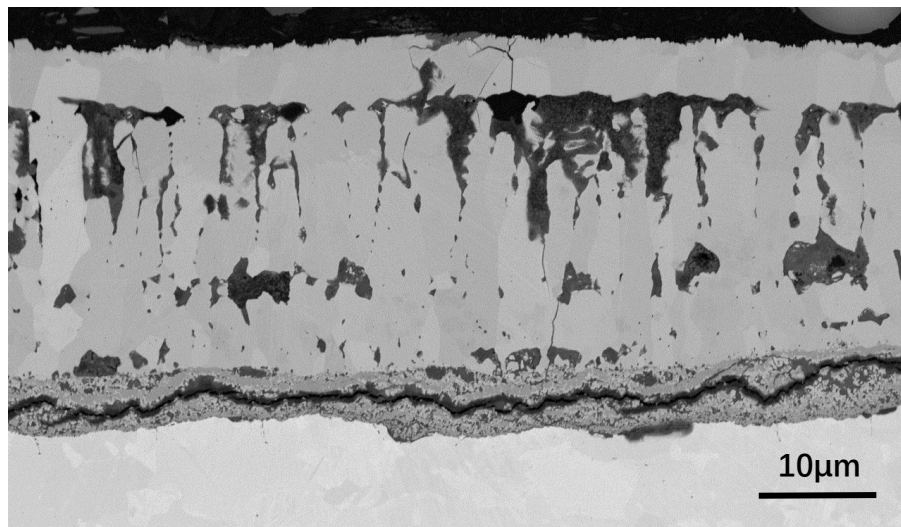
Fig. 115. Scale microstructure of the pre-heated DP1000 sample (No.1).

O   Si
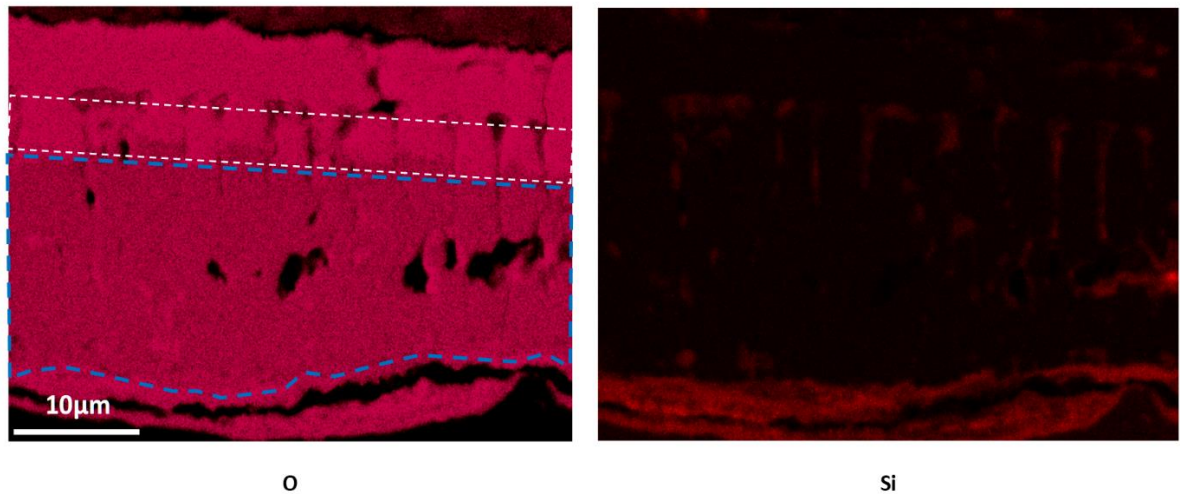
Fig. 116. BSE Image and EDS maps of the oxygen and Si concentration within the scale of the pre-heated DP1000 sample (No.1). Both of the micrographs share the same scale bar.

The scale microstructure of sample No.2 is illustrated in Fig. 117. A 3 μm internal oxidation layer forms at 650°C after 1 hour. The holding took placed in an Ar atmosphere, which means the majority of oxygen for internal oxidation is coming from decomposition of the external oxide layer. However, unlike the pure iron sample (No.5), the total scale thickness of sample No.2 remains unchanged after holding at 650°C for 1 hour. The thickness of each layer within the scale is also identical to the sample No.1. The only difference can be found within the fayalite layer. In Fig. 115, a horizontal crack is found throughout the fayalite layer. From previous experience, this type of long horizontal crack formed within the fayalite is mainly caused by sample preparation and not the actual heat treatment. All SEM samples were hot mounted in bakelite, with high temperature and pressure applied during the mounting process, which may potentially damage the brittle oxide layer. Apart from the long crack, the nano-wustite and silicon oxide grains within the fayalite layer remain dense and compact. However, after the 1 h holding period, pores are found within the fayalite layer (highlighted in Fig. 117). It was known that the fayalite layer is formed by a mixture of wustite and nano-silicon oxide. The pores are suggested to be the signs of wustite reduction. According to Fig. 50, the silicon oxide is not likely to be reduced.
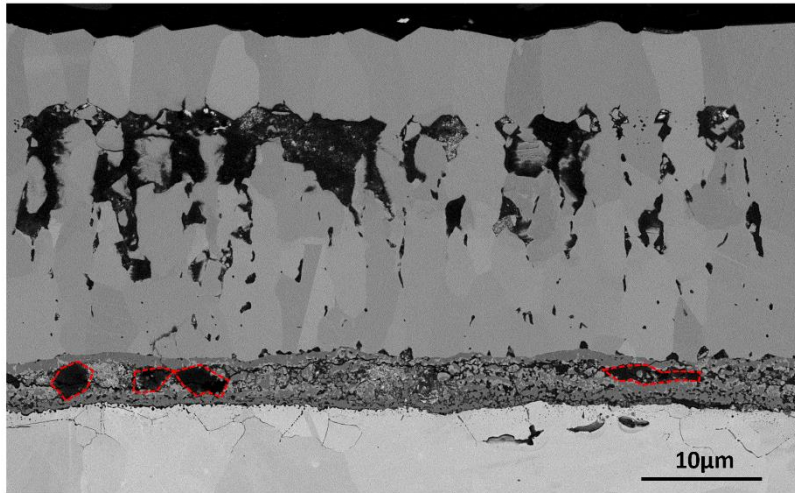
Fig. 117. Microstructure of the DP1000 sample scale that was pre-heated and held at 650°C for 60 minutes (No.2). Pores within the fayalite layer are highlighted.

When the holding time extends to 3 hours, changes are found in the scale, as shown in Fig. 118. The total scale thickness has reduced to 16 µm. The top layer thickness remains unchanged, whereas the interfacial layer shrank significantly from 20.8 to 8.1 µm.

The EDS results proved that almost all of the magnetite within these two layers transformed to wustite. As mentioned earlier, the same cooling rate is applied to samples No. 1, 2 and 3 (from 650°C to room temperature), which is fast enough to prevent phase transformations during this stage. It means that the magnetite to wustite phase transformation found in the sample No.3 occurs during the holding period. Therefore, oxygen is generated during this phase transformation.

Also, a continuous silicon oxide layer can now be seen to form at the scale-steel interface, rather than the mixture of wustite and silicon oxides found in samples No.1 and 2. More pores are found at the wustite-fayalite interface as well. These are evidence of wustite decomposition, which leaves a higher SiO_2-FeO ratio within the fayalite. The decomposition of wustite will also generate oxygen.

Both of the magnetite-wustite transformation and wustite decomposition found within the scale of sample No.3 will lead to a rise of local oxygen availability for internal oxidation. By comparing with sample No.2, the IOZ depth in this sample has increased from 3 to 4 µm.

(a)   **(b)**
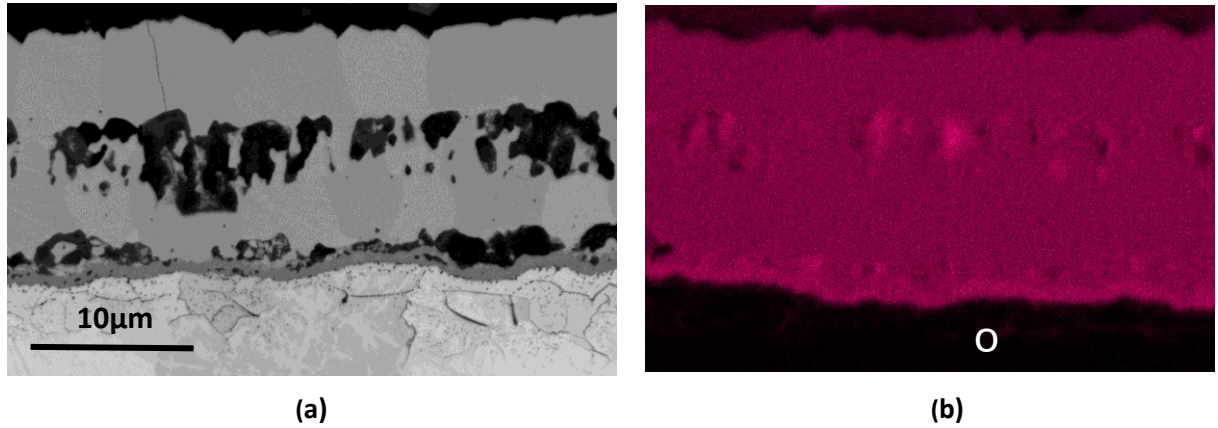
Fig. 118. (a), BSE Image of the DP1000 sample scale that was pre-heated and held at 650°C for 180 minutes (No.3); (b), EDS oxygen map of the scale. The BSE and EDS images are taken from the same sample and similar positions. Both of the micrographs share the same scale bar.

Similar to the pure iron sample No 8, the full industrial coil cooling history is simulated in the DP1000 sample No.7. By comparing with the sample No.3, the IOZ has grown further to 5μm, as shown in Fig. 119. Wustite to magnetite transformation occurs during the cooling, where a clear contrast can be seen on both of the backscattered image and the EDS map. As mentioned earlier in the sample No.8 section, either of the FeO to Fe_3O_4 or to Fe+ Fe_3O_4 phase transformation will not generate oxygen. Therefore, the growth in IOZ is resulting from the wustite reduction within the fayalite layer or dissolving of the interfacial oxide layer.

(a)   **(b)**
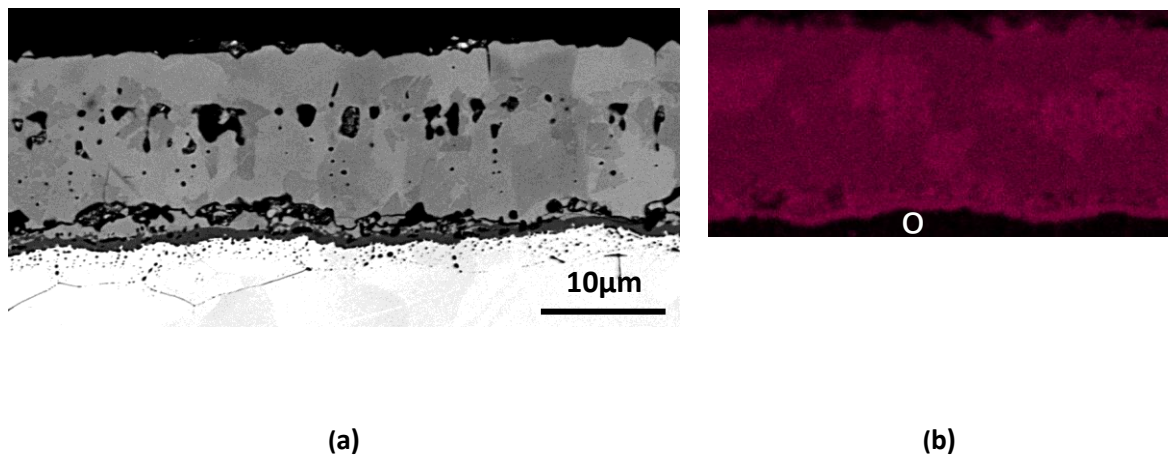
Fig. 119. (a), BSE image of the lab coil cooled DP1000 sample (No.7); (b), EDS oxygen map of the scale. The BSE and EDS images are taken from the same sample and similar positions. Both of the micrographs share the same scale bar.

6.3.3. Residual gas characterisation results

Many of the samples (No. 2, 3, 5 and 6) mentioned earlier were held at 650°C in Ar directly after the pre-oxidation in air. The Ar, O, CO and CO_2 concentrations within the furnace chamber during the holding periods were analysed. The first test was applied when no sample was in the furnace, and followed the same heat treatment and atmosphere used for the samples. The results are shown in Fig. 120. In this empty chamber test, >99.9% of the residual gas measured from the furnace is Ar. The Ar curve is not plotted in the following figures resulting from the sample tests as it is not involved in either of the iron/steel oxidation or reduction reactions. The other gases are showing relatively high signals at the beginning of the holding but decrease quickly, reaching negligible levels within 3 minutes. These high signals are influenced by the residual gases or contaminates within the gas pipes and the chamber. The values become stable at approximately 35 minutes. The proportions of O, CO and CO_2 measured from the empty chamber test are 0.009%, 0.005% and 0.006%, respectively. It is equal to 88.09, 49.76 and 60.65 ppm in concentration, respectively.
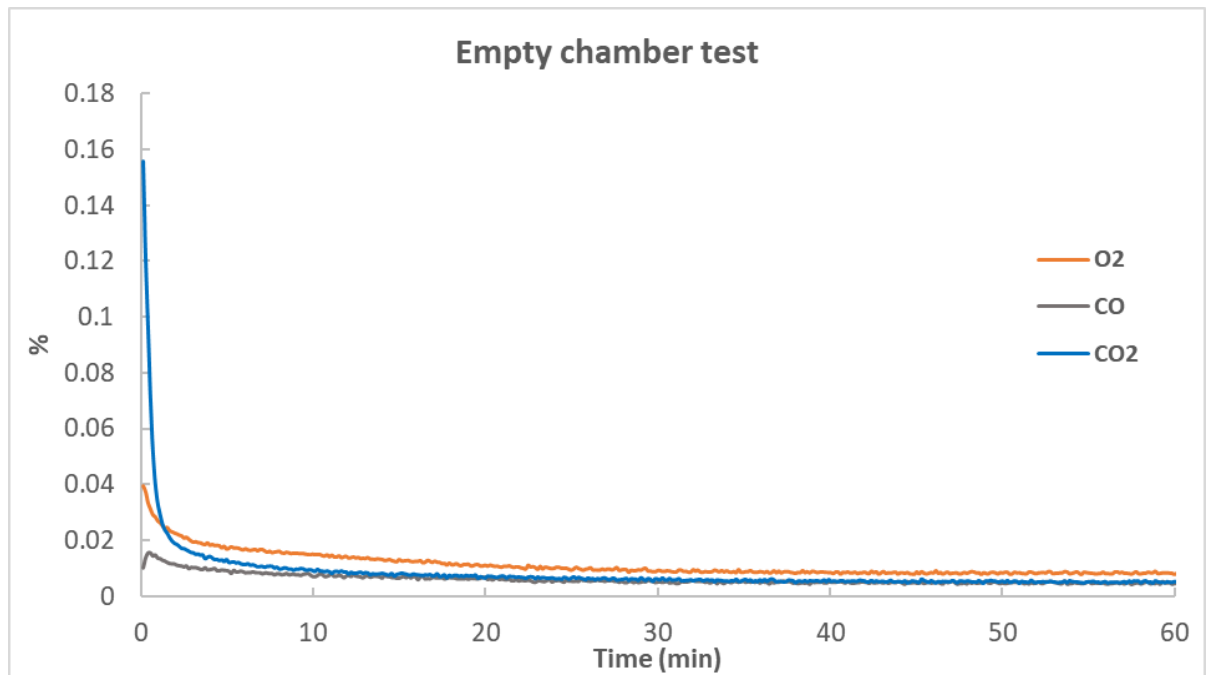
Fig. 120. Gas spectra of the residual gases from the empty furnace chamber. The values plotted are the average over three identical runs. The trial was performed at 650°C with Ar flow.

The gas spectra obtained from the pure iron and DP1000 samples are recorded while holding at 650 °C. They are compared with the empty chamber trial curves in Fig. 121. The curves are plotted to start

from 35 minutes to eliminate the influence of contaminants. By comparing with the empty chamber trial, significant amounts of CO, CO_2 and O_2 appear in the residual gases when the DP1000 sample was pre-heated and held at 650°C. At 35 minutes, the concentration of CO is 2.5 times higher than that recorded in the empty chamber run. The CO_2 and O concentrations are 5.1 and 2.4 times higher. According to the internal conversations, the discovery of oxygen proves that some of the external oxides could be reduced directly at 650°C in Ar. However, majority of the reduction reactions are achieved with the assistance of carbon. The carbon content within the DP1000 acts as the catalyst to reduce the surface oxides and generate CO and CO_2. The previous results from decabrisation characterisations (refer to Fig. 73 and p91) have confirmed the presence of outward carbon diffusion during the coiling process.

It is assumed that when holding the pure iron at 650°C, no decarburisation should occur due to the extremely low carbon content. Indeed, the CO and CO_2 concentrations found in the pure iron trial are identical to the empty chamber trial.

The only difference is the 1.22 times higher O_2 concentration found in the pure iron trial at 35 minutes of holding. The oxygen concentration decreases slowly during the holding and reaching a negligible value in around 2 hours. The value is now identical to the empty chamber trial, which corresponds to the oxygen contained in the Ar cylinder. Therefore, all the reduction reactions taking place within the pure iron sample scale should complete in 2 hours. As mentioned earlier, the wustite scale thickness of the pure iron samples continuously decreased while holding at 650 °C, even after 3 hours. The gas analysis results prove that the reduction in wustite thickness is not related to the oxygen generation and internal oxidation. In this case, for the pure iron sample, the only oxygen for internal oxidation to happen during the coil cooling is coming from decomposition of the top surface magnetite layer (refer to Fig. 111 and Fig. 112). In addition, no CO/CO_2 variation means the decomposition of this thin magnetite layer occurs spontaneously at 650°C and has no relationship with the decarburisation effect.
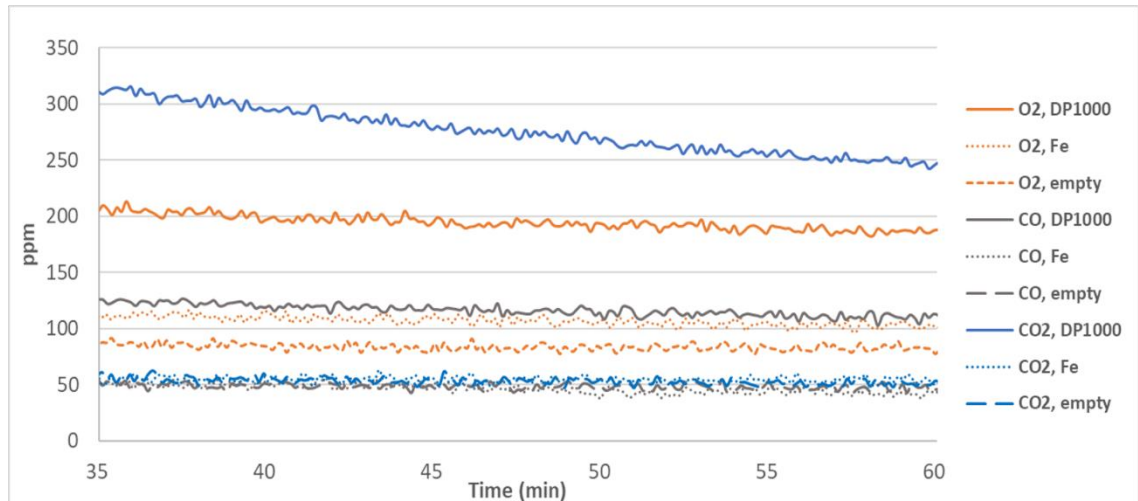
Fig. 121. Spectra of the residual gases from the DP1000, pure iron and empty chamber trials.

In contrast, the O_2, CO and CO_2 concentrations in the DP1000 trial decrease continuously and shows no sign of stopping at end of the test (3 hours), as shown in Fig. 122. By combining this behaviour with the observed microstructures, it seems that the oxygen is generated by reduction of the magnetite at the top surface layer and the upper intermediate layer (refer to Fig. 116 and Fig. 118). By comparing the DP1000 with the pure iron samples, the strong CO and CO_2 signals found in the DP1000 trials prove that the wustite grains within the fayalite layer were reduced (refer to Fig. 115, Fig. 117 and Fig. 118).
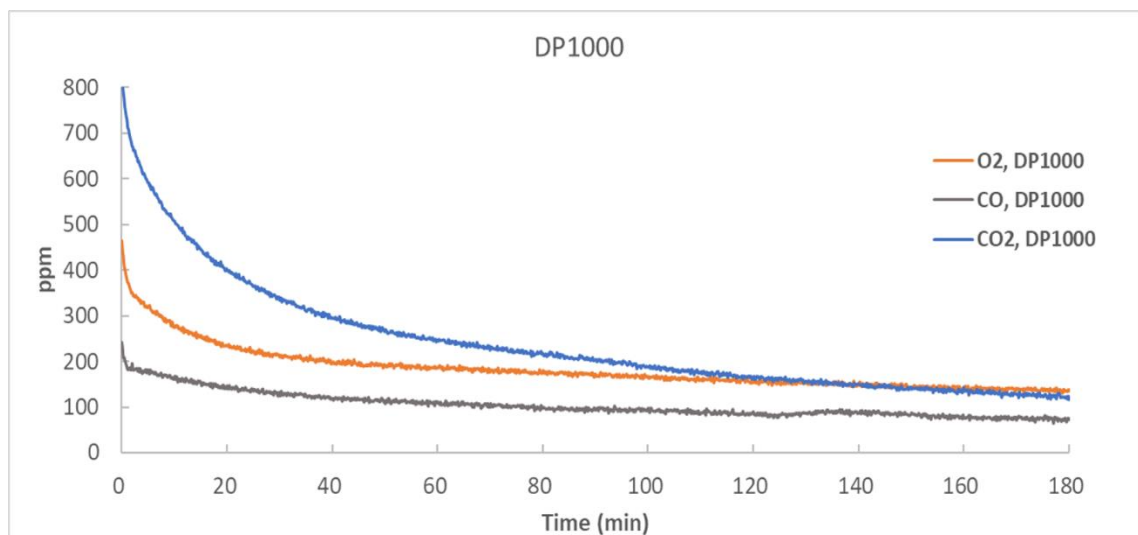
Fig. 122. Full spectra of the residual gases from the pre-heated DP1000 sample held at 650°C.

171

6.3.4. Influence of the coiling starting temperature

With respect to the confocal heat treatment results, although the top sample surface can be monitored by the microscope in real-time, the external oxides grew too fast during the pre-heating stage. The fast growth of fine and complex oxides constantly change the surface brightness and contrast. In addition, features become out of focus quickly due to the variation in the sample height and the small depth of focus of the objective lens in the confocal microscope.

By analysing the cross-sections of each sample after the heat treatment, relatively large differences in the IOZ depth are found, as shown in Fig. 123. At the standard coiling starting temperature (650°C), the internal oxidation layer grows from 0 to 20 µm after 30 minutes holding. When the other parameters stay constant, a 50°C lower coiling starting temperature leads to a 66% reduction of IOZ depth. This value further reduced to 77% if the coiling starts at 500°C.
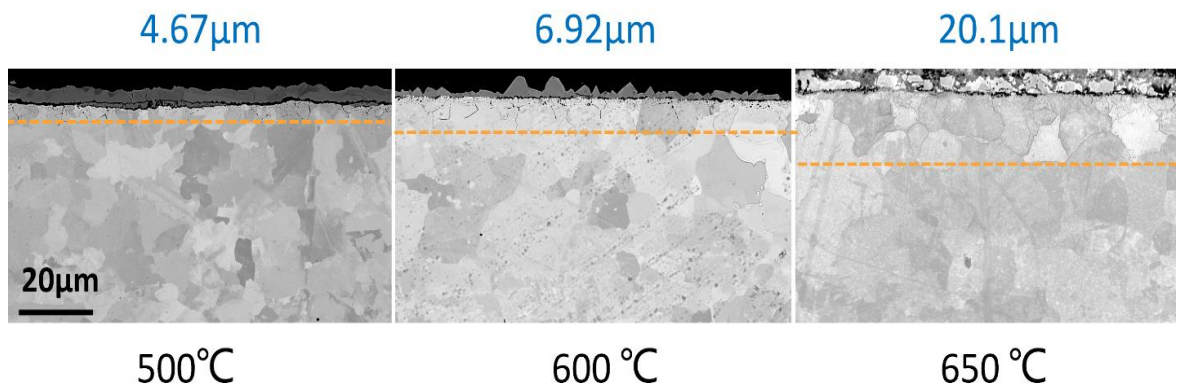
Fig. 123. Illustration of the internal oxides formed at different coiling starting temperatures. The front of subscales are highlighted by the dashed lines. All microstructures were taken under the same magnification.

The heat-treated samples are prepared by using the same methods detailed earlier. However, the integrity of the external oxide layers are completely different between these three samples. The scale remains dense and flat after starting at 500°C. At higher temperatures, the layer becomes uneven and less compact to the substrate. This phenomenon once again proved the strong scale-subscale interactions during the coil cooling, the details have been discussed in sections 6.3.1, 6.3.2 and 6.3.3. As a result, the subscale growth can be suppressed effectively by simply lowering the coiling starting

temperature. In industrial conditions, this can possibly be achieved by adjusting the flow rate of the descaling water or by applying further cooling once the sheet passes through the finishing rolling mills. However, the feasibility in reality is unknown. Any processing modification may lead to changes in the microstructure and properties of the hot rolled steel sheet. This may influence the subsequent processing steps and also alter the quality of the final products.

6.4. Summary

The iron oxide phases can be quickly identified by combing the oxygen concentration and the phase contrast information. These are obtained via EDS mapping and backscattered SEM image, respectively. By pre-heating the pure iron sample in air, small magnetite grains from the top scale layer. The majority of the scale is comprised of columnar wustite grains as a thick intermediate layer. The magnetite layer can be decomposed and leaves a loose powder-like layer after holding in the Ar. Oxygen is generated during the decomposition.

At the same time, the wustite grains are recrystallised and the local porosity increased. When slower cooling is applied after the holding period, phase transformations occur, and some of the wustite is transformed into magnetite and the iron-magnetite eutectic phases. However, no oxygen should be generated during these phase transformations.

In the case of the Fe samples, a thinner, but highly porous, intermediate layer forms on the pre-heated DP1000 sample surface. The upper part of this intermediate layer is formed by magnetite, whereas the rest is wustite. The iron diffusion paths are limited due to the formation of a fayalite layer at the scale-steel interface. The top scale layer consists of magnetite and remains compact. It is the only layer that remains compact, thus it should be formed earlier than the other layers. In this case, the iron diffusion is not yet been inhibited by the fayalite layer.

During the holding period, pores are found to form within the fayalite layer, which are signs of wustite reduction. The gas analysis results show the reduction of these wustites is assisted by the steel decarburisation as concentrated CO and CO_2 signals are detected. The top magnetite scales are reduced after 3 hours holding, and oxygen is detected. The reduction of these outer oxides is not likely to be affected by the decarburisation effect. The reduction of the external oxides is a continuous

process, which promotes the internal oxidation consistently during the coil cooling. The shrinkage of the overall scale thickness has no direct influence on the gas generation.

When the other parameters stay constant, a lower coiling starting temperature should effectively reduce the scale-subscale interaction and lead to significant IOZ depth reduction.

Chapter 7. Conclusions

7.1. Scale and subscale characterisations

Through OM and SEM characterisation, banding textures are observed in the hot rolled and coil cooled UHSS, and the texture is more significant at the head and edge of the coil. More recrystallised grains are found at the near-surface regions, which is a sign of decarburisation and loss of the alloying elements within the grains. The hot rolled samples consist mainly ferrite and pearlite while the martensite and ferrite mixture is found in annealed samples.

After the coil cooling process, the typical light grey scale consists of two distinct layers, a brighter surface layer and a darker interfacial layer. High-density of fayalite clusters appears within the darker layer.

Two other forms of oxide structures appear locally, - the darker grey scale consists an extra loose powder-like layer at the surface and the grey scale is simply thicker. The internal oxidation depth appeared to be inversely related to the scale thickness. Due to the complexity of scale structure across the coil surface, a new IOZ depth measurement method is designed based on the OM bright-field and dark-field imaging functions. Areas like fayalite deficient or poor scale adhesion regions are avoided when counting the average IOZ depth.

After in-depth analysis, wustite, magnetite, hematite, fayalite and manganese oxides are identified and localised within a typical coil cooled scale structure. The fayalite interfacial layer is actually formed by a mixture of nano-sized wustite and Si oxide. The IOZ consists of even smaller Si-enriched intergranular and transgranular inclusions. They are observed using the STEM and the built-in EDS detectors. It was also found that iron oxide phases can be quickly identified by combing the local oxygen concentration (EDS) and the phase contrast (BSE imaging) information.

7.2. Scale and subscale development through steel processing.

The scale and subscale morphologies changed during steel processing. When Mn and Si are contained within the dual phase steel, multi-layered external oxides are formed during hot rolling. This scale theoretically provides sufficient local oxygen partial pressure for internal oxidation to happen in the

tightly wrapped coil. The deepest IOZ could be found at the mid-coil and mid-width position, whereas the subsurface is only slightly influenced at the head and edge of the coil. Cracks occur at the oxidised grain boundaries after the cold rolling simulation. The IOZ is squeezed and the internal oxides are elongated parallel to the cold rolling direction. During annealing, molten zinc penetrates into the opened surface cracks and the bendability of the sheet is potentially reduced. Cross-linked horizontal cracks weaken the bonding between the subsurface and the steel matrix, which leads to coating failure during bending/forming.

7.3 Bending behaviour

During bending, the entire subsurface layer tends to separate from the bulk. Voids are found at the boundary of ferrite and martensite grains and are linked to load value drops beyond the ultimate point. By combining the BSE SEM and DIC results, deformation was observed to occur evenly across the bulk when approaching the maximum load. Localised strains start to form at the crossover of slip bands at the maximum load, which is a sign of void formation. At higher bending angles, the localised strain fields tend to connect together and form shear bands, which is a sign of void interconnection.

When an IOZ is present, higher strains tend to localise at the subsurface, and new cracks tend to form at the tips of the opened and oxidised grain boundaries. When an IOZ is absent, the surface and bulk suffer from the same amount of local strains during bending, which shows no sign for the sample to fail solely from the surface defects.

The stress-strain curve is more dependent on the microstructure of the bulk material during elastic deformation, whereas the IOZ depth has greater influence during plastic deformation. A thicker IOZ will undoubtedly weaken the work hardening effect. The IOZ becomes thicker when approaching the mid-width of the coil, and the samples from this region show lower bendability than at the outer width. However, the precise relationship between the IOZ depth and the critical bending angle before failure is unknown as the microstructure heterogeneities inherent in the steel grade also need to be considered.

At higher bending angles when using the modified bending grip configuration that allow a greater bending, cracks are observed to propagate along the strain bands, starting from the oxidised and opened grain boundaries.

The presence of voids plays an important role, and crack splitting or deflection will occur once a crack propagates to a void. The void size grows more rapidly if it is located at the intersection of two concentrated strain field bands. The formation of voids is more dependent on the grain size, shape and phase proportion, whereas the growth and connection of voids are more dependent on the strain field localisation and the shearing direction, respectively.

By looking at the fracture surfaces, more intergranular fractures are found at the surface when the IOZ is present. Transgranular fracture dominated the areas beyond the IOZ. Shear zones are found close to the IOZ, which indicates the locations where the initial cracks start during bending. Horizontal fractures appear beyond the IOZ, owing to the banding texture. The interface of two adjacent bands near shear zones are more likely to crack when an IOZ is present. The banding structure promotes crack propagation, although the bands itself does not initiate any cracks in this study.

7.4. Scale and subscale experimental simulations

By pre-heating the pure iron in air, small magnetite grains form at the top scale layer. The majority of the scale is formed by columnar wustite grains as a thick intermediate layer. The magnetite layer is decomposed and leaves a loose powder-like layer after holding in Ar. Oxygen is generated during the holding time by the decomposition of magnetite.

At the same time, the wustite grains are recrystallised. When slower cooling is applied after the holding period, phase transformations occur, and some of the wustite is transformed into magnetite and the iron-magnetite eutectic phases. However, no oxygen is generated during these phase transformations. By compare with the pure iron samples, a thinner, but highly porous intermediate layer forms at the surface of the pre-heated, Mn and Si rich sample. The upper part of this intermediate layer is formed by magnetite, whereas the rest is wustite. The iron diffusion paths are limited due to the formation of a fayalite layer at the scale-steel interface. The top scale layer is formed by magnetite. This layer remains compact as it was formed before fayalite developed a continuous layer.

During the holding period, pores are found within the fayalite layer, which are signs of wustite reduction. The gas analysis results show the reduction of these wustites are assisted by the steel decarburisation as concentrated CO and CO_2 signals are detected. The top magnetite scales are reduced after 3 hours holding, and oxygen is detected. The reduction of these outer oxides is not likely

to be affected by the decarburisation effect. The reduction of the external oxides is a continuous process, which promotes the internal oxidation consistently during the coil cooling. The shrinkage of the overall scale thickness has no direct influence on the gas generation.

When the other parameters stay constant, a lower coiling starting temperature can effectively reduce the scale-subscale interaction and lead to significant IOZ depth reduction.

1. Micro-hardness tests were applied for measurement to compare the ferrite and pearlite, and also to check the decarburisation of the annealed sheets. It was planned to check the hardness change between the oxidised subsurface region and the bulk. However, it was impracticable due to the large indent size (approximately 50 μm diagonal for 500 g load indent, as shown in Fig. 124) compared to the IOZ depth (less than 20 μm). The nano-indentation facility can effectively solve the problem, but the instrument is not yet commissioned at the end of this project. The smaller indent size and high sensitivity make it also suitable to differentiate the oxide phases within the scale.
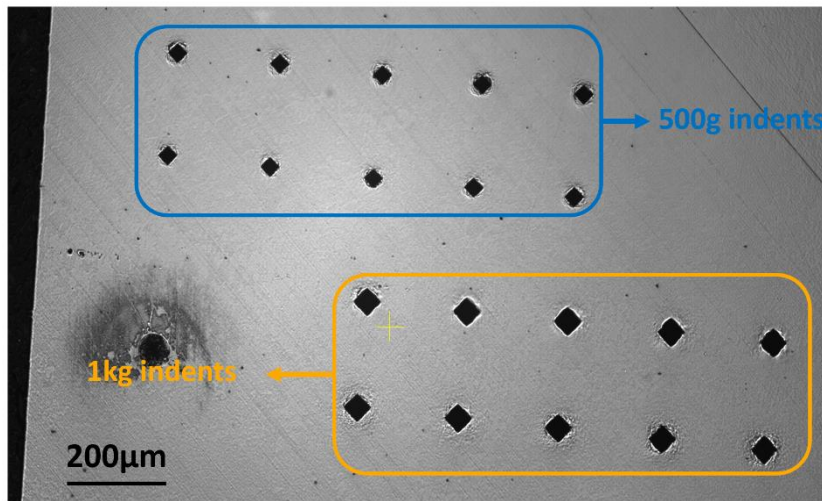
Fig. 124. 20 indent marks on the sample surface. The top 10 has indent load of 500g while the bottom 10 has 1kg load.

2. Complementary studies were performed on the nano-sized internal oxides by using SEM, STEM and EDS. The Mn-Si ratio within the oxides is constant throughout the IOZ. However, previous studies and internal documents have shown certain variation in the Mn-Si ratio, especially when a deep IOZ present. From a previous study [81], a strong Si signal and larger bulbous inclusions were found at the tips of the oxidised grain boundaries (refer to Fig. 51). However, these Si inclusions are not found in this study, from both of the SEM and TEM images. The current STEM sample was cut from the top surface of the scale and reached certain depth into the IOZ (reaching the depth li), as shown in Fig. 125. A deeper FIB cut from the surface, or a few cuts through the

179

cross-section can be performed in the subscale region to allow characterisation of the Mn-Si ratio change across the IOZ.
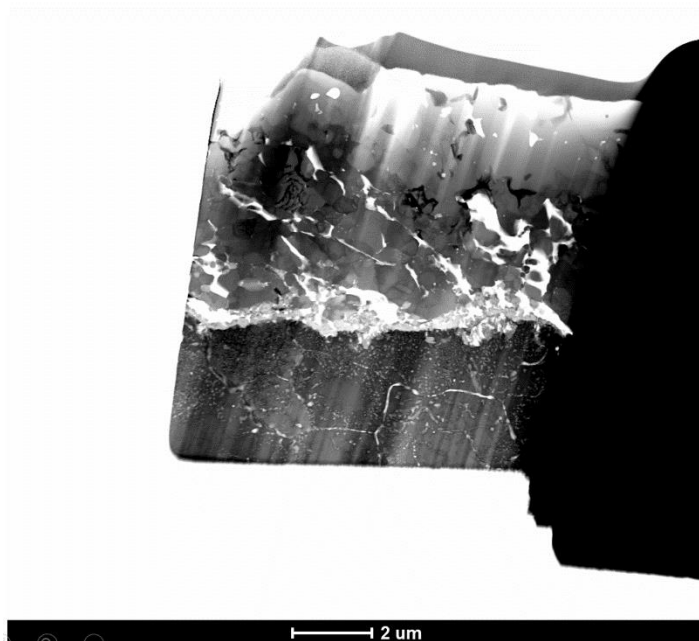
Fig. 125. FIB cut sample for TEM characterisation. The cutting starts from the scale surface and reaches around 5μm into the IOZ.

3. Lab cast and rolled samples were supplied by the industry with different Mn and Si compositions. The list of samples received is shown in Table 11. These samples were aiming to be used for the coil cooling simulations. Therefore, the influences of Mn-Si ratio on the surface/subsurface development can be determined to assist in developing an approach to minimise the internal oxidation problems with no compromise in the bendability. The lab hot rolled samples were characterised by using SEM and EBSD before applying the coil cooling simulation heat treatments. Significant inhomogeneity in grain size were found between these samples; details are shown in Appendix 2 (p. 188). Also, the surface grains size is not identical between the samples. The influence of grain size on the oxidation behaviour adds another variable that will influence the development of the IOZ. The relationship between the grain boundary oxidation and the grain size is not clear. Therefore, the original plan was put on hold due to the concerns of adding an unknown variant to the oxidation tests.

Table 11. Lab cast and rolled steel samples with varies amount of Mn and Si added in.

Sample No.	Mn	Si	Si/Mn
1	0	1	/
2	2.2	0	0
3	2.2	0.4	0.182
4	2.2	1	0.455
5	2.2	1.4	0.636

4. The in-situ tensile/bending stage was mounted onto the SEM stage to perform imaging and mechanical testing simultaneously. The stage cannot tilt toward the EBSD detector (70° tilting) due to its size and configurations. Therefore, the change in grain orientations cannot be monitored in real-time. The spring-back effect is relatively large (up to 5 degrees) for the bending test. It will be difficult to pause the test, take out the sample for EBSD mapping at specific areas and then remount it onto the bending stage to continue the test. A new Micromecha Proxima biaxial stage was installed before the end of this project. The configurations of this stage make *in-situ* EBSD and mechanical tests feasible. Therefore, in-depth research on the local (e.g. near the micro-pores, or at the internal oxidation affected grains) texture development during bending becomes possible in the future.

5. It was reported by Tanei *et al.* [77] that when holding the sample at 450°C or below, the degree of supercooling, or the driving force is sufficient for magnetite to nucleate, preferentially at the scale-steel interface to form a continuous magnetite seam. However, in this project, no magnetite seams were found in the as-received and lab cooled samples although slow cooling from 650 to the room temperature was conducted. In contrast, the fayalite layer present at the scale-steel interface and the iron oxide contained within this layer was wustite. It is worth to investigate whether this is due to the effect of a high silicon composition in the steel or the coil cooling atmospheres.

6. It is now clear that the oxygen for internal oxidation results from the reduction of iron oxides. In addition, the reduction process is probably only achievable when a sufficient amount of carbon is diffused outward from the steel matrix to the oxides. A new question arises - will CO and CO_2 (reaction products) diffuse into the steel matrix to promote the internal oxidation?

References

1. Regulation (EU) 2019 / 631 of the European parliament and of the council of 17 April 2019 setting CO2 emission performance standards for new passenger cars and for new light commercial vehicles, and repealing regulations (EC) No 443/2009 and (EU) No 510 / 2011 (Text with EEA relevance.). [cited 2019, 12; Available at: http://data.europa.eu/eli/reg/2019/631/oj].
2. D.Reche, Relations between microstructure and bendability on TRIP-aided steels for automotive products. Engineering Sciences. HAL. , 2014.
3. Vehicle safety 2016. European Road Safety Observatory. [cited 2019, 12; Available at: https://www.google.com.hk/url?sa=t&source=web&rct=j&url=https://ec.europa.eu/transport/road_safety/sites/roadsafety/files/ersosynthesis2016-vehiclesafety15_en.pdf&ved=2ahUKEwiNl93hvojnAhWDad4KHWVGAZsQFjAAegQIAhAB&usg=AOvVaw1n8g-0ttAiCfNpSHFBE741].
4. S. Tetsuo, F. Yoshimasa, K. Shinjiro, High strength steel sheets for automobile suspension and chassis use —High strength hot-rolled steel sheets with excellent press formability and durability for critical safety parts. JFE GIHO, 2004(4): p. 22–27.
5. Sheet Metal Stamping Dies& Processes. Fundamental manufacturing processes series study guide. DV11PUB9(Society of Manufacturing Engineers). [cited 2020, 02; https://manufacturing.stanford.edu/processes/SheetMetalDies.pdf].
6. K.Olsson, J.Sperle, High strength and ultra high strength steels for weight reduction in structural and safety related applications. SSAB Tunnplat AB, 1996.
7. V.A.Lashgari, Internal and External Oxidation of Manganese in Advanced High Strength Steels. Delft University of Technology. Materials innovation institute (M2i), 2014. project number MC7.07295a.
8. S.K.Hazra, P.Efthymiadis, A.Alamoudi, R.L.V. Kumar, B.Shollock and R.Dashwood, The Bendability of Ultra High strength Steels. Journal of Physics, 2016. 734(3).
9. Vlack, L. H. Van, (C) Internal oxidation of steel. Maney online, 1977. 22(1): p. 207-212.
10. M.Kaupper, M.Merklein, Bendability of advanced high strength steels—A new evaluation procedure. CIRP Annals - Manufacturing Technology, 2013. 62: p. 247-250.
11. K.Yamazaki, Y.Mizuyama, M.Oka, Y.Tokunaga, Influence of microstructure on bendability of ultrahigh-strength steel sheet. Journal of the Japan Society for Technology of Plasticity, 1995. 36: p. 973-978.
12. H.Okada, Deformation Behavior of Oxide Scale in Hot Strip Rolling. Nippon Steel & Sumitomo Metal Technical Report, 2016. 111: p. 73-78.
13. G.C.Wood, The oxidation of iron-chromium alloys and stainless steels at high temperatures. Corrosion Science, 1962. 2: p. 173-196.
14. Environmental Case Study, Automotive. 2018 [cited 2019, 08; Available at: https://www.smdisteel.org/Sustainability/Life%20Cycle%20Information/~/media/Files/SRI/Media%20Center/AutomotiveCaseStudy.ashx].
15. D.K.Matlock, J.G.Speer, Third generation of AHSS: microstructure design concepts. Microstructure and texture in Steels, 2009: p. 185-205.
16. S.Keeler, M.Kimchi, P.J.Mooney, Advanced High-Strength Steels Application Guidelines.

World Auto Steel, 2017. 6.0.

17. C.D.Horvath, Advanced steels for lightweight automotive structures. Materials, Design and Manufacturing fro Lightweight Velcles. 2010, Composites Science and Engineering: Composites Science and Engineering.

18. W.L.Roberts, Hot rolling steel. CRC Press, 1983. ISBN 978-0-8247-1345-4.

19. M.B.Bettaieb, X.Lemoine, L.Duchene, A.M.Habraken, Study of bendability of steel sheets. Verlag Stahleisen GmbH, 2008. 79(1): p. 225-232.

20. B.Pawlowski, Critical points of hypoeutectoid steel prediction of the pearlite dissolution finish temperature Ac1f. JAMME, 2011. 49: p. 311-312.

21. N.V.Landschoot, C.Dane, R.Bleeker,M.Vlot, Zinc-Magnesium coated hot dip galvanised steel. 2013, Tata Steel Europe: Cover Story Materials.

22. Hot dip galvanized steel sheet.   [cited 2018, 05; Available at: http://www.jfe-steel.co.jp/en/products/sheets/catalog/b1e-004.pdf].

23. W.Bleck, D.Beste, Surface Conditioning of High Strength Steels by Gas-Metal Reactions prior to Hot-Dip Galvanising. Galvatech 04 conference proceedings, 2004: p. 349-361.

24. M.Norden, Recent Trends in Hot Dip Galvanizing of Advanced High Strength Steel at ThyssenKrupp Steel Europe. AISTech Proceedings, 2012: p. 1791-1798.

25. Y.Nagataki, Y.Hosoya, T.Okita, S.Tsuyama, Effect of microstructure on bendability of ultra-high strength steel sheet. High-strength steels for automotive symposium proceedings. Acta University of Oulu. 1994: p. 239-244.

26. K.Mori, S.Maki, Y.Tanaka, Warm and Hot Stamping of Ultra High Tensile Strength Steel Sheets Using Resistance Heating. CIRP Annals - Manufacturing Technology, 2005. 54(1): p. 209-212.

27. W.Y.Chien, J.Pan, S.C.Tang, A combined necking and shear localization analysis for aluminum sheets under biaxial stretching conditions. International Journal of Plasticity, 2004. 20: p. 1953-1981.

28. F.Han, Z.Ai, J.Liu, Z.Jing, Robust Optimization Design of Ultra High Strength Steel Roll Forming Based on Response Surface Method Applied Mechanics and Materials, 2010. 20-23: p. 1416-1422.

29. X.Chen, H.Jiang, Z.Cui, C.Lian, C.Lu, Hole expansion characteristics of ultra high strength steels. Procedia engineering, 2014. 81: p. 718-723.

30. M.Lindgren, Cold roll forming of a U-channel made of high strength steel. Journal of Materials Processing Technology, 2007. 186: p. 77-81.

31. G.Beranger, G.Henry, G.Sanz, Le livre de l'acier. Lavoisier, 1994. [cited from Carbon Science and Technology: From Energy to Materials].

32. Understanding tension bend cracks. Rollforming Prepainted Galvanized & Prepainted GALVALUME® Steel Sheet Products. [cited 2019, 05; Available at: https://www.colourroof.com/pdf/CHOOSING%20RIGHT%20MATERIAL%20&%20PAINT%20-%20UNDERSTANDING%20TENSION%20BEND%20CRACKING.pdf].

33. J.Steninger, A.Melander, The Relation between bendability, tensile properties and particle structure of low-carbon steel. Scandinavian Journal of Metallurgy, 1982. 11: p. 55-71.

34. W.Y.Chien, J.Pan, S.C.Tang, A combined necking and shear localization analysis for aluminum sheets under biaxial stretching conditions. International Journal of Plasticity, 2004. 20: p. 1953-1981.

35.   A.Kaijalainen, L.P.Karjalainen, D.Porter, P.P.Suikkanen, Effect of Inclusions on the Properties of Ultra-high-strength Low-alloy Steel with a Martensitic-bainitic Microstructure. Conference: Proceedings of the 8th International Conference on Clean Steel, 2012.

36.   D.Huin, P.Flauder, J.B.Leblond, Numerical Simulation of Internal Oxidation of Steels during Annealing Treatments. Oxidation of metals, 2005. 64: p. 131-167.

37.   V.A.Lashgari, Internal and External Oxidation of Manganese in Advanced High Strength Steels. Delft University of Technology. Doctoral thesis, Delft University of Technology, 2014.

38.   S.Allain, A.Perlade, Modern bainitic steels for automotive applications. Arcelor Mittal, 2012.

39.   E.Billur, M.S. Billur, T Altan Challenges in Forming Advanced High Strength Steels. Engineering Research Center for Net Shape Manufacturing (ERC/NSM).

40.   D.Suh, C.Oh, H.Nam, S.Kim, Dilatometric Analysis of Phase Fraction during Austenite Decomposition into Banded Microstructure in Low-Carbon Steel. Metallurgical and Materials Transactions A, 2007. 38 (12): p. 2963-2973.

41.   E.J.Pickering, Macrosegregation in Steel Ingots: The Applicability of Modelling and Characterisation Techniques. ISIJ International, 2013. 53(6): p. 935–949.

42.   M.Graf, R.Kawalla, Scale development on steel during hot strip rolling. Acciaio, 2013: p. 43-49.

43.   Hot rolling mill plant. [cited 2019, 08; Available at: http://luhoriputed.pev.pl/hot-rolling-mill-plant.php].

44.   P.C.Pistorius, N.A.Quagraine, C.Coetzee, Descaling behaviour of stainless steel following simulated reheating. The Journal of The South African Institute of Mining and Metallurgy, 2003: p. 607-616.

45.   K.Min, K.Kim, S.K.Kim, D. Lee, Effects of Oxide Layers on Surface Defects during Hot Rolling Processes. Met. Mater. Int., 2012. 18(2): p. 341-348.

46.   R.Bhattacharya, G.Jha, S.Kundu, R.Shankar, N.Gope, Influence of cooling rate on the structure and formation of oxide scale in low carbon steel wire rods during hot rolling. Surface and Coatings Technology, 2006. 201: p. 526-532.

47.   D.P.Burke, R.L.Higginson, Characterisation of multicomponent scales by electron back scattered diffraction (EBSD). Scripta Mater., 2000. 42: p. 277-281.

48.   N.Birks, G.Meier and F.Pettit, Mechanisms of oxidation. In introduction to the high temperature oxidation of metals. Cambridge University Press. doi:10.1017/CBO9781139163903.005., 2006: p. 39-74.

49.   Y.Zhu, D.Proprentner, V.Basabe, D.Hanlon, R.Dashwood, W.M.Melfo, B.A.Shollock, Characterization of Scale and Sub-Scale Development in Ultrahigh-Strength Steels During Processing. Association for Iron & Steel Technology, 2017. ISBN: 978-1-935117-68-1.

50.   J.Janowski, J.Nowotny, M.Rekas, Non-stoichiometric compounds, surface, grain boundaries and structural defects. Springer, 1989. 276: p. 115-121.

51.   C.Wagner, Zeitschrift Fur Physikalische. Z. Phys. Chem., 1933. 21B: p. 25.

52.   N.Birks, G.Meier and F.Pettit, Oxidation of pure metals. Introduction to the high temperature oxidation of metals. Cambridge University Press. doi:10.1017/CBO9781139163903.006., 2006: p. 75-100.

53.   W.Schwenk, A.Rahmel, Theoretical considerations on phase boundary reactions and mass transfer during the oxidation of iron. Oxidation of metals, 1986. 25(5): p. 293-303.

54.   N.Bertrand, C.Desgranges, D.Poquillon, M.C.Lafont, D.Monceau, Iron oxidation at low

temperature (260-500 C) in air and the effect of water vapor. Oxidation of Metals, 2009. 73: p. 139-162.

55. M.Trull, J.H.Beynon, High temperature tension tests and oxide scale failure. Materials Science and Technology, 2003. 19 (6): p. 749-755.

56. E.J.Song, High Temperature Oxidation of Si-Containing Steel, in Computational Metallurgy. 2011, Pohang University of Science and Technology: Graduate Institute of Ferrous Technology.

57. E.J.Song, D.W. Suh, H.K.D.H.Bhadeshia, Oxidation of silicon containing steel. Ironmaking and Steelmaking, 2012. 39(08): p. 600.

58. Q.Yuan, G.Xu, M.Zhou, B.He, The Effect of the Si Content on the Morphology and Amount of Fe2SiO4 in Low Carbon Steels. Metals, 2016. 6.

59. W.Melfo, H.Bolt, M.Rijnders, D.Staalman, C. Benitocastro, D.Crowther, B. Jana, Experimental Study on Primary Scale Formation and Descalability on Steels Containing Ni and Ni+Si. ISIJ International, 2013. 53(5): p. 866-873.

60. A.Chattopadhyaya, T.Chanda, Role of silicon on oxide morphology and pickling behaviour of automotive steels. Scripta Materialia, 2008. 58: p. 882-885.

61. S.Li, Y.Liu, W.Zhang, Q.Sun, L.Wang, Effects of silicon on spring steel oxidation rate under 2% residual oxygen atmosphere. Journal of Iron and Steel Research International, 2015. 55: p. 27-60.

62. P.Gillstro, M.Jarl, Mechanical descaling of wire rod using reverse bending and brushing. Journal of Materials Processing Technology 2006. 172: p. 332–340.

63. A.Chattopadhyay, P.Kumar, D.Roy, Study on formation of "easy to remove oxide scale" during mechanical descaling of high carbon wire rods. Surface & Coatings Technology, 2009. 203: p. 2912–2915.

64. L.Bendig, M. Raudensky, J. Horsky, Descaling with high pressure nozzles, in ILASS-Europe Zurich 2-6. 2001, Brno university of technology, faculty of mechanical engineering.

65. J.Shi, D.R.Wang, Y.D.He, H.B.Qi, G.Wei., Reduction of oxide scale on hot-rolled strip steels by carbon monoxide. Materials Letters 2008. 62: p. 3500–3502.

66. L.A.Ronqueti, J.Favergeon, M.Risbet, M.Picard, Study of Grain Boundary Oxidation of High Alloyed Carbon Steels at Coiling Temperature. ABM week, 2016(53).

67. C.Wagner, Z.Elektrochem. Society, 1959. 63: p. 772.

68. J.H.Swisher, Trans. TMS-AIME, 1968. 242: p. 1035.

69. R.A.Rapp, H.D.Colson, Trans. AIME, 1966. 236: p. 1616.

70. I.Ya.Arkhipov, V.A.Batyrev, M.S.Polotskii, Internal oxidation of carburized layers of alloyed steels. Metalloved. Term. Obrab. Met., 1972. 6: p. 40-44.

71. J.L.Meijering, Internal oxidation in alloys, in advances in materials research. Wiley-Interscience, 1971: p. 1-81.

72. R.A.Rapp, The transition from internal to external oxidation and the formation of the interruption bands in silver-indium alloys. Acta Metallurgica, 1961. 9: p. 730-741.

73. R. Y. Chen, W. Y. D. Yuen, A study of the scale structure of hot-rolled steel strip by simulated coiling and cooling. Oxidation of metals, 2000. 53(5/6).

74. Metallic coated - Structural steel. [cited 2016, 09; Available at: http://www.tatasteeleurope.com/en/products-and-services/flat/metallic-coated/structural].

75.   V. V. Chashchin, E. S. Popov, A. V. Kuklev, S. S. Toropovb, V. A. Kapitanovc, Sh. B. Manyurov, Improving the controlled cooling of hot-rolled steel coils. Steel in translation, 2010. 40(9): p. 839-843.

76.   S. Birosca, G. D. West, R. L. Higginson, Microstructural investigation of the oxide scale on low carbon steel. METAL, 2005. 24.

77.   H.Tanei, Y.Kondo, Phase Transformation of Oxide Scale and Its Control. Nippon Steel & Sumitomo Metal Technical Report, 2016. 111: p. 87-91.

78.   M. Lee, F. Chang, J. Huang, Y. Lin, H. Huang, K. Kang, Development of Hot-Rolled Extra Thick Steel Coil for Pipe Piles. China Steel Technical Report, 2010. 23: p. 78-82.

79.   S.Brust, Transformation of surface oxides during vacuum heat treatment of a powder metallurgical hot work tool steel. Department of materials and manufacturing technology, Chalmers University of Technology, 2013.

80.   E.Hryha, E.Dudrova, L.Nyborg, On-line control of processing atmospheres for proper sintering of oxidation-sensitive PM steels. Jounal of Materials Processing Technology, 2012. 212: p. 977-987.

81.   R. Brocking, W. Melfo, S. Sengo, Scale appearance, pickleability and internal oxide depth of LFAA rolled in trial 523 at the DSP. Tata steel R&D, 2015.

82.   W.Schatt, K.P.Wieters, powder metallurgy: processing and materials. European Metallurgy Association, 1997.

83.   V.C.F.Holm, Elimination of oxide films on ferrous materials by heating in vacuum. National Bureau of Standards, 1942. 28: p. 569-579.

84.   H.Chen, Z.Zheng, Z.Chen, X.Bi, Reduction of hematite to metallic iron by CO in a micro fluidzed bed reaction analyser: A multistep kinetics study. Powder Technology, 2017. 316: p. 410-420.

85.   M.Z.Yi, J.S.Lin, A study on diffusion coefficient of oxygen in steel. Chinese Journal of Mechanical Engineering, 1990. 3(2): p. 194-203.

86.   E. I. Akpan, I. A. Haruna, Structural evolution and properties of hot rolled steel alloys. Journal of Minerals & Materials Characterization & Engineering 2012. 11(4): p. 417-426.

87.   F.Zhao, C.L.Zhang, Y.Z.Liu, Ferrite Decarburization of High Silicon Spring Steel in Three Temperature Ranges. Archives of Metallurgy and Materials, 2016. 61: p. 1715-1722.

88.   D.Phelan, R.Dippenaar, Widmanstatten ferrite plate formation in low-carbon steels. Metallurgical and Materials Transactions A, 2004. 35 (12): p. 3701-3706.

89.   A.Turkeli, D.H.Hirkwood, Microsegregation in Manganese Steels. Proceedings of the 4th Decennial International Conference on Solidification Processing, 1997: p. 308-311.

90.   M.Auinger, V.G.Praig, B.Linder, H.Danninger, Grain Boundary Oxidation in Iron- Based Alloys, investigated by 18O enriched Water Vapour - The Effect of Mixed Oxides in binary and ternary Fe- {Al, Cr, Mn, Si} Systems. Corrosion Science, 2015. 63: p.133-143.

91.   Y.Ma, Kinetics of Internal Oxidation of Fe-Mn-Cr Steel Alloy MaterThesis, Delft University of Technology, 2017.

92.   W.Mao, Y.Ma, W.G.Sloof, Internal Oxidation of Fe–Mn–Cr Steels, Simulations and Experiments. Oxidation of metals, 2017. 90: p. 237-293.

93.   W.Mao, R.W.A.Hendrikx, W.G.Sloof, Prediction of Oxide Phases Formed upon Internal Oxidation of Advanced High-Strength Steels. Oxidation of Metals, 2017. 89: p531-549.

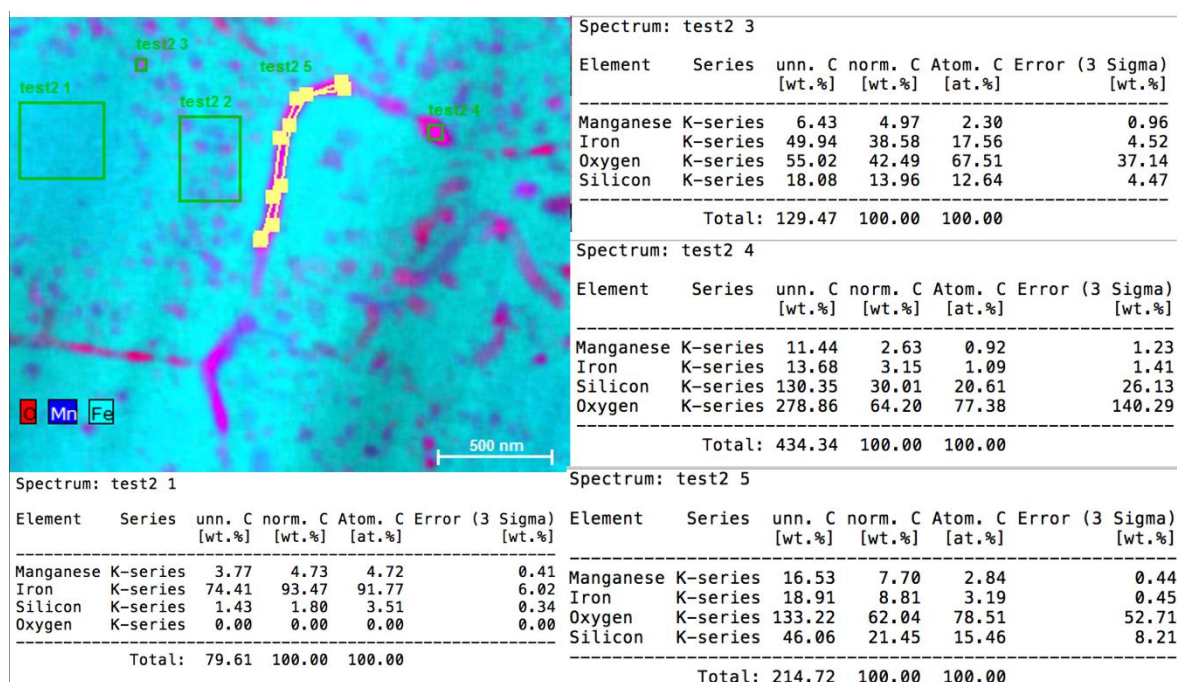94.   M.Watanabe, Pridiction of Leakage Life and Deterioation in Water for Fiberglass Reinforced

Plastic Vessels. Composite Materials, 1979. Fifth conference.

95.   LaVision GmbH, Gottingen, Product-Manual for DAVIS 8.2. 2014: p. 88-89.

96.   BS EN ISO 7435: Metallic materials-Bend test. 2005.

97.   C.Ren, X.Zhang, H.Ji, N.Zhan, Z.Qiao, Effect of banded morphology and grain size on the tensile behavior of acicular ferrite in HSLA steel. Materials Science and Engineering A, 2017. 705: p. 394-401.

98.   D.Vanaken, Engineering Concepts: Segregation and Banding in Steel. [cited 2020, 02; Available at: http://www.industrialheating.com/articles/85048-engineering-concepts-segregation-and-banding-in-steel?v=preview].

99.   J.Bian, H.Z.Lu, W.J.Wang and A.M.Guo, Development of high performance press hardening steel through microstructure engineering. 3rd International conference on advenced high strength steel and press hardening, 2016: p. 8.

100.   H.Ghadbeigi, C, Pinna, S.Celotto and J.R.Yates, Local plastic strain evolution in a high strength dual phase steel. Materials Science and Engineering, 2010. A(527): p. 5026-5032.

101.   K.Alharbi, H.Ghadbeigi, P.Efthymiadis, M.Zanganeh, S.Celotto, R.Dashwood and C.Pinna, Damage in dual phase steel DP1000 investigated using digital image correlation and microstructure simulation. Modelling and Simulation in Materials Science and Engineering, 2015. 23: p. 17.

102.   J.Pokluda, P.Andera, Micromechanisms of Fracture and Fatigue In a Multi-scale Context. Springer, 2010. 13(293): p. 96.

103.   S.Chacko, S.Vasani, A.K.Ray, Scale formation and its removal in hot rolling process. Lechler (India) Pvt. Ltd. Thane, India. [cited 2020, 02; https://shop.lechler.de/is-bin/intershop.static/WFS/LechlerIN-Shop-Site/LechlerIN-Shop/en_IN/PDF/Lechler%20India/Scale%20formation%20and%20its%20removal%20in%20Hot%20Rolling%20process.pdf].

104.   C.Slater, C.Davis, Using confocal scanning laser microscopy to characterise as-cast microstructures using cooling rates representative of thin slab direct cast steels. La Metallurgia Italiana, 2016. 2: p. 23-30.

105.   C.Juricic, H.Pinto, D.Cardinali, M.Klaus, Ch. Genzel, A.R.Pyzalla, Effect of Substrate Grain Size on the Growth, Texture and Internal Stresses of Iron Oxide Scales Forming at 450 degree C. Oxidation of Metals, 2010. 73: p. 15-41.

106.   L.Blaney, Magnetite (Fe3O4): Properties, Synthesis, and Applications. Lehigh Review, 2007. 15: p. 33-81.

Appendix

Appendix. 1. STEM-EDS analyse results on the internal oxides

Refer to p. 108, the elemental analyse results carried out by the STEM-EDS. The iron signal is weak in all oxygen-enriched regions. Moreover, Si, O and Mn signals appear at the same locations (at nm scale).

Semi-quantitative results revealed extremely high oxygen concentration (up to 79 at%) at the grain boundaries with moderate Si content (15.5 at%). Fe and Mn were at lower levels, 8.8 wt% and 7.7 wt% respectively. From the data collected, it is still difficult to tell if the internal oxides belong to SiO_2, Fe_2SiO_4 or the other phases, because the error in oxygen measuring is too high.


```
Spectrum: test2 3

Element     Series   unn. C norm. C Atom. C Error (3 Sigma)
                     [wt.%]  [wt.%]  [at.%]           [wt.%]
-----------------------------------------------------------
Manganese K-series    6.43    4.97    2.30             0.96
Iron      K-series   49.94   38.58   17.56             4.52
Oxygen    K-series   55.02   42.49   67.51            37.14
Silicon   K-series   18.08   13.96   12.64             4.47
-----------------------------------------------------------
              Total: 129.47  100.00  100.00

Spectrum: test2 4

Element     Series   unn. C norm. C Atom. C Error (3 Sigma)
                     [wt.%]  [wt.%]  [at.%]           [wt.%]
-----------------------------------------------------------
Manganese K-series   11.44    2.63    0.92             1.23
Iron      K-series   13.68    3.15    1.09             1.41
Silicon   K-series  130.35   30.01   20.61            26.13
Oxygen    K-series  278.86   64.20   77.38           140.29
-----------------------------------------------------------
              Total: 434.34  100.00  100.00

Spectrum: test2 1

Element     Series   unn. C norm. C Atom. C Error (3 Sigma)
                     [wt.%]  [wt.%]  [at.%]           [wt.%]
-----------------------------------------------------------
Manganese K-series    3.77    4.73    4.72             0.41
Iron      K-series   74.41   93.47   91.77             6.02
Silicon   K-series    1.43    1.80    3.51             0.34
Oxygen    K-series    0.00    0.00    0.00             0.00
-----------------------------------------------------------
              Total:  79.61  100.00  100.00

Spectrum: test2 5

Element     Series   unn. C norm. C Atom. C Error (3 Sigma)
                     [wt.%]  [wt.%]  [at.%]           [wt.%]
-----------------------------------------------------------
Manganese K-series   16.53    7.70    2.84             0.44
Iron      K-series   18.91    8.81    3.19             0.45
Oxygen    K-series  133.22   62.04   78.51            52.71
Silicon   K-series   46.06   21.45   15.46             8.21
-----------------------------------------------------------
              Total: 214.72  100.00  100.00
```

Appendix. 2. EBSD band contrast maps on the lab cast and hot rolled samples received from the industry.

Refer to p. 179, which is the lab cast and hot rolled samples, characterised by using SEM and EBSD. Significant inhomogeneity in grain size were found between these samples. The influence of grain size on the oxidation behaviour adds another variable that will influence the development of the IOZ. The relationship between the grain boundary oxidation and the grain size have not been studied in this project.
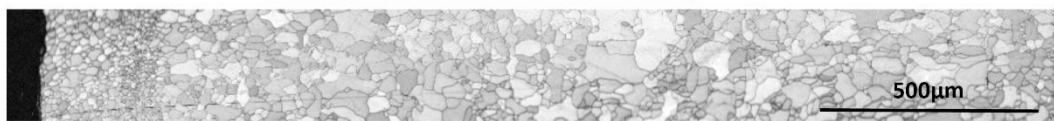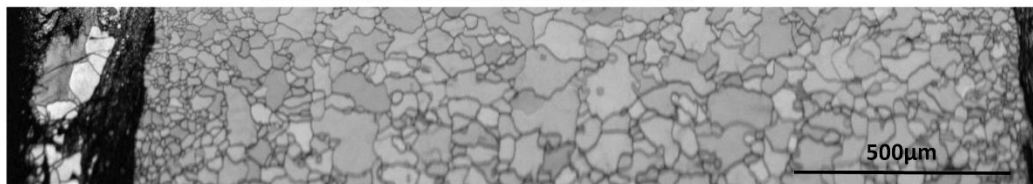
	Mn	Si	Si/Mn
1	0	1	/
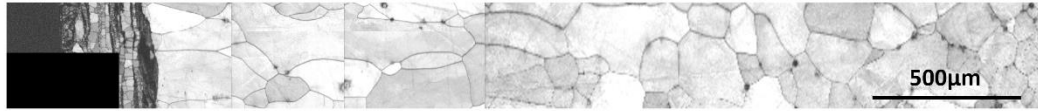
	Mn	Si	Si/Mn
2	2.2	0	0
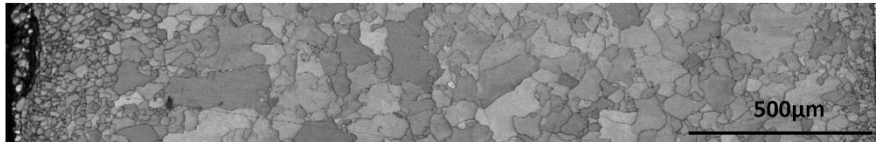
	Mn	Si	Si/Mn
3	2.2	0.4	0.182

	Mn	Si	Si/Mn
4	2.2	1	0.455

	Mn	Si	Si/Mn
5	2.2	1.4	0.636